

Computational Optical Imaging Systems:
Sensing Strategies, Optimization Methods,
and Performance Bounds

by

Zachary T. Harmany

Department of Electrical and Computer Engineering
Duke University

Date: _____
Approved:

Rebecca Willett, Supervisor

Robert Calderbank

Guillermo Sapiro

Roummel Marcia

Nirmala Ramanujam

Dissertation submitted in partial fulfillment of the requirements for the degree of
Doctor of Philosophy in the Department of Electrical and Computer Engineering
in the Graduate School of Duke University

2012

ABSTRACT

Computational Optical Imaging Systems:
Sensing Strategies, Optimization Methods,
and Performance Bounds

by

Zachary T. Harmany

Department of Electrical and Computer Engineering
Duke University

Date: _____
Approved:

Rebecca Willett, Supervisor

Robert Calderbank

Guillermo Sapiro

Roummel Marcia

Nirmala Ramanujam

An abstract of a dissertation submitted in partial fulfillment of the requirements for
the degree of Doctor of Philosophy in the Department of Electrical and Computer
Engineering in the Graduate School of Duke University
2012

Copyright © 2012 by Zachary T. Harmany
All rights reserved except the rights granted by the
Creative Commons Attribution-Noncommercial Licence

Abstract

The emerging theory of compressed sensing has been nothing short of a revolution in signal processing, challenging some of the longest-held ideas in signal processing and leading to the development of exciting new ways to capture and reconstruct signals and images. Although the theoretical promises of compressed sensing are manifold, its implementation in many practical applications has lagged behind the associated theoretical development. Our goal is to elevate compressed sensing from an interesting theoretical discussion to a feasible alternative to conventional imaging, a significant challenge and an exciting topic for research in signal processing. When applied to imaging, compressed sensing can be thought of as a particular case of computational imaging, which unites the design of both the sensing and reconstruction of images under one design paradigm. Computational imaging tightly fuses *modeling of scene content, imaging hardware design, and the subsequent reconstruction algorithms* used to recover the images.

This thesis makes important contributions to each of these three areas through two primary research directions. The first direction primarily attacks the challenges associated with designing practical imaging systems that implement incoherent measurements. Our proposed snapshot imaging architecture using compressive coded aperture imaging devices can be practically implemented, and comes equipped with theoretical recovery guarantees. It is also straightforward to extend these ideas to a video setting where careful modeling of the scene can allow for joint spatio-temporal

compressive sensing. The second direction develops a host of new computational tools for photon-limited inverse problems. These situations arise with increasing frequency in modern imaging applications as we seek to drive down image acquisition times, limit excitation powers, or deliver less radiation to a patient. By an accurate statistical characterization of the measurement process in optical systems, including the inherent Poisson noise associated with photon detection, our class of algorithms is able to deliver high-fidelity images with a fraction of the required scan time, as well as enable novel methods for tissue quantification from intraoperative microendoscopy data. In short, the contributions of this dissertation are diverse, further the state-of-the-art in computational imaging, elevate compressed sensing from an interesting theory to a practical imaging methodology, and allow for effective image recovery in light-starved applications.

In loving memory of Charles C. Harmany.

Contents

Abstract	iv
List of Tables	xii
List of Figures	xiii
List of Abbreviations and Symbols	xvi
Acknowledgements	xix
1 Introduction: Background and Summary of Thesis Contributions	1
1.1 Image Formation	1
1.2 Sampling	2
1.3 Gaussian Noise	3
1.4 Poisson Noise	4
1.4.1 Rare Events	5
1.4.2 Exponential Decay	6
1.4.3 Consequences for Image Processing	7
1.5 Compressed Sensing	8
1.6 Sparse Recovery	10
1.7 Wavelet Shrinkage	11
1.8 Compressed Sensing Theory	15
1.9 Practical Imaging Systems	16
1.10 Reconstruction From Noisy Measurements	17

1.11	Reconstruction Algorithms for Poisson Noise	18
1.12	Beyond Sparsity	19
1.13	Summary of Contributions	21
1.13.1	Image and Scene Models	22
1.13.2	Imaging Hardware	23
1.13.3	Reconstruction Algorithms	24
1.14	Conclusions	24
2	Compressive Coded Aperture and Coded Aperture Keyed Exposure Sensing	25
2.1	Introduction	26
2.1.1	Problem Formulation	27
2.1.2	Contributions	29
2.1.3	Organization of the Chapter	29
2.2	Background	30
2.2.1	Coded Aperture Imaging	30
2.2.2	Coded (Keyed) Exposure Imaging	31
2.2.3	Compressed Sensing	33
2.3	Compressive Coded Apertures for Snapshot Imaging	34
2.3.1	CCAs Generated in the Spatial Domain	35
2.3.2	CCAs Generated in the Fourier Domain	39
2.3.3	Hardware and Practical Implementation Considerations	41
2.3.4	Reconstruction	45
2.3.5	Experimental Comparison on Static Images	49
2.3.6	Optical Architecture Comparison	51
2.4	Coded Aperture Keyed Exposure Sensing for Dynamic Scenes	56
2.4.1	Sparse Transformation Sensing	57

2.4.2	Implementation and Normalization Details	59
2.4.3	Reconstruction for Video	59
2.4.4	Numerical Experiments	60
2.5	Conclusions	63
2.6	Proof of the RIP for Spatial-Domain CCA Sensing	66
2.6.1	Proof of RIP for CAKE	68
3	SPIRAL: Sparse Poisson Intensity Reconstruction ALgorithms	71
3.1	Introduction	72
3.1.1	Problem Formulation	73
3.1.2	Related Work	75
3.1.3	Contributions of the Proposed Method	77
3.2	Algorithms	77
3.2.1	Canonical Basis With Sparsity Penalty	80
3.2.2	Non-Canonical Basis	80
3.2.3	Total Variation Penalty	83
3.2.4	Partition-Based Methods	84
3.3	Algorithmic Details	86
3.3.1	Computational Complexity and Nonmonotonicity	86
3.3.2	Initialization	87
3.3.3	Termination Criteria	87
3.3.4	Convergence Proof	90
3.3.5	Uniqueness of the Minimizer	95
3.4	Numerical Experiments	99
3.4.1	Simulation Setup	99
3.4.2	Algorithm Setup	100

3.4.3	Results Analysis	102
3.5	Other Applications of SPIRAL	108
3.6	Conclusion	111
4	Photon-Limited Quantitative Tissue Analysis	113
4.1	Introduction	114
4.2	Problem Formulation	118
4.3	Tradeoffs	120
4.3.1	Incoherence of Multispectral Measurements of Tissue Mixtures	120
4.3.2	Connections to Poisson Compressed Sensing	122
4.4	Algorithms	123
4.4.1	Augmented Lagrangian	124
4.4.2	The θ Subproblem	126
4.4.3	The u Subproblem	128
4.4.4	The v Subproblem	129
4.4.5	The Lagrange Multiplier Update	129
4.4.6	Convergence of the AL Method	129
4.4.7	Sparse Poisson Intensity Reconstruction Algorithm (SPIRAL)	130
4.5	Algorithmic Comparison	131
4.6	Simulations	132
4.6.1	Simulation Setup	132
4.6.2	Simulation Result	137
4.7	Experiments on Real Data	139
4.7.1	Comparison of Nuclear Size and Density Quantified using SCA+CT and TH to Histology	142
4.7.2	Comparison of Nuclear Size and Density in Positive and Negative Excised Tumor Margins	145

4.7.3	Quantification of Nuclear Size and Density from Images of the Resected Tumor Cavity	147
4.7.4	Discussion of Results on Real Data	150
4.8	Conclusions	150
5	Multiphoton Fluorescence Microscopy Image Formation Using Exponentiated Total Variation	151
5.1	Introduction	151
5.1.1	Data Acquisition Modes	153
5.2	Problem Formulation	154
5.3	Prior Work	155
5.3.1	Adaptive Gridding	155
5.3.2	Total Variation Regularized Poisson Denoising	159
5.4	SPIRAL-TVX Reconstruction for Poisson Data	160
5.4.1	Optimization algorithm	161
5.5	Cross-Validation Method for Choosing τ	162
5.6	Experimental Results on Multiphoton Microscopy Data	163
5.7	Conclusions	165
6	Conclusion	172
6.1	Summary of Contributions	172
6.2	Future Work	174
6.3	Online Subspace Tracking from Streaming Poisson Data	176
6.3.1	Preliminary Experimental Results	179
6.3.2	Future Work Conclusions	180
	Bibliography	182
	Biography	195

List of Tables

1.1	Statistics of regions in example image	9
2.1	RMSE results for static image reconstruction	52
2.2	Reconstruction RMSE table	65
3.1	Reconstruction time and RMSE for SPIRAL experiments	104
4.1	MSE and coherence results	139

List of Figures

1.1	Comparison of Poisson and Gaussian noise	8
1.2	Sample signals used in wavelet denoising example	13
1.3	Wavelet denoising estimate	14
1.4	Demonstration that natural images contain structure beyond sparsity	20
2.1	Block circulant with circulant block structured matrix	36
2.2	Ground truth and conventional imager images	46
2.3	Reconstructions for static imaging	47
2.4	Saturn and Mimas test image	53
2.5	Rice camera versus CCA reconstruction results	54
2.6	Example frame from test video sequence	61
2.7	CAKE reconstruction results	62
2.8	Squared error vs frame plots	64
3.1	Example of partition-based approximation	86
3.2	Experimental setup for SPIRAL simulations	100
3.3	Results for SPIRAL numerical experiments	103
3.4	Intensity cross sections for SPIRAL simulations	105
3.5	RMSE convergence plot for SPIRAL experiments	106
3.6	RMSE convergence plot for SPIRAL experiments	107
3.7	RMSE convergence plot for SPIRAL experiments	108
3.8	Saturn Reconstructions using sparse dictionary learning method . . .	110

3.9	Flag Reconstructions using sparse dictionary learning method	111
4.1	Fiber bundle microendoscope photo	115
4.2	Example data from fiber bundle microendoscope	116
4.3	Tissue components	120
4.4	Spectral profiles and coherence behavior	121
4.5	Intensity image used in experiments	132
4.6	Decomposition results	133
4.7	Objective behavior for $T/n = 1000$	134
4.8	Objective behavior for $T/n = 100$	135
4.9	Objective behavior for $T/n = 10$	136
4.10	Observations in simulations	137
4.11	Reconstruction results	138
4.12	Histology comparison	140
4.13	Histology comparison statistics	141
4.14	Ex vivo comparison	143
4.15	Ex vivo comparison statistics	144
4.16	In vivo comparison	146
4.17	In vivo comparison	147
4.18	In vivo comparison	148
4.19	In vivo comparison statistics	149
5.1	Adaptive gridding example	157
5.2	Stationary specimens	166
5.3	Stationary specimens ROI subset	167
5.4	Dynamic specimens	168
5.5	Dynamic specimens ROI subset	169

5.6	Mouse embryonic stem cells	170
5.7	Mouse embryonic stem cells ROI subset	171
6.1	Preliminary subspace tracking results	180

List of Abbreviations and Symbols

Symbols

Here is a quick reference for the notation used throughout this document.

f	Vector in \mathbf{R}^n to be estimated or reconstructed
\hat{f}	Estimate of the signal or image
h	A point spread function
m	Length of the observation vector y , m for measurements
n	Length of the vector f to be reconstructed
t	Time index for video sequences
w	Vector in \mathbf{R}^m containing measurement noise or errors
y	Vector in \mathbf{R}^m or \mathbf{Z}_+^m of observations
A	Observation matrix which linearly projects f to y
D	Downsampling operator
F	Orthonormal matrix corresponding to the DFT basis vectors
P	Partition of $[0, 1]^d$
R	Shorthand for the matrix product AW
W	Orthonormal matrix corresponding to a basis for f
\mathcal{F}	Two dimensional DFT matrix, $\mathcal{F} = F \otimes F$.
\mathcal{N}	Gaussian probability distribution
\mathcal{P}	A collection of partition-based estimates

α	Hessian approximation parameter in the Barzilai-Borwein method
δ	Isometry constant in the Restricted Isometry Property
θ	Coefficients of f in some (sparsifying) basis W
λ	Lagrange multiplier vector
ν	Lagrange multiplier vector
τ	Regularization parameter
Γ	A collection of nonnegative estimates
$\nabla\phi(x)$	Gradient of the function $\phi : \mathbf{R}^n \rightarrow \mathbf{R}$ evaluated at x
$\nabla^2\phi(x)$	Hessian matrix of $\phi : \mathbf{R}^n \rightarrow \mathbf{R}$ evaluated at x
$\mathbf{1}$	A vector or matrix with each element equal to 1
$\mathbf{I}_{\{E\}}$	Binary $\{0, 1\}$ indicator function of the event E
I	The identity matrix
I_n	The size- n identity matrix
e_k	The k th canonical basis vector

Abbreviations

AG	Adaptive Gridding
AL	Augmented Lagrangian
CAKE	Coded Aperture Keyed Exposure
CCA	Compressive Coded Aperture
CS	Compressed Sensing
CT	Circle Transform
EM	Expectation Maximization
FM	Fluorescence Microscopy
FPA	Focal Plane Array
H&E	Hematoxylin and Eosin (used for histology)

iid	Independent and Identically Distributed
LR	Local Recurrence
MPLE	Maximum Penalized Likelihood Estimator
MPLSM	Multiphoton Fluorescence Laser Scanning Microscope
MPM	Multiphoton Fluorescence Microscopy
MURA	Modified Uniformly Redundant Array
PSF	Point Spread Function
RDP	Recursive Dyadic Partition
RIP	Restricted Isometry Property
ROI	Region of Interest
SCA	Sparse Component Analysis
SPIRAL	Sparse Poisson Intensity Reconstruction ALgorithms
TH	Thresholding
TI	Translation Invariant
TV	Total Variation

Acknowledgements

Reflecting on my journey towards my doctorate, I am incredibly fortunate to have met such a wonderful and diverse cast of characters. Some learned and wise, others kind and supportive, the rest uproarious swashbucklers. A few idealistic dreamers, some unfailing pragmatists, the rest comfortably between. The lessons you've taught and the times we've shared, I'm thankful for you all.

I owe the sincerest debt of gratitude to my advisor, Prof. Rebecca Willett. Your unwavering support was crucial to my academic success. You taught me to be unafraid when asking big questions and to strive for excellence in scholarship. Knowing I've been stuck on a project and had made little progress, I would sometimes dread our meetings. Yet our discussions turned seemingly daunting challenges into manageable tasks. To circumvent roadblocks, you would often show me new avenues to explore that renewed my zest and enthusiasm. I have always valued your ability to juggle the small details without losing sight of the bigger picture, and maintaining your kindheartedness, even when you needed to deliver a firm nudge to keep me on path. Thank you, Becca, for being an excellent mentor.

I would also like to acknowledge the support of my dissertation committee members, Prof. Robert Calderbank, Prof. Guillermo Sapiro, Prof. Nimmi Ramanujam, and Prof. Roummel Marcia. Without your insightful discussions, fruitful collaborations, and intriguing questions, this thesis would not be as strong. I would also like to acknowledge support for this work provided by NSF CAREER Award No. CCF-

06-43947, NSF Award No. DMS-08-11062, DARPA Grant No. HR0011-07-1-003, and AFRL Grant No. FA8650-07-D-1221.

I'm also sure that there is not a more diverse, entertaining, and friendly set of lab mates. I've had the opportunity to learn from an excellent set of postdocs and research scientists associated with our lab: Dr. Jorge Silva, for sharing his perspective on life, helping me diversify my investment portfolio, and making me aware of ways to limit my tax liability; Prof. Roummel Marcia, deserving of a second mention, for allowing me to spend time at Merced, sharing his Delta Gold Medallion perks, and being evicted from many coffee shops together hours before paper deadlines; Prof. Maxim Raginsky, for his encyclopedic knowledge and instigating many trips to Chai's; Dr. Joseph Salmon, for knowing when I needed a coffee break, always being available for vibrant discussions, and refining my sensibilities about French wines and cheeses; Dr. Yao Xie, for always being excited in research and sharing her sense of humor. I am also grateful to the many students that have been a part of our lab and now count as friends: Nooshin Kiarashi, Peng Guan, Eric Hall, Shirisha Reddy, Rubenka Bandyopadhyay, Viola Gomes, Xin Jiang, Jiaji Huang, Albert Oh, and Juan Ramirez. There's also two unofficial members of our lab: Dr. Lorne Applebaum and John Marcus. I'm glad Robert stuck you with us and that I had the opportunity to know you both. I'm sure the feeling is mutual. Lorne, thanks for all the fun times floating on logs at the Eno River quarry. Lastly, I'm especially thankful to Dr. Kalyani Krishnamurthy, for being there with me since the beginning and always being a good friend, I'm glad we could share so much of this adventure together.

I would also like to thank the many other graduate students at Duke whose camaraderie gives Duke its character. I'd like to mention a few by name: Dr. Jeff Rogers; Dr. Kenny Morton; Dr. Josh Stohl; Dr. Vito Mecca; Dr. Chris Ratto, and his wife Dr. Allie Ratto; Stewart Thomas; Phil Brown; Jason Yu; the rest of the Krzyzew's Chefs; Jeffrey Doyle; Alex Mrozack; Ken Colwell; Jill Desmond; Bethany

DiPrete; Adam Jacobvitz; Paige Sholar; Sara Durán; Tiffany Wilson; Jenna Mueller; and Dr. Stephanie Kennedy. I would also like to thank Joseph Heras and Corey Cain for being great roommates while I was visiting Merced.

Special thanks to my family for always encouraging my dreams. Mom and Dad, thanks for supporting me through all life's twists and turns, and always patiently letting me forge my own path. Jacob, thanks for always visiting when I'm home and helping me relax over breaks. I'm eternally thankful to my late grandfather, Charles C. Harmany, to whom this thesis is dedicated. As a teacher and principal, and with his endless bookshelves, he instilled in me a desire for learning. Without your attitude towards education, it's doubtful I would have come this far.

1

Introduction: Background and Summary of Thesis Contributions

This chapter serves as a brief introduction to the background on imaging, including the elementary modeling assumptions in image formation, compressed sensing, and a central theme of this thesis, Poisson statistics. I conclude by describing the contributions of this thesis.

1.1 Image Formation

In incoherent imaging, the object of interest is a real-valued intensity function $f : \mathbf{R}^d \rightarrow \mathbf{R}$, where d is the dimension of the image. Depending on the application, the notion of an image and the dimension d may vary; consider the following list of examples.

Case $d = 1$: Consider spectroscopy, where we are interested in determining the spectral response $f(\lambda)$ where λ would correspond to the wavelength of light. In spectroscopic applications, successful estimation of f may allow for the correct identification of a drug [1], or the atmospheric composition of exoplanets [2].

Case $d = 2$: Perhaps the most familiar application, where $f(x_1, x_2)$ would denote the intensity of the image at particular spatial location (x_1, x_2) .

Case $d = 3$: A temporally evolving scene, such as a video, can be modeled as a three-dimensional function where the intensity $f(x_1, x_2, t)$ varies with both spatial position (x_1, x_2) and time t . Alternatively, spectral imaging seeks to estimate a spectral response $f(x_1, x_2, \lambda)$, a function of both position and wavelength λ . Standard color photography can be thought of as a very simple example of spectral imaging, where we limit ourselves to three (red, green, blue) spectral channels. Spectral imaging can help identify scene content in remote sensing and satellite imaging examples, and even identify suspicious materials [3].

Optical systems take as input the scene f and produce a second intensity function y that is subsequently discretized by a detector array or other sensing device. We model linear variants of such systems as linear integral operators that act on f . We let A denote such an operator, and write $y = A(f)$. With a slight overloading of notation, such systems can be fully described by a kernel function A such that

$$y(z) = \int_{\mathbf{R}^d} A(x, z)f(x) dx \quad (1.1)$$

For example, if $A(x, z) = A(z - x)$, then (1.1) reduces to a convolution which can model uniform blurring due to aberrations in an optical system. More details on the continuous modeling of imaging systems can be found in the excellent tome by Barrett and Myers [4, Sec. 7.2].

1.2 Sampling

Modeling the domain of f and y as continuous-valued is often unnecessary for the successful application of signal processing to the problem of image recovery and

reconstruction. Firstly, the measurements we acquire (the subsequent samples of y) are already discretized by a detector array. Secondly, we often wish to reconstruct a discrete approximation to the image f to store and transmit digitally, or display on a pixel-based display.

Instead of the model (1.1), we adopt the discrete analog (with slight overloading of notation)

$$y = Af \quad (1.2)$$

where $y \in \mathbf{R}^m$ is a vector of measurements (hence the mnemonic m), $f \in \mathbf{R}^n$ is a vectorized representation of our discrete image. For multidimensional ($d > 1$) signals, we adopt lexicographic ordering of the corresponding discrete measurements. As a result $A \in \mathbf{R}^{m \times n}$ is the *sensing matrix* that models our optical system.

Note that defining an appropriate discretization domain for f introduces bias into the resulting estimate that may impact the quality of reconstruction, especially for the sparse models this thesis will subsequently detail. This bias is referred to as *basis mismatch* in many signal processing domains [5].

1.3 Gaussian Noise

A deterministic model such as (1.2) will fail to capture the fact that the sensing process may yield imperfect measurements. As such an additive error term $w \in \mathbf{R}^m$ must be augmented to the model:

$$y = Af + w. \quad (1.3)$$

The two most common models for w are that of bounded or Gaussian noise. If the noise is of bounded energy (measured by the ℓ_2 norm), we have that

$$\|w\|_2 = \|Af - y\|_2 \leq \epsilon. \quad (1.4)$$

In the Gaussian case, it is assumed that

$$w \sim \mathcal{N}(0, \sigma^2 I), \quad (1.5)$$

meaning the entries of w are iid Gaussian with variance σ^2 . These models are more-or-less equivalent: if we examine the negative log-likelihood under the Gaussian model, we have

$$-\log p(y | Af) \propto \frac{1}{2} \|Af - y\|_2^2, \quad (1.6)$$

and as such in both cases the deviation is measured isotropically and independently of the signal intensity Af .

1.4 Poisson Noise

While the above bounded or Gaussian modeling assumptions are accurate when the sources of error are independent of the intensity, such as readout noise introduced in the sensing electronics, they fundamentally neglect an important property of light in that its energy is delivered in discrete packets of photons. As such, there is an intrinsic variability in the acquired measurements that is due to the statistics of the photon counting process at the detector. This *shot noise* is manifest in the extremely light-starved applications at the forefront of modern imaging: night-vision, PET, astronomical imaging, and fluorescent microscopy are a few examples of where the dominant source of data variability is due to the discrete capturing of photons.

An inhomogeneous Poisson process model has been successfully used to model the photon counting statistics of imaging detectors. Under this model, the data collected is a nonnegative vector of counts ($y \in \mathbf{Z}_+^m$) with a likelihood

$$p(y | Af) = \prod_{i=1}^m \frac{(e_i^\top Af)^{y_i} \exp(-e_i^\top Af)}{y_i!}, \quad (1.7)$$

where e_i is the i th canonical basis vector. For this model to be valid, Af must be nonnegative. This is accomplished by considering its components separately; to

correspond to a valid intensity vector f must be nonnegative, and A then corresponds to a nonnegative transition matrix describing the probability that a photon observed in an entry y originated from a particular location in the vector f .

The use of the Poisson distribution can be motivated in two ways. The first arises by considering the arrival of a photon as a rare event, the other is motivated more from the physics of the photon emission process.

1.4.1 Rare Events

For this section, consider one particular detector element. Say over our observation duration we have an average arrival rate of λ photons. If we further subdivide our observation duration into N subintervals, the probability of observing a photon in any of the subintervals will be $p = \lambda/N$. If we consider the success of detecting a photon in each subinterval as independent Bernoulli processes, then the probability of observing k photons will be governed by a binomial distribution with parameters p and N ,

$$p(k | p, N) = \binom{N}{k} (1-p)^{N-k} p^k. \quad (1.8)$$

With $p = \lambda/N$, we can manipulate the above expression as follows:

$$p(k | \lambda/N, N) = \frac{\lambda^k}{k!} \left(1 - \frac{\lambda}{N}\right)^N \left[\frac{N!}{(N-k)!N^k} \left(1 - \frac{\lambda}{N}\right)^{-k} \right]. \quad (1.9)$$

If $N \rightarrow \infty$, the k photon arrivals become a rare event ($p \rightarrow 0$) in the subinterval, however $\lambda = pN$ will remain constant. Since

$$\lim_{N \rightarrow \infty} \left(1 - \frac{\lambda}{N}\right)^N = e^{-\lambda} \quad \text{and} \quad \lim_{N \rightarrow \infty} \left[\frac{N!}{(N-k)!N^k} \left(1 - \frac{\lambda}{N}\right)^{-k} \right] = 1,$$

we have

$$p(k | \lambda) = \frac{\lambda^k e^{-\lambda}}{k!}.$$

Therefore we establish convergence in probability to a Poisson random variable.

1.4.2 Exponential Decay

Photons are emitted by an atom or molecule when an electron decays from an excited energy state to a ground state. In most imaging examples, objects are illuminated by reflections of ambient light. These reflections may be diffuse or specular in nature, but in any case are described by the scattering properties of the material. In such scattering phenomenon, one can treat the photon emission as occurring due to a decay from a virtual state. Rigorously treating this phenomena is outside the scope of this discussion, and frankly, this thesis as a whole. As such, we will consider the more simple phenomenon of photon emission.

In an emission process, the duration $T \geq 0$ between the excitation and emission can be assumed to follow an exponential distribution

$$p(T | \lambda) = \lambda e^{-\lambda T}, \quad (1.10)$$

and hence the expected time is the reciprocal of the rate: $\mathbf{E}[T] = 1/\lambda$.

Consider an experiment in which we have an ensemble of such emission processes. Because of the memoryless property of the exponential distribution, the inter-arrival times of the photons will be iid exponential random variables, which we denote by T_i for the i th interval. If we observe k photons over a unit observation interval, the probability of such an event is the same as the probability that we observed k inter-arrival events, but have not yet observed the $(k+1)$ th event, mathematically this is expressed as

$$\mathbf{P} \left(T_1 \leq 1, T_1 + T_2 \leq 1, \dots, \sum_{l=1}^k T_l \leq 1, \sum_{l=1}^{k+1} T_l > 1 \right). \quad (1.11)$$

Manipulating the above expression, and using the exponential distribution, we can

evaluate the above probability as follows:

$$\begin{aligned}
& \mathbf{P} \left(T_1 \leq 1, T_2 \leq 1 - T_1, \dots, T_k \leq 1 - \sum_{l=1}^{k-1} T_l, T_{k+1} > 1 - \sum_{l=1}^k T_l \right) \\
&= \int_0^1 \int_0^{1-t_1} \cdots \int_0^{1-\sum_{l=1}^{k-1} t_l} \int_{1-\sum_{l=1}^k t_l}^\infty \lambda^{k+1} \exp \left(-\lambda \sum_{l=1}^{k+1} t_l \right) dt_{k+1} dt_k \cdots dt_2 dt_1 \\
&= \lambda^k e^{-\lambda} \int_0^1 \int_0^{1-t_1} \cdots \int_0^{1-\sum_{l=1}^{k-1} t_l} dt_k \cdots dt_2 dt_1 = \frac{\lambda^k e^{-\lambda}}{k!},
\end{aligned} \tag{1.12}$$

where we recognize the last iterated integral is the volume of a k -simplex, and can be shown to have a value of $1/k!$. Therefore we establish that the desired probability is given by the Poisson distribution.

1.4.3 Consequences for Image Processing

So far we've discussed image formation, and the source of Poisson noise. However, we have only hinted at its ramifications for image processing. An important property for the Poisson distribution is that its mean and variance are linked; if $k \sim \text{Poisson}(\lambda)$, we have that $\mathbf{E}[k] = \lambda$ and $\text{var}[k] = \lambda$. As a consequence, Poisson noise is necessarily heteroscedastic and dependent on the intensity of the underlying scene.

As an example, consider the following experiment using the 64×64 test image in Fig. 1.1(a). In this image, we have four different regions which we label A–D in Fig. 1.1(b). Region A is at the level of the background, 0.1. Regions B, C, and D are of intensity 1, 2, and 3 respectively. We make a Poisson observation this image (Fig. 1.1(c)), calculate the variance of the residuals, and create a Gaussian noise corrupted image of identical variance (Fig. 1.1(d)). We then compute the variance in each of the corresponding regions in the two noisy images, and summarize the results in Table 1.1. As we can deduce from the images and the tabulated results, the noise deviations in higher intensity regions are more pronounced due to their

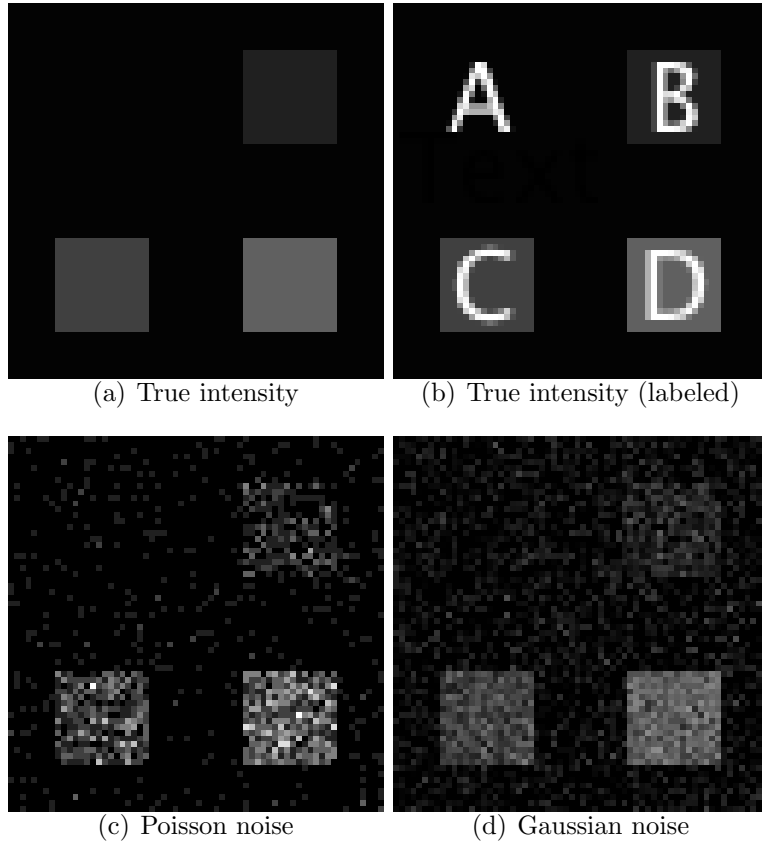


FIGURE 1.1: Comparison of Poisson and Gaussian noise. Note the grayscale has been normalized such that a value of zero is black, and the maximal value is white.

increased variance. This non-uniform and signal-dependent noise is a distinguishing feature of images dominated by Poisson noise.

1.5 Compressed Sensing

The compressed sensing (CS) paradigm in signal processing has lead to exciting new ways of thinking about signal acquisition and reconstruction [6, 7, 8]. The revelation of CS theory is that we require far fewer measurements than previously imagined for the highly accurate recovery of sparse signals. In fact, CS allows us to drastically under-sample during signal acquisition, yet guarantee a stable, accurate, and in some cases *exact* reconstruction [6]. The key to this capability depends on our ability to

Table 1.1: Statistics of regions in example image.

Region	True Mean	Poisson Variance	Gaussian Variance
A	0.100	0.092	0.453
B	1.000	1.098	0.470
C	2.000	1.985	0.412
D	3.000	2.603	0.426

capture measurements that are incoherent with respect to the underlying sparsity of the signal [9]. When the signal energy is concentrated in only a few locations, the incoherence of the measurement process assures that this energy is spread out over our observations, assuring that each measurement we make yields useful information about the signal.

For example, consider the classic board game *Battleship*. A player’s objective is to locate the positions of our opponent’s ships, which only occupy a small portion of the game board, and are thus sparse in the spatial domain. Each round the players take turns firing shots at particular grid locations, revealing a miss or hit if the a ship is absent or present in that square. By only taking measurements of specific spatial locations, the players are actually taking the *worst* kind of measurement—from a CS perspective—as these measurements are perfectly coherent with the sparsity pattern of the signal of interest. Suppose that instead, we could make incoherent measurements of the opponent’s ship positions, e.g., by asking if the opponent has any ships anywhere in the first five rows of the board. If the opponent does not, we are able to eliminate half of the game board from further consideration. If the opponent does have ships in these first five rows, we could then take a second incoherent measurement and ask if they were any ships in columns A–E, and so on. Clearly, this *Compressive Battleship* would be a much shorter game, requiring fewer turns to sink your opponent’s fleet.

The CS advantage of taking fewer measurements is extremely important when

these measurements are expensive to acquire. For instance, high-resolution imaging hardware is more costly than lower resolution alternatives. In surveillance, considering the *SWaP* (size, weight, and power) is of paramount importance. High-resolution optics and electronics may simply be too bulky for the task at hand, and is often necessary to make sacrifices measurement resolution due to physical constraints placed on the sensor.

However, this up-front savings is not without its cost. By their very nature, these incoherent measurements do not resemble the signal of interest, and require the use of state-of-the-art computational tools to reconstruct a decipherable image. Luckily, the raw computational power needed to recover such signals does not need to be integrated with the sensing hardware. The sensor may simply transmit the compressive measurements directly to a receiver or base station that has sufficient processing power at its disposal. Much of the excitement of CS theory is that it naturally leads to a way to design simple and inexpensive sensing hardware that makes use of the growing computational resources of the computer revolution.

Although the theoretical support for compressed sensing is now well-developed, it has yet to gain widespread use in practical imaging due to several challenges associated with implementing the theory. My contribution to this area of signal processing is in addressing some of the key challenges that exist in translating CS theory into practice, as described in Chapter 2. However, before expounding on these challenges and proposed approaches, it is best to highlight the topic of sparse recovery to best situate these challenges as a part of a larger trend in signal processing.

1.6 Sparse Recovery

A useful heuristic in science is to prefer the simplest acceptable explanation of a phenomenon—Occam’s razor. However, it was only recently that this idea has found a new application within signal processing with the advent of compressed sensing

[6, 7, 8]. In CS, simple explanations take the form of sparse vectors. A vector $f \in \mathbf{R}^n$ is s -sparse if f has at least $n - s$ zero entries. Often $s \ll n$, which suggests that the ambient dimension n belies the true simplicity of a s -sparse vector, a fact that is now widely exploited when solving inverse problems in imaging [7].

Widely speaking, an inverse problem is one where we are attempting to recover an original true signal f from a set of measurements y . As the name suggests, a linear inverse problem is one where there is a linear relationship between f and y , precisely the model described in (1.2), hence solving linear inverse problems are of great interest to image scientists.

Historically, we would require more measurements than unknowns ($m \geq n$) to accurately recover f , since in the ill-posed $m < n$ case, we would be unable to uniquely identify an f that is responsible for the observed y . However, if the signal we wish to reconstruct is sparse we can overcome the ill-posed nature of the problem and choose an estimate that is highly accurate. In fact, when we make incoherent measurements of an s -sparse signal, the number of measurements required for accurate reconstruction depends more strongly on the sparsity s than the size of the signal n [10]. This link between sparsity and accurate reconstruction is prevalent throughout modern estimation theory [11]. Candès states that “efficient representations lead to efficient estimations,” [11] a theme we will see throughout this thesis. To see just how signal recovery benefits from sparse representations, we will first briefly examine wavelet denoising, then we will describe the more technical details of compressed sensing.

1.7 Wavelet Shrinkage

Thus far, we have made the assumption of sparsity on the signal f itself. In certain applications this is a very reasonable assumption, e.g., in astronomical imaging we image bright isolated stars against a weak background. However, it is far more likely that the signal of interest f admits a sparse representation in some alternate (e.g.,

Fourier, wavelet) basis W . In this case we express $f = W\theta$, where the vector θ is sparse.

In a denoising problem, we observe the signal f corrupted with some additive zero-mean noise w ,

$$y = f + w = W\theta + w,$$

and we wish to accurately estimate f from y . For simplicity, assume that w is well-modeled as iid Gaussian. As an example, consider the set of images in Fig. 1.2. We see immediately that the signal f is very sparse in the wavelet domain. In fact, only 5.7% of the coefficients differ from zero. We also see that because W is an orthogonal transform, w is also white Gaussian noise in the wavelet domain. Therefore when we examine the wavelet transform of our noisy image y , we still discern the concentrated nature of the true signal energy while the noise is uniformly distributed throughout.

This structure in the wavelet coefficients immediately suggests that we could recover the true signal by retaining the large amplitude coefficients and threshold the smaller coefficients to zero. This is precisely the recipe we follow to estimate f in a wavelet denoising scheme [12]:

1. Perform the forward wavelet transform of the observations y ,
2. Apply some thresholding rule to *shrink* the wavelet coefficients $W^\top y$ to obtain an estimate $\hat{\theta}$,
3. Perform the inverse wavelet transform of the thresholded coefficients to yield an estimate $\hat{f} = W\hat{\theta}$.

The most popular choices of thresholding rules are the hard and soft thresholding rules. A hard threshold, denoted $\text{hard}(u, a)$, is a keep-or-kill estimate that zeros small coefficients, but keeps the larger coefficients unchanged:

$$[\text{hard}(u, a)]_i = u_i \mathbf{I}_{\{|u_i| > a\}}, \quad i = 1, \dots, n,$$

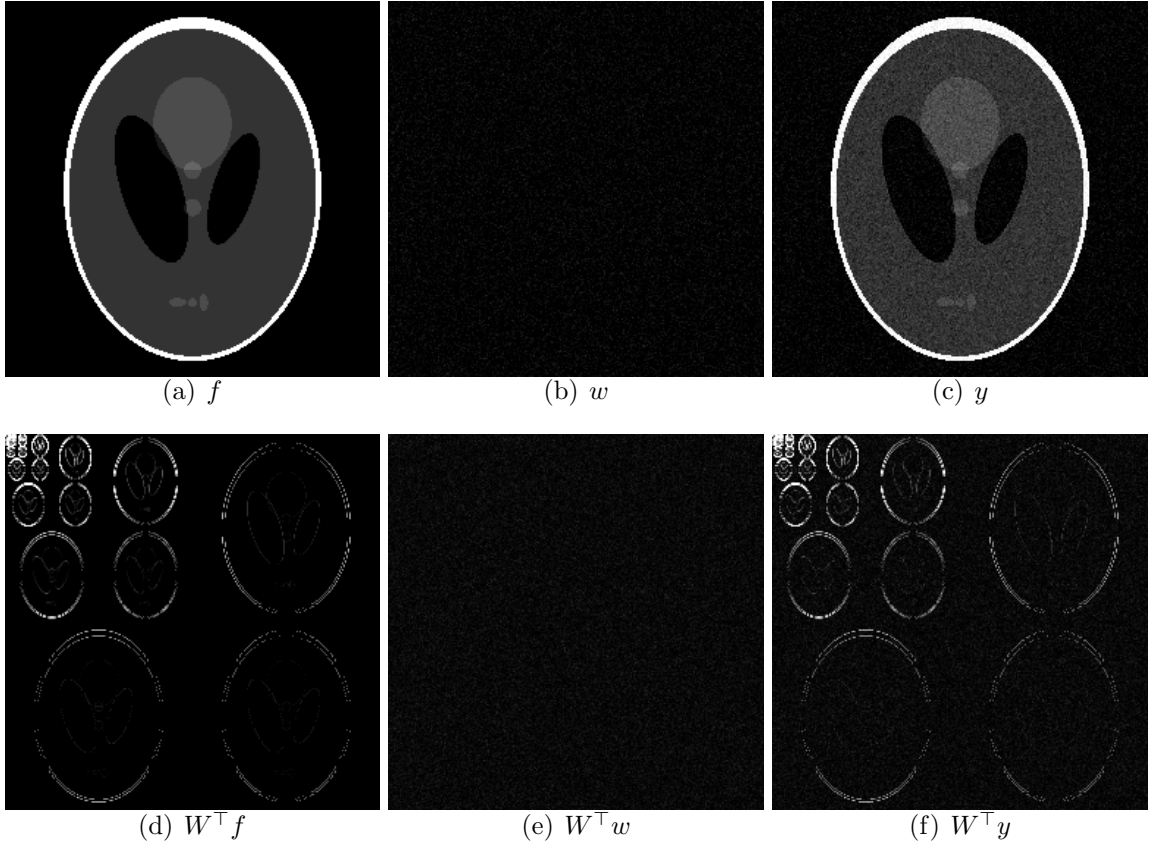


FIGURE 1.2: Here we show (a) the original signal f , (b) the additive noise w , (c) the observed noisy signal y . In addition, we also show the Haar wavelet transform of (d) the original signal, (e) the additive noise, and (f) the observations.

where $\mathbf{I}_{\{\cdot\}}$ is the $\{0, 1\}$ indicator function of its argument. A soft threshold, denoted $\text{soft}(u, a)$, is a more gentle estimator that sets small coefficients to zero, but decreases the magnitude of the larger coefficients by the threshold amount [13]:

$$[\text{soft}(u, a)]_i = \text{sign}(u_i) \max\{|u_i| - a, 0\}, \quad i = 1, \dots, n.$$

Figure 1.3 shows the results after applying the best soft-thresholding rule to the wavelet coefficients. We chose the threshold to yield the smallest (normalized) root-mean-square error (RMSE) $\|\hat{f} - f\|_2 / \|f\|_2$. While not perfect, this simple estimator was able to remove the majority of the noise present in the observations y by simply taking advantage of the sparse representation of f in the basis W . Despite its

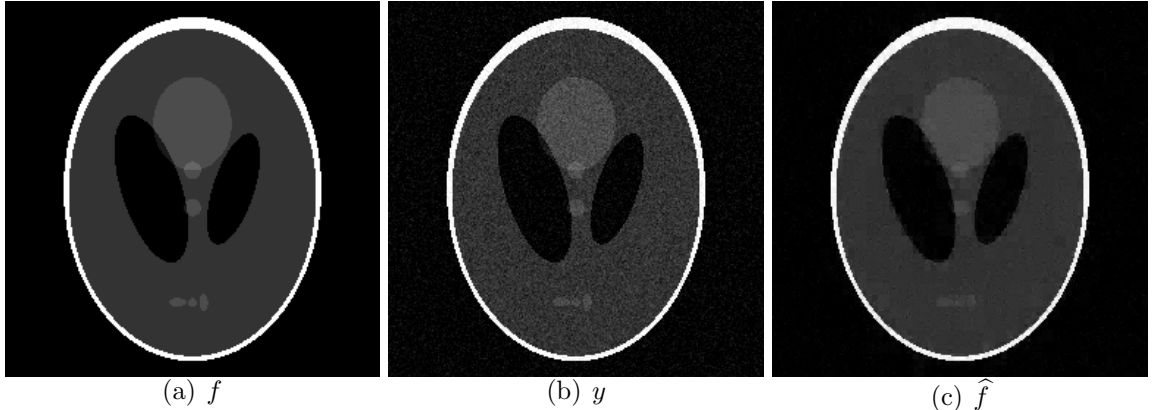


FIGURE 1.3: For a side-by-side comparison we show (a) the original signal f , (b) the noisy signal y , and (c) the minimum RMSE soft-thresholding estimate \hat{f} . For this example we achieved $\text{RMSE} = \|\hat{f} - f\|_2/\|f\|_2 = 0.09$.

apparent simplicity, this class of shrinkage estimators can be shown to be optimal in many circumstances, provided the regularization parameter τ is chosen appropriately [12].

These thresholding rules are intuitively a very reasonable approach to denoising. However, they can also be motivated from another direction by noting that the hard and soft thresholding rules are solutions to the following optimization problems [13]:

$$\hat{\theta} = \arg \min_{\theta \in \mathbf{R}^n} \frac{1}{2} \|y - W\theta\|_2^2 + \tau \|\theta\|_0 = \text{hard}\left(W^\top y, \sqrt{2\tau}\right), \quad (1.13)$$

$$\hat{\theta} = \arg \min_{\theta \in \mathbf{R}^n} \frac{1}{2} \|y - W\theta\|_2^2 + \tau \|\theta\|_1 = \text{soft}\left(W^\top y, \tau\right), \quad (1.14)$$

where the ℓ_0 “norm” counts the number of non-zero entries, and the ℓ_1 norm is given by $\|\theta\|_1 = \sum_{i=1}^n |\theta_i|$. These two measures reflect the sparsity of our estimate. On the other hand, the ℓ_2 term offers a measure of data fidelity, measuring how well our estimate matches the observations. The parameter $\tau \geq 0$ then tunes the balance between these two terms. A larger τ places a heavier emphasis on sparsity, and we must threshold more. Due to the presence of the regularizer term, we say that this type of minimization solves a *sparsity regularized* inverse problem.

Note that although the two problems in (1.13) and (1.14) appear very similar, the fact that the ℓ_0 regularizer in (1.13) is not convex while the ℓ_1 regularizer in (1.14) *is* convex has large implications for more general problems. In fact, ℓ_0 problems are combinatorially complex and are computationally intractable to solve for large n , whereas large ℓ_1 problems can be solved quickly and accurately in practice [9].

1.8 Compressed Sensing Theory

The aforementioned case of compressed sensing is another regime in which sparsity plays a key role. The simplest situation one encounters in CS is when we are given noise-free linear observations $y \in \mathbf{R}^m$ of the form $y = Af$, where $A \in \mathbf{R}^{m \times n}$ is a known sensing matrix. Our goal is to recover f from y when $m < n$, the ill-posed underdetermined case. The archetypical result of CS states that as long as f is suitably sparse, and the matrix A is of a particular type, then we are guaranteed to be able to recover f *exactly*. In particular, as long as f is s -sparse with $m \geq O(s \log n)$, and A satisfies the *restricted isometry property* of order $2s$, then f can be recovered without error as the solution to the convex optimization problem

$$\begin{aligned} & \underset{f \in \mathbf{R}^n}{\text{minimize}} \quad \|f\|_1 \\ & \text{subject to } y = Af \end{aligned} \tag{1.15}$$

This convex program can be restated as a simple linear program, for which many efficient algorithms exist.

The restricted isometry property (morbidly abbreviated RIP) is a condition on the sensing matrix A . We say that the matrix A satisfies RIP of order s if there exists an isometry constant $\delta_s \in (0, 1)$ such that

$$(1 - \delta_s)\|f\|_2^2 \leq \|Af\|_2^2 \leq (1 + \delta_s)\|f\|_2^2 \tag{1.16}$$

holds for all s -sparse f [14]. In essence, RIP assures that when A operates on sparse

vectors, their Euclidean lengths suffer little distortion. From a systems perspective, A preserves the energy of sparse signals. Intuitively, we can think of A “rotating” s -sparse vectors onto a lower-dimensional space. The program (1.15) is effectively performing the opposite rotation. While it is computationally intractable to verify that a given matrix A satisfies RIP, we are nearly guaranteed that if we randomly constitute A from a suitable probability distribution, RIP will hold. For instance, drawing the entries of A as iid Gaussian or Bernoulli guarantees that with overwhelming probability, the matrix A will satisfy RIP [14].

At this point, one may surmise that using CS theory in practical imaging systems could not be more straightforward. Simply generate A randomly, collect measurements y , then solve (1.15) to recover f . However, several important details have been overlooked in this simple exposition of the CS theory. First, it is often intractable to implement an imaging system based on iid random A using optical hardware. Second, measurement noise must be taken into account in the acquisition process. Third, these and other issues have a direct impact on what optimization problem we are required to solve to recover our signal. Lastly, there may exist additional structure in a signal, or may be simple in some other regard that is not adequately captured by the number of significant components of the signal.

1.9 Practical Imaging Systems

While the theory of compressed sensing has been widely studied, its implementation in any form of practical imaging hardware is still much in its infancy. Although there are many prototype camera architectures that utilize CS, they are not without their respective drawbacks. First, as described in Sec 1.1, optical elements are modeled by nonnegative linear operators. However, if there is no special structure of the matrix A , implementing the matrix multiplication Af is often a challenge. If one can afford a long acquisition time, one can implement each row of the matrix multiplication

sequentially, as is done in the Rice single-pixel camera [15]. However, we obviously lose the ability to capture scenes with large amounts of motion. On the other hand, if one wishes to capture a scene all at once in a snapshot acquisition, we would need to capture m different random projections simultaneously. Since there is no structure to exploit between different projections, each projection would require independent acquisition hardware, greatly increasing the bulk of such design.

Recent work in compressed sensing theory has allowed the development of theoretical guarantees associated with random convolutions [16, 10]. As convolutions occur naturally in many imaging modalities, this opens the door to many new practical camera designs that incorporate compressed sensing ideas. For optical imaging, we have developed a few novel camera architectures based on compressive coded apertures (CCA) that extends traditional coded aperture designs to a compressive sensing framework by considering random mask patterns. These designs are described in depth in Chapter 2.

1.10 Reconstruction From Noisy Measurements

To accurately model a practical imaging system, one needs to take into account the effects of measurement noise. Restating (1.3), we model noisy measurements according to

$$y = Af + w = AW\theta + w,$$

where w is a vector of noise or errors. While the theory of compressed sensing is mature enough to have guarantees that CS is robust to certain amounts of noise, there are several important modifications that need to be made [9]. First, we are no longer solving as simple an optimization problem as (1.15). To recover f , we need to solve a more challenging optimization problem. If we know that the noise w is bounded such that $\|w\|_2 = \|y - Af\|_2 \leq \epsilon$, and assuming we are attempting to find

an estimate $\hat{\theta}$ to the wavelet coefficients of $f = W\theta$, we would solve

$$\begin{aligned} & \underset{\theta \in \mathbf{R}^n}{\text{minimize}} \quad \|\theta\|_1 \\ & \text{subject to} \quad \|y - AW\theta\|_2 \leq \epsilon, \end{aligned} \tag{1.17}$$

where ϵ is the known bound on the noise [17]. If the true θ is sparse and A satisfies RIP, the solution to (1.17) is guaranteed to be accurate. In many real-world settings, we do not know an exact bound on the noise and typically consider an alternate formulation of (1.17) where we instead attempt to simultaneously minimize an ℓ_2 data-fit term combined with an ℓ_1 sparsity penalty,

$$\underset{\theta \in \mathbf{R}^n}{\text{minimize}} \quad \frac{1}{2} \|y - AW\theta\|_2^2 + \tau \|\theta\|_1, \tag{1.18}$$

where the parameter τ dictates how heavily we encourage sparsity in the solution [9, 18].

The above formulations both contain an ℓ_2 data fit term, which one may interpret as statistically characterizing the additive noise as iid Gaussian. As we push the envelope of signal acquisition, the total amount of light collected is often constrained. Essentially, the data is a sequence of counts of the individual photons collected. In this extreme regime, Gaussian noise is an invalid assumption, and the noise distribution is more suitably characterized by Poisson statistics. We next describe the consequences for image reconstruction.

1.11 Reconstruction Algorithms for Poisson Noise

In many low-light settings, imaging is typically modeled using a Poisson process, where we attempt to reconstruct the underlying Poisson intensities in the scene. These intensities are always nonnegative. As such, special care must be placed in our reconstruction algorithms to handle this restriction. While it is typically

straightforward to make these modifications when the image is sparse in the canonical basis, it is not so easy when the image is sparse in some other basis.

When we are modeling photon-limited measurements, we would use the negative Poisson log-likelihood,

$$-\log p(y | AW\theta) \propto \sum_{i=1}^m [e_i^\top AW\theta - y_i \log e_i^\top AW\theta], \quad (1.19)$$

as a measure of data fidelity instead of the ℓ_2 term present in (1.17) or (1.18) [19]. We ignore terms with $y_i!$ as they are constant with respect to θ . Also, we would also restrict our estimates to those such that the reconstructed intensities are non-negative. In summary, for sparse recovery in Poisson noise, we would instead solve the following:

$$\begin{aligned} & \underset{\theta \in \mathbb{R}^n}{\text{minimize}} && -\log p(y | AW\theta) + \tau \|\theta\|_1 \\ & \text{subject to} && W\theta \geq 0 \end{aligned} \quad (1.20)$$

Examining this formulation to (1.18) we see that what was once an unconstrained problem now has additional constraints that make the optimization problem more challenging. In addition, the negative Poisson log-likelihood is not as simple as the quadratic ℓ_2 term before. These changes necessitate the development of novel reconstruction algorithms. Chapter 3 details a class of computationally efficient algorithms that solve (1.20) in addition to formulations based on other complexity penalties discussed below.

1.12 Beyond Sparsity

While the ℓ_1 penalty traditionally used in CS is an adequate measure of the sparsity of f , typical real-life signals have a structure that extends beyond a parsimonious representation in a particular basis. For example, consider the experiment where

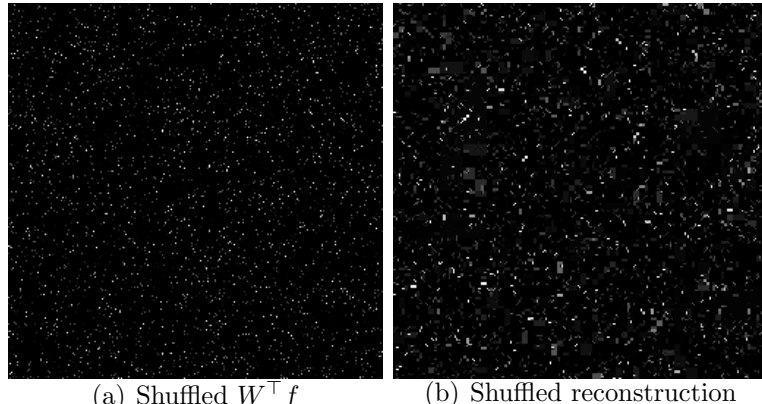


FIGURE 1.4: Result of randomly shuffling the wavelet coefficients of the phantom shown in Fig. 1.3: (a) wavelet coefficients, (b) reconstructed signal resembles nothing like the original signal.

we shuffle the locations of the coefficients in Fig. 1.2(d), and reconstruct the image. The results of this experiment are shown in Fig. 1.4. As we would expect, this new image looks nothing like a natural image, even though it has the same amount of sparsity as measured by both the ℓ_0 and ℓ_1 norms. What this suggests is that natural images, while often permitting a sparse representation, contain a structure that is not captured by traditional sparsity metrics.

There are indeed more intricate signal models that capture this structure that, when used in conjunction with observation likelihood models, offer performance beyond that of sparse models. Examples of these types of models are partition models [20], hidden Markov trees [21], sparse wavelet tree models [22], and the hierarchical models used in Bayesian compressed sensing (BCS) [23]. In Chapters 2 and 3, we demonstrated that the use of RDPs and total variation (TV) regularization was more effective in reconstructing signals than a simple sparse wavelet representation.

RDP-based models fit a constant to each cell in the partition, the resulting estimate is piecewise constant. Therefore, one can think of these models as being very similar to a Haar wavelet estimate, except that we take advantage of the natural tree structure of the wavelet coefficients. That is, we cannot have very large isolated

wavelet coefficients, they must be part of a larger tree structure that extends across the different levels of the wavelet transform [20]. This hereditary constraint encourages the coefficient structure in the wavelet transform that is readily apparent from examining Fig. 1.2(d), and is therefore able to boost reconstruction accuracy. TV measures the strength of the image gradients over the entire image, and encourages these gradients to be sparse. As such, it more realistically models images as being piecewise constant regions separated by smooth edges.

1.13 Summary of Contributions

The field of computational imaging seeks to unite both the design of optical imaging hardware and the associated reconstruction algorithms one may use in producing a final image suitable for human viewing or further image analysis tasks. As such, a system designer must be cognizant of the multifaceted nature of a complete imaging solution. A coarse dissection of the problem would identify three key areas, each with associated challenges.

Image and scene models The properties of the scene to be imaged must be well-understood, and appropriate models must be designed in order to best facilitate the extraction of pertinent information.

Imaging hardware A designer must identify sensing constraints (e.g., size, cost, power, available light, and acquisition rate) and be able to effectively navigate the associated tradeoffs to yield a realistic and implementable optical design.

Reconstruction algorithms Taking advantage of modern computing technology, reconstruction methods must be developed that use knowledge of the imaging design and scene models in order to successfully recover salient information about the scene from the collected data.

My thesis makes important contributions to each of these key areas and furthers the state of the art in computational imaging. The remainder of this chapter presents an overview of the thesis and places the work within the context of the above goals.

1.13.1 *Image and Scene Models*

In my work on compressive coded aperture imaging systems [24, 25, 26], I utilize a wide variety of image models to design effective priors for image reconstruction. These include sparsity as measured by the ℓ_1 norm of the image coefficients in a sparsity-promoting wavelet basis; using the framework of recursive dyadic partitions (RDPs) which construct piecewise-constant models by recursively splitting the image domain; and using a total-variation (TV) seminorm which constrains the magnitude of the image gradients. My work in [24] also considered an extension to video, whereby the sparsity of the interframe differences was exploited to improve reconstruction performance. This idea was also used in my coded aperture keyed exposure (CAKE) system [27] where a mixed regularizer was used by enforcing low TV on video keyframes, and sparse interframe differences using an ℓ_1 regularizer. I describe this system in Chapter 2.

I also considered extensions to the above work where known bounds are known on the signal. For instance, including nonnegativity constraints in optical imaging settings may improve performance, especially in low SNR situations [25, 28]. Similar gains can be seen in video reconstruction [29]. I also showed that when known lower and upper bounds are known on a signal (such as when a peak intensity or power is known, or we have a fixed dynamic range to use), further gains can be realized [30].

Using coded aperture imaging systems, I have also investigated image models that explicitly model motion and occlusion in video sequences [31]. By using the occlusion information, sensing resources can be adaptively focused on these regions in order to increase the reconstruction fidelity.

The same set of ideas can be leveraged in photon-limited imaging systems [19, 32, 33, 34, 35]; I incorporated sparsity, RDPs, and TV into the reconstruction algorithms and demonstrated their effectiveness at reconstructing images in an inverse problem setting from photon-limited observations. These contributions are detailed in Chapter 3.

In quantitative tissue analysis, I have successfully used sparse decomposition techniques [36] in photon-limited scenarios to successfully separate nuclei in images of heterogeneous tissue [37, 38]. These techniques model each tissue component as being sparse in a particular dictionary, with signal separation possible if the dictionaries are sufficiently incoherent between issue types. I detail this work in Chapter 3.

1.13.2 Imaging Hardware

Many of my contributions have consequences for imaging hardware design. Foremost is my work on compressive coded aperture imaging devices [24, 25, 26]. These imaging devices allow snapshot acquisition of compressive measurements, eliminating the need for taking many sequential measurements that many other compressive imaging devices rely upon, e.g. the Rice single-pixel camera [15]. We also propose a spatio-temporal compressive imager that allows for the reconstruction of high-rate high-resolution measurements from a set of reduced-rate low-resolution frames. All of these imaging systems come with a performance guarantees that are well-understood using the theory of compressed sensing. We detail this work within this thesis in Chapter 2.

My work on Poisson inverse problems [19, 32, 33, 34, 35] has shown that the photon noise that results from decreased scan can be overcome using our reconstruction methods. As such, this opens the doorway for intra-operative scanners for performing tissue quantification [37, 38], and minimizing scan time in multiphoton microscopy (See Chapter 5).

1.13.3 Reconstruction Algorithms

My thesis also places heavy emphasis on the effective design of reconstruction algorithms that yield an effective computational optical system. If bounds on the signal are known, effective reconstruction algorithms may be designed to incorporate such prior knowledge [25, 28, 29, 30].

However, my main contribution is this area is in an effective suite of algorithms for Poisson inverse problems we call SPIRAL [19, 32, 33, 34, 35]. Such algorithms are detailed in this thesis in Chapter 3. These algorithms have been shown to be state of the art for many imaging problems, such as limited-angle SPECT. I am also able to provide global convergence guarantees under mild conditions. This work also forms the base from which I developed our photon-limited sparse decomposition techniques applied to tissue analysis [37, 38].

1.14 Conclusions

In this chapter, we have introduced the basics of image formation, CS, noisy measurements, Poisson noise, and the particular impact on imaging and image reconstruction. All these considerations are important as imaging applications are increasingly driven to applications with limited measurements, and constrained sensing resources that drive us to photon-starved regimes. I have also summarized the contributions of this thesis, and subsequent chapters will be dedicated to the details of these contributions.

2

Compressive Coded Aperture and Coded Aperture Keyed Exposure Sensing

Optical systems which measure independent random projections of a scene according to compressed sensing (CS) theory face a myriad of practical challenges related to the size of the physical platform, photon efficiency, the need for high temporal resolution, and fast reconstruction in video settings. This chapter describes a coded aperture and keyed exposure approach to compressive measurement in optical systems. The proposed projections satisfy the Restricted Isometry Property for sufficiently sparse scenes, and hence are compatible with theoretical guarantees on the video reconstruction quality. These concepts can be implemented in both space and time via either amplitude modulation or phase shifting, and this chapter describes the relative merits of the two approaches in terms of theoretical performance, noise and hardware considerations, and experimental results. Fast numerical algorithms which account for the nonnegativity of the projections and temporal correlations in a video sequence are developed and applied to microscopy and short-wave infrared data.

2.1 Introduction

The theory of compressed sensing (CS) suggests that we can collect high-resolution imagery with relatively few photodetectors or a small focal plane array (FPA) when the scene is sparse or compressible in some dictionary or basis and the measurements are chosen appropriately [6, 8]. There has been significant recent interest in building imaging systems in a variety of contexts to exploit CS (cf. [39, 40, 41, 42, 43, 44, 45, 46, 47, 48]). By designing optical sensors to collect measurements of a scene according to CS theory, we can use sophisticated computational methods to infer critical scene structure and content. One particularly famous example in optical imaging is the Single Pixel Camera [49], which collects individual projections of the scene sequentially. While these measurements are supported by the CS literature, there are several practical challenges associated with the tradeoff between temporal resolution physical system footprint. In this chapter we describe an alternative approach to designing a low frame-rate *snapshot* CS camera which naturally parallelizes the compressive data acquisition. Our approach is based on two imaging techniques called coded apertures and keyed exposures, which we explain next.

Coded apertures [50, 51] have a long history in low-light astronomical applications. Coded apertures were first developed to increase the amount of light hitting a detector in an optical system without sacrificing resolution (by, say, increasing the diameter of an opening in a pinhole camera). The basic idea is to use a mask, i.e. an opaque rectangular plate with a specified pattern of openings, that allows significantly brighter observations with higher signal-to-noise ratio than those from conventional pinhole cameras [50, 51]. These masks encode the image before detection, inducing a more complicated point spread function than that associated with a pinhole aperture. The original scene is then recovered from the encoded observations in post-processing using an appropriate reconstruction algorithm which

exploits the mask pattern. These multiplexing techniques are particularly popular in astronomical [52, 53] and medical [54, 55, 56] applications because of their efficacy at wavelengths where lenses cannot be used, but recent work has also demonstrated their utility for collecting both high resolution images and object depth information simultaneously [57].

Keyed exposure (also called coded exposure [58], flutter shutter [59], or coded strobining [60]) imaging was initially developed to facilitate motion deblurring in video using a relatively low frame rate. In some cases motion has been inferred from a single keyed exposure snapshot. The basic idea is that the camera sensor continuously collects light while the shutter is rapidly opened and closed; the shutter movement effectively modulates the motion blur point spread function, and with well-chosen shutter movement patterns it becomes possible to deblur moving objects. Similar effects can be achieved using a strobe light instead of moving a shutter.

Despite the utility of the above methods in specific settings, they both face some limitations. The design of conventional coded apertures does not account for the inherent structure and compressibility of natural scenes, nor the potential for non-linear reconstruction algorithms. Likewise, existing keyed exposure methods focus on direct (uncoded) measurements of the spatial content of the scene and have limited reconstruction capabilities, as we detail below. The Coded Aperture Keyed Exposure (CAKE) sensing paradigm we propose in this chapter is designed to allow nonlinear high-resolution video reconstruction from relatively few measurements in more general settings.

2.1.1 Problem Formulation

We consider the problem of reconstructing an N -frame video sequence f , where each frame is an $n_1 \times n_2$ two-dimensional image denoted f_t . Using standard vector representation, we have that $f_t \in \mathbf{R}^n$ for $t = 1, \dots, N$ where $n := n_1 n_2$ is the total

number of pixels. As a result, the vector representation of the video sequence is $f = (f_1, \dots, f_N) \in \mathbf{R}^{nN}$.

The observations y of f are also acquired as a video sequence. We do not assume that the observations are acquired at the same rate at which we will ultimately reconstruct f . In general, we assume y is an M -frame video sequence, with each frame y_k of size $m_1 \times m_2$. Similarly to f , we have $y_k \in \mathbf{R}^m$ for $k = 1, \dots, M$, where $m := m_1 m_2$, therefore $y = (y_1, \dots, y_M) \in \mathbf{R}^{mM}$.

We observe f via a spatio-temporal *sensing matrix* $A \in \mathbf{R}^{mM \times nN}$ which linearly projects the spatio-temporal scene onto an mM -dimensional set of observations:

$$y = Af + w, \quad (2.1)$$

where $w \in \mathbf{R}^{mM}$ is noise associated with the physics of the sensor. This acquisition model specializes to a snapshot camera when $N = M = 1$.

CS optical imaging systems must be designed to meet several competing objectives:

- The sensing matrix A must satisfy some necessary criterion (such as the RIP, defined below) which provides theoretical guarantees on the accuracy with which we can estimate f from y .
- The total number of measurements, mM , must be lower than the total number of pixels to be reconstructed, nN . This is achievable via compressive spatial acquisition ($m < n$), frame rate reduction ($M < N$), or simultaneous spatio-temporal compression.
- The measurements y must be *causally* related to the temporal scene f , which restricts the structure of the projections A .
- The optical measurements modeled by A must be implementable in a way that results in a smaller, cheaper, more robust, or lower power system.

- The sensing matrix structure must facilitate fast reconstruction algorithms.

This chapter demonstrates that compressive Coded Aperture Keyed Exposure systems achieve all these objectives.

2.1.2 Contributions

The primary contribution of this chapter is the design and theoretical characterization of compressive Coded Aperture Keyed Exposure (CAKE) sensing. We explore amplitude modulating and phase shifting masks and describe theoretical and implementation aspects of both. We further describe how keyed exposure ideas can be used in conjunction with coded apertures to increase both the spatial and temporal resolution of video from relatively few measurements. We prove hitherto unknown theoretical properties of such systems and demonstrate their efficacy in several simulations. In addition, we discuss several important algorithmic aspects of our approach, including a mean-subtraction pre-processing step which allows us to sidestep challenging theoretical aspects associated with nonnegative sensing matrices (such as amplitude modulating coded apertures). This chapter builds substantially upon earlier preliminary studies by the authors [61, 62, 25] and related independent work by Romberg [10].

2.1.3 Organization of the Chapter

The chapter is organized as follows. Section 2.2.2 describes conventional coded aperture imaging techniques and Section 2.2.2 describes keyed exposure techniques currently in the literature. We describe the compressive sensing problem and formulate it mathematically in Section 2.2.3. In Section 2.3, we show how CS theory can be used for constructing coded aperture masks that can easily be implemented for improving image reconstruction resolution in snapshot imaging; this includes theoretical results, a discussion of implementation details and tradeoffs in practical optical systems, and

experimental results. We consider applications to video compressed sensing using the full CAKE paradigm in Section 2.4, including theory and experimental results.

2.2 Background

Prior to detailing our main contributions, we first review pertinent background material. This review touches upon the development of coded aperture imaging, coded exposure photography, and a brief review of salient concepts in compressed sensing theory.

2.2.1 Coded Aperture Imaging

Seminal work in coded aperture imaging includes the development of masks based on Hadamard transform optics [63] and pseudorandom phase masks [64]. Modified Uniformly Redundant Arrays (MURAs) [65] are generally accepted as optimal mask patterns for coded aperture imaging. These mask patterns (which we denote by h^{MURA}) are binary, square patterns, whose *grid size matches the spatial resolution of the photo-detector*. Each mask pattern is specifically designed to have a complementary pattern \bar{h}^{MURA} such that $h^{\text{MURA}} * \bar{h}^{\text{MURA}}$ is a single peak with flat side-lobes (i.e. a Kronecker δ function).

In practice, the resolution of a detector array dictates the properties of the mask pattern and hence resolution at which f can be reconstructed. We model this effect as f being downsampled to the resolution of the detector array and then convolved with the mask pattern h^{MURA} , which has the same resolution as the FPA and the downsampled f , i.e.

$$y = (D_{\text{int}}f) * h^{\text{MURA}} + w, \quad (2.2)$$

where $*$ denotes circular convolution, w corresponds to noise associated with the physics of the sensor, and $D_{\text{int}}f$ is the *integration* downsampling of the scene, which

consists of partitioning f into uniformly sized $d_1 \times d_2$ blocks, where $d_i := n_i/m_i$ for $i = 1, 2$, and measuring the total intensity in each block.

Because of the construction of h^{MURA} and \bar{h}^{MURA} , $D_{\text{int}}f$ can be reconstructed using

$$\hat{f} = y * \bar{h}^{\text{MURA}}.$$

However, the resulting resolution is often lower than what is necessary to capture some of the desired details in the image. Clearly, the estimates from MURA reconstruction are limited by the spatial resolution of the photo-detector. Thus, high resolution reconstructions cannot generally be obtained from low-resolution MURA-coded observations.

It can be shown that this mask design and reconstruction result in minimal reconstruction errors *at the FPA resolution and subject to the constraint that linear, convolution-based reconstruction methods would be used*. However, when the scene of interest is sparse or compressible, and nonlinear sparse reconstruction methods may be employed, then CS ideas can be used to design coded aperture which yield higher resolution images. Before describing the details of this, we briefly review two key relevant concepts from CS.

2.2.2 Coded (Keyed) Exposure Imaging

Coded (or keyed) exposures were developed recently in the computational photography community. Initial work in this area was focused on engineering the temporal component of a motion blur point spread function by rapidly opening and closing the shutter during a single exposure or a small number of exposures at a low frame rate [58, 59]. That is,

$$y = A^{\text{KE}}f + w = \sum_{i \in S} f_i + w,$$

where the keyed exposure (KE) measurement matrix A^{KE} selects the subset of frames during which the shutter is open. We refer to this subset as the exposure code $S \subseteq \{1, \dots, N\}$.

If an object is moving during image acquisition, then a static shutter would induce a typical motion blur, making the moving object difficult to resolve with standard deblurring methods. However, by “fluttering” the shutter during the exposure using carefully designed patterns, the induced motion blur can be made invertible and moving objects can be accurately reconstructed. Instead of a moving shutter, more recent work uses a strobe light to produce a similar effect [60].

While this novel approach to video acquisition can produce very accurate deblurred images of moving objects, there is significant overhead associated with the reconstruction process. To see why, note that every object moving with a different velocity or trajectory will produce a different motion blur. This means that (a) any stationary background must be removed during preprocessing and (b) multiple moving objects must be separated and processed individually.

More recently, it was shown that these challenges could be sidestepped when the video is temporally periodic (e.g. consider a video of an electronic toothbrush spinning) [60]. The periodic assumption amounts to a sparse temporal Fourier transform of the video, and this approach, called coded stroboscopes, is a compressive acquisition in the temporal domain. As a result, the authors were able to leverage ideas from compressed sensing to achieve high-quality video reconstruction.

The assumption of a periodic video makes it possible to apply much more general reconstruction algorithms that do not require background subtraction or separating different moving components. However, it is a very strong assumption, which places some limits in its applicability to real-world settings. The approach described in this chapter has similar performance guarantees but operates on much more general video sequences.

2.2.3 Compressed Sensing

In this section we briefly define the Restricted Isometry Property (RIP) and explain its significance to reconstruction performance. In subsequent sections, we demonstrate our primary theoretical contribution, which is to prove the RIP for compressive coded aperture and keyed exposure systems.

Definition 1 (Restricted Isometry Property (RIP) [14]). *A matrix A satisfies the RIP of order s if there exists a constant $\delta_s \in (0, 1)$ for which*

$$(1 - \delta_s)\|f\|_2^2 \leq \|Af\|_2^2 \leq (1 + \delta_s)\|f\|_2^2. \quad (2.3)$$

holds for all s -sparse $f \in \mathbf{R}^n$. If this property holds, we say A is $\text{RIP}(s, \delta_s)$.

Matrices which satisfy the RIP are called CS matrices; and when combined with sparse recovery algorithms, they are guaranteed to yield accurate estimates of the underlying function f :

Theorem 1 (Sparse Recovery with RIP Matrices [66, 67]). *Let A be a matrix satisfying $\text{RIP}(2s, \delta_{2s})$ with $\delta_{2s} < \sqrt{2} - 1$, and let $y = Af + w$ be a vector of noisy observations of any signal $f \in \mathbf{R}^n$, where the w is a noise or error term with $\|w\|_2 \leq \epsilon$ for some $\epsilon > 0$. Let f_s be the best s -sparse approximation of f ; that is, f_s is the approximation obtained by keeping the s largest entries of f and setting the others to zero. Then the estimate*

$$\begin{aligned} \hat{f} &= \arg \min_{f \in \mathbf{R}^n} \|f\|_1 \\ &\text{subject to } \|y - Af\|_2 \leq \epsilon, \end{aligned} \quad (2.4)$$

obeys

$$\|f - \hat{f}\|_2 \leq C_{1,s}\epsilon + C_{1,s} \frac{\|f - f_s\|_1}{\sqrt{s}},$$

where $C_{1,s}$ and $C_{2,s}$ are constants which depend on s but not on n or m .

Note that the reconstruction (2.4) in Theorem 1 is equivalent to

$$\widehat{f} = \arg \min_{f \in \mathbf{R}^n} \frac{1}{2} \|y - Af\|_2^2 + \tau \|f\|_1 \quad (2.5)$$

where $\tau > 0$, which depends on ϵ , can be viewed as a regularization parameter.

2.3 Compressive Coded Apertures for Snapshot Imaging

This section first considers a snapshot acquisition model. Our goal is to recover a static high-resolution scene from a single image where all pixels are collected simultaneously. In terms of the notation in Sec. 2.1.1, we have $N = M = 1$, so that A is of size $m \times n$. The sensing matrix for compressive coded aperture (CCA) systems can be modeled mathematically as

$$Af = D(f * h); \quad (2.6)$$

where h is a coding mask, and D is a subsampling operator (detailed below). Here the coding mask, h , is at the size and resolution at which f will be reconstructed; this is in contradistinction to the MURA system, in which h^{MURA} is at the size and resolution of the FPA. Thus in (2.6), we model the measurements as the scene being convolved with the coded mask and *then* downsampled.

Using a similar model, Romberg [10] conducted related work concurrent and independent of our initial investigations [61]. We will summarize the key features of this model and compare with our approach in Sec. 2.3.2. While these models share common elements, we will see in Sec. 2.3.3 that there are important tradeoffs associated with the theory and implementation of each strategy.

Recent work by Bajwa et al. [16, 68], showed that random circulant matrices (and Toeplitz matrices, in general) are sufficient to recover sparse f from y with high probability. In particular, they showed that a Toeplitz matrix whose first row contains elements drawn independently from a Gaussian distribution are $\text{RIP}(s, \delta_s)$

when $m \geq Cs^2 \log(n)$ for some constant C . Here, we extend these results to pseudo-circulant matrices and use them to motivate our mask design. Our model differs from that in [10] in that we consider a different generative model for the coded aperture mask, as well as a different subsampling strategy:

- The elements of the coding mask h are generated iid according to a particular generating distribution (e.g. an appropriately scaled Rademacher, uniform, or Gaussian distribution).
- Our analysis allows for deterministic downsampling in which we collect one sample per nonoverlapping block.

In our notation, we distinguish mask patterns in this manner using the abbreviations BS, US, and GS, where the first character denotes the distribution used to generate the mask, i.e. binary, uniform, or Gaussian, and the second is a reminder that these masks are generated directly in the spatial domain.

2.3.1 CCAs Generated in the Spatial Domain

The two-dimensional convolution of h with an image f as in (2.6) can be represented as the application of the Fourier transform to f and h , followed by element-wise multiplication and application of the inverse Fourier transform. In matrix notation, this series of linear operations can be expressed as

$$(f * h) = \mathcal{F}^{-1} \operatorname{diag}(\mathcal{F}h) \mathcal{F}f = Rf, \quad (2.7)$$

where (f) is a vectorized representation of an image f , \mathcal{F} is the two-dimensional Fourier transform matrix, and $\operatorname{diag}(\mathcal{F}h)$ is a diagonal matrix whose elements correspond to the transfer function, which is the Fourier transform of h . The matrix product $R = \mathcal{F}^{-1} \operatorname{diag}(\mathcal{F}h) \mathcal{F} \in \mathbf{R}^{n \times n}$ is block-circulant and each block is in turn

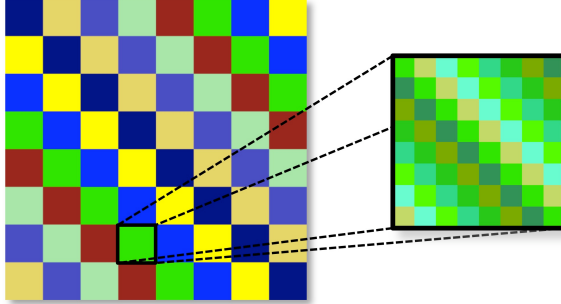


FIGURE 2.1: The $n \times n$ matrix $\mathcal{F}^{-1} \text{diag}(\mathcal{F}h)\mathcal{F}$ is block-circulant with n_2 blocks in each row and column. Each block is $n_1 \times n_1$ and is circulant.

circulant. In matrix notation, R consists of $n_2 \times n_2$ blocks,

$$R = \begin{bmatrix} R_1 & R_{n_2} & \cdots & R_3 & R_2 \\ R_2 & R_1 & \cdots & R_4 & R_3 \\ \vdots & \vdots & \ddots & \ddots & \vdots \\ R_{n_2} & R_{n_2-1} & \cdots & R_2 & R_1 \end{bmatrix}, \quad (2.8)$$

where each $R_j \in \mathbf{R}^{n_1 \times n_1}$ is circulant; i.e. R_j is of the form

$$R_j = \begin{bmatrix} r_{j,1} & r_{j,n_1} & \cdots & r_{j,3} & r_{j,2} \\ r_{j,2} & r_{j,1} & \cdots & r_{j,4} & r_{j,3} \\ \vdots & \vdots & \ddots & \ddots & \vdots \\ r_{j,n_1} & r_{j,n_1-1} & \cdots & r_{j,2} & r_{j,1} \end{bmatrix},$$

(see Fig. 2.1). This block-circulant with circulant-block (BCCB) structure of R is a direct result of the fact that the k -point one-dimensional Fourier transform F_k diagonalizes any $k \times k$ circulant matrix (such as R_j with $k = n_1$) and so $\mathcal{F} \equiv F_{n_2} \otimes F_{n_1}$ diagonalizes block-circulant matrices (such as R). Here \otimes denotes the Kronecker matrix product.

We now examine the generation of a compressed sensing matrix from the convolution R by restricting the number of measurements collected of the vector Rf . Here we simply subsample the vector Rf by applying a pointwise subsampling matrix

D_{sub} . The operation of applying D_{sub} consists of retaining only one measurement per uniformly sized $d_1 \times d_2$ block, i.e. we subsample by d_1 in the first coordinate and d_2 in the second coordinate so that the result is an $m_1 \times m_2$ image with $m_i = n_i/d_i, i = 1, 2$. For compactness of notation we assume that d_i evenly divides n_i for $i = 1, 2$. In matrix form D_{sub} can be thought of as retaining a certain number of rows of the identity matrix. Because of the structure and deterministic nature of this type of downsampling, it is often more straightforward to realize in practical imaging hardware (see Sec. refsec:CAKE.CCA.Hardware).

The resulting projection matrix A is then given by

$$A = D_{\text{sub}}R = D_{\text{sub}}\mathcal{F}^{-1} \text{diag}(\mathcal{F}h)\mathcal{F}.$$

We now show that if the elements of h are drawn from an appropriate probability distribution, then A will be $\text{RIP}(s, \delta_s)$ with high probability.

Theorem 2 (Spatial-Domain CCA Sensing). *Let h^{BS} be a mask with entries generated iid according to the scaled Rademacher distribution*

$$h_{k_1, k_2}^{\text{BS}} = \begin{cases} \sqrt{d/n} & \text{with probability } 1/2, \\ -\sqrt{d/n} & \text{with probability } 1/2, \end{cases} \quad (2.9)$$

for $k_1 = 1, \dots, n_1, k_2 = 1, \dots, n_2$. Let $A^{\text{BS}} = D_{\text{sub}}R$ be an $m \times n$ matrix, where $R \in \mathbf{R}^{n \times n}$ is the BCCB matrix generated from h^{BS} , and $D_{\text{sub}} \in \mathbf{R}^{m \times n}$ is the pointwise subsampling matrix. Then, there exists constants $c_1, c_2 \geq 0$ depending on δ_s such that for any

$$m \geq c_1 s^2 \log(n), \quad (2.10)$$

A^{BS} is $\text{RIP}(s, \delta_s)$ with probability exceeding

$$1 - 2n^2 e^{-c_2 m/s^2}. \quad (2.11)$$

Remark 1. This binary-valued distribution was selected to model coded apertures with two states – open and closed – per mask element. We discuss the issue of implementing these masks in Section 2.3.3.

Remark 2. It is straightforward to extend the result to other mask generating distributions, such as uniform and Gaussian, which we denote h^{US} and h^{GS} , with associated sensing matrices A^{US} and A^{GS} .

We present the proof of Theorem 2 in Section 2.6.

For successful recovery, the coded aperture masks are designed to be satisfy $\text{RIP}(2s, \delta_{2s})$ as described in (2.3) with high probability when $m \geq c_1 s^2 \log(n)$. Note that this is somewhat weaker than what can be achieved by a purely unstructured iid randomly generated sensing matrix which satisfies (2.3) with high probability when $m \geq \tilde{c}_1 s \log(n/s)$ for some constant $\tilde{c}_1 > 0$. Intuition may lead one to believe the extra factor of s is due to the fact that the m projections sensed using the amplitude modulated mask framework exhibit dependencies. However, in many settings this theoretical disadvantage is offset by advantageous practical implementations.

Sparse Gradients Scenes

The above theory is applicable to reconstructing f when f is sparse in the pixel basis; similar results hold when the gradient of f is sparse. For simplicity of notation we will show then in a 1d setting; the extension to 2d is straightforward. Let ∇f denote the first-order gradient of f , so that

$$\nabla := \begin{bmatrix} 1 & 0 & 0 & \cdots & 0 \\ -1 & 1 & 0 & \ddots & \vdots \\ 0 & -1 & 1 & \ddots & 0 \\ \vdots & \ddots & \ddots & \ddots & 0 \\ 0 & \cdots & 0 & -1 & 1 \end{bmatrix}. \quad (2.12)$$

As noted in [16], $f = \nabla^{-1}\theta$, where θ is the sparse gradient image. Thus if we sense $y = A\nabla f + w = A\nabla\nabla^{-1}\theta + w = A\theta + w$, we can expect to recover θ using sparse reconstruction methods.

2.3.2 CCAs Generated in the Fourier Domain

The random convolution in [10] follows the same structure as that in Sec. 2.3.1. However, in that work the convolution is generated randomly in the frequency domain. More specifically, the entries of the transfer function correspond to random *phase shifts* (with some constraints to keep the resulting observation matrix real-valued). We denote the resulting convolution kernel as h^{UP} , where “UP” refers to “uniform phase”. For simplicity of presentation, we describe the generating distribution for a one-dimensional convolution for even-length masks. In particular, let $\sigma = Fh^{\text{UP}}$, and generate σ such that for $k = 1, \dots, n$,

$$\sigma_k = \begin{cases} \pm 1 \text{ with equal probability} & \text{if } k = 1, \\ e^{i\phi} \text{ with } \phi \sim \mathcal{U}(0, 2\pi) & \text{if } 2 \leq k \leq n/2, \\ \pm 1 \text{ with equal probability} & \text{if } k = n/2 + 1 \\ \sigma_{n-k+2}^* & \text{if } n/2 + 2 \leq k \leq n. \end{cases} \quad (2.13)$$

Here $\mathcal{U}(0, 2\pi)$ denotes the uniform distribution over $[0, 2\pi]$. The real-valued convolution kernel is then given by $h^{\text{UP}} = F^{-1}\sigma$. This result can be extended easily for two-dimensional convolutions.

To form a compressed sensing matrix from this random convolution, [10] considers two different downsampling strategies: sampling at random locations, and random demodulation. The first method entails selecting a random subset $\Omega \subset \{1, \dots, n\}$ of indices. We form a downsampling matrix D_Ω by retaining only the rows of the identity matrix indexed by Ω , hence the resulting measurement matrix is given by

$$A^{\text{UP}} = D_\Omega \mathcal{F}^{-1} \text{diag}(\sigma) \mathcal{F}, \quad (2.14)$$

where σ is generated according to the two-dimensional analog of (2.13). The random demodulation method multiplies the result of the random convolution by a random sign sequence $s \in \{-1, 1\}^n$, such that $s_i = \pm 1$ with equal probability for all $i = 1, \dots, n$, then performs an integration downsampling of the result. Therefore in this case the measurement matrix is

$$A^{\text{UP}} = D_{\text{int}} \text{diag}(s) \mathcal{F}^{-1} \text{diag}(\sigma) \mathcal{F}. \quad (2.15)$$

It can be shown that both of these strategies yield RIP-satisfying matrices with high probability.

Theorem 3 (Fourier-Domain CCA Sensing). *Let A^{UP} be an $m \times n$ sensing matrix resulting from random convolution with phase shifts followed by a downsampling strategy, and let W denote an arbitrary orthonormal basis. If the downsampling is random subsampling as in (2.14), then there exists constant $c_3 > 0$ such that with probability exceeding $1 - O(n^{-1})$, for*

$$m \geq c_3 \delta^{-2} \min(s \log^6 n, s^2 \log^2 n),$$

$A^{\text{UP}}W$ satisfies $\text{RIP}(2s, \delta_{2s})$ with $\delta_{2s} \leq \delta$. If the downsampling is random demodulation as in (2.15), then there exists constant $c_4 > 0$ such that with probability exceeding $1 - O(n^{-1})$, for

$$m \geq c_4 \delta^{-2} \min(s \log^6 n, s^2 \log n),$$

$A^{\text{UP}}W$ satisfies $\text{RIP}(2s, \delta_{2s})$ with $\delta_{2s} \leq \delta$.

These theoretical results are stronger than those in Theorem 2, especially since they allow sparsity in arbitrary orthonormal bases. However, there are important differences between the observation models which have a significant impact on the feasibility and ease of hardware implementation. We elaborate on this in Section 2.3.3. Nevertheless, the theory developed in [10] lends important theoretical support to the general concept of compressive coded apertures.

2.3.3 Hardware and Practical Implementation Considerations

In this section we describe how we shift from modeling the coded aperture masks in a way that is compatible with compressed sensing theory, to a model that describes their actual implementation in an optical system. Our analysis does not account for the bandwidth of the lenses; in particular, we implicitly assume that the bandwidth of the lenses is high enough that band-limitation effects are negligible at the resolution of interest. In all of the hardware settings described below, precise alignment of the optical components (e.g. the mask and the focal plane array) is critical to the performance of the proposed system. Often a high-resolution FPA is helpful for alignment and calibration.

In this chapter we focus on *incoherent* light settings (consistent with many applications in astronomy, microscopy, and infrared imaging). In this case, the coded aperture must be real-valued and flux-preserving (i.e. the light intensity hitting the detection cannot exceed the light intensity of the source). In this section, we consider the following apertures:

- **Binary Spatial Mask:** $h \in \{0, 1/n\}^{n_1 \times n_2}$, drawn with equal probability,
- **Uniform Spatial Mask:** $h \in [0, 1/n]^{n_1 \times n_2}$, where each element is drawn independently from a uniform distribution, or
- **Uniform Phase Mask:** $h = |\mathcal{F}p|^2$ for some p , where p corresponds to a phase-shifting mask in an incoherent light setting.

Amplitude Modulation Masks

In a conventional lensless coded aperture imaging setup, the point spread function associated with the aperture is the mask pattern h itself. To shift a RIP-satisfying aperture as in Theorem 2 to an implementable aperture, one simply needs to apply

an affine transform to h mapping $[-\sqrt{d/n}, \sqrt{d/n}]$ to $[0, 1/n]$. This transform ensures that the resulting mask pattern is nonnegative and flux-preserving.

These amplitude modulating masks may be implemented using a spatial light modulator (SLM) or placing chrome on quartz. The SLMs may be preferable in video settings where the underlying scene contains motion and using a different mask pattern at each time step boosts performance. However, in order for the proposed approach to work, the mask or SLM used must be higher resolution than the FPA. Currently, very high resolution SLMs are still in development. Chrome on quartz masks can be made with higher resolution than many SLMs, but cannot be changed on the fly unless we mount a small number of fixed masks on a rotating wheel or translating stage. The uniform amplitude modulation masks in particular could be constructed using a high-resolution halftoning procedure, which is easiest to implement at the necessary resolution with chrome on quartz.

Both Robucci *et al.* [69] and Majidzadeh *et al.* [70] have proposed performing the analog, random convolution step in complementary, metal-oxide-semiconductor (CMOS) electronics. A clear advantage to this architecture is that the additional optics required for spatial light modulation are removed in favor of additional circuitry, immediately reducing the imager size.

Phase Shift Masks

Phase shifting masks for coded aperture imaging have been implemented recently using a phase screen [71]. This approach allows one to account for diffraction in the optical design. However, depending on the precise optical architecture, phase shift masks may be much less photon-efficient than amplitude modulation masks. Additionally, the mask generation distribution described in Eq. (2.13) will result in negative entries for the corresponding PSF $h^{\text{UP}} = \mathcal{F}^{-1}\sigma$. To compensate for this, the phase mask must be mean-shifted to make all entries nonnegative, so that we

are actually implementing

$$h_+^{\text{UP}} = c(h^{\text{UP}} - \min(h^{\text{UP}})\mathbf{1}), \quad (2.16)$$

with the constant c selected so that the implementable PSF h_+^{UP} is flux-preserving and $\mathbf{1}$ is a matrix of ones and of the same dimension as h^{UP} .

Implementable Masks for Sparse Gradients Scenes

As described in Section 2.3.1, theoretical results for scenes with sparse gradients hold for the sparse difference operator ∇ defined in (2.12). The problem with this approach is that ∇ is invertible but not circulant – and hence the sensing matrix $A\nabla$ cannot be implemented with a coded aperture system. We address this by noting that if the upper right element of ∇ were -1 instead of 0 , then the resulting sensing matrix, denoted $\tilde{\nabla}$, could be implemented physically and is a close approximation to the theoretically supported ∇ . In short, the theoretically supported solution is to set

$$\begin{aligned} y &= A\nabla f + w \\ \hat{\theta} &= \arg \min_{\theta} \frac{1}{2}\|y - A\theta\|_2^2 + \tau\|\theta\|_1 \\ \hat{f} &= \nabla^{-1}\hat{\theta} \end{aligned}$$

while an implementable close approximation is to set $A^G := A\tilde{\nabla}$ and

$$\begin{aligned} y &= A^G f + w \\ \hat{f} &= \arg \min_f \frac{1}{2}\|y - A^G f\|_2^2 + \tau\|f\|_{\text{TV}}, \end{aligned}$$

where $\|\cdot\|_{\text{TV}}$ is the total variation seminorm which causes \hat{f} to have sparse gradients. In our numerical experiments we compare the performance of TV regularization to sparsity penalization for the task of reconstructing static scenes.

Downsampling Implementation

In developing RIP-satisfying AMM coded apertures, Theorem 2 assumes the subsampling operation selects one measurement per $d_1 \times d_2$ block. From an implementation standpoint, this operation effectively discards a large portion $((d-1)/d)$ of the available light, which would result in much lower signal-to-noise ratios at the detector. A more pragmatic approach is to use larger detector elements that essentially sum the intensity over each $d_1 \times d_2$ block, making a better use of the available light. We call this operation *integration downsampling* to distinguish it from subsampling. The drawback to this approach is that we lose many of the desirable features of the system in terms of the RIP. Integration downsampling causes a large coherence between neighboring columns of the resulting sensing matrix A .

An intermediate approach would randomly sum a fraction of the elements in each size d block, which increases the signal-to-noise ratio versus subsampling, but yields smaller expected coherence. This approach is motivated by the random demodulation proposed in [10] and described in Sec 2.3.2, whereby the signal is multiplied by a random sequence of signs $\{-1, +1\}$, then block-wise averaged. The pseudo-random summation proposed here can be thought of as an optically realizable instantiation of the same idea where we multiply by a random binary $\{0, 1\}$ sequence. We explore the effects of these choices in our numerical results section.

Noise and Quantization

While CS is particularly useful when the FPA needs to be kept compact, it should be noted that CS is more sensitive to measurement errors and noise than more direct imaging techniques. The experiments conducted in this chapter simulated very high signal-to-noise ratio (SNR) settings and showed that CS methods can help resolve high resolution features in images. However, in low SNR settings CS reconstructions can exhibit significant artifacts that may even cause more distortion than the low-

resolution effects associated with conventional coded aperture techniques such as MURA.

Similar observations are made in [72], which presents a direct comparison of the noise robustness of CS in contrast to conventional imaging techniques both in terms of bounds on how reconstruction error decays with the number of measurements and in a simulation setup; the authors conclude that for most real-world images, CS yields the biggest gains in high signal-to-noise ratio (SNR) settings. Related theoretical work in [73] show that in the presence of low SNR photon noise, theoretical error bounds can be large, and thus the expected performance of CS may be limited unless the number of available photons to sense is sufficiently high. These considerations play an important role in choosing the type of downsampling to implement.

Similar issues arise when considering the bit-depth of focal plane arrays, which corresponds to measurement quantization errors. Future efforts in designing optical CS systems must carefully consider the amount of noise anticipated in the measurements to find the optimal tradeoff between the focal plane array size and image quality.

2.3.4 Reconstruction

To solve the CS minimization problem (2.5), we use well-established gradient-based optimization methods. They are particularly suitable in our setting because the block-circulant structure of A described in the previous section allows for very fast matrix-vector products that are critical to the speed of their performance. However, our observation matrix A is not zero mean and, therefore, negatively impacts the performance of these CS-based reconstruction algorithms. In this section, we describe how we take full advantage of the structure of A and address how we mitigate the negative effects of A having nonzero-mean.

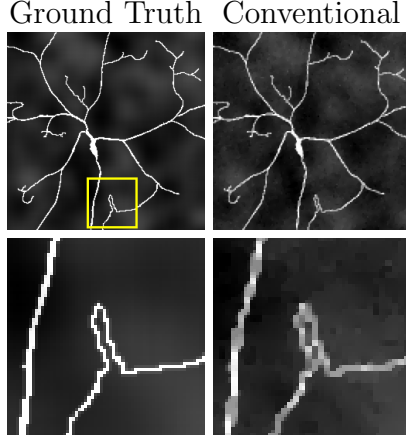


FIGURE 2.2: Ground truth and conventional imager reconstructions For each set of images, the bottom shows the region indicated by the yellow square in the ground truth image.

Sparsity-promoting Methods

We note that most popular and effective methods for performing the above reconstruction are iterative algorithms with repeated applications of the operators A and A^\top to scene estimates and residuals [13, 74]. In most CS settings, computing these matrix-vector multiplications is a large computational burden. However, because of the circulant structure of A , this computation is very efficient using fast Fourier transform algorithms. In particular, we compared the computation time for reconstructing a 256×256 scene using 128×128 CCA measurements with the time required to reconstruct the same scene using the same number of measurements computing using a dense random projection matrix; our reconstruction was 250 times faster because of our exploitation of the Toeplitz structure in A . This example is shown in Section 2.3.6.

Mean Subtraction

Generative models for random projection matrices used in CS involve drawing elements independently from a zero-mean probability distribution [6, 18, 14, 16, 75], and likewise a zero-mean distribution was used to analyze the coded aperture masks

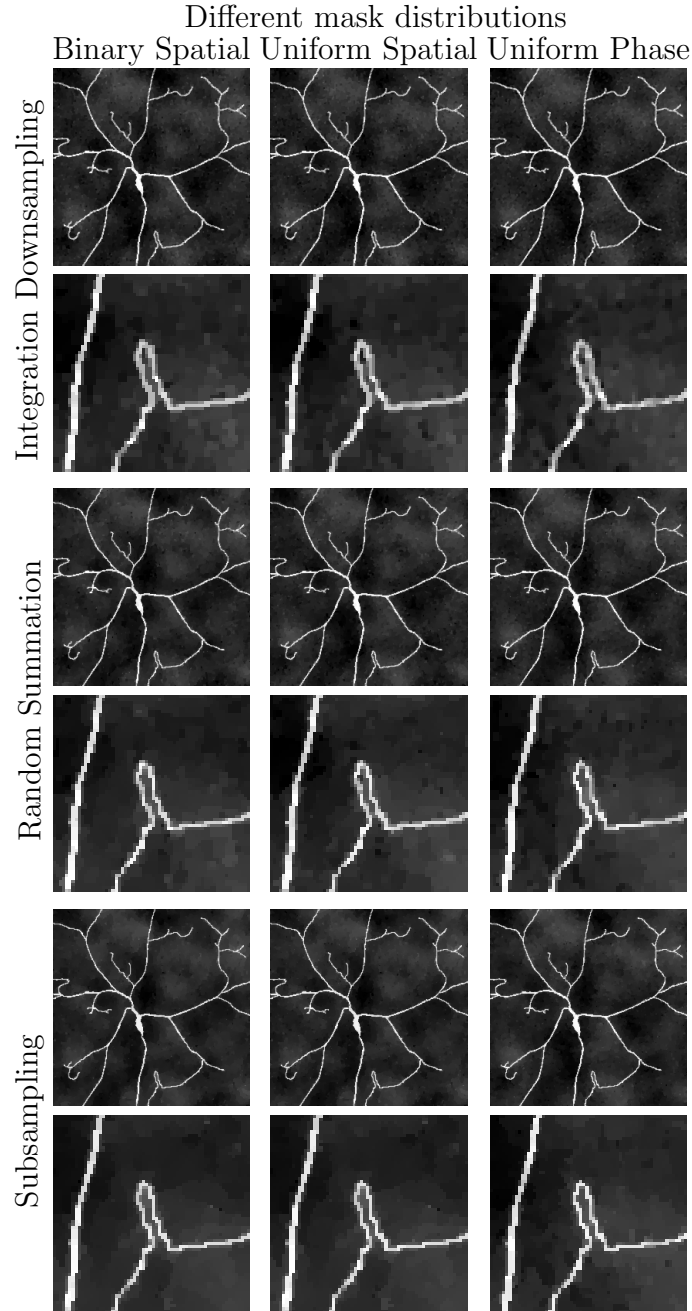


FIGURE 2.3: Best performing reconstructions for the different downsampling strategies (integration downsampling, random summation, and subsampling) and for each downsampling strategy, the different mask distributions (binary spatial, uniform spatial, and uniform phase). For each set of images, the bottom shows the region indicated by the yellow square in the ground truth image, Fig. 2.2. Clearly, significant gains in performance can be achieved by the compressive architectures over conventional imaging.

described in Sec. 2.3. However, as coded aperture masks with zero mean are not physically realizable in optical systems, we generate our physically realizable masks from an appropriately scaled Bernoulli distribution with values $\{0, 1/n\}$. This shifting ensures that the coded aperture corresponds to an implementable (i.e. nonnegative and intensity preserving) mask pattern which does satisfies the assumptions needed to model photon propagation through an optical system.

While necessary to accurately model real-world optical systems, this shifting negatively impacts the performance of well-established ℓ_2 - ℓ_1 reconstruction algorithms for the following reason. Several of these algorithms (e.g. [13, 74]) assume that the ℓ_2 data fidelity term $\phi(f) = \frac{1}{2}\|Af - y\|_2^2$ (proportional to the negative log Gaussian likelihood) is such that $\nabla^2\phi(x) = A^T A$ can be well-approximated by αI , $\alpha > 0$. This assumption is crucial to the performance of these algorithms.

If we collect measurements using a realizable mask with elements in the range $[0, 1/n]$, the resulting matrix A does not satisfy this condition due to the mean offset. Therefore in the reconstruction we use a mean-shifted sensing matrix

$$A^0 = A - \mu_A \mathbf{1}_{m \times n},$$

where $\mu_A = (1/mn)\mathbf{1}_m^T A \mathbf{1}_n$ is the mean value of A . This new matrix is such that $(A^0)^T A^0 \approx \alpha I$ is a valid assumption. However, to use this matrix in the reconstruction, we need to adjust our estimate accordingly. To compensate for this, we decompose our estimate f into its mean component μ_f and a zero-mean deviation f^0 : $f = f^0 + \mu_f \mathbf{1}_n$. So then

$$\begin{aligned} Af &= (A^0 + \mu_A \mathbf{1}_{m \times n})(f^0 + \mu_f \mathbf{1}_n) \\ &= A^0 f^0 + n\mu_A \mu_f \mathbf{1}_m + \mu_f A^0 \mathbf{1}_n + \mu_A (\mathbf{1}_n^T f^0) \mathbf{1}_m \\ &\approx A^0 f^0 + n\mu_A \mu_f \mathbf{1}_m. \end{aligned}$$

The data y can be decomposed in a similar fashion, so that $y = y^0 + \mu_y \mathbf{1}_m$. Thus a

straightforward estimate for the mean of our solution is $\mu_f = \mu_y / \mu_A n$, and we can use the zero-mean quantities in our data fidelity term

$$\phi^0(f^0) = \frac{1}{2} \|A^0 f^0 - y^0\|_2^2 \quad (2.17)$$

within the iterative algorithm, which now has the desired property that $\nabla^2 \phi^0(f^0) \approx \alpha I$.

We have motivated this mean subtraction approach from an estimation setting where we first estimate the mean, then deviations about the mean. However, it can be equally motivated from a pure optimization perspective by viewing the mean subtraction step as a preconditioning strategy. The gradient-based reconstruction methods considered are known to exhibit poor convergence when the Hessian has large condition number, and the mean subtraction operation essentially improves the conditioning of the problem by eliminating the single dominant eigenvalue that occurs due to the nonzero mean.

2.3.5 Experimental Comparison on Static Images

Here we present numerical experiments supporting the proposed architectures for snapshot compressive imaging. We compare the simulated performance of the described imaging architectures in the task of high-fidelity image reconstruction. We utilize a 256×256 pixel realistic phantom image of a neuron (ground truth image in Fig. 2.2) which is designed to test the resolution limits of our architectures with its high-resolution features. This image is inspired by a real microscopic image found at <http://www.lsi.umich.edu/facultyresearch/labs/bingye/research>. We examine a traditional imaging system and a total of six convolution-based compressive imaging systems. These systems are constructed by considering each combination of the following design considerations:

- the mask generation method, including binary spatial (BS) and uniform phase

(UP) models,

- switching among integration downsampling, pseudo-random summation (randomly summing $d/2$ values in each $d_1 \times d_2$ block), and subsampling.

To analyze the effect of the number of measurements we collect, we vary the scene-to-sensor downsampling ratio d to be either 4, 16, or 64 (i.e. downsampling in both directions by a factor of 2, 4, or 8). While each architecture has its own unique considerations in terms of signal-to-noise efficiency (see Section 2.3.3), we choose to normalize the experiments in such a way as to keep a constant signal-to-noise ratio at the detector. This is achieved by fixing the variance of the additive white Gaussian noise to be $\sigma^2 = \text{var}(Af)/16$ for each architecture when we choose a downsampling ratio of $d = 4$. This variance is then fixed for each architecture as we vary the downsampling ratio, the rationale being that this allows us to showcase the impact of the various subsampling operations.

We consider a comparison of many penalization schemes for image reconstruction, such as sparsity in an orthonormal wavelet (Haar) basis, isotropic and anisotropic total-variation [76], as well as an ℓ_1 sparsity penalty in the overcomplete curvelet basis [77]. Curvelets are similar to wavelets in that they capture more spatially localized information than the Fourier components, however they are designed to be more well-adapted for capturing curvilinear singularities in images (e.g. edges). To reconstruct the image, we use our own implementation of the SpaRSA algorithm [13] which utilizes the mean subtraction procedure described in Section 2.3.4. A coarse initialization is found by solving an unpenalized least-squares minimization via a conjugate gradient method using only the compressive data. We terminate the reconstruction when the relative change in the iterates falls below a pre-specified tolerance of 1e-3. We choose the regularization weighting to minimize the final reconstruction RMSE, measured by $\text{RMSE}(\hat{f}) = \|\hat{f} - f\|_2/\|f\|_2$. A table of the

resulting RMSE values is presented in Table 2.1.

As evidenced by both the RMSE values and the images, significant gains in performance can be achieved by the compressive architectures. The UP mask architectures slightly outperform the BS-based approaches in this simulation, but the type of subsampling has a greater effect on the quality of the reconstruction. Focusing on the $d = 4$ case, we see that subsampling performs best overall, followed by random summation, then integration downsampling. This is readily apparent from the RMSE values and the greater clarity by which we can resolve fine-scale features in the dendrites of the neuron. This is exactly predicted by the theory: larger coherence yields poorer performance. However, pushing the level of undersampling, we see that simple subsampling is not always the solution, since the performance degrades quite rapidly, as the per-measurement signal to noise ratio does not naturally increase as it does with the other subsampling architectures. An optimal architecture must strike a careful balance between low coherence and robustness to noise.

2.3.6 Optical Architecture Comparison

Thus far we have only considered comparing our approach to other mask generation strategies. In this section, we compare to several other different optical mechanisms via a simulation study in this section. We consider several different optical mechanisms which could be used to image Saturn and its rings using a “ground truth” image displayed in Fig. 2.4; this image was originally obtained by the Cassini Orbiter [78] and was cropped and downsampled to size 256×256 for our numerical experiments. After this, the pixel intensities range from 0 to 4.53. We add white Gaussian noise to the projected measurements Af to model the sensor noise associated with the focal plane array. In the pinhole and coded aperture experiments, we acquire m measurements over a total time T sec. We assume that this averaged noise has standard deviation $\sigma = 10^{-5}$. The Rice single-pixel camera collects measurements

Table 2.1: Summary of the RMSE values for the different mask generation and down-sampling schemes, including the conjugate gradient initialization, and the various reconstruction methods considered. The images associated with the best performing methods indicated by the bold RMSE values are shown in Fig. 2.3

Sensing Architecture			Reconstruction RMSE (%)				
Subsampler	Mask	d	CG Init	ℓ_2 -Haar	ℓ_2 -TV(Ani)	ℓ_2 -TV(Iso)	ℓ_2 -Curvelet
Integration downsampling	BS	4	43.553	31.908	23.632	23.712	34.552
		16	52.509	47.604	44.602	43.340	43.606
		64	60.435	58.592	57.538	56.961	56.748
	US	4	43.221	31.861	23.497	23.643	34.325
		16	52.126	47.552	44.400	43.070	43.611
		64	59.643	58.146	57.118	56.685	56.542
	UP	4	38.475	30.797	23.266	23.215	32.476
		16	50.285	46.654	44.638	43.091	44.232
		64	58.816	58.168	57.184	56.786	56.558
Random Summation	BS	4	56.890	34.102	18.993	20.536	35.203
		16	62.275	51.431	45.573	44.644	45.539
		64	65.672	60.160	58.297	57.790	57.630
	US	4	56.544	33.660	17.484	19.021	34.322
		16	61.951	50.978	44.857	43.642	45.218
		64	65.350	59.697	57.574	57.159	57.096
	UP	4	54.473	29.831	16.034	17.729	33.652
		16	60.297	48.902	44.940	43.734	45.220
		64	64.318	60.910	57.361	57.106	56.934
Pointwise Subsampling	BS	4	61.579	39.743	17.130	18.612	35.794
		16	67.787	65.570	51.912	50.843	52.625
		64	69.245	69.202	64.772	64.693	64.741
	US	4	61.579	39.780	17.201	18.704	35.813
		16	67.787	65.570	51.928	50.884	52.629
		64	69.245	69.202	64.792	64.687	64.742
	UP	4	61.006	36.260	14.108	15.883	34.282
		16	67.676	64.606	48.280	47.380	48.925
		64	69.188	69.190	63.591	63.515	63.350
Conventional Imager	4	38.158	36.655	36.067	32.946	33.157	
	16	50.138	50.118	49.836	47.933	45.466	
	64	58.873	58.873	58.473	57.806	56.765	

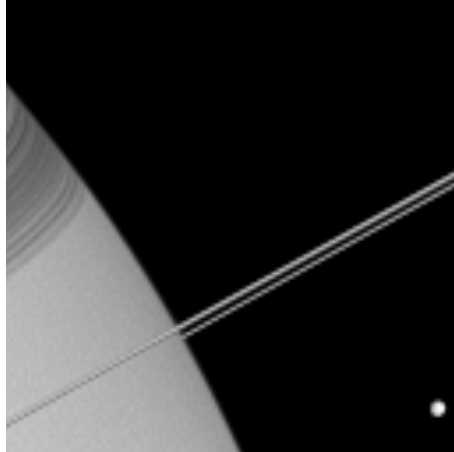


FIGURE 2.4: Edge view of Saturn and its moon, Mimas, as captured by the Cassini spacecraft. Us as a true test image in these experiments.

sequentially, and consequently, it has at most T/m sec to obtain each of the m measurements. Thus, the noise variance associated with the Rice single-pixel camera model must be scaled appropriately. We do this scaling to make a fair comparison across optical architectures where we consider a *fixed time* sensing budget.

For brevity, we only show results from a reconstruction method based on the theory of recursive dyadic partitions (RDPs). We initialize this algorithm with the result obtained using the GPSR algorithm [74], using the Haar wavelet basis as the sparsity basis for the ℓ_2 - ℓ_1 reconstruction. The details of this algorithmic approach are described in detail in [26].

Since these are iterative algorithms, an important consideration is deciding when to terminate the reconstruction. While a variety of different convergence criteria have been successfully employed for the reconstruction algorithms, in this section we simply display the result after 100 iterations, which is sufficient to yield a converged solution for all the methods. A more detailed perspective on RMS error decay across iterations or computation time is described in [19]; that work considers a Poisson noise model but otherwise uses reconstruction methods equivalent to the ones considered here.

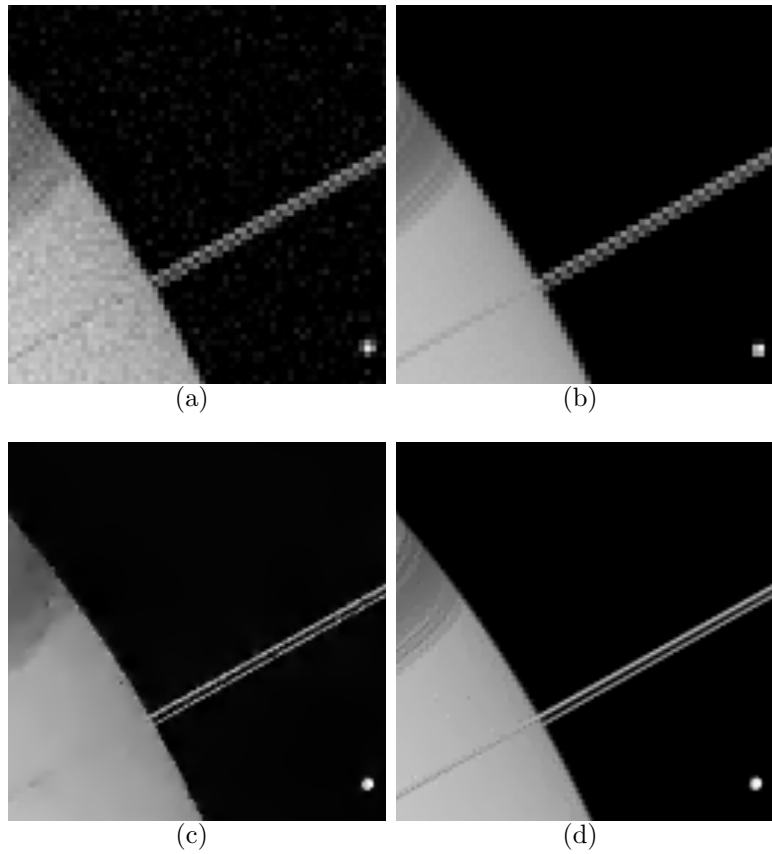


FIGURE 2.5: Simulation results comparing different image acquisition and reconstruction strategies. (a) Observations from a pinhole aperture, upsampled using nearest-neighbor interpolation; RMSE = 11.7%. (b) Reconstruction from a MURA coded aperture camera system, upsampled using nearest-neighbor interpolation; RMSE = 7.1%. (c) RDP-based reconstruction from the Rice single-pixel camera system; RMSE = 6.4%. (d) RDP-based reconstruction from the CCA system; RMSE = 3.2%. Note the higher resolution in the reconstructions from a CCA camera system.

Fig. 4.4.7(a) shows the result of observing the scene with a pinhole camera and an FPA of size 128×128 . This image is clearly lower in resolution than the original (i.e., it is an image with 128×128 pixels, upsampled here via nearest neighbor interpolation for visualization and computing errors). It also exhibits noise artifacts due to the relatively low light intensity reaching the camera detectors relative to the noise level. The root-mean-squared error (RMSE) of this image, $\|\hat{f} - f\|_2 / \|f\|_2$, is 11.7%. Conventional coded aperture techniques, such as the MURA methods

described above, can be used to improve the noise performance of a camera. This is demonstrated in Fig. 4.4.7(b), where use of the MURA code has decreased the RMSE to 7.1%. However, these conventional coded aperture systems cannot resolve details smaller than the pixel size of the FPA. Note the pixelization of Saturn's moon (Mimas), rings, and edges in the MURA reconstruction.

Next, we describe the improvements gained by taking compressive measurements. First, we simulate the image acquisition process in the Rice single-pixel camera by taking random projections of the image and then solve the corresponding CS minimization problem using an RDP-based penalty. The reconstruction for the Rice single-pixel camera is shown in Fig. 4.4.7(c). We note the improved resolution of Mimas and Saturn's rings compared to the MURA reconstruction.

We observe that the compressive coded aperture techniques described in this chapter can lead to further gains. Figure 4.4.7(d) shows the reconstructed 256×256 image from compressive coded aperture observations using the same RDP-based algorithm that reconstructed the Rice single-pixel camera data. As the CCA is a snapshot imaging architecture, the SNR of each CCA measurement is much higher leading to an improved RMSE of 3.2%, a 50% improvement over the Rice single-pixel camera result. Besides the decrease in error, the visual quality is much higher as Fig. 4.4.7 shows that compressive coded apertures significantly improve our ability to resolve fine features, such as the side-view of Saturn's rings, its moon, and bands in the planet's atmosphere.

Lastly, one other advantage that compressive coded apertures have over the Rice single-pixel camera is the computational time necessary to perform reconstruction. Because the observation matrices associated with CCA involve Fourier transforms and diagonal matrices, matrix-vector products are very fast and memory efficient. In contrast, the numerical methods associated with the Rice single-pixel camera are significantly slower and more memory intensive due to the dense, unstructured

projection matrix. In our experiments, reconstructing images from the Rice camera data required two orders of magnitude longer time than the CCA images.

2.4 Coded Aperture Keyed Exposure Sensing for Dynamic Scenes

Here we detail our compressive video acquisition method that combines coded apertures and keyed exposures to address all the competing challenges detailed in Sec. 2.1.1. Specifically, in our CAKE imaging method, each observed frame y_k is given by an exposure of B high-rate coded observations:

$$y_k = \sum_{t=1}^B A_{(k-1)B+t} f_{(k-1)B+t} + w_k, \quad (2.18)$$

where each A_t describes an AMM CCA sensing matrix. Note that since in our theory, the downsampling operator D_{sub} is a structured nonrandom operator, we can rewrite the above as

$$y_k = D_{\text{sub}} \left[\sum_{t=1}^B R_{(k-1)B+t} f_{(k-1)B+t} \right] + w_k. \quad (2.19)$$

Hence all that is required to implement this sensing paradigm is modulating the coded aperture mask over the B -frame exposure time. Because of this, one can think of our system as performing a coded exposure acquisition *for each coded aperture element*.

Since our sensing strategy is independent across each low-resolution frame, and also for simplicity of presentation, we only consider the recovery of a length B block of frames from a single snapshot image in our theoretical analysis.

Theorem 4 (Coded Aperture Keyed Exposure Sensing). *Let $A = [A_1 \cdots A_B]$ be an $m \times nB$ sensing matrix for the CAKE system where the coded aperture pattern for each A_t is drawn iid from a suitable probability distribution. Then there exists constants $c_1, c_2 \geq 0$ depending on δ_s such that for any*

$$m \geq c_1 s^2 \log(nB), \quad (2.20)$$

A is $\text{RIP}(s, \delta_s)$ with probability exceeding

$$1 - 2n^2B^2e^{-c_2m/s^2}. \quad (2.21)$$

Note here that s denotes the sparsity of the first B frames of the video sequence, rather than simply the sparsity of an individual frame as in Thm. 2. The proof of Thm. 4 is presented in Section 2.6.1. Similar to Thm. 2, this proof assumes that the entries of each h_t , $t = 1, \dots, B$ are generated iid according to the scaled Rademacher distribution (2.9). Again, it is straightforward to extend the result to other mask generating distributions.

2.4.1 Sparse Transformation Sensing

It is most often the case that the original frames f are not sparse, but can be sparsely represented by a temporal transform of the frames. For simplicity, consider the first coded measurement. Within this acquisition, the coefficient sequence

$$\theta_k = \sum_{t=1}^B W_{k,t} f_t, \quad k = 1, \dots, B,$$

may be more sparse for a well-chosen sparse temporal transform W . Notationally this is equivalent to $\theta = (W \otimes I_n)f$, where \otimes denotes the Kronecker matrix product. A preferred sensing strategy would be to use our RIP-satisfying CAKE acquisition to sense the coefficient sequence θ :

$$y = \sum_{k=1}^B A_k \theta_k + w. \quad (2.22)$$

Surprisingly, this can be accomplished using an identical architecture, with some slight adjustment to the coded aperture mask patterns used during the keyed acquisition.

To see this, we examine the resulting sensing matrix in terms of f :

$$\begin{aligned} \sum_{k=1}^B A_k \theta_k &= \sum_{k=1}^B A_k \sum_{t=1}^B W_{k,t} f_t = \sum_{t=1}^B \left[\sum_{k=1}^B W_{k,t} A_k \right] f_t \\ &= \sum_{t=1}^B A_t^W f_t, \end{aligned}$$

where we define

$$A_t^W = \sum_{k=1}^B W_{k,t} A_k. \quad (2.23)$$

Therefore (2.22) is also a CAKE acquisition using the sensing matrices A_t^W . Because of the linear dependence on the generating mask patterns, this amounts to using *the an identical architecture with adjusted mask patterns*

$$h_t^W = \sum_{k=1}^B W_{k,t} h_k. \quad (2.24)$$

If we denote $h^W = (h_1^W, \dots, h_B^W)$, then this can be written more simply as $h^W = (W^T \otimes I_n)h = (W \otimes I_n)^T h$. Hence the CAKE system can adapt to any temporal sparse coding of the video sequence over the block of coded frames. In summary, to incorporate the sparse transform W applied to the frames, we simply apply the adjoint transform to the independently generated mask patterns.

A useful transformation that allows the exploitation of dependencies between frames is to assume that the *difference* between subsequent frames are sparse. In this case, we select $W = \nabla$, as defined in (2.12). In particular, we sense using the coded sequence of aperture patterns h^∇ where

$$h_t^\nabla = \begin{cases} h_k - h_{k+1} & k = 1, \dots, B-1, \\ h_B & k = B, \end{cases}$$

and the generating aperture patterns h are drawn from a suitable distribution.

It is of interest to note that since the CAKE sensing matrix is a concatenation of downsampled Toeplitz matrices, this sensing strategy has clear connections to [79] where they consider concatenations of Toeplitz matrices as a sensing matrix for performing multiuser detection in wireless sensor networks. The important conceptual link is that their sensing matrix is used to determine a sparse set of simultaneously active users, where in our system, we are using it to infer a sequence of sparse frames, or a sequence of sparse difference frames.

2.4.2 Implementation and Normalization Details

Recall that these RIP-satisfying sensing matrices are generated using a zero-mean probability distribution and cannot be directly implemented in an optical system. As before, we apply an affine transformation to each of the A_k so that the resulting mask elements for each h_k are within the range $[0, 1/n]$. If we are generating a sensing matrix that satisfies RIP with respect to the difference frames, then even a binary generating distribution will cause the resulting mask patterns to have elements that are neither fully open nor fully closed. This can be accomplished using half-toning as discussed in Sec. 2.3.3. If such an implementation is difficult, then one strategy would be to set these intermediate values to 0 or $1/n$ at random with equal probability.

2.4.3 Reconstruction for Video

Given measurements from the proposed CAKE imaging system, where we have designed the mask patterns for sparsity in a temporal transform, we recover the frames by solving

$$\begin{aligned}\widehat{\theta} &= \arg \min_{\theta} \frac{1}{2} \|A\theta - y\|_2^2 + \tau \|\theta\|_1 \\ \widehat{f} &= (W^{-1} \otimes I_n) \widehat{\theta}.\end{aligned}$$

For the case of sparse difference frames ($W = \nabla$), improvements in empirical performance are made by penalizing the total variation of the first frame, instead of simply

the sparsity in that frame:

$$\widehat{\theta} = \arg \min_{\theta} \frac{1}{2} \|A\theta - y\|_2^2 + \tau_{\text{TV}} \|\theta_1\|_{\text{TV}} + \tau_1 \sum_{k=2}^B \|\theta_k\|_1$$

$$\widehat{f} = (L \otimes I_n) \widehat{\theta},$$

here $L = \nabla^{-1}$ is a lower triangular matrix of all ones.

In addition, by using more than one low-rate observation per reconstruction step, we are typically able to improve performance by coding the difference frames across more than one length- B block of high-rate frames. This is the reconstruction technique we use in the experimental results section. In previous work, we noticed that when the amount of processing time allotted per frame is held constant, the accuracy generally increases with the number of frames processed simultaneously. However, one simply cannot solve for arbitrarily many frames simultaneously, as the improvement in accuracy diminishes when the size of the problem is such that only a very small number of reconstruction iterations can be run within the allotted time. We refer the reader to [62] for details.

For video sequences of longer duration, we may wish to process the video in an online fashion, solving for only a few blocks of frames simultaneously. In many applications, such as surveillance and monitoring, the video frames are strongly correlated, and the solution to a previous block of frames may be used as an initialization to the algorithm to solve the next block of frames. This estimate will generally be very accurate, and therefore, relatively few iterations are needed to obtain a solution to each optimization problem.

2.4.4 Numerical Experiments

In this section, we demonstrate the effectiveness of the proposed CAKE architecture at successfully recovering a video sequence of short-wave infrared (SWIR) data



FIGURE 2.6: Example frame (frame 21) from the ground truth video sequence used in the numerical experiments.

collected (courtesy of Jon Nichols at NRL) by a short-wave IR ($0.9 - 1.7\mu\text{m}$) camera. The camera is based on a 1024×1280 InGaAs (Indium, gallium arsenide) focal plane array with $20\mu\text{m}$ pixel pitch. Optically, the camera was built around a fixed, $f/2$ aperture and provides a 6° field of view along the diagonal with a focus range of $50\text{m} \rightarrow \infty$. Imagery were output at the standard 30Hz frame rate with a 14 bit dynamic range. An example frame is shown in Fig. 2.6. In this sequence, the three boats are traveling at different velocities with respect to the slowly-changing background of the waves. The size of each frame is 128×256 , and we consider reconstructing 28 frames of the sequence.

We consider CAKE observations where we downsample spatially by a factor of 2 in both directions ($d_1 = d_2 = 2$), and use a coded exposure block length of $B = 4$. We compare acquiring the sequence with independent mask codes, and mask codes designed to exploit the sparse difference frames directly. We reconstruct the entire video sequence using all 7 low-resolution low-rate frames using a total variation penalty on the first frame, and ℓ_1 sparsity penalty on all subsequent difference frames.

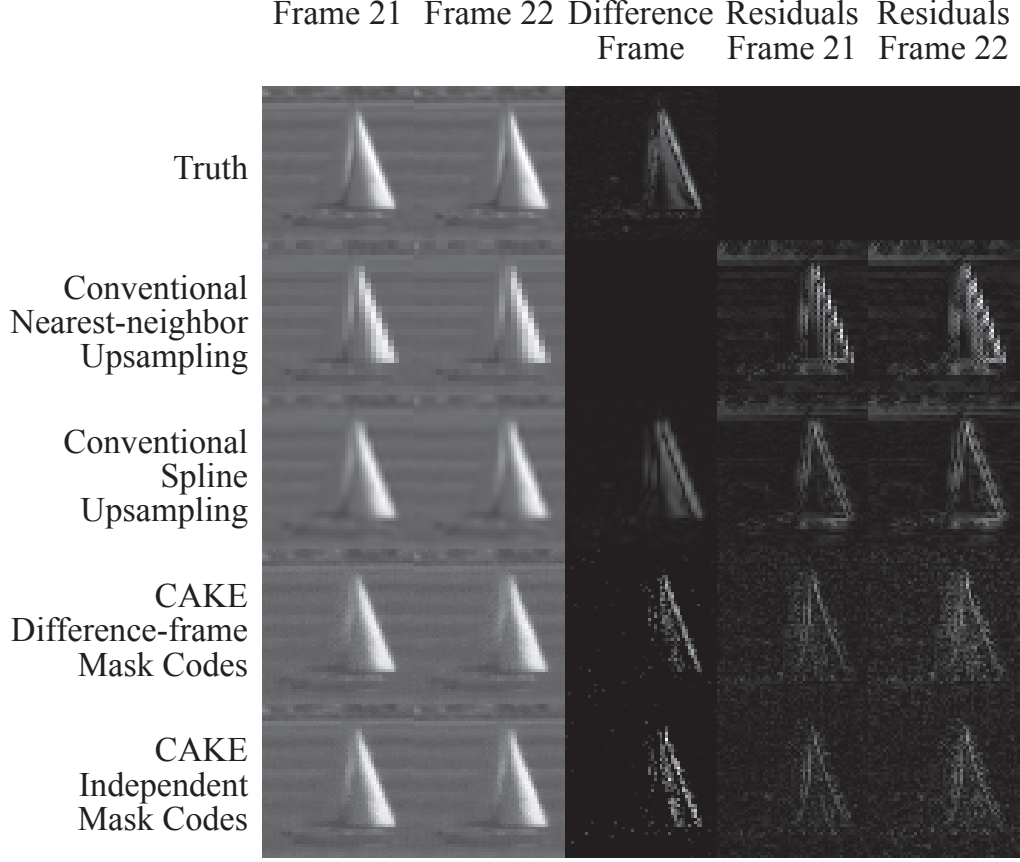


FIGURE 2.7: Results obtained for the sailboat ROI for an example pair of frames (frames 21 and 22). Shown are the true frames, the reconstruction from traditionally sampled data, and the reconstruction from CAKE sensed data. For comparison we show the residuals as compared with the truth, as well as the difference between the frames. Note that using nearest neighbor interpolation results in no motion over the block of frame, hence a zero difference frame.

We optimize the regularization parameters to minimize the reconstruction error. For comparison, we consider traditionally captured data (i.e. by simply averaging over $d_1 \times d_2 \times B$ blocks of the spatiotemporal video sequence). To interpolate this data to the original resolution of the video sequence, we consider both nearest-neighbor and spline interpolation.

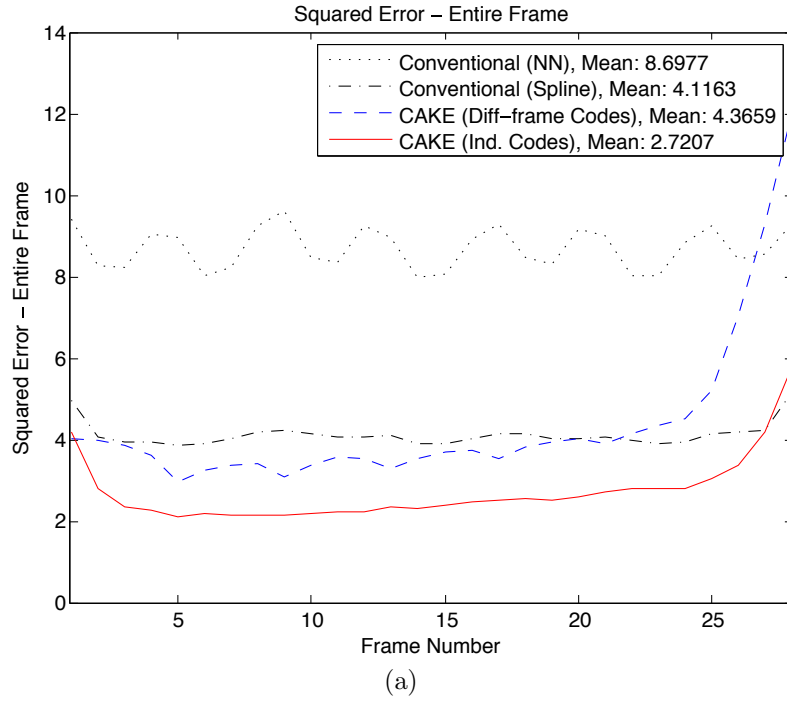
We show the estimates for the different acquisition and reconstruction methods in Fig. 2.7. Here we focus only on a ROI of the sailboat. We see that the CAKE

sensing is able to reconstruct the scene with a higher spatial and temporal resolution. This is evidenced in the residuals, which include much less critical scene structure than the conventional system. We see from the examination of the difference frame that the nearest-neighbor reconstruction from conventionally sampled data yields no motion over the two frames and suffers from poor spatial resolution. Using spline interpolation helps improve the spatial resolution, but it is still insufficient to recover the scene with high temporal resolution, as can be seen in the blur on the leading edge of the sail. Numerically we quantify the performance over the entire video sequence in terms of the RMSE (%), $100 \cdot \|\hat{f} - f\|_2 / \|f\|_2$, calculated both over the entire frame, and only over the sailboat ROI. We show a plot of the contribution to the error of each frame in Fig. 2.8. The total error is then tabulated in Table 2.2. In summary we see that the CAKE acquisitions are able to outperform traditionally sampled video in terms of reconstruction accuracy and reconstructing salient motion.

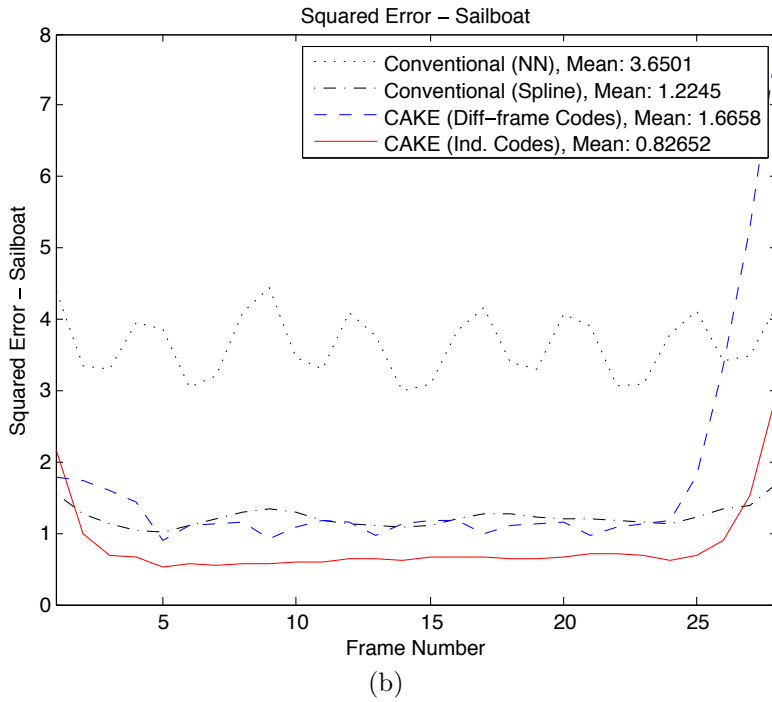
It should be noted that there are limitations to the CAKE system in the presence of strong motion. In this case, the sparsity level of the difference frames may drastically increase as the previous frame ceases to be a good prediction of the next frame. As such, the RIP bound in Theorem 4 states the number of measurements we require to reconstruct the scene must necessarily increase, requiring either a faster temporal resolution measurements or higher resolution FPA to achieve the same accuracy. Because of this balance, a system designer may need to make important engineering tradeoffs to implement CAKE acquisition for a particular application.

2.5 Conclusions

Compressed sensing offers a strong theoretical foundation for sparse signal recovery. However, practical and implementable imaging system designs based on CS theory have lagged far behind. In this chapter, we demonstrate how CS principles can be applied to physically realizable optical system designs, namely coded aperture imag-



(a)



(b)

FIGURE 2.8: The squared error ($\|\hat{f}_t - f_t\|$) obtained for (a) each frame of the video sequence, (b) over the sailboat ROI.

Table 2.2: Reconstruction RMSE achieved for the conventional and CAKE architectures over the video sequence. Results are reported both for the full frame and the ROI of the sailboat. Due to boundary issues (see Fig. 2.8), we report the RMSE discounting the first and last block of B frames. The RMSE values for the entire sequence are given in parentheses.

Sensing Architecture	Reconstruction RMSE (%)	
	Full Frame	Sailboat ROI
Conventional (Nearest-neighbor)	5.5163 (5.5305)	10.3525 (10.4241)
Conventional (Spline)	3.7654 (3.8047)	5.9335 (6.0377)
CAKE (Difference-frame Codes)	3.5840 (3.9183)	5.6971 (7.0421)
CAKE (Independent Codes)	2.9079 (3.0932)	4.3266 (4.9604)

ing. Numerical experiments show that CS methods can help resolve high resolution features in images and videos that conventional imaging systems cannot.

We have also demonstrated that our CAKE acquisition system can recover video sequences from highly under-sampled data in much broader settings than those considered in initial coded exposure studies. However, our derived theoretical limits show that there are important tradeoffs involved that depend on the spatial sparsity, and temporal similarity of the scene that ultimately govern the accuracy of our reconstructions for a specified number of compressive measurements. Finally, we note that our proposed approach performs well in high signal-to-noise ratio settings, but like all CS reconstructions, it can exhibit significant artifacts in photon-limited settings.

Two practical issues associated with coded aperture imaging in general are the blur due to misalignment of the mask and diffraction and interference effects. Non-compressive aperture codes have been developed to be robust to these effects [80]. One important avenue for future research is the development of *compressive* coded aperture masks with similar robustness properties. Noncompressive coded apertures have also been shown useful in inferring the depth of different objects in a scene; similar inference may be possible with the compressive coded apertures described in

this chapter.

2.6 Proof of the RIP for Spatial-Domain CCA Sensing

Here we present the proof that appropriately scaled compressive coded apertures satisfy the RIP.

Proof of Theorem 2. In the interest of notational simplicity, it is easier to work on the two-dimensional images versus their one-dimensional vectorial representations. For concreteness, we assume the entries of h are generated iid according to the scaled Rademacher distribution

$$h_{k_1, k_2} = \begin{cases} \sqrt{d/n} & \text{with probability } 1/2, \\ -\sqrt{d/n} & \text{with probability } 1/2, \end{cases}$$

for $k_1 = 1, \dots, n_1$ and $k_2 = 1, \dots, n_2$. The proof uses the same techniques as that of Theorem 4 in [68], where the RIP is established by shifting the analysis of the submatrices of A to the entries of the Gram matrix $G = A^T A$ by invoking Geršgorin's disc theorem [81]. This theorem states that the eigenvalues of an $n \times n$ complex matrix G all lie in the union of n discs $d_j(c_j, r_j)$, $j = 1, 2, \dots, n$, centered at $c_j = G_{j,j}$ with radius

$$r_j = \sum_{\substack{i=1 \\ i \neq j}}^m |G_{i,j}|.$$

In essence, we show that with high probability $G \approx I$, so that the eigenvalues of G are clustered around one with suitably high probability.

From the discussion above, we have that

$$A_{l,k} = h_{\text{mod}[(l_1-1)d_1-k_1+1, n_1]+1, \text{mod}[(l_2-1)d_2-k_2+1, n_2]+1},$$

so the entries of the resulting Gram matrix G are

$$G_{p,q} = \sum_{l_1=1}^{n_1/d_1} \sum_{l_2=1}^{n_2/d_2} h_{\text{mod}[(l_1-1)d_1-p_1+1, n_1]+1, \text{mod}[(l_2-1)d_2-p_2+1, n_2]+1} \\ h_{\text{mod}[(l_1-1)d_1-q_1+1, n_1]+1, \text{mod}[(l_2-1)d_2-q_2+1, n_2]+1}. \quad (2.25)$$

From the normalization introduced for h , we can show that $\mathbf{E}[G] = I$. Now we need to bound the deviation about the mean via concentration. We consider first the diagonal entries of G , when $p = q$. Each term is a sum of $n = n_1 n_2$ bounded iid entries, and applying Hoeffding's inequality yields

$$\mathbf{P}(|G_{q,q} - 1| \geq \delta_d) \leq 2 \exp\left(\frac{-2n\delta_d^2}{d}\right).$$

Next we consider the off-diagonal entries in the special case that either $\text{mod}(p_1 - q_1, d_1) \neq 0$ or $\text{mod}(p_2 - q_2, d_2) = 0$. In this case, each of the terms in the summand in (2.25) picks out a *different* set of coefficients from h , and hence there are no dependencies between different terms in the sum, hence it is also a sum of $n = n_1 n_2$ bounded iid entries, and thus from Hoeffding's inequality, we have

$$\mathbf{P}(|G_{p,q}| \geq \delta_o/s) \leq 2 \exp\left(\frac{-n\delta_o^2}{2ds^2}\right).$$

Lastly, we have the case that both $\text{mod}(p_1 - q_1, d_1) = 0$ and $\text{mod}(p_2 - q_2, d_2) = 0$ with $p \neq q$. This case deserves special care since each of the terms in the summand in (2.25) picks out *the same* set of coefficients from h . Therefore there necessarily exist dependencies within the terms of the sum. However, due to the special nature by which we select the coefficients, we can partition the sum $G_{p,q}$ into two sums, denoted S_1 and S_2 such that each of these is a sum of $n/2d$ independent terms. We

can then apply the Hoeffding bound to each of these to yield

$$\mathbf{P}(|S_i| \geq \delta_o/2s) \leq 2 \exp\left(\frac{-n\delta_o^2}{4ds^2}\right), i = 1, 2.$$

Then applying the union bound gives us

$$\mathbf{P}(|G_{p,q}| \geq \delta_o/s) \leq 4 \exp\left(\frac{-n\delta_o^2}{4ds^2}\right).$$

Since this latter bound decays more slowly, and in the interest of simplicity, we overbound using this latter expression. What remains is to now apply the union bound over all the diagonal and off-diagonal elements. For this we need to count the number of elements in the union. For the diagonal entries, there are clearly n elements. And since the entries of G are symmetric, we only have $n(n - 1)/2$ remaining terms. Hence taking $\delta_d = \delta_o = \delta_s/2$,

$$\begin{aligned} & \mathbf{P}(A \text{ does not satisfy } \text{RIP}(s, \delta_s)) \\ & \leq 2n \exp\left(\frac{-n\delta_s^2}{2d}\right) + 4[n(n - 1)/2] \exp\left(\frac{-n\delta_s^2}{16ds^2}\right) \\ & \leq [2n + 2n(n - 1)] \exp\left(\frac{-n\delta_s^2}{16ds^2}\right) \\ & = 2n^2 \exp\left(\frac{-n\delta_s^2}{16ds^2}\right) \leq 2n^2 \exp\left(\frac{-c_2 n}{ds^2}\right), \end{aligned}$$

where $c_2 \leq \delta_s^2/16$. If $n \geq 2$, this probability is less than one provided $n/d \geq c_1 s^2 \log(n)$ where $c_1 \geq 3/c_2$, noting that $m = n/d$ establishes the theorem. \square

2.6.1 Proof of RIP for CAKE

Proof of Theorem 4. This section details the proof of Theorem 4. Our strategy here is the same as that of a single frame, we bound the entries of the Gram matrix.

First note that in this case the Gram matrix has a certain block structure; since $A = [A_1 \cdots A_B]$, we have

$$G = A^T A = \begin{bmatrix} A_1^T A_1 & A_1^T A_2 & \cdots & A_1^T A_B \\ A_2^T A_1 & A_2^T A_2 & \cdots & A_2^T A_B \\ \vdots & \vdots & \ddots & \vdots \\ A_B^T A_1 & A_B^T A_2 & \cdots & A_B^T A_B \end{bmatrix}.$$

This block structure allows us to utilize the results established in Sec 2.6. For the diagonal elements of G , we simply use the same bound for one particular block $A_k^T A_k$, since this is the situation for a sensing a single frame. Therefore

$$\mathbf{P}(|G_{q,q} - 1| \geq \delta_d) \leq 2 \exp\left(\frac{-2n\delta_d^2}{d}\right).$$

For the off-diagonal entries of G , we need to consider the off-diagonal entries of $A_k^T A_k$ and any entry of $A_k^T A_l$, $k \neq l$. Recall that in the Sec. 2.6, we simply used the worst-case slower-decaying bound when the off-diagonal entry of the Gram matrix was no longer a sum of all independent terms. Here we use the same overbound and hence have

$$\mathbf{P}(|G_{p,q}| \geq \delta_o/s) \leq 2 \exp\left(\frac{-n\delta_o^2}{2ds^2}\right).$$

Lastly, we need to perform a union bound over all the entries of the matrix. We have nB diagonal entries, and exploiting symmetry, we only have $nB(nB - 1)/2$ remaining entries. Hence taking $\delta_d = \delta_o = \delta_s/2$,

$$\begin{aligned} & \mathbf{P}(A \text{ does not satisfy RIP}(s, \delta_s)) \\ & \leq 2nB \exp\left(\frac{-n\delta_s^2}{2d}\right) + 4[nB(nB - 1)/2] \exp\left(\frac{-n\delta_s^2}{16ds^2}\right) \\ & \leq [2nB + 2nB(nB - 1)] \exp\left(\frac{-n\delta_s^2}{16ds^2}\right) \\ & = 2n^2 B^2 \exp\left(\frac{-n\delta_s^2}{16ds^2}\right) \leq 2n^2 B^2 \exp\left(\frac{-c_2 n}{ds^2}\right), \end{aligned}$$

where $c_2 \leq \delta_s^2/16$. If $nB \geq 2$, this probability is less than one provided $n/d \geq c_1 s^2 \log(nB)$ where $c_1 \geq 3/c_2$, again noting that $m = n/d$ establishes the theorem.

□

3

SPIRAL: Sparse Poisson Intensity Reconstruction ALgorithms

The observations in many applications consist of counts of discrete events, such as photons hitting a detector, which cannot be effectively modeled using an additive bounded or Gaussian noise model, and instead require a Poisson noise model. As a result, accurate reconstruction of a spatially or temporally distributed phenomenon (f) from Poisson data (y) cannot be effectively accomplished by minimizing a conventional penalized least-squares objective function. The problem addressed in this chapter is the estimation of f from y in an inverse problem setting, where (a) the number of unknowns may potentially be larger than the number of observations and (b) f admits a sparse approximation. The optimization formulation considered in this chapter uses a penalized negative Poisson log-likelihood objective function with nonnegativity constraints (since Poisson intensities are naturally nonnegative). In particular, the proposed approach incorporates key ideas of using separable quadratic approximations to the objective function at each iteration and penalization terms related to ℓ_1 norms of coefficient vectors, total variation seminorms, and partition-based

multiscale estimation methods.

3.1 Introduction

In a variety of applications, ranging from nuclear medicine to night vision and from astronomy to traffic analysis, data are collected by counting a series of discrete events, such as photons hitting a detector or vehicles passing a sensor. The measurements are often inherently noisy due to low count levels, and we wish to reconstruct salient features of the underlying phenomenon from these noisy measurements as accurately as possible. The inhomogeneous Poisson process model [82] has been used effectively in many such contexts. Under the Poisson assumption, we can write our observation model as

$$y \sim \text{Poisson}(Af), \quad (3.1)$$

where $f \in \mathbf{R}_+^n$ is the signal or image of interest, $A \in \mathbf{R}_+^{m \times n}$ linearly projects the scene onto an m -dimensional set of observations, and $y \in \mathbf{Z}_+^m$ is a length- m vector of observed photon counts.

The problem addressed in this chapter is the estimation of f from y when f is sparse or compressible in some basis W (i.e., $f = W\theta$ and θ admits an accurate sparse approximation) and the number of unknowns n may be larger than the number of observations m . This challenging problem has clear connections to *compressed sensing* (CS) [14, 8, 6, 7], but arises in a number of other settings as well, such as tomographic reconstruction in nuclear medicine, superresolution image reconstruction in astronomy, and deblurring in confocal microscopy. In recent work [83, 73], we explored some of the theoretical challenges associated with CS in a Poisson noise setting, and in particular highlighted two key differences between the conventional CS problem and the Poisson CS problem:

- unlike many sensing matrices in the CS literature, the matrix A must contain

all nonnegative elements, and

- the intensity f is nonnegative, and hence any estimate \hat{f} hereof must also be nonnegative.

The nonnegativity of \hat{f} and A results in challenging optimization problems. In particular, the restriction that \hat{f} is nonnegative introduces a set of inequality constraints into the minimization setup; as shown in [84, 19], these constraints are simple to satisfy when \hat{f} is sparse in the canonical basis, but they introduce significant challenges when enforcing sparsity in an arbitrary basis.

3.1.1 Problem Formulation

Under the Poisson model (3.1), the probability of observing a particular vector of counts y is given by

$$p(y|Af) = \prod_{i=1}^m \frac{(e_i^\top Af)^{y_i}}{y_i!} \exp(-e_i^\top Af) \quad (3.2)$$

where e_i is the i th canonical basis unit vector. Thus the negative Poisson log-likelihood is given by

$$F(f) = \mathbf{1}^\top Af - \sum_{i=1}^m y_i \log(e_i^\top Af), \quad (3.3)$$

where $\mathbf{1}$ is an m -vector of ones. (Here we neglect $\log(y_i!)$ terms since they are constant with respect to f and hence do not impact our objective.) We will see later that in order to avoid the singularity at $f = 0$, it is advantageous to introduce a small parameter $\beta > 0$ where typically $\beta \ll 1$:

$$F(f) \equiv \mathbf{1}^\top Af - \sum_{i=1}^m y_i \log(e_i^\top Af + \beta). \quad (3.4)$$

Similar techniques are used in [85] in the form of known background intensities, where the observations are modeled by $y \sim \text{Poisson}(Af + b)$ with $b \in \mathbf{R}_+^n$ known a priori. If $\min(b)$ is large enough β is not explicitly needed, however in our experiments we assume $b = 0$ and use $\beta = 1 \times 10^{-10}$, much smaller than any reasonable background count magnitude. This small parameter will also appear in the gradient

$$\nabla F(f) = A^\top \mathbf{1} - \sum_{i=1}^m \frac{y_i}{e_i^\top A f + \beta} A^\top e_i, \quad (3.5)$$

and the Hessian

$$\nabla^2 F(f) = A^\top \left[\sum_{i=1}^m \frac{y_i}{(e_i^\top A f + \beta)^2} e_i e_i^\top \right] A. \quad (3.6)$$

Our Poisson reconstruction algorithms take the form of the following constrained optimization problem:

$$\begin{aligned} & \underset{f \in \mathbf{R}^n}{\text{minimize}} \Phi(f) := F(f) + \tau \text{pen}(f) \\ & \text{subject to } f \geq 0, \end{aligned} \quad (3.7)$$

where

- $F : \mathbf{R}^n \rightarrow \mathbf{R}$ is the negative Poisson log-likelihood in (3.4), and
- $\text{pen} : \mathbf{R}^n \rightarrow \mathbf{R}$ is a finite, usually nonsmooth, and potentially nonconvex penalty functional.

In this chapter, we will consider several variants of the penalty term, including $\|f\|_1$, $\|W^\top f\|_1$ for some arbitrary orthonormal basis W , a total-variation seminorm $\|f\|_{\text{TV}}$, and a complexity regularization penalty based upon recursive dyadic partitions. We refer to our approach as SPIRAL (Sparse Poisson Intensity Reconstruction ALgorithm).

3.1.2 Related Work

Various regularization techniques are often employed to compensate for the ill-posedness of the estimation problem. Outside the Poisson context, for example in the presence of additive white Gaussian noise, regularization methods based on wavelet or curvelet sparsity [7], models of wavelets' clustering and persistence properties [22], and a variety of other penalties (cf. [13]) have proven successful.

The key challenge in Poisson intensity estimation problems is that the mean and the variance of the observed counts are the same. As a result, conventional approaches based on a penalized least-squares objective function (cf. [13, 74]) will yield suboptimal results when applied to Poisson data with low intensities. Variance-stabilizing transforms (VSTs), such as the Anscombe transform [86] and the Haar-Fisz [87, 88] transform, are widely used to address this issue and to approximate the Poisson observations by Gaussian random variables [89, 90]. Jansen proposes a wavelet based Poisson estimation method based on data-adaptive VSTs and Bayesian priors on the stabilized coefficients [91]. However, as pointed out in [92, 93], such approximations are inaccurate when the observed number of photons per pixel or voxel is very low and tend to oversmooth the resulting estimate. In a more recent work, Zhang et al. [94] propose a multiscale variance-stabilizing transform (MSVST) which applies a VST to the empirical wavelet, ridgelet or curvelet transform coefficients. However, theoretical analysis of this approach is not available and it is not clear how to extend the MSVST to Poisson inverse problems.

Several authors have investigated reconstruction algorithms specifically designed for Poisson noise without the need for VSTs. In [95, 96], Nowak and Kolaczyk describe multiscale Bayesian approach in an Expectation-Maximization (EM) framework to reconstruct Poisson intensities. In their seminal paper [97], Kolaczyk and Nowak present a multiscale framework for likelihoods similar to wavelet analysis and

propose a denoising algorithm based on the complexity-penalized likelihood estimation (CPLE). The CPLE objective function is minimax optimal over a wide range of isotropic likelihood models. There are several variants of the CPLE method depending upon the nature of the image or signal being denoised [20, 98, 99].

Regularization based on a *total variation* (TV) seminorm has also garnered significant recent attention (cf. [100, 101]). This seminorm is described in detail below; in general, it measures how much an image varies across pixels, so that a highly textured or noisy image will have a large TV seminorm, while a smooth or piecewise constant image would have a relatively small TV seminorm. This is often a useful alternative to wavelet-based regularizers, which are also designed to be small for piecewise smooth images but can result in spurious large, isolated wavelet coefficients and related image artifacts.

In the context of Poisson inverse problems, however, adaptation of these regularization methods can be challenging for two main reasons. First, the negative Poisson log-likelihood used in the formulation of an objective function often requires the application of relatively sophisticated optimization theory principles. Second, because Poisson intensities are inherently nonnegative, the resulting optimization problem must be solved over a constrained feasible set, increasing the complexity of most algorithms. Some recent headway has been made using multiscale or smoothness-based penalties[20, 102, 34]. In one recent work [103], the Poisson statistical model is bypassed in favor of an additive Gaussian noise model through the use of the Anscombe variance stabilizing transform. This statistical simplification is not without cost, as the linear projections of the scene must now be characterized as nonlinear observations. Other recent efforts [104, 105] solve Poisson image reconstruction problems with TV seminorm regularization using a split Bregman approach [106], but the proposed methods involves a matrix inverse operation which can be extremely difficult to compute for large problems outside of deconvolution settings. TV semi-

norm regularization is also explored in the context of a Richardson-Lucy algorithm [107], but nonnegativity and convergence were not explicitly addressed. Finally, the approaches in [108, 109] apply proximal functions to solve more general constrained convex minimization problems. These methods use projection to obtain feasible iterates (i.e., nonnegative intensity values), which may be difficult for recovering signals that are sparse in a noncanonical basis.

3.1.3 Contributions of the Proposed Method

In the proposed work, we present a general algorithmic framework for solving Poisson inverse problems. This framework requires no special structure in the sensing matrix A , yet can take advantage fast matrix-vector multiplications when available. The success of this approach hinges on the ability to solve certain constrained subproblems quickly. We show that this can be done for a variety of regularization schemes. Additionally, we consider a step selection procedure that is better suited for the Poisson log-likelihood versus the corresponding generalizations from the Gaussian log-likelihood. In the subsequent analysis, we establish global convergence of the constrained optimization under a set of mild assumptions which are easily satisfied in practice. We establish properties of the solution set, which yield conditions for a unique solution to the minimization. Our approach is then supported by numerical simulations which show state-of-the-art performance on a simulated limited-angle emission tomography inverse problem.

3.2 Algorithms

Our approach to solve the minimization problem (3.7) employs sequential quadratic approximations to the Poisson log-likelihood $F(f)$. More specifically, at iteration k we compute a separable quadratic approximation to $F(f)$ using its second-order Taylor series approximation at f^k ; this approximation is denoted $F^k(f)$. The next

iterate is then given by

$$\begin{aligned} f^{k+1} &= \arg \min_{f \in \mathbf{R}^n} F^k(f) + \tau \operatorname{pen}(f) \\ &\quad \text{subject to } f \geq 0. \end{aligned} \tag{3.8}$$

Similar to the framework described in [13], F^k is a second-order Taylor series approximation to F with the Hessian $\nabla^2 F(f^k)$ approximated by a scaled identity matrix $\alpha_k I$, with $\alpha_k > 0$. This yields

$$F^k(f) = F(f^k) + (f - f^k)^\top \nabla F(f^k) + \frac{\alpha_k}{2} \|f - f^k\|_2^2. \tag{3.9}$$

With this separable approximation, simple manipulation of (3.8) yields a sequence of subproblems of the form

$$\begin{aligned} f^{k+1} &= \arg \min_{f \in \mathbf{R}^n} \phi^k(f) = \frac{1}{2} \|f - s^k\|_2^2 + \frac{\tau}{\alpha_k} \operatorname{pen}(f) \\ &\quad \text{subject to } f \geq 0, \end{aligned} \tag{3.10}$$

where

$$s^k = f^k - \frac{1}{\alpha_k} \nabla F(f^k). \tag{3.11}$$

This formulation has the benefit of being easily recognized as a nonnegatively constrained ℓ_2 denoising of the gradient descent step s^k .

The parameter α_k is chosen via a sequence of two repeated steps. First, a modified Barzilai-Borwein (BB) method [110] is used to choose the initial value of α_k . With $\delta^k = f^k - f^{k-1}$, we initially choose

$$\alpha_k = \frac{(\delta^k)^\top \nabla^2 F(f^k) \delta^k}{\|\delta^k\|_2^2} = \frac{\|\sqrt{y} \cdot (A\delta^k)/(Af^k + \beta)\|_2^2}{\|\delta^k\|_2^2}, \tag{3.12}$$

with α_k safeguarded to be within the range $[\alpha_{\min}, \alpha_{\max}]$. Here $\sqrt{\cdot}$, \cdot , and $/$ are understood as component-wise. This method allows our separable approximation

(3.9) to capture the curvature of the Poisson log-likelihood $F(f)$ along the most recent step δ^k , in the vicinity of the current iterate f^k .

The astute reader will recognize (3.12) as a Rayleigh quotient, and hence always has a value within the spectrum of the Hessian. Since F is convex, this guarantees $\alpha_k \geq 0$, even without the safeguard. The traditional BB scheme chooses $\alpha_k = (\gamma^k)^\top \delta^k / \|\delta^k\|_2^2$, where $\gamma^k = \nabla F(f^k) - \nabla F(f^{k-1})$. When applied to a quadratic objective, such as arising from considering the Gaussian log-likelihood, these two schemes are identical. However, when applied to the Poisson log-likelihood, our choice is more strongly effected by the curvature at the current iteration. Our modified BB choice is no more expensive to compute than the original BB scheme since $A\delta^k$ and Af^k are already available from the gradient computations, and computing α_k in (3.12) is a simple sequence of $O(n)$ operations.

This initial choice of α_k is used if the resulting solution of (3.10) satisfies the acceptance criteria

$$\Phi(f^{k+1}) \leq \max_{i=[k-M]_+, \dots, k} \Phi(f^i) - \frac{\sigma \alpha_k}{2} \|f^{k+1} - f^k\|_2^2, \quad (3.13)$$

where M is a nonnegative integer, $\sigma \in (0, 1)$ is a small constant, and the operation $[\cdot]_+ = \max\{0, \cdot\}$. If it fails this acceptance criteria, α_k is repeatedly increased by a factor η until the solution to (3.10) satisfies (3.13). This gentle criteria allows the nonmonotonic objective behavior characteristic of the Barzilai-Borwein methods [13, 110], yet enforces that the next iterate have a slightly smaller objective than the largest value over the past M iterations. Note that choosing $M = 0$ results in a purely monotonic algorithm. For clarity, we describe our general procedure in Algorithm 1.

Algorithm 1 Sparse Poisson Intensity Reconstruction ALgorithm (SPIRAL)

```
1: Initialize Choose  $\eta > 1$ ,  $\sigma \in (0, 1)$ ,  $M \in \mathbf{Z}_+$ ,  $0 < \alpha_{\min} \leq \alpha_{\max}$ , and initial  
solution  $f^0$ . Start iteration counter  $k \leftarrow 0$ .  
2: repeat  
3:   choose  $\alpha_k \in [\alpha_{\min}, \alpha_{\max}]$  by (3.12)  
4:    $f^{k+1} \leftarrow$  solution of (3.10)  
5:   while  $f^{k+1}$  does not satisfy (3.13) do  
6:      $\alpha_k \leftarrow \eta \alpha_k$   
7:      $f^{k+1} \leftarrow$  solution of (3.10)  
8:   end while  
9:    $k \leftarrow k + 1$   
10: until stopping criterion is satisfied

---


```

3.2.1 Canonical Basis With Sparsity Penalty

When $\text{pen}(f) = \|f\|_1$, the minimization subproblem (3.10) has the following analytic solution:

$$f^{k+1} = \left[s^k - \frac{\tau}{\alpha_k} \mathbf{1} \right]_+,$$

with $[\cdot]_+$ acting component-wise. Thus solving (3.7) subject to nonnegativity constraints with an ℓ_1 penalty function measuring sparsity in the canonical basis is straightforward. An alternative algorithm for solving this Poisson inverse problem with sparsity in the canonical basis was also explored in the recent literature [84].

3.2.2 Non-Canonical Basis

Now suppose that the signal of interest is sparse in some other basis. Then the ℓ_1 penalty term is given by

$$\text{pen}(f) := \|W^\top f\|_1 = \|\theta\|_1,$$

where

$$\theta := W^\top f \tag{3.14}$$

for some orthonormal basis W . When the reconstruction $\hat{f} = W\hat{\theta}$ must be non-negative (i.e., $W\hat{\theta} \geq 0$), the minimization problem

$$\begin{aligned}\theta^{k+1} := \arg \min_{\theta \in \mathbf{R}^n} \phi^k(\theta) &:= \frac{1}{2}\|\theta - s^k\|_2^2 + \frac{\tau}{\alpha_k}\|\theta\|_1, \\ \text{subject to } W\theta &\geq 0\end{aligned}\tag{3.15}$$

no longer has an analytic solution necessarily. We can solve this minimization problem by solving its Lagrangian dual. First, we reformulate (3.15) so that its objective function $\phi^k(\theta)$ is differentiable by defining $u, v \geq 0$ such that $\theta = u - v$. The minimization problem (3.15) becomes

$$\begin{aligned}(u^{k+1}, v^{k+1}) := \arg \min_{u, v \in \mathbf{R}^n} \frac{1}{2}\|u - v - s^k\|_2^2 + \frac{\tau}{\alpha_k}\mathbf{1}^\top(u + v) \\ \text{subject to } u, v \geq 0, \quad W(u - v) \geq 0,\end{aligned}\tag{3.16}$$

which has twice as many parameters and has additional nonnegativity constraints on the new parameters, but now has a differentiable objective function. The Lagrangian function corresponding to (3.16) is given by

$$\begin{aligned}\mathcal{L}(u, v, \lambda_1, \lambda_2, \lambda_3) &= \frac{1}{2}\|u - v - s^k\|_2^2 + \frac{\tau}{\alpha_k}\mathbf{1}^\top(u + v) \\ &\quad - \lambda_1^\top u - \lambda_2^\top v - \lambda_3^\top W(u - v),\end{aligned}$$

where $\lambda_1, \lambda_2, \lambda_3 \in \mathbf{R}^n$ are the Lagrange multipliers corresponding to the constraints in (3.16). Setting the derivative of \mathcal{L} with respect to u and v to zero, we obtain

$$\begin{aligned}u - v &= s^k + \lambda_1 - \frac{\tau}{\alpha_k}\mathbf{1} + W^\top\lambda_3, \text{ and} \\ \lambda_2 &= \frac{2\tau}{\alpha_k}\mathbf{1} - \lambda_1,\end{aligned}\tag{3.17}$$

which leads to the Lagrangian dual function

$$g(\lambda_1, \lambda_3) = -\frac{1}{2}\|s^k + \lambda_1 - \frac{\tau}{\alpha_k}\mathbf{1} + W^\top\lambda_3\|_2^2 + \frac{1}{2}\|s^k\|_2^2.$$

We define $\gamma := \lambda_1 - \frac{\tau}{\alpha_k} \mathbf{1}$. For the Lagrange dual problem corresponding to (3.16), the Lagrange multipliers $\lambda_1, \lambda_2, \lambda_3 \geq 0$. Since $\lambda_2 = \frac{2\tau}{\alpha_k} \mathbf{1} - \lambda_1$, then $-\frac{\tau}{\alpha_k} \mathbf{1} \leq \gamma \leq \frac{\tau}{\alpha_k} \mathbf{1}$. Also, let $\lambda = \lambda_3$. The Lagrange dual problem associated with this problem is thus given by

$$\begin{aligned} & \underset{\lambda, \gamma \in \mathbf{R}^n}{\text{minimize}} \quad h(\lambda, \gamma) := \frac{1}{2} \|s^k + \gamma + W^\top \lambda\|_2^2 - \frac{1}{2} \|s^k\|_2^2 \\ & \text{subject to} \quad \lambda \geq 0, \quad -\frac{\tau}{\alpha_k} \mathbf{1} \leq \gamma \leq \frac{\tau}{\alpha_k} \mathbf{1} \end{aligned} \quad (3.18)$$

and at the optimal values γ^* and λ^* , the primal iterate θ^{k+1} is given by

$$\theta^{k+1} := u^{k+1} - v^{k+1} = s^k + \gamma^* + W^\top \lambda^*.$$

We note that the minimizers of the primal problem (3.16) and its dual (3.18) satisfy $\phi^k(\theta^{k+1}) = -h(\gamma^*, \lambda^*)$ since (3.16) satisfies (a weakened) Slater's condition [111]. In addition, the function $-h(\gamma, \lambda)$ is a lower bound on $\phi^k(\theta)$ at any dual feasible point.

The objective function of (3.18) can be minimized by alternately solving for λ and γ , which is accomplished by taking the partial derivatives of $h(\lambda, \gamma)$ and setting them to zero. Each component is then constrained to satisfy the bounds in (3.18). At the j^{th} iteration, the variables can, thus, be defined as follows:

$$\begin{aligned} \gamma^{(j)} &= \text{mid}\left\{-\frac{\tau}{\alpha_k} \mathbf{1}, -s^k - W^\top \lambda^{(j-1)}, \frac{\tau}{\alpha_k} \mathbf{1}\right\} \\ \lambda^{(j)} &= [-W(s^k + \gamma^{(j)})]_+, \end{aligned} \quad (3.19)$$

where the operator $\text{mid}\{a, b, c\}$ chooses the middle value of the three arguments component-wise. Note that at the end of each iteration j , the approximate solution

$\theta^{(j)} := s^k + \gamma^{(j)} + W^\top \lambda^{(j)}$ to (3.15) is feasible with respect to the constraint $W\theta \geq 0$:

$$\begin{aligned}
W\theta^{(j)} &= Ws^k + W\gamma^{(j)} + \lambda^{(j)} \\
&= W(s^k + \gamma^{(j)}) + [-W(s^k + \gamma^{(j)})]_+ \\
&= [W(s^k + \gamma^{(j)})]_+ \\
&\geq 0.
\end{aligned} \tag{3.20}$$

Thus, we can terminate the iterations for the dual problem early and still obtain a feasible point. By solving the subproblem “loosely” (see Sec. 3.3.3), the algorithm can converge faster but to a potentially less accurate estimate. In Sec. 3.4, we show results from both “loose” and “tight” criteria for solving the subproblem. We call this approach SPIRAL- ℓ_1 .

3.2.3 Total Variation Penalty

We also consider an approach where the TV seminorm is used as a penalization scheme, i.e., $\text{pen}(f) = \|f\|_{\text{TV}}$. We define the anisotropic TV seminorm as

$$\|f\|_{\text{TV}} := \sum_{k=1}^{\sqrt{n}-1} \sum_{l=1}^{\sqrt{n}} |f_{k,l} - f_{k+1,l}| + \sum_{k=1}^{\sqrt{n}} \sum_{l=1}^{\sqrt{n}-1} |f_{k,l} - f_{k,l+1}|,$$

where – for simplicity of presentation, not algorithmic necessity – we use a slight abuse of notation by using 2D pixel indices instead of vector indices by assuming that $f \in \mathbf{R}^n$ is a square $\sqrt{n} \times \sqrt{n}$ image. This highlights the fact that the TV seminorm is simply a measure of the magnitude of all vertical and horizontal first-order differences. Said differently, one can think of an image with a small TV seminorm as one that is sparse with respect to an overcomplete representation of these first-order differences (neglecting the mean of f), meaning the image has few abrupt changes in pixel intensity yet many regions of homogeneous signal level. This property makes TV especially well suited for image denoising and inverse problems.

Recent work by Beck and Teboulle [101] presents a fast computational method for solving the TV-regularized problem

$$\begin{aligned}\tilde{f} = \arg \min_{f \in \mathbf{R}^n} \quad & \frac{1}{2} \|\tilde{A}f - b\|_2^2 + \lambda \|f\|_{\text{TV}} \\ \text{subject to} \quad & f \in C,\end{aligned}\tag{3.21}$$

where $\lambda > 0$ is a tuning parameter, C is a closed convex set and \tilde{A} is a linear, *spatially invariant* blur operator. This method utilizes a gradient-based optimization approach founded on a monotone iterative shrinkage and thresholding algorithm. When we choose $\tilde{f} = f^{k+1}$, $\tilde{A} = I$, $b = s^k$, $\lambda = \tau/\alpha_k$, and $C = \{f \in \mathbf{R}^n : f \geq 0\}$, (3.21) then reduces to an ℓ_2 denoising of s^k with a total variation regularizer:

$$\begin{aligned}f^{k+1} = \arg \min_{f \in \mathbf{R}^n} \quad & \frac{1}{2} \|f - s^k\|_2^2 + \frac{\tau}{\alpha_k} \|f\|_{\text{TV}} \\ \text{subject to} \quad & f \geq 0,\end{aligned}\tag{3.22}$$

precisely the form (3.10) required for use in our algorithmic framework. We call this approach with a total variation penalty SPIRAL-TV.

3.2.4 Partition-Based Methods

An alternative to the ℓ_1 - and TV-norm penalties can be formulated using model-based estimates that utilize structure in the coefficients beyond that of a sparse representation. In particular, we build upon the framework of *recursive dyadic partitions* (RDP), which we summarize here and are described in detail in [20]. Let \mathcal{P} be the class of all recursive dyadic partitions of $[0, 1]^2$ where each cell in the partition has a sidelength at least $1/\sqrt{n}$, and let $P \in \mathcal{P}$ be a candidate partition. The intensity on P , denoted $f(P)$, is calculated using a nonnegative least-squares method to fit a model (such as a constant) to s^k in (3.15) in each cell in the RDP. As an example, consider Fig. 3.1. Here we approximate the true image (Fig. 3.1(a)) on the recursive dyadic partition defined in Fig. 3.1(b)). The result is a piecewise constant

approximation to the emission image (Fig. 3.1(c)). We see that the partition model is able to accurately capture the image in clear multiresolution fashion: large homogeneous regions are well-modeled by large cells, whereas edges are approximated via the deeper recursive partitioning. Furthermore, a penalty can be assigned to the resulting estimator which is proportional to $|P|$, the number of cells in P . Thus we set

$$\begin{aligned}\widehat{P}^{k+1} &= \arg \min_{P \in \mathcal{P}} \frac{1}{2} \|s^k - f(P)\|_2^2 + \frac{\tau}{\alpha_k} |P|, \\ f^{k+1} &= f(\widehat{P}^{k+1}).\end{aligned}\tag{3.23}$$

A search over \mathcal{P} can be computed quickly using a dynamic program. When using constant partition cell models, the nonnegative least-squares fits can be computed non-iteratively in each cell by simply using the maximum of the average of s^k in that cell and zero. Because of this, enforcing the constraints is trivial and can be accomplished very quickly. The disadvantage of using constant model fits is that it yields piecewise constant estimates. However, a cycle-spun translation-invariant (TI) version of this approach [20] can be implemented with high computational efficiency and can be used for solving this nonnegative regularized least-squares subproblem that results in a much smoother estimator. We refer to these approaches as SPIRAL-RDP and SPIRAL-RDP-TI.

It can be shown that partition-based denoising methods such as this are closely related to Haar wavelet denoising with an important hereditary constraint placed on the thresholded coefficients – if a parent coefficient is thresholded, then its children coefficients must also be thresholded [20]. This constraint is akin to wavelet-tree ideas which exploit persistence of significant wavelet coefficients across scales and have recently been shown highly useful in compressed sensing settings [22]. Since in this context the penalty can be thought of an ℓ_0 measure, the resulting RDP-based penalty function is not a convex function. Hence we can only guarantee convergence

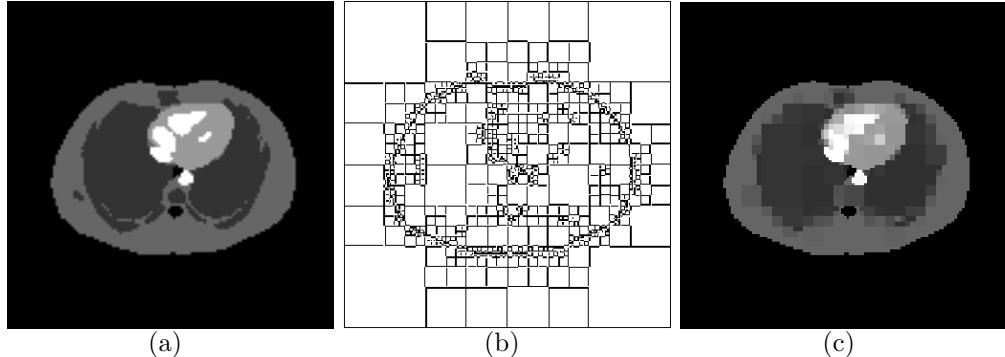


FIGURE 3.1: Example of a partition-based approximation. (a) True image. (b) Recursive dyadic partition (RDP). (c) RDP-based approximation of the true image.

to a local minimizer. Given a sufficiently accurate initialization, the RDP-based method performs competitively in both speed and accuracy to convex penalties, for which global convergence is assured.

3.3 Algorithmic Details

3.3.1 Computational Complexity and Nonmonotonicity

It should be noted that in determining an acceptable next iterate f^{k+1} in (3.8), the main computational burden is often checking the acceptance criteria (3.13) as testing each candidate solution involves recomputing Af^{k+1} . In the worst case, A may be a dense unstructured matrix for which computing matrix-vector products is costly. Although enforcing near-monotonicity of the objective aids convergence to a more accurate solution to the reconstruction problem (3.7), significant demonstrable gains in computational speed may be achieved by forgoing this criteria and simply accepting the choice (3.12). In this case, an efficient implementation of our algorithm only requires two matrix-vector multiplications involving A per iteration, one computing Af^k for defining α_k in (3.12), and the other using A^\top in the computation of $\nabla F(f^k)$ for defining the gradient descent result s^k in (3.11). Since (3.10) requires only α_k and s^k , there are no matrix-vector multiplications involving A in

the denoising subproblem.

3.3.2 Initialization

While global convergence proofs – such as the one in Section 3.3.4 – guarantee convergence for any initial point $f^0 \geq 0$, the choice of initialization is an important practical consideration. Iterative algorithms are rarely allowed to execute long enough to converge to an optimal solution, meaning the approximate solution may be strongly dependent on the starting point of the algorithm. Further, nonconvex penalties such as our RDP-based penalization scheme, may introduce local optima that are difficult to avoid if the initialization is chosen poorly. Although in both these cases a better initialization typically yields better performance, it is undesirable to spend significant computational resources in doing so.

In practice, one approach is to initialize with an appropriately-scaled $A^\top y$. We have found this approach particularly effective in compressive sensing contexts where the sensing matrix A acts as a near-isometry. In many applications, a Fourier-based inversion scheme often leads to an effective initialization. In the emission tomography example we consider in Sec. 3.4, a filtered back-projection estimate provides a sufficiently good initialization with low computational cost. In particular, the initialization we use in the numerical experiments results from two iterations of a non-convergent version of the EPL-INC-3 algorithm, initialized by the filtered back-projection estimate. The EPL-INC-3 method employs an incremental penalized Poisson likelihood EM algorithm with an image roughness penalty, more details are available in Section 3.4.2.

3.3.3 Termination Criteria

In this section, we list criteria by which SPIRAL decides whether the iterates in the subproblem (3.10) and for the main problem (3.7) are acceptable approximations

to the true minimizers to terminate the algorithm. Here, we only provide criteria for the SPIRAL- ℓ_1 subproblem since the global solution to the partition-based SPIRAL subproblem (3.23) can be easily and exactly obtained using a non-iterative tree-pruning algorithm [20], even though its objective function is nonconvex (due to the nonconvex penalty). For the TV-based method, we use the standard convergence criteria implemented by Beck and Teboulle [101].

SPIRAL- ℓ_1 subproblem

The criterion for termination for the SPIRAL- ℓ_1 subproblem measures the duality gap. Since the objective function $\phi^k(\theta)$ in (3.15) is convex and all the constraints are affine, then (a weaker) Slater's condition holds [111] and, therefore, the duality gap is zero, i.e.,

$$\phi^k(\theta^{k+1}) = -h(\gamma^*, \lambda^*),$$

where (γ^*, λ^*) solves (3.18). Recall that, at the j th iterate, $\theta^{(j)} = s^k + \gamma^{(j)} + W^\top \lambda^{(j)}$ can be viewed as an approximate solution to θ^{k+1} . Thus, the SPIRAL approach for the ℓ_1 subproblem will consider the iterates to be sufficiently close to the optimal solution if

$$\frac{|\phi^k(\theta^{(j)}) + h(\gamma^{(j)}, \lambda^{(j)})|}{|\phi^k(\theta^{(j)})|} \leq \text{tol}_{\text{SUB}},$$

where $\text{tol}_{\text{SUB}} > 0$ is some small constant. In our numerical experiments, we often found that it is not necessary to solve this subproblem very accurately, especially at the beginning of the algorithm where the iterate θ^k is still far from the optimal solution.

SPIRAL

Since the global minimizer f^* of (3.7) is not known *a priori*, criteria to terminate the SPIRAL algorithm must be established to determine whether a computed minimizer

\hat{f} is an acceptable solution. We list two such criteria. The first of these criteria is simple: terminate if consecutive iterates or the corresponding objective values do not change significantly, i.e.,

$$\|f^{k+1} - f^k\|_2 / \|f^k\|_2 \leq \text{tolP} \quad (3.24)$$

or

$$|\Phi(f^{k+1}) - \Phi(f^k)| / |\Phi(f^k)| \leq \text{tolP},$$

where tolP is a small positive constant. The advantage of these criteria is that they apply to general penalty functions. The disadvantage, however, is that it is possible that the change between two consecutive iterates may be small or that they result in only small improvements in the objective function even though iterates are still far from the true solution. However, we have yet to observe this premature termination in practice.

The next criterion applies only to SPIRAL- ℓ_1 , where the penalty is convex and, after a change of variables, differentiable. This criterion is based on the Karush-Kuhn-Tucker (KKT) conditions for optimality: at the k th iteration, given θ^k and the corresponding Lagrange multipliers λ^k computed from (3.18), we determine whether

$$\|\nabla\Phi(\theta^k) - W^\top \lambda^k\|_2 \leq \text{tolP}, \quad (3.25)$$

The left hand side corresponds to the gradient of the Lagrangian function, which criterion (3.25) forces to be sufficiently close to zero. A complementarity condition could also be required, but by construction, it is always satisfied, i.e., $(\lambda^k)^\top W\theta^k = 0$ using (3.19) and (3.20).

3.3.4 Convergence Proof

In this section we consider the minimization problem

$$\begin{aligned} & \underset{f \in \mathbf{R}^n}{\text{minimize}} \quad \Phi(f) := F(f) + \tau \text{pen}(f) \\ & \text{subject to} \quad f \geq 0, \end{aligned} \tag{3.26}$$

where F is the negative Poisson log-likelihood defined in (3.3). To ease analysis, we consider the equivalent problem of

$$\underset{f \in \mathbf{R}^n}{\text{minimize}} F(f) + \rho(f), \tag{3.27}$$

where $\rho : \mathbf{R}^n \rightarrow \overline{\mathbf{R}} = \mathbf{R} \cup \{-\infty, \infty\}$ is defined to be

$$\rho(f) = \tau \text{pen}(f) + \delta_+(f), \tag{3.28}$$

with $\delta_+ = \delta_{\mathbf{R}_+^n}$ being the indicator function of the nonnegative orthant (our feasible set):

$$\delta_+(f) = \begin{cases} 0 & \text{if } f \geq 0, \\ \infty & \text{otherwise.} \end{cases} \tag{3.29}$$

For notational simplicity, we still refer to the objective as $\Phi(f) = F(f) + \rho(f)$. Considering the constraints in this manner allows one to avoid explicit examination of the convergence of the Karush-Kuhn-Tucker (KKT) conditions, and only consider subgradient calculus. For more details, see Rockafellar and Wets [112].

We make the following mild assumptions:

- (A1) F is proper convex (i.e., F is convex with $F(f) > -\infty$ for all f and $F(f) < \infty$ for some f) and Lipschitz continuously differentiable on \mathbf{R}_+^n ,
- (A2) ρ is proper convex and continuous on \mathbf{R}_+^n ,
- (A3) Φ is coercive (i.e., $\lim_{\|f\| \rightarrow \infty} \Phi(f) = \infty$),

We show that the assumption (A1) is satisfied by the negative Poisson log-likelihood through the following lemma.

Lemma 5. *The negative Poisson log-likelihood with parameter $\beta > 0$ is Lipschitz continuously differentiable on \mathbf{R}_+^n with Lipschitz constant*

$$L \leq \frac{\max(y)}{\beta^2} \|A\|_2^2 \leq \frac{\max(y)}{\beta^2} \max(A^\top \mathbf{1}) \max(A \mathbf{1}).$$

Proof. Clearly the Hessian of F (3.6) is positive semidefinite; therefore all that is required is a bound on the largest eigenvalue of $\nabla^2 F(f)$ over the feasible set. That is, we need to bound

$$\lambda_{\max} = \sup_{f \geq 0} \sup_{\|z\|_2 \leq 1} z^\top \nabla^2 F(f) z.$$

Since A is nonnegative, the supremum over $f \geq 0$ is attained at $f = 0$, as this minimizes the denominator of the fraction in (3.6). Therefore we simply need to bound the largest eigenvalue of $\nabla^2 F(0) = \frac{1}{\beta^2} A^\top \text{Diag}(y) A$. Using properties of matrix norms, we have

$$\begin{aligned} \lambda_{\max} &= \frac{1}{\beta^2} \|A^\top \text{Diag}(y) A\|_2 \leq \frac{1}{\beta^2} \|A\|_2^2 \|\text{Diag}(y)\|_2 \\ &= \frac{\max(y)}{\beta^2} \|A\|_2^2 \leq \frac{\max(y)}{\beta^2} \|A\|_1 \|A\|_\infty \\ &= \frac{\max(y)}{\beta^2} \max(A^\top \mathbf{1}) \max(A \mathbf{1}). \end{aligned}$$

Since a bound on the largest eigenvalue of the Hessian is the same as a bound on the Lipschitz constant of the gradient, this completes the proof. \square

We present the latter bound in Lemma 5 since the matrix A is often such that computing $\|A\|_2$ may be difficult, yet matrix-vector products with A and A^\top can be computed at far lower cost.

Before launching into the details of our convergence proof, let us recall a few facts. A point \bar{f} is said to be critical for (3.27) if

$$0 \in \partial\Phi(\bar{f}) = \nabla F(\bar{f}) + \partial\rho(\bar{f}),$$

where $\partial g(\bar{f})$ denotes the subdifferential (set of all subgradients) of g at \bar{f} [112]. A minimizer \bar{f} and corresponding minimum $\Phi(\bar{f})$ are guaranteed to exist for Φ coercive, proper convex, and lower semicontinuous, with criticality of \bar{f} sufficient for \bar{f} to optimize (3.27). In solving (3.27), we generate a sequence of iterates $\{f^k\}_{k \in \mathbf{Z}_+}$, which due to the nonnegativity constraint, we have $f^k \geq 0$ for all $k \in \mathbf{Z}_+$.

We also simplify notation. Recall $\delta^{k+1} = f^{k+1} - f^k$, and let

$$l(k) = \arg \max_{i=[k-M]_+, \dots, k} \Phi(f^i), \quad (3.30)$$

i.e., the index where Φ is largest over the past M iterations. Then (3.13) is more simply written as

$$\Phi(f^{k+1}) \leq \Phi(f^{l(k)}) - \frac{\sigma\alpha_k}{2} \|\delta^{k+1}\|_2^2. \quad (3.31)$$

It can be shown that the sequence $\Phi(f^{l(k)})$ is nonincreasing, and further that $\Phi(f^0) = \Phi(f^{l(0)}) \geq \Phi(f^{l(k)}) \geq \Phi(f^k)$. Hence from assumption (A3), all the iterates are contained in a compact convex subset of \mathbf{R}_+^n (namely the initial sublevelset $\{f : \Phi(f) \leq \Phi(f^0)\}$), and, therefore, we are guaranteed to have at least one convergent subsequence of iterates.

Following the construction in [13], the proof of our global convergence result (stated in Theorem 9 below) is best presented by first proving a set of supporting lemmas. The proofs of these lemmas are inspired by [13] and [113], which consider the unconstrained setting only. Many important results hinge only on the analysis of the objective values and the acceptance rule (3.31), and can be carried over to the constrained setting without any modification. In such cases we only highlight what restrictions must be in effect.

However, some care must be taken in restricting the feasible domain to \mathbf{R}_+^n in the proof of Lemma 6. The proof in [13] relies on a result in [114], which holds only for open sets, not the closed set \mathbf{R}_+^n . To show this result in the constrained setting, we assume that ρ is continuous on \mathbf{R}_+^n . This assumption is stronger than the lower semicontinuity assumed in the unconstrained case; however it is still satisfied by the penalization schemes considered in Section 3.2.

Lemma 6. *Suppose $\bar{f} \in \mathbf{R}_+^n$ is not critical for (3.27). Then for any $\bar{\alpha} \geq \alpha_{\min}$, there exists an $\epsilon > 0$ such that for any subsequence $\{f^{k_j}\}_{j \in \mathbf{Z}_+}$ with $\lim_{j \rightarrow \infty} f^{k_j} = \bar{f}$, $f^{k_j} \in \mathbf{R}_+^n$ for all $j \in \mathbf{Z}_+$, and $\alpha_{\min} \leq \alpha_{k_j} \leq \bar{\alpha}$, we have*

$$\|\delta^{k_j+1}\|_2 = \|f^{k_j+1} - f^{k_j}\|_2 \geq \epsilon$$

for all j sufficiently large.

Proof. Assume $\|\delta^{k_j+1}\|_2 \rightarrow 0$ for contradiction, implying $\lim_{j \rightarrow \infty} f^{k_j+1} = \lim_{j \rightarrow \infty} (\delta^{k_j+1} + f^{k_j}) = \bar{f}$, where $f^{k_j+1} \in \mathbf{R}_+^n$ for all $j \in \mathbf{Z}_+$. Now since f^{k_j+1} is critical for the subproblem (3.8), we have

$$0 \in \nabla F(f^{k_j}) + \alpha_{k_j} \delta^{k_j+1} + \partial \rho(f^{k_j+1}).$$

From the definition of $\partial \rho(f^{k_j+1})$, we have

$$\rho(z) \geq \rho(f^{k_j+1}) - [\nabla F(f^{k_j}) + \alpha_{k_j} \delta^{k_j+1}]^\top (z - f^{k_j+1}).$$

for all $z \in \mathbf{R}^n$. We now take the limit as $j \rightarrow \infty$. Since both ρ and ∇F are continuous on \mathbf{R}_+^n , $\rho(f^{k_j+1}) \rightarrow \rho(\bar{f})$ and $\nabla F(f^{k_j}) \rightarrow \nabla F(\bar{f})$. Additionally, since $\delta^{k_j+1} \rightarrow 0$ with α_{k_j} bounded, $\alpha_{k_j} \delta^{k_j+1} \rightarrow 0$, hence for all $z \in \mathbf{R}^n$ we have

$$\rho(z) \geq \rho(\bar{f}) - \nabla F(\bar{f})^\top (z - \bar{f}),$$

showing $0 \in \nabla F(\bar{f}) + \partial \rho(\bar{f})$, implying \bar{f} is a critical point for (3.27), the desired contradiction. Hence we cannot have $\|\delta^{k_j+1}\|_2 \rightarrow 0$ as assumed. \square

Lemma 7. *Given $\sigma \in (0, 1)$, then there exists an $\tilde{\alpha} > 0$ such that for any sequence $\{f^i\}_{i=1}^k$ with $f^i \in \mathbf{R}_+^n$ for all $i = \mathbf{Z}_+$, the acceptance criterion (3.31) is satisfied whenever $\alpha_k \geq \tilde{\alpha} = 2L/(1 - \sigma)$, where L is the Lipschitz constant for ∇F over \mathbf{R}_+^n .*

Proof. The proof follows similarly from the proof of Lemma 4 in [13], where we only consider $f^i \in \mathbf{R}_+^n$, and hence only require F to be Lipschitz continuously differentiable over \mathbf{R}_+^n . \square

Lemma 8. *The sequence $\{f^k\}_{k \in \mathbf{Z}_+}$ generated by SPIRAL is such that $\lim_{k \rightarrow \infty} \delta^{k+1} = 0$, and there exists $\bar{\Phi} \in \mathbf{R}$ such that $\lim_{k \rightarrow \infty} \Phi(f^k) = \bar{\Phi}$.*

Proof. The proof follows identically as the proof of Lemma 4 in [13] as no modifications are required for the constraints within the proof. \square

With the above lemmas in hand, we are now ready to state the convergence result.

Theorem 9. *Suppose that SPIRAL is applied to (3.27), where (A1) through (A3) hold, then all accumulation points are critical points, and hence SPIRAL converges to a minimizer of (3.27). Moreover, the sequence of objective values converges sublinearly to the minimal value. Additionally, if F is strongly convex, the sequence of objective values converges R-linearly.*

Proof. Using the above lemmas, the proof that the objective values converge follows from [13]. Assume for contradiction that \bar{f} is an accumulation point that is not critical. Let $\{f^{k_j}\}_{j \in \mathbf{Z}_+}$ a subsequence such that $\lim_{j \rightarrow \infty} f^{k_j} = \bar{f}$. If the sequence $\{\alpha_{k_j}\}_{j \in \mathbf{Z}_+}$ were bounded, we would have from Lemma 6 that $\|\delta^{k_j+1}\|_2 \geq \epsilon$ for some $\epsilon > 0$ and all j large enough. However, this is in contradiction Lemma 8, hence $\{\alpha_{k_j}\}_{j \in \mathbf{Z}_+}$ must be unbounded. In particular, we must have that for some j large enough, $\alpha_{k_j} \geq \eta \max(\alpha_{\max}, \tilde{\alpha})$, meaning $\alpha = \alpha_{k_j}/\eta \geq \tilde{\alpha}$ must have been tried yet failed the acceptance criterion, which is prohibited by Lemma 7, since any $\alpha \geq \tilde{\alpha}$

satisfies the acceptance criterion. This further contradiction shows that any noncritical point cannot be an accumulation point, hence all critical points are accumulation points, and due to the convexity of Φ , \bar{f} optimizes (3.27).

Following [113], it can be shown that for some constant $c \geq 0$

$$\Phi(f^k) - \Phi(\bar{f}) \leq \frac{c}{k},$$

that is the objective values converge at a sublinear rate. Moreover, if F is strongly convex, then there exist constants $C > 0$ and $r \in (0, 1)$ such that

$$\Phi(f^k) - \Phi(\bar{f}) \leq Cr^k (\Phi(f^0) - \Phi(\bar{f})),$$

hence the objective values exhibit R -linear convergence. \square

3.3.5 Uniqueness of the Minimizer

Under the general assumptions (A1)–(A3) in Section 3.3.4, the set $\arg \min_f \Phi(f)$ will be a compact convex set (c.f. [112]) and may not be the singleton $\{\hat{f}\}$. That is, the solution to the minimization (3.7) may not be unique. The most general condition under which the minimizer \hat{f} is unique is when the objective Φ is strictly convex, which is obtained when either ϕ or the penalty pen is strictly convex. In the underdetermined case of interest, ϕ cannot be strictly convex, since it is trivial to find a vector z in the kernel of A , and as a consequence $F(f + \alpha z) = F(f)$ for any $\alpha \in \mathbf{R}$. In this case, a strictly convex objective can be obtained if the penalty is strictly convex, however most interesting choices for the penalty term (e.g., ℓ_1 -norm, total variation) preclude this possibility. More precisely, the penalty need only be strictly convex on the null space of A , however this condition is difficult to verify in practice.

A different approach must then be taken which utilizes the precise choice of pen and functional form for F , in which conditions for a unique minimizer are established

on a case-by-case basis. We do not consider the RDP-based penalty, since convergence to a global optimum cannot be explicitly guaranteed, and therefore only focus on the ℓ_1 and TV penalties. We show for these two penalties that if the solution is not unique, then there exist two distinct solutions \hat{f} and \tilde{f} such that $A\hat{f} = A\tilde{f}$ and $\text{pen}(\hat{f}) = \text{pen}(\tilde{f})$. This means that these solutions are identical in the sense that they are equally faithful to the data and equally sparse or smooth as measured by the penalty. In certain cases, A is such that $A\hat{f} = A\tilde{f}$ only if $\hat{f} = \tilde{f}$, hence the solution is unique.

We begin the analysis by expressing the TV seminorm as $\|f\|_{\text{TV}} = \|Df\|_1$, with $D = [D_1; D_2]$ where D_1 and D_2 are respectively the horizontal and vertical first-order difference matrices. Therefore both the ℓ_1 and TV penalties can be cast into the form $\text{pen}(f) = \|Bf\|_1$ where $B = \tau W^\top$ for the ℓ_1 penalty, and $B = \tau D$ for the TV penalty. The KKT optimality conditions for a solution \hat{f} are such that there exists a corresponding Lagrange multiplier vector $\hat{\lambda}$ (not necessarily unique) such that, together with \hat{f} ,

$$\begin{aligned} 0 &\in \nabla F(\hat{f}) + \partial \text{pen}(\hat{f}) - \hat{\lambda}, \quad \hat{f} \geq 0, \\ 0 &= \hat{\lambda}^\top \hat{f}, \quad \hat{\lambda} \geq 0. \end{aligned} \tag{3.32}$$

To examine the subdifferential of the penalty, note the composition rule that if $g(x) = h(Bx)$, then $\partial g(x) = B^\top \partial h(Bx)$, that is if b_i are the rows of B , then

$$\partial g(x) = \left\{ \sum_i s_i b_i, s_i \in (\partial h(Bx))_i \right\}.$$

When $h(x) = \|x\|_1$, the subdifferential is

$$(\partial h(x))_i = \begin{cases} \text{sign}(x_i) & \text{if } x_i \neq 0, \\ [-1, 1] & \text{if } x_i = 0, \end{cases}$$

and thus the first KKT condition in (3.32) is equivalent to

$$0 \in \left\{ \nabla F(\hat{f}) - \hat{\lambda} + \sum_{i \in \hat{S}} \text{sign}(b_i^\top \hat{f}) b_i + \sum_{i \notin \hat{S}} s_i b_i : s_i \in [-1, 1] \right\}$$

where $\hat{S} = \{i : b_i^\top \hat{f} \neq 0\}$ is the support set of $B\hat{f}$.

If \hat{f} is not the unique solution, then there exists another solution \tilde{f} , distinct from \hat{f} , that also satisfies the KKT conditions with a corresponding $\tilde{\lambda}$. What we show next is that, without loss of generality, we can assume that \hat{f} and \tilde{f} share certain properties that simplifies the proceeding analysis.

We know that \hat{f} and \tilde{f} must lie on a compact convex set. In particular, any point $z(\gamma) = (1 - \gamma)\hat{f} + \gamma\tilde{f}$ with $\gamma \in [0, 1]$ must also be a solution. Define the following index sets:

$$S(x) = \{i : b_i^\top x \neq 0\}, \quad Q(x) = \{i : x_i \neq 0\}.$$

Now clearly $S(z(\gamma)) \subseteq S(\hat{f}) \cup S(\tilde{f})$ and $Q(z(\gamma)) \subseteq Q(\hat{f}) \cup Q(\tilde{f})$, but as we sweep through γ , the sets $S(z(\gamma))$ and $Q(z(\gamma))$ may not remain constant. However they will be constant on certain intervals. To see this, define the following:

$$\Gamma_S = \{\gamma \in [0, 1] : b_i^\top z(\gamma) = 0 \text{ for some } i \in S(\hat{f}) \cup S(\tilde{f})\},$$

$$\Gamma_Q = \{\gamma \in [0, 1] : z_i(\gamma) = 0 \text{ for some } i \in Q(\hat{f}) \cup Q(\tilde{f})\},$$

$$\Gamma = \Gamma_S \cup \Gamma_Q.$$

These sets basically count the number of zero-crossings that occur in $z(\gamma)$, excluding the components that are always zero (e.g., if the line segment between \hat{f} and \tilde{f} lies on a coordinate plane), and hence they are finite sets. Therefore, $\Gamma = \{\gamma_i\}_{i=1}^N$ for some $N < \infty$, hence there exist open intervals (γ_i, γ_{i+1}) on which $S(z(\gamma))$ and $Q(z(\gamma))$ are constant. So without loss of generality, we can select \hat{f} and \tilde{f} to be two distinct points in one of these intervals, so that we now have $S := S(\hat{f}) = S(\tilde{f})$ and

$Q := Q(\hat{f}) = Q(\tilde{f})$. Furthermore, we will also have $\text{sign}(b_i^\top \hat{f}) = \text{sign}(b_i^\top \tilde{f})$ for all $i \in S$.

Using the properties established above, and from the first KKT condition for both $(\hat{f}, \hat{\lambda})$ and $(\tilde{f}, \tilde{\lambda})$, we have that

$$0 \in \left\{ \nabla F(\tilde{f}) - \nabla F(\hat{f}) - \tilde{\lambda} + \hat{\lambda} + \sum_{i \notin S} (\tilde{s}_i - \hat{s}_i) b_i : \tilde{s}_i, \hat{s}_i \in [-1, 1] \right\}.$$

From here we multiply componentwise by $(\tilde{f} - \hat{f})$ and sum to yield

$$0 = (\tilde{f} - \hat{f})^\top (\nabla F(\tilde{f}) - \nabla F(\hat{f})) + \hat{f}^\top \tilde{\lambda} + \tilde{f}^\top \hat{\lambda},$$

where we have used the complementarity KKT condition that $\hat{f}^\top \hat{\lambda} = \tilde{f}^\top \tilde{\lambda} = 0$, and the fact that $b_i^\top \hat{f} = b_i^\top \tilde{f} = 0$ for all $i \notin S$. Now since $\tilde{\lambda}_i > 0$ only if $\tilde{f}_i = 0$ (similarly $\hat{\lambda}_i > 0$ only if $\hat{f}_i = 0$), and since $\tilde{f}_i = \hat{f}_i = 0$ for all $i \notin Q$, we also have that $\hat{f}^\top \tilde{\lambda} = \tilde{f}^\top \hat{\lambda} = 0$. Therefore we deduce that

$$0 = \sum_{i=1}^m \frac{y_i}{(e_i^\top A \tilde{f} + \beta)(e_i^\top A \hat{f} + \beta)} [e_i^\top A(\tilde{f} - \hat{f})]^2,$$

and since this is a sum of nonnegative terms (if $y > 0$, the fraction is strictly positive) it can only assume a zero value if $A(\hat{f} - \tilde{f}) = 0$. This means that if both \hat{f} and \tilde{f} are solutions, they need to be equivalent up to their projections. Since they are both minimizers of the objective, they necessarily have identical objective values, and since they both achieve the same value for F , it is clear that $\text{pen}(\hat{f}) = \text{pen}(\tilde{f})$. Hence the solutions are also equally sparse or smooth with respect to the penalty.

In the case of the ℓ_1 norm, we can be a bit more precise by considering the fact that we often examine the solution in terms of the coefficients $\hat{\theta} = W^\top \hat{f}$. In this case, if AW satisfies a restricted-isometry type property [14] for vectors of sparsity $s = 2|S|$, we have $(1 - \delta_s) \|\hat{\theta} - \tilde{\theta}\|_2 \leq \|AW(\hat{\theta} - \tilde{\theta})\|_2$, and hence $AW(\hat{\theta} - \tilde{\theta}) = 0$ only

if $\hat{\theta} - \tilde{\theta} = 0$, contradicting the distinctness of $\hat{\theta}$ and $\tilde{\theta}$, hence if AW satisfies RIP, the solution is unique.

3.4 Numerical Experiments

3.4.1 Simulation Setup

Although the algorithms described heretofore are applicable to a wide range of imaging contexts, here we demonstrate the effectiveness of the proposed methods on a simulated limited-angle emission tomography dataset. We compare our algorithm with the currently available state-of-the-art emission tomography reconstruction algorithms [102].

In this experimental setup, we wish to reconstruct the true axial emission map f (Fig. 3.2(a)) as accurately as possible. The photon flux described by this emission map is subject to the attenuation effects caused by the various densities of tissue through which the photons must travel to reach the detector array. The simulated attenuation map μ (Fig. 3.2(b)) is assumed known during the reconstruction process. The simulated emission and attenuation images are standard test images included in the Image Reconstruction Toolbox (IRT) by Fessler [115].

The limited-angle tomographic projection R , corresponding to parallel strip-integral geometry with 128 radial samples and 128 angular samples spaced uniformly over 135 degrees, was also generated by the IRT software [115]. The resulting sensing matrix is then given by $A \equiv \text{diag}[\exp(-R\mu)]R$, with the noisy tomographic data y simulated according to the inhomogeneous Poisson process (3.1). We simulated ten realizations of the data y in order to examine the ten-trial average performance of all the reconstruction methods presented. We only show images reconstructed using a particular realization of the data shown in Fig. 3.2(c)). In this case, the noisy sinogram observations have a total photon count of 2.0×10^5 , a mean count over the support of the tomographic projections of 18.08, and a maximum count of 44.

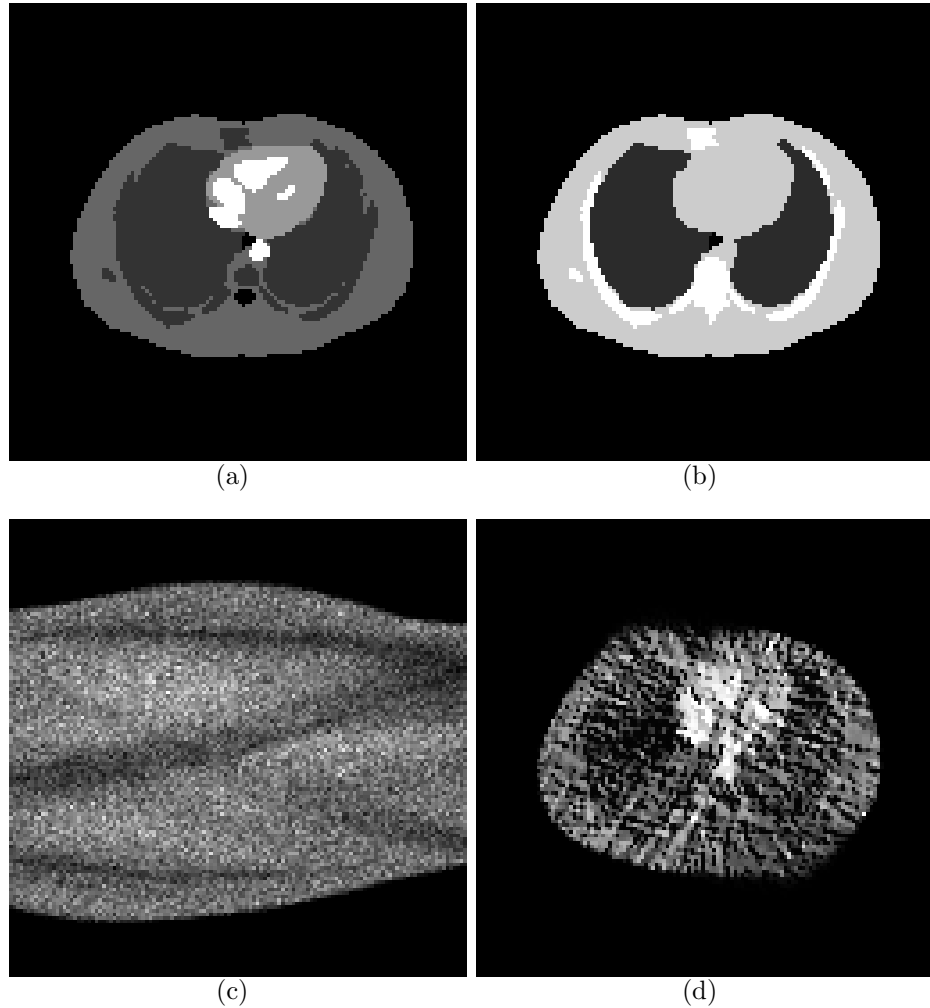


FIGURE 3.2: Experimental setup: (a) true emission image, (b) attenuation map, (c) noisy projection data, (d) estimate used as initialization.

3.4.2 Algorithm Setup

We evaluate the proposed SPIRAL approaches (ℓ_1 , TV, RDP, and RDP-TI), two competing Poisson reconstruction methods [102, 115], and the SpaRSA algorithm [13]. For the SPIRAL- ℓ_1 method, the Daubechies family (DB-2 through DB-8) were evaluated as the basis W . Here we only present results using the DB-6 wavelet basis as the results were similar across bases with DB-6 having a marginal lead in performance. Using the SPIRAL-TV method, we investigate the effects of not enforcing the

near-monotonicity acceptance criterion (3.13). For all methods that enforce (3.13), we used $\eta = 2$, $\sigma = 0.1$, $M = 10$. Also, as described in Section 3.3.3, we evaluate how the accuracy of solving the subproblem impacts the global performance of the SPIRAL- ℓ_1 and TV methods. When solving these subproblems stringently (denoted Tight in the figures and tables), a minimum of 10 and a maximum of 100 iterations were used, with a convergence tolerance $\text{tol}_{\text{SUB}} = 1 \times 10^{-8}$; these parameters were relaxed to a maximum of 10 iterations, and a tolerance $\text{tol}_{\text{SUB}} = 1 \times 10^{-4}$ when the subproblems are solved less exactly (denoted Loose). In all the SPIRAL methods, we set $\alpha_{\max} = 1/\alpha_{\min} = 1 \times 10^{30}$.

We compare our proposed approaches with two competing Poisson reconstruction methods. The first, denoted SPS-OS, uses a separable paraboloidal surrogate with ordered subsets algorithm [102]. The second, denoted EPL-INC-3, employs an incremental penalized Poisson likelihood EM algorithm and was suggested by Prof. Fessler as representative of the current state-of-the-art in emission tomographic reconstruction. Both of these methods are available as part of the IRT [115]; specifically, we used the `pwls_sps_os` and `epl_inc` functions from the toolbox. In addition to these Poisson methods, we also compare to the SpaRSA algorithm [13] which solves the ℓ_1 -regularized least-squares (ℓ_2 - ℓ_1) problem. Like the SPIRAL- ℓ_1 approaches, we only present results when W is the DB-6 wavelet basis. As the solution provided by SpaRSA is not guaranteed to be nonnegative, we threshold the result to obtain a feasible – and therefore more accurate – solution. Including this result allows us to demonstrate the effectiveness of solving the formulation (3.7) that utilizes the Poisson likelihood.

All of the methods considered here were initialized with the estimate shown in Fig. 3.2(d). This initialization results from two iterations of a non-convergent version of the EPL-INC-3 algorithm, itself initialized by the filtered back-projection estimate. All algorithms executed for a minimum of 50 iterations, and global convergence was

declared when the relative change in the iterates (3.24) fell below $\text{tolP} = 5 \times 10^{-4}$.

Lastly, in all of the experiments presented in this chapter, we chose any parameters associated with each algorithm (such as τ) to minimize the RMS error ($\text{RMSE} (\%) = 100 \cdot \|\hat{f} - f\|_2 / \|f\|_2$) of the reconstruction. While this would not be possible in practice, it does allow us to compare the *best-case* performance of various algorithms and penalization methods. In practical settings, regularization parameters can be chosen via cross-validation. This is particularly well-suited to many photon-limited imaging applications in which each detected photon has a time stamp associated with it; this timing information can be used to construct multiple independent and identically distributed realizations of the underlying Poisson process in software. The details of this procedure are a significant component of our ongoing research.

3.4.3 Results Analysis

From the results presented in Table 3.1, we see that out of the proposed SPIRAL approaches, the method utilizing the total variation penalization achieves the lowest RMSE and highest visual quality, followed by SPIRAL-RDP-TI and SPIRAL- ℓ_1 . This bolsters the notion that there is much to be gained by considering additional image structure beyond that of a sparse representation in the basis W . The SPIRAL-RDP method based on the non-cycle-spun partitions simply are not competitive due to the high bias in considering only a single shift of the RDP structure. Examining Fig. 3.3(f), we see that this bias is manifest in the image as blocking artifacts due to the RDP structure not fortuitously aligning to any strong edges in the image. Also from Table 3.1 we see that the EPL-INC-3 method with the Huber potential offers the toughest competition to the RMSE achieved by the SPIRAL-TV approaches.

Examining the reconstructed images in Fig. 3.3, we see that the visual fidelity correlates strongly with the RMSE. The SPIRAL-TV and EPL-INC-3 results clearly

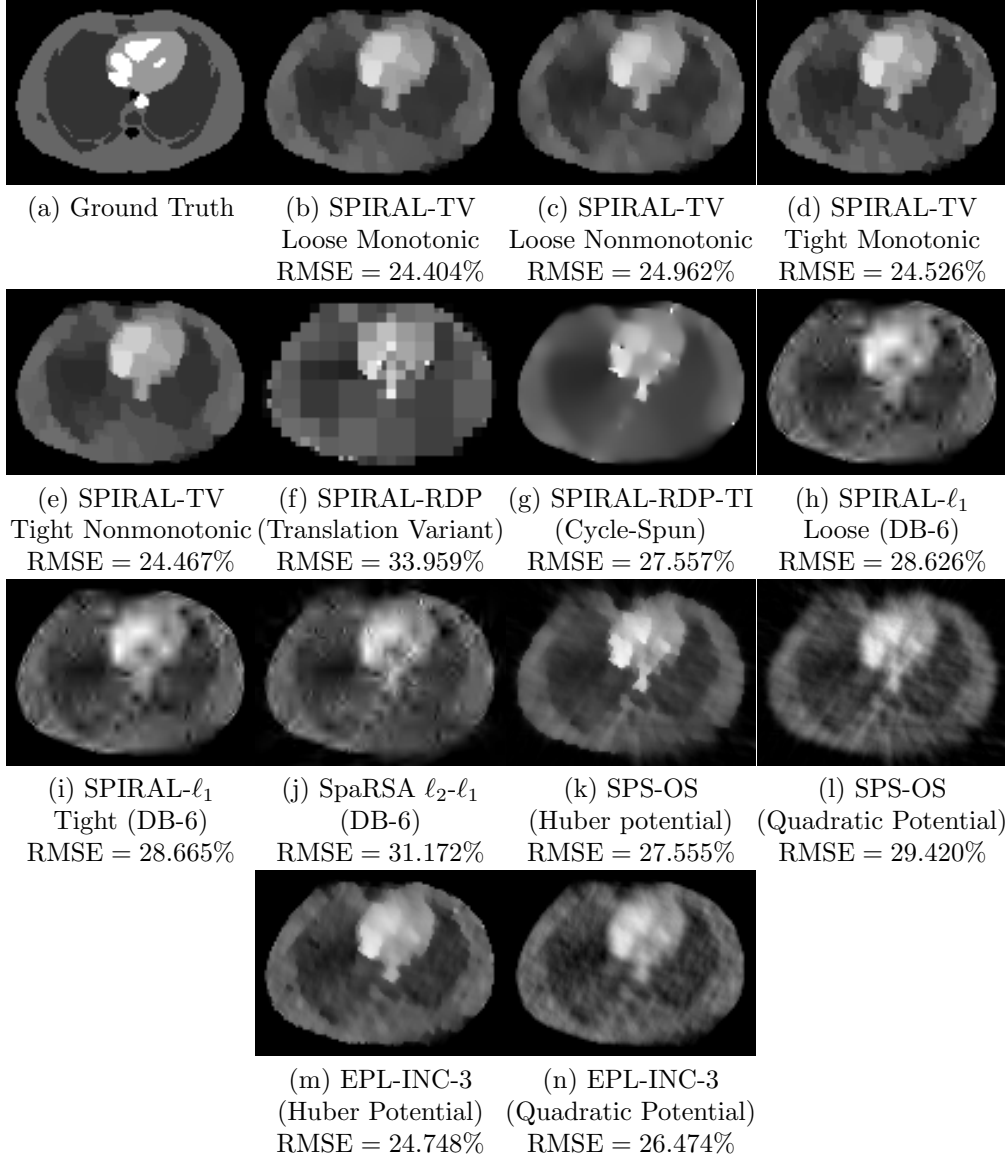


FIGURE 3.3: Single-trial reconstructed images for all methods considered. Note $\text{RMSE}(\%) = 100 \cdot \|\hat{f} - f\|_2 / \|f\|_2$.

do best at capturing strong edges in the image while smoothing noise in the homogeneous regions, with the SPIRAL-TV method more correctly smoothing homogeneous regions. This conclusion is supported by Fig. 3.4 in which we further analyze the best-in-class SPIRAL and EPL-INC-3 methods. Between the EPL-INC-3 methods, the Huber potential is more effective at reducing the rough noise-like deterioration that is quite pronounced when using the quadratic potential. Here we see that

Table 3.1: Reconstruction RMSE and computation time for both the single-trial results, and results averaged over ten trials. Note: L = Loose, T = Tight, M = Monotonic, NM = Nonmonotonic, RMSE (%) = $100 \cdot \|\hat{f} - f\|_2 / \|f\|_2$.

Method	Single-Trial		Ten-Trial Average	
	RMSE (%)	Time (s)	RMSE (%)	Time (s)
SPS-OS Huber	27.555	9.078	27.057	9.094
SPS-OS Quad	29.420	5.354	29.049	5.574
EPL-INC-3 Huber	24.748	20.302	24.462	16.704
EPL-INC-3 Quad	26.474	8.713	26.013	9.647
SpaRSA	31.172	5.946	29.987	3.730
SPIRAL- ℓ_1 (L)	28.626	6.933	28.050	5.396
SPIRAL- ℓ_1 (T)	28.665	15.547	27.980	20.006
SPIRAL-TV (L, M)	24.404	15.418	24.270	10.102
SPIRAL-TV (L, NM)	24.962	7.821	24.868	4.721
SPIRAL-TV (T, M)	24.526	25.423	24.352	20.900
SPIRAL-TV (T, NM)	24.467	21.505	24.571	15.046
SPIRAL-RDP	33.959	3.118	34.946	2.323
SPIRAL-RDP-TI	27.557	5.313	27.669	4.756

both SPIRAL-TV and EPL-INC-3 results have sharp edges, but significant variations in the regions of homogeneous intensity are a consistent source of error for the EPL-INC-3 method. These variations cause many darker spots that could be misinterpreted as regions of low uptake. Figures 3.3 and 3.4 both show that the SPIRAL-RDP-TI and ℓ_1 -based approaches tend to over-smooth the entire image; however the SPIRAL-RDP-TI method better captures the high intensity regions. High-scale wavelet artifacts are seen throughout the SPIRAL- ℓ_1 and SpaRSA reconstructions. In the SpaRSA results shown in this section, we clipped the final reconstruction to be nonnegative. Even after this clipping operation, the RMSE of the final result was significantly higher than the RMSE associated with methods using the Poisson log-likelihood. This suggests that the effort required to use the Poisson log-likelihood is justified by tangible performance gains over methods associated with a penalized least-squares objective. Lastly, prominent streaking artifacts in the SPS-OS methods hinder their accuracy, with using a Huber potential resulting

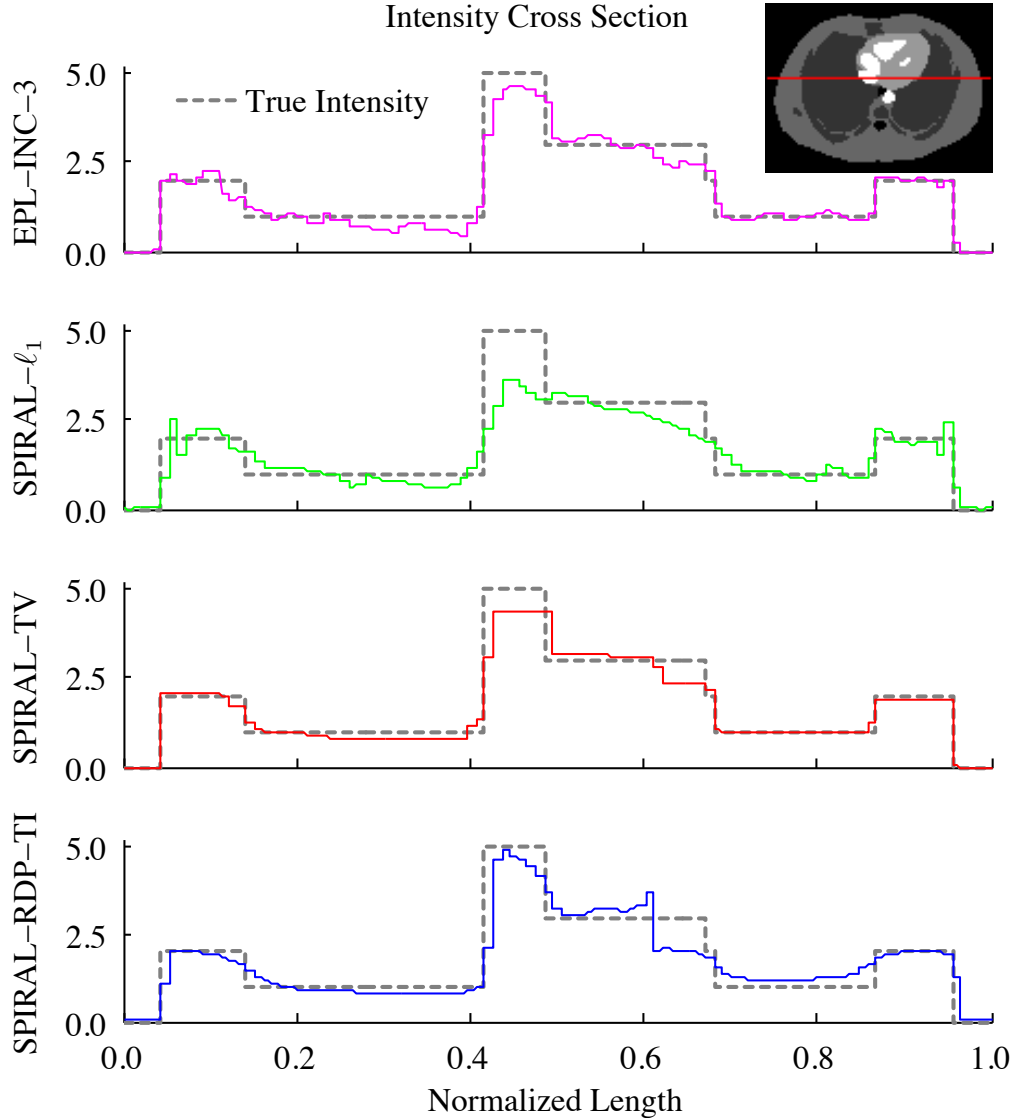


FIGURE 3.4: Intensity cross sections of the best-in-class methods: EPL-INC-3 with Huber potential, SPIRAL- ℓ_1 with loose subproblem convergence criteria, monotonic SPIRAL-TV with loose subproblem convergence criteria, and SPIRAL-RDP-TI. The insert image shows the location of the cross section. Note that the pixel boundaries in the image cause the stepwise nature of the profiles.

in a slightly better performance than a quadratic potential.

While accuracy and visual quality are held paramount in tomographic reconstruction, the computational cost and convergence behavior of the chosen methods should not be neglected. Figure 3.5 shows the convergence behavior of the best-in-class

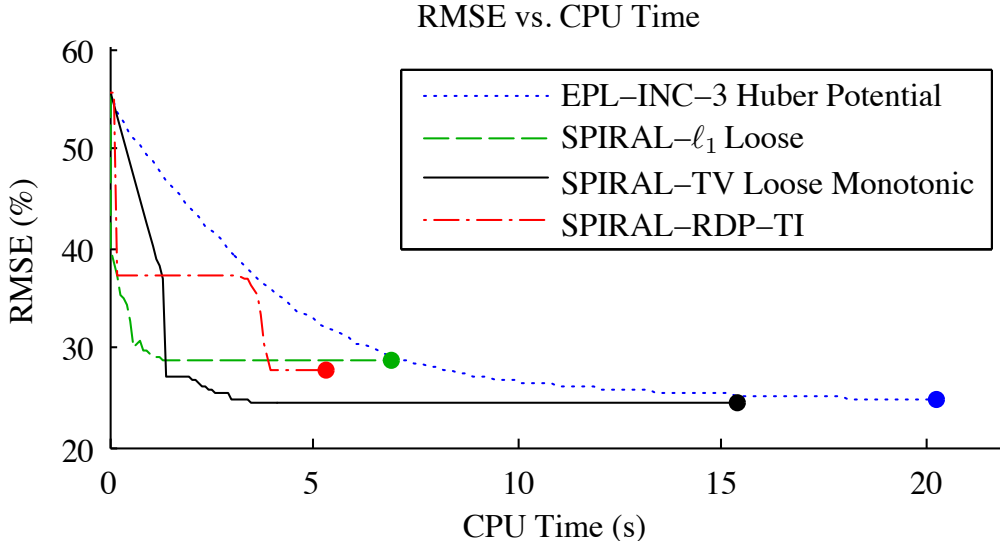


FIGURE 3.5: Convergence of the RMSE vs computation time for the best-in-class methods. The termination criteria was reached at the point indicated by the solid circle.

methods. Although the SPIRAL- ℓ_1 and RDP-TI approaches yield higher RMSE, they show desirable convergence behavior with sharp initial decreases in RMSE and termination in under eight seconds. The SPIRAL-TV method also shows this sharp decrease, but exhibits a prolonged period where the RMSE changes little. The EPL-INC-3 method shows none of these traits, slowly changing the RMSE throughout its execution until it finally reaches the termination criteria after 20 seconds.

Next consider Fig. 3.6, where we show the RMSE convergence for the variations of the SPIRAL-TV algorithm. Comparing the top and bottom axes, we see that by not enforcing the near-monotonicity acceptance criteria in (3.13) accelerates the convergence rate at the potential cost of large increases of the RMSE during the execution of the algorithm (seen at the near the two second mark when tightly solving the TV subproblem). Although the nonmonotonic algorithms typically yield early sharp decreases in RMSE, the ten-trial average behavior in Table 3.1 shows that the monotonic algorithm will achieve a more accurate solution at termination. This suggests that a two-stage approach of starting with a nonmonotonic algorithm

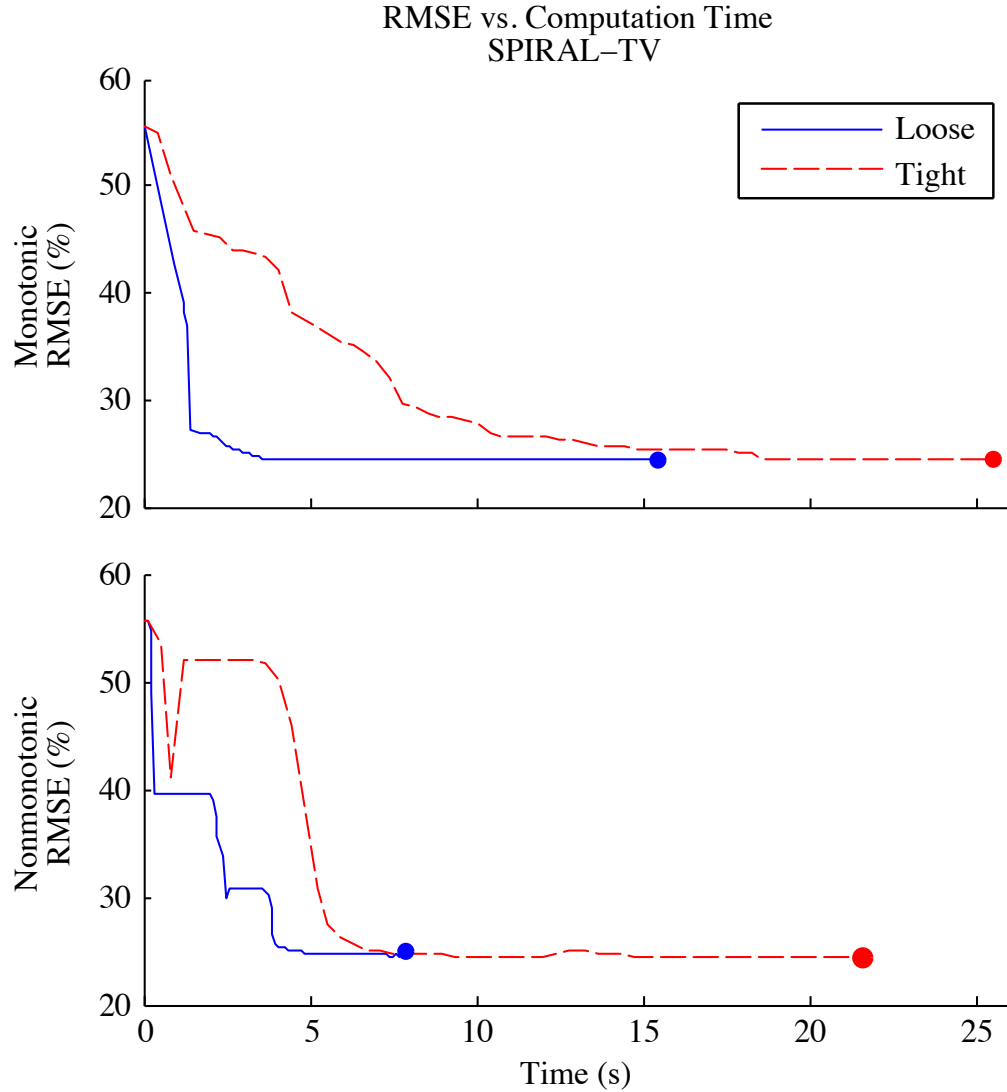


FIGURE 3.6: Comparison of the RMSE convergence rates for the different variations of the SPIRAL-TV method. The termination criteria was reached at the point indicated by the solid circle.

to achieve quick, yet approximate, convergence then switching to the monotonic algorithm may be the best overall approach.

Figures 3.6 and 3.7 support the use of relaxed convergence criteria for the TV and ℓ_1 subproblems, Table 3.1 also shows that little is lost in terms of final RMSE by using this less-stringent criterion. In fact, by combining the nonmonotonic option and loose subproblem convergence criteria results in a SPIRAL-TV approach that, on average,

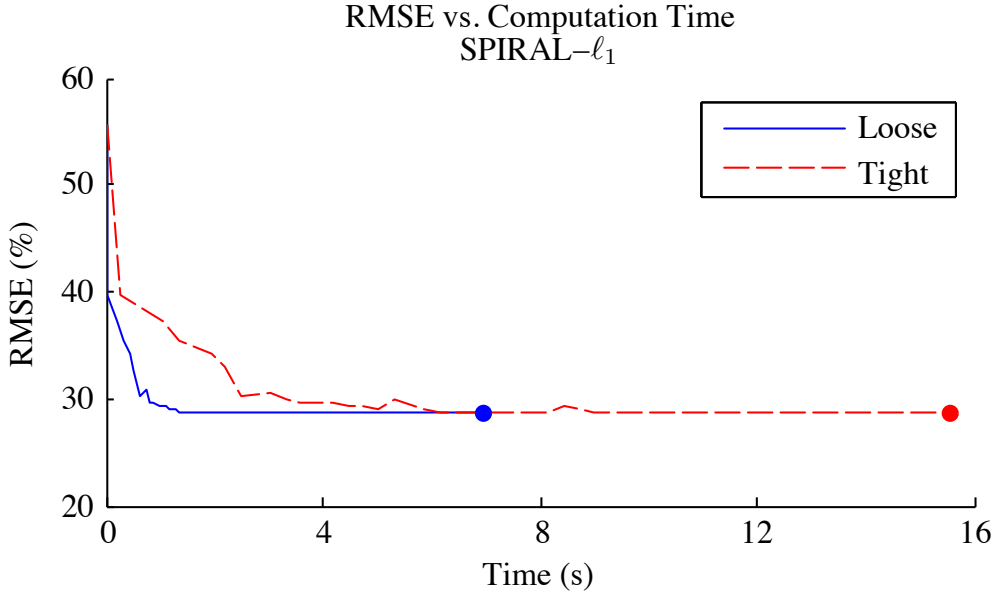


FIGURE 3.7: Comparison of the RMSE convergence rates for the different variations of the SPIRAL- ℓ_1 method. The termination criteria was reached at the point indicated by the solid circle.

nearly matches the best EPL-INC-3 method in terms of RMSE, yet is approximately four times faster. Further, this algorithm is even faster than the *least* accurate SPS-OS method. Therefore, we believe that further investigation of nonmonotonic and approximate subproblem algorithms is a fruitful area of research for fast and accurate image reconstruction. We finish the discussion of the numerical results by directing the interested reader to additional experimental results in [73, 116] which demonstrate the effectiveness of the proposed SPIRAL method in a compressed sensing context.

3.5 Other Applications of SPIRAL

We have successfully used SPIRAL to extend our work on dictionary learning [117] by incorporating a sparsity constraint on the coefficients [118]. Given a collection of N images $\{f_i\}_{i=1}^N$, where each $f_i \in \mathbf{R}_+^n$, and where we observe corresponding Poisson observations y_i of each f_i , we can collect these images and observations into

corresponding matrices F and Y where the i th column of F and Y are f_i and y_i respectively. In this case we have the statistical model that

$$Y \sim \text{Poisson}(F).$$

The crucial assumption in this work is that F can be approximated by a low-rank matrix. Here we assume that

$$F \approx \exp(UV),$$

where the exponential is understood entry-wise, $U \in \mathbf{R}^{n \times l}$ and $V \in \mathbf{R}^{l \times N}$, and hence the matrix product UV has rank at most l . The exponential formulation ensures nonnegativity of the result. In this model, U can be interpreted as a dictionary of vectors for each of the images, with coefficients V in that

$$f_i = \exp(Uv_i), i = 1, \dots, n,$$

where v_i is the i th column of v .

We then estimate F by finding U and V by solving a regularized maximum likelihood problem,

$$(\widehat{U}, \widehat{V}) = \arg \min_{U, V} -\log p(Y | \exp(UV)) + \tau \|V\|_1. \quad (3.33)$$

A reconstruction of the final image set is then given by

$$\widehat{F} = \exp(\widehat{U}\widehat{V}).$$

In solving (3.33), an alternating minimization is used between the matrices U and V . The minimization with respect to U can be accomplished by using a Newton-like method, and the minimization with respect to V can be accomplished quickly using SPIRAL. We show experimental results where we form a data matrix Y consisting of a patch-based model of the images, where some spatial aggregation techniques are

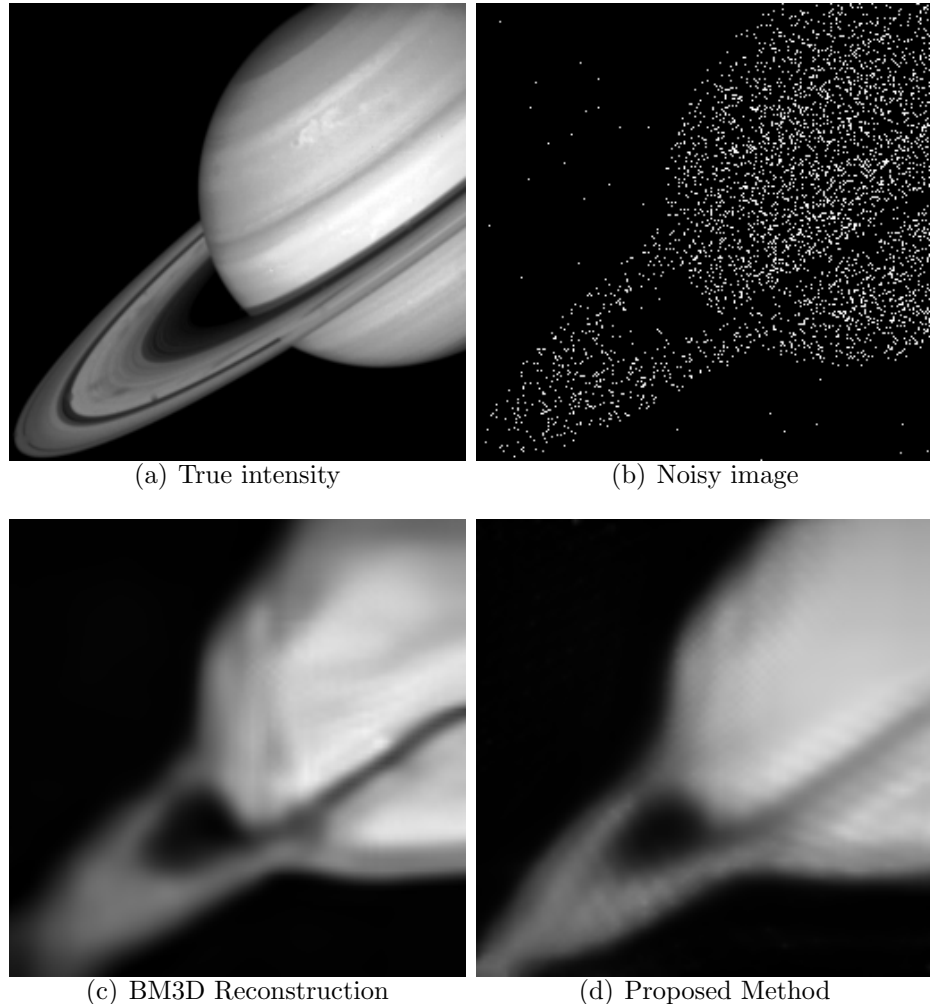


FIGURE 3.8: Examples of reconstructions for the sparse dictionary learning method. The Saturn image has a peak intensity of 0.2, and we show (a) the true image, (b) Poisson realization used as data, (c) the reconstruction using BM3D (PSNR = 23.17), and (d) the reconstruction using the proposed method (PSNR = 22.16).

used prior to the application of the algorithm, further details can be found in [118]. We compare our method to the well established BM3D method [119]. The results are shown in Fig. 3.8 and 3.9. We see from this that the proposed result achieves state-of-the-art reconstruction performance and faithfully reconstruct images at extremely low photon counts.

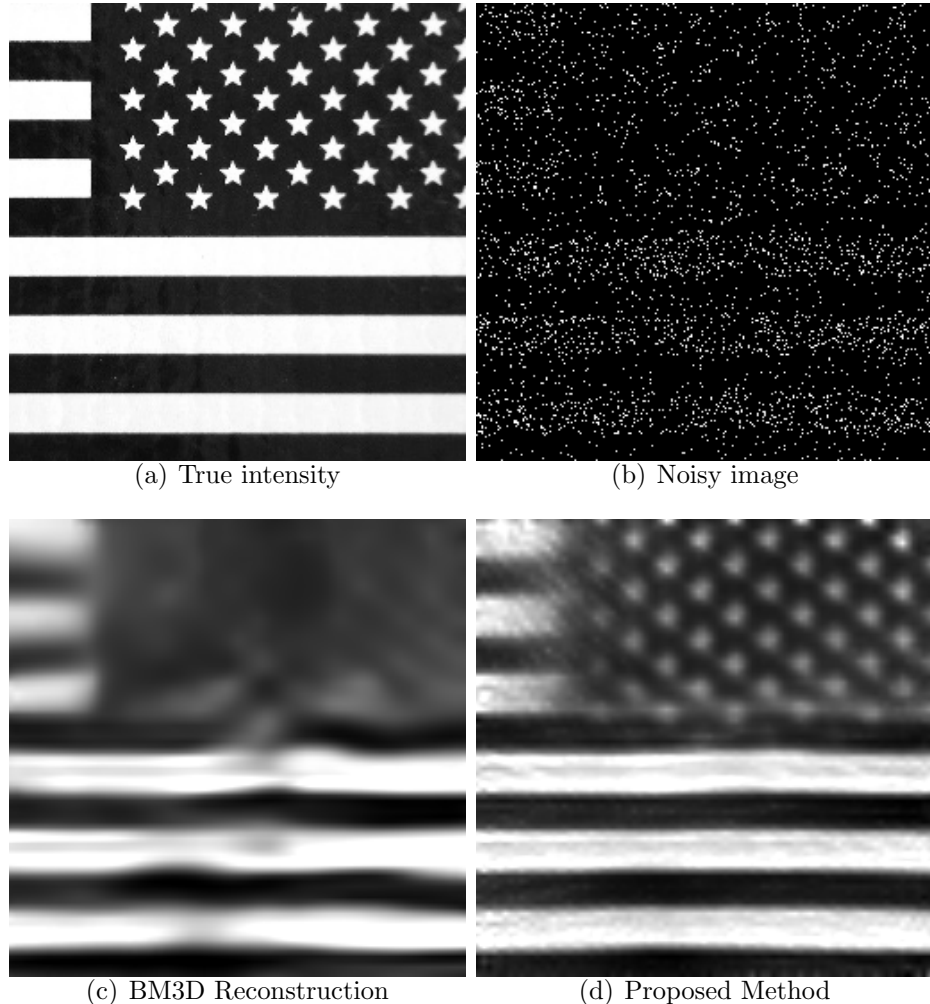


FIGURE 3.9: Examples of reconstructions for the sparse dictionary learning method. The Flag image has a peak intensity of 0.1, and we show (a) the true image, (b) Poisson realization used as data, (c) the reconstruction using BM3D (PSNR = 13.19), and (d) the reconstruction using the proposed method (PSNR = 15.99).

3.6 Conclusion

We have formulated the general goal of reconstructing an image from photon-limited measurements as a penalized maximum Poisson likelihood estimation problem. To obtain a solution to this problem, we have proposed an algorithm that allows for a flexible choice of penalization methods, and focused particularly on sparsity-promoting penalties. In particular, we detail the cases where the penalty corresponds to the

sparsity-promoting ℓ_1 norm of the expansion coefficients in a sparsifying basis, is related to the complexity of a partition-based estimate, or is proportional to the total variation of the image. We establish mild conditions for which this algorithm has desirable convergence properties, although in practice it is beneficial to relax these conditions to attain faster (albeit nonmonotonic) convergence. We demonstrate the effectiveness of our methods through a simulated emission tomography example. When our total variation regularized method is applied to this problem, the resulting estimates outperform the current state-of-the-art approaches developed specifically for emission tomography. In particular, it results in fewer spurious artifacts than wavelet-regularized methods, and unlike partition-regularized methods, is the result of a convex optimization procedure.

4

Photon-Limited Quantitative Tissue Analysis

This chapter explores the use of Poisson sparse decomposition methods for computationally separating tumor nuclei from normal tissue structures in photon-limited microendoscopic images. Sparse decomposition tools are a natural fit for this application with promising results. However, there are significant tradeoffs among different algorithms used for Poisson sparse decomposition which are described in detail and demonstrated via simulation.

Extensions to multispectral fluorescence data can be used within sparse decomposition methods to separate key cellular structures, even when the number of photons per spectral band is very small. However, there are two key costs associated with multispectral data acquisition: (a) for a fixed data acquisition time, increasing the number of spectral bands means decreasing the number of photons (and hence SNR) per band, and (b) the optical system becomes more complex and expensive. These costs lead to important tradeoffs between the information content and the noise of the observations. This paper describes a mathematical framework for assessing this tradeoff and supporting experimental results.

We consider an application to real data from a high-resolution microendoscope.

On this data, we are able to show that we can accurately identify the presence of diseased tissue through subsequent analysis of the output of our sparse decomposition method.

4.1 Introduction

Early diagnosis of many cancers, including breast and esophageal cancer, relies on the detection of pockets of microscopic tumor cells. However, standard imaging methods such as white-light endoscopy cannot easily resolve these cells in the presence of otherwise normal tissue. Additionally such methods are time-consuming and expensive, while biopsies are risky. New endoscopic microscopes provide a high-resolution, low-cost alternative to current clinical practices [120, 121]. Such devices use fiberoptic bundles on the order of 1mm diameter for quasi-confocal fluorescence imaging (see Fig. 4.1). One of the key features of this imaging method is that it provides real-time images that mimic histopathology (microscopic anatomical information) through utilizing vital fluorescent dyes that highlight tissue structure. A representative image collected with this device is shown in Fig. 4.2. This image shows elongated muscle fibers with small circular tumor nuclei superimposed. The small honeycomb pattern corresponds to the geometry of the fiber-optics.

In this paper, we describe methods which can be used to separate nuclei from normal tissue structure in microendoscopic images. This task is important because scientists and clinicians need automated tools for quantifying nuclear properties (e.g. nuclear density or average nuclear size) in order to diagnose the nuclei as malignant (tumor) or benign (normal). The presence of nuclei as well as the surrounding tissue context for each nuclei is important for diagnosis. For example in a microendoscopic image of normal adipose (fat) tissue, we would expect to see nuclei pushed to the periphery of the adipose (fat) cell as it is seen in normal histopathology. These nuclei, since they are part of the normal tissue architecture, do not indicate the presence

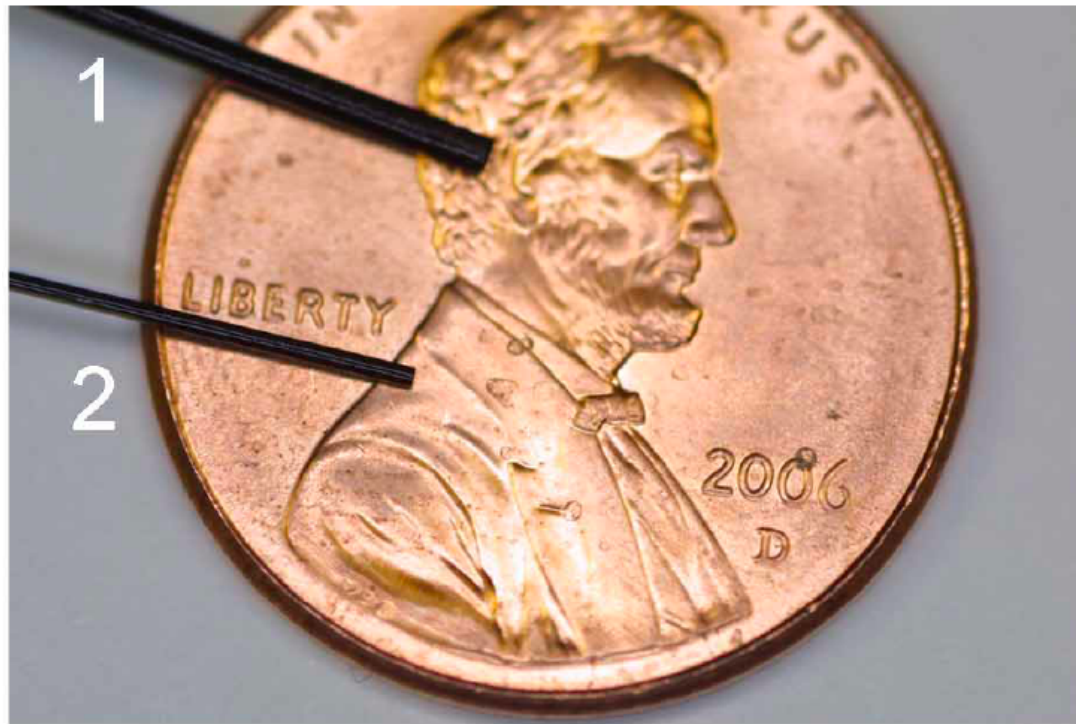


FIGURE 4.1: Photograph of the fiber bundle microendoscope in size comparison to a penny.

of malignancy (disease). However, if we see a dense collection of nuclei on top of normal muscle fibers (as seen in Fig. 4.2), which is not typical of normal muscular structure, we would expect that those nuclei are indicative of diseased tissue.

Our main application for this technology is to provide a platform for intra-operative *margin assessment*. When a physician excises a tumor from a cancer patient, they actually remove a portion of healthy tissue as well that should ideally surround the tumor mass. This healthy portion of tissue is called the *surgical margin*. This precaution is to ensure that no cancerous tissue is left behind. The excised tissue is then pathologically processed to determine if the surgical team was successful in surrounding the tumor with healthy tissue (a negative margin), or if there are cancerous cells on the boundary of the tissue (a positive margin). A positive margin may indicate the presence of residual disease in the patient, and would

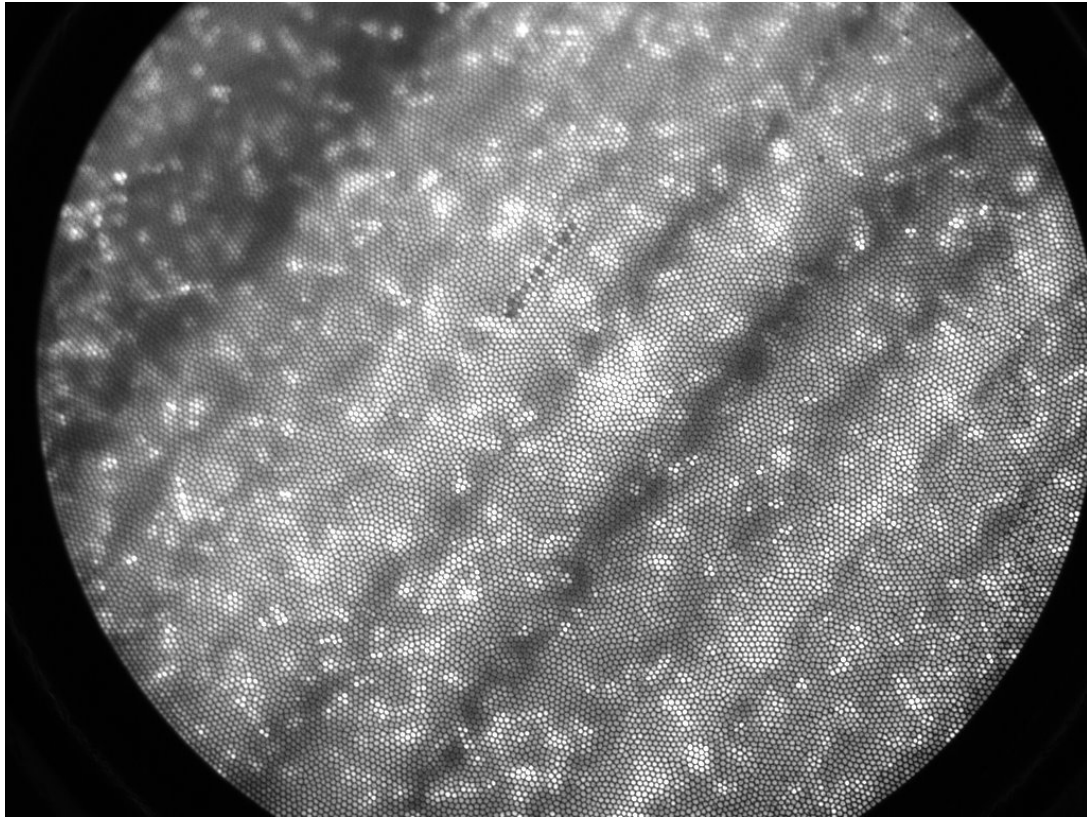


FIGURE 4.2: Representative image collected with microendoscope. This image shows elongated muscle fibers with small circular nuclei superimposed. The abundance of nuclei in this image is due to the presence of a malignant tumor.

need to undergo a second operation. As the patient requires time to recover from the initial surgery, this follow up procedure often occurs many weeks later, in which time the cancer may regrow or metastasize.

To aid with margin assessment during surgery, engineers have developed fluorescent micro-endoscopes which can be used to probe and image tissue around a small incision quickly. However, due to fluorescence and tight time constraints, the observations are often photon-limited. From this data, we wish to estimate a decomposition of the image into nuclei, muscle, and fat (adipose) components. Computational tissue analysis along these lines has been considered previously for relatively low noise settings using sparse decomposition techniques [122]. In our context, photon

limitations are a dominant source of errors. However, we have limited control of the diversity of our observations via the ability to collect multispectral observations. This paper explores the tradeoffs between photon limitations and the measurement diversity associated with multispectral observations.

In particular, assume that the fluorescence occurs in the range of wavelengths $0 \leq \lambda \leq \Lambda$, and that the spectral signatures of the different tissues and fluorescent dyes are known (for example, based on prior laboratory measurements from a spectrometer). We must then decide on the ideal spectral resolution of the instrument – i.e., the number of bins of wavelengths, M , spanning $[0, \Lambda]$; this decision introduces a key tradeoff between measurement diversity and the signal-to-noise ratio. For simplicity in this work, we consider a uniform binning of $[0, \Lambda]$; extensions to nonuniform sampling are possible. Specifically, larger M means that each spectral bin will contain fewer observed photons and will hence be noisier, but it also provides us with a more disparate set of measurements which can aid in separating different tissue components. This leads to the following question addressed by this paper: *What is the information value associated with multi-spectral observations for photon-limited image decomposition?*

The work described in this paper has several interesting connections to the authors' previous work on Poisson compressed sensing [73]. In that problem, we saw that there was a critical number of measurements required for accurate reconstruction of the underlying sparse signal, and that as we increased the number of measurements beyond this critical threshold, the reconstruction quality decreased along with the SNR of each observation. The authors developed a theoretical analysis of this phenomenon. This paper empirically demonstrates a similar effect in a real-world Poisson inverse problem. Lastly, in Sec. 4.7, we show that these methods can robustly identify nuclei in heterogeneous tissue samples taken from a fluorescence microendoscope, providing a promising method for intraoperative margin assessment.

4.2 Problem Formulation

Here we describe a general model for multi-wavelength imaging. Each $x_i \in \mathbf{R}^n$ is a vector representation of an n -pixel image. In this model, we have N tissue components $\{x_j\}_{j=1}^N$ that combine linearly to produce M images $\{z_i\}_{i=1}^M$ acquired using different wavelengths or spectral bands:

$$z_i = \sum_{j=1}^N A_{i,j} x_j, \quad i = 1, \dots, M, \quad (4.1)$$

where $A \in \mathbf{R}^{M \times N}$ is the multispectral mixing weight matrix. Element $A_{i,j}$ describes how brightly tissue component j appears in spectral band i . More specifically, assume tissue type j has spectrum $f_j(\lambda)$, and let

$$A_{i,j} := \int_{(i-1)\Lambda/M}^{i\Lambda/M} f_j(\lambda) d\lambda.$$

Then the j th column of A , denoted a_j , corresponds to the spectrum of tissue type j discretized to M elements. In this way we can write $A = [a_1, \dots, a_N]$. If we let $x = (x_1, \dots, x_N)$ and $z = (z_1, \dots, z_M)$, then this model can be more succinctly expressed as

$$z = (A \otimes I_n)x, \quad (4.2)$$

where \otimes denotes the Kronecker matrix product and I_n is the size- n identity matrix. We then acquire photon-limited observations of the M images, which can be accurately described by a inhomogeneous Poisson process [82]:

$$\begin{aligned} y_i &\sim \text{Poisson}(z_i), \quad i = 1, \dots, M, \\ p(y_i | z_i) &= \prod_{k=1}^n \frac{e^{-[z_i]_k} [z_i]_k^{[y_i]_k}}{[y_i]_k!}, \quad i = 1, \dots, M. \end{aligned} \quad (4.3)$$

With the compact notation $y = (y_1, \dots, y_M)$, we would have simply

$$y \sim \text{Poisson}(z). \quad (4.4)$$

In order to facilitate the recovery of the tissue components x from the data y , we utilize the assumption that each tissue component x_i can be sparsely represented or approximated in a dictionary $D_i \in \mathbf{R}^{n \times p_i}$, meaning that

$$x_i = D_i \theta_i, \quad i = 1, \dots, N \quad (4.5)$$

where the coefficient sequence θ_i is mostly comprised of very few large coefficients. Again we may compactly express this as $x = D\theta$, where $D = \text{bdiag}(D_1, \dots, D_N)$ is a block-diagonal dictionary matrix and $\theta = (\theta_1, \dots, \theta_N) \in \mathbf{R}^p$ ($p := \sum_{i=1}^N p_i$) is the concatenation of the coefficients. In the most general situation, each dictionary may be over-complete ($p_i > n$) or under-complete ($p_i < n$). For simplicity of presentation in this paper, we assume that each dictionary is a 1-tight (Parseval) frame, which necessitates $p_i \geq n$ for all $i = 1, \dots, N$. This assumption ensures that $D_i D_i^\top = I_n$ for all $i = 1, \dots, N$, as is true for curvelet dictionaries, and (normalized) concatenations of orthonormal bases. From this, we will also have that $D D^\top = I_{nN}$.

With this model and a set of assumptions, we recover x by solving the sparsity-regularized maximum likelihood problem

$$\begin{aligned} & \underset{\theta}{\text{minimize}} \quad -\log p(y | (A \otimes I_n)D\theta) + \|\tau \odot \theta\|_1 \\ & \text{subject to} \quad D\theta \geq 0, \end{aligned} \quad (4.6)$$

where $\tau \in \mathbf{R}_+^p$ is a vector of regularization parameters, and \odot denotes componentwise (Hadamard) multiplication. The common case (and used in our numerical experiments) is that there is a single regularization parameter associated with each $\theta_i, i = 1, \dots, N$, which controls the relative sparsity tradeoff in each dictionary. In this simplified case, the sparsity penalty may be written as $\sum_{i=1}^N \tau_i \|\theta_i\|_1$. The nonnegativity constraints are required since each of the tissue component fluorescence images are Poisson intensities, which are required to be nonnegative. We briefly describe an approach that can be used to effectively solve this minimization in Sec. 4.4.

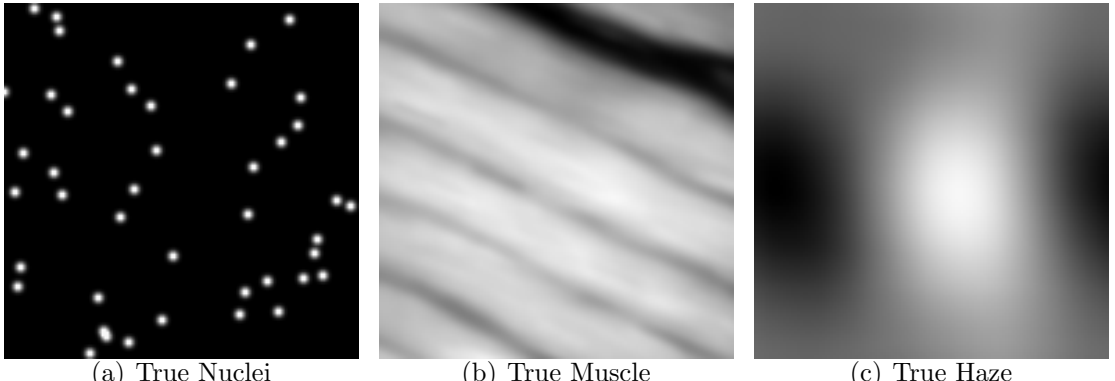


FIGURE 4.3: Tissue components

4.3 Tradeoffs

Let $R := (A \otimes I_n)D$ denote the full spatio-spectral sensing matrix. As we show below, depending on the dictionaries and spectral profiles available, the number of spectral bands (M) necessary to ensure reliable reconstruction of θ from y depends critically on the coherence properties of this resulting sensing matrix. For example, if $R^\top R = I_{nN}$, then in the absence of noise, the different tissue components can be perfectly separated from the observations. More generally, we need to quantify how close $R^\top R$ is to I_{nN} , and how the number of spectral bands influences this distance. The analysis below shows that the structure of $R^\top R$ depends on both the structure of the sparsifying dictionaries and the weight matrix A . Usually increasing M results in better coherence properties. In a practical setup, however, this improvement is mitigated by the fixed amount of total available light and its dispersion across the M spectral bands.

4.3.1 Incoherence of Multispectral Measurements of Tissue Mixtures

We define the Gram matrix as $G := R^\top R$. When G is close to an identity matrix, we can expect a better performance in reconstructing θ . This is formally expressed using notions of *incoherence* [123, 124] or the *Restricted Isometry Property* [14] in

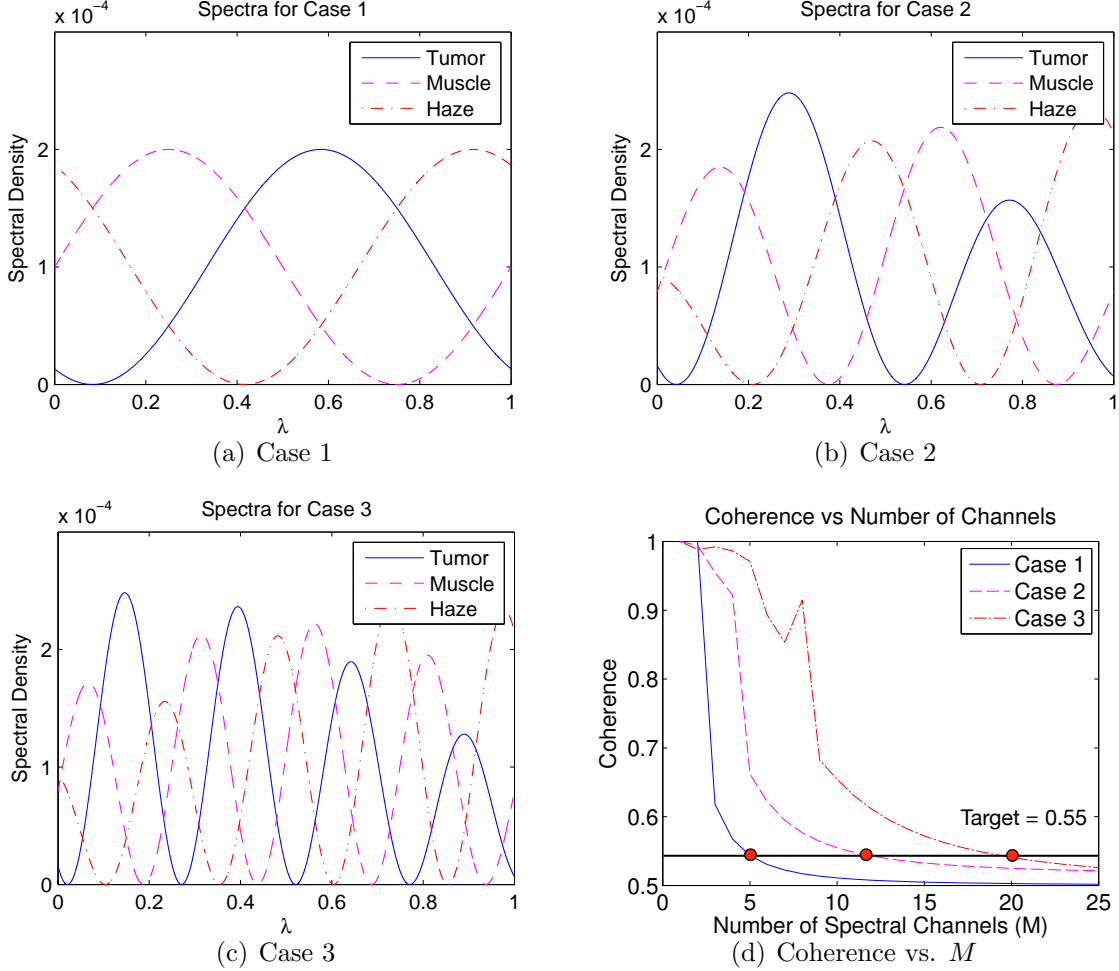


FIGURE 4.4: Spectral profiles of three simulated tissue components in three cases (a)-(c), and (d) coherence behavior as a function of the number of spectral bands, M , for each case.

the compressed sensing literature. Here we define the *coherence* of a matrix B as

$$\mu(B) = \max_{i \neq j} \frac{b_i^\top b_j}{\|b_i\| \|b_j\|} \quad (4.7)$$

where b_i denotes the i th column of B . A sensing matrix that has low coherence $\mu(R)$ translates to a Gram matrix that is close to an identity matrix.

In our setting, Kronecker product properties can be used to show

$$G = R^\top R = [(A \otimes I_n)D]^\top [(A \otimes I_n)D] = D^\top [(A^\top A) \otimes I_n]D,$$

which can be partitioned into blocks of the form $a_i^\top a_j D_i^\top D_j$. This shows that the closer each block is to zero for $i \neq j$, the closer G is to an identity matrix. When the sampled spectra of the tissue components are very similar, we may only resolve these tissue types if there exist correspondingly incoherent sparsifying bases for each tissue type. Consider the tissue components in Fig. 4.3. Even if the spectral characteristics are similar, it may be possible to resolve isolated nuclei (sparse in the spatial domain) against a background of longitudinal muscle fibers (sparse in the DCT domain) simply due to their incoherent dictionaries. The additional flexibility of the spectral response can be leveraged when two tissue types are sparse in very similar bases, such as muscle tissues, adipose (fat) tissue, and the haze component (described in more detail in the simulations section).

This analysis yields the property $\mu(R) \leq \mu(A)\mu(D)$. This allows us to simply analyze the coherence of the multispectral mixing matrix as a worst-case analysis for our simulations section. In particular, we examine the coherence behavior versus M using three different spectral signatures for the tissue types. Each of the three sets of spectra are shown in Fig. 4.4. In each of the different cases, the spectra oscillate more rapidly, which translates to requiring more spectral channels to separate out the different spectral profiles. For instance, if we select a target coherence level of 0.55, we need $M = 5, 12$, and 20 spectral channels to achieve this level for Case 1, 2, and 3 respectively.

4.3.2 Connections to Poisson Compressed Sensing

In previous work [73], we examined the performance of compressed sensing in the presence of photon noise, the dominating noise measure in a spectral imaging system with a large number of spectral bands. We demonstrated that if R satisfies a variant of the restricted isometry property, so that $R^\top R \approx I$, then a reconstruction of the

form

$$\widehat{\theta} = \arg \min_{\theta} -\log p(y|R\theta) + \tau \|\theta\|_1$$

resulted in a mean squared error

$$\mathbf{E}[\|\widehat{\theta} - \theta^*\|_2^2] \preceq Mn \left(\frac{\log Nn}{T} \right)^{2\alpha/(2\alpha+1)} + \frac{\log(N/M)}{Mn}, \quad (4.8)$$

where τ is a tuning parameter, $T := \sum_i (D\theta)_i$ is the total intensity of the scene (proportional to the total amount of time required to collect the photon data), and $\alpha > 1$ reflects the sparsity or compressibility of the θ vectors. The bound in (4.8) suggests that M should be chosen as small as possible (while still ensuring the necessary degree of incoherence) to ensure that the estimate has as little error as possible. This is because larger M causes the limited number of photons to be dispersed across more detectors and limits the signal-to-noise ratio of the observations.

4.4 Algorithms

In the Poisson observation model, estimating θ from y using the minimization in (4.12) can be a significant computational challenge. The authors developed methods for solving this inverse problem, where (a) the number of unknowns may potentially be larger than the number of observations and (b) x admits a sparse approximation or representation [33]. Our optimization formulation uses a penalized negative Poisson log-likelihood objective function with nonnegativity constraints (since Poisson intensities are naturally nonnegative). In particular, our approach incorporates key ideas of using separable quadratic approximations to the objective function at each iteration and penalization terms related to ℓ_1 norms of coefficient vectors, total variation seminorms, and partition-based multi-scale estimation methods. Our approach is very stable relative to alternative methods based on augmented Lagrangians (AL)

because there is no need to choose a good value of the AL parameter, which is a significant practical challenge [37].

4.4.1 Augmented Lagrangian

First we reformulate the optimization problem (4.12) by first defining

$$f(z) := \sum_{i=1}^{nM} \{[z]_i - [y]_i \log([z]_i + \beta)\} \propto -\log p(y | z), \quad (4.9)$$

where β is a small parameter (1e-10 in our numerical experiments) that avoids the singularity that occurs when we have $[z]_i = 0$ yet $[y]_i \neq 0$. Note that we discount the $\log([y]_i!)$ terms as they are constant with respect to z (and thus θ) and do not impact the value of the minimizer. This technique is similar to the case when we have a known vector of background intensity and is not explicitly needed if the minimal value of such a background is sufficiently high. From an optimization perspective, this small parameter yields an objective that is Lipschitz continuously differentiable over the feasible domain and helps to improve the stability of the algorithm. Because of this small parameter, the logarithmic term would only enforce $[z]_i \geq -\beta$, and hence the nonnegativity constraint must be kept. However, we will see that this constraint can be handled efficiently by the algorithm.

Next we use the unconstrained formulation of (4.12) by employing the indicator function on the nonnegative orthant, δ_+ where

$$\delta_+(x) = \begin{cases} 0 & x \geq 0, \\ +\infty & \text{otherwise.} \end{cases} \quad (4.10)$$

Additionally, we employ a variable splitting where we let $u = (A \otimes I_n)D\theta$, $v = \theta$, and hence

$$G\theta = \begin{bmatrix} u \\ v \end{bmatrix}$$

where

$$G := \begin{bmatrix} (A \otimes I_n)D \\ I_p \end{bmatrix}. \quad (4.11)$$

After these transformations we have the following form:

$$\begin{aligned} & \underset{\theta, u, v}{\text{minimize}} \quad f(u) + \delta_+(u) + \|\tau \odot v\|_1 \\ & \text{subject to} \quad G\theta = \begin{bmatrix} u \\ v \end{bmatrix}. \end{aligned} \quad (4.12)$$

In this form, we can employ the alternating direction method of multipliers (ADMM) approach by first forming the augmented Lagrangian

$$\begin{aligned} L_A(\theta, u, v, \tilde{\lambda}, \tilde{\gamma}; \mu) = & f(u) + \delta_+(u) + \|\tau \odot v\|_1 \\ & + \begin{bmatrix} \tilde{\lambda} \\ \tilde{\gamma} \end{bmatrix}^\top \left(G\theta - \begin{bmatrix} u \\ v \end{bmatrix} \right) + \frac{\mu}{2} \left\| G\theta - \begin{bmatrix} u \\ v \end{bmatrix} \right\|_2^2 \end{aligned} \quad (4.13)$$

where $\mu \geq 0$ is the augmented Lagrangian parameter, and $\tilde{\lambda}$ and $\tilde{\gamma}$ are the corresponding Lagrange multipliers for the equality constraints. This form can be simplified by defining $\lambda = -\tilde{\lambda}/\mu$, $d = -\tilde{\gamma}/\mu$ and completing the square:

$$\begin{aligned} L_A(\theta, u, v, \lambda, \gamma; \mu) = & f(u) + \delta_+(u) + \|\tau \odot v\|_1 \\ & + \frac{\mu}{2} \left\| G\theta - \left(\begin{bmatrix} u \\ v \end{bmatrix} + \begin{bmatrix} \lambda \\ \gamma \end{bmatrix} \right) \right\|_2^2 - \frac{\mu}{2} \left\| \begin{bmatrix} \lambda \\ \gamma \end{bmatrix} \right\|_2^2 \end{aligned} \quad (4.14)$$

The algorithm alternates between two steps, first minimizing L_A with respect to the primal variables θ, u , and v in sequence, then by updating the Lagrange multipliers. We detail each step below, with a summary of the resulting algorithm in Algorithm 2.

Algorithm 2 ADMM Method for Solving (4.12).

```

1: Initialize Choose AL parameter  $\mu > 0$ , and initial solution  $\theta^0$ . Set  $u^0 = (A \otimes I_n)D\theta^0$ ,  $v^0 = \theta^0$ . Select initial Lagrange multiplier vectors  $\lambda^0$  and  $\gamma^0$ . Set iteration counter  $k \leftarrow 0$ .
2: repeat
3:    $\theta^{k+1} \leftarrow$  result of (4.20)
4:    $u^{k+1} \leftarrow$  result of (4.23)
5:    $v^{k+1} \leftarrow$  result of (4.25)
6:    $(\lambda^{k+1}, \gamma^{k+1})$  updated according to (4.26)
7:    $k \leftarrow k + 1$ 
8: until stopping criterion is satisfied return Solution  $\theta^k$ 

```

4.4.2 The θ Subproblem

At the k th iteration, the current values for our variables are $(\theta^k, u^k, v^k, \lambda^k, \gamma^k)$. We find θ^k by minimizing with respect to θ keeping all other variables fixed:

$$\begin{aligned}\theta^{k+1} &= \arg \min_{\theta} L_A(\theta, u^k, v^k, \lambda^k, \gamma^k; \mu) \\ &= \arg \min_{\theta} \frac{1}{2} \left\| G\theta - \left(\begin{bmatrix} u^k \\ v^k \end{bmatrix} + \begin{bmatrix} \lambda^k \\ \gamma^k \end{bmatrix} \right) \right\|_2^2.\end{aligned}\tag{4.15}$$

As the matrix G always has full column rank, the unique minimizer can be found by applying the pseudoinverse:

$$\theta^{k+1} = (G^\top G)^{-1} G^\top \left(\begin{bmatrix} u^k \\ v^k \end{bmatrix} + \begin{bmatrix} \lambda^k \\ \gamma^k \end{bmatrix} \right).\tag{4.16}$$

However, the inverse above cannot be easily computed in general, and relies on the particular structure in our problem. To wit, note that

$$\begin{aligned}G^\top G &= \begin{bmatrix} D^\top (A^\top \otimes I_n) & I_p \end{bmatrix} \begin{bmatrix} (A \otimes I_n)D \\ I_p \end{bmatrix} \\ &= D^\top (A^\top A \otimes I_n) D + I_p,\end{aligned}\tag{4.17}$$

where we can use this structure to simplify the computation of the inverse. Here we use the identity [125, 126]

$$(A + UCV)^{-1} = A^{-1} - A^{-1}U(I + CVA^{-1}U)^{-1}CVA^{-1}, \quad (4.18)$$

which, if C is invertible, can be simplified to the more familiar matrix inversion lemma. After some simplification, we have

$$(G^\top G)^{-1} = I_p - D^\top [(A^\top A + I_N)^{-1} A^\top A] \otimes I_n] D \quad (4.19)$$

If one wanted to apply the matrix inversion lemma here, we would require that $A^\top A$ be invertible, requiring (at a minimum) that $M \geq N$, which may lead one to the false conclusion that this algorithm may not be applied in the underdetermined case when the number of tissue components exceeds the number of spectral channels. The result of using this identity shows that we only require the numerical inversion of an $N \times N$ positive-definite matrix, since the number of tissue components in our model is typically small (on the order of 2-10), this inversion does not represent a bottleneck in the algorithm. Even if N is potentially large, this inversion need only be performed a single time during the execution of the algorithm. As a final result to the θ subproblem, we have

$$\begin{aligned} \theta^{k+1} &= (v^k + \gamma^k) \\ &\quad - D^\top [(B \otimes I_n)D(v^k + \gamma^k) + (C \otimes I_n)(u^k + \lambda^k)] \end{aligned} \quad (4.20)$$

where we have defined

$$\begin{aligned} B &:= (A^\top A + I_N)^{-1} A^\top A, \\ C &:= (B - I_N)A^\top. \end{aligned} \quad (4.21)$$

4.4.3 The u Subproblem

To update u , we follow the same strategy: minimize with respect to u fixing all other variables:

$$\begin{aligned} u^{k+1} &= \arg \min_u L_A(\theta^{k+1}, u, v^k, \lambda^k, \gamma^k; \mu) \\ &= \arg \min_u f(u) + \frac{\mu}{2} \|u - r^k\|_2^2 \\ &\text{subject to } u \geq 0, \end{aligned} \tag{4.22}$$

where we define $r^k = (A \otimes I_n)D\theta^{k+1} - \lambda^k$. Since all terms in both the objective and constraint are separable in the components of u , this minimization reduces to a set of univariate minimization problems:

$$\begin{aligned} [u^{k+1}]_i &= \arg \min_u u - y_i \log(u + \beta) + \frac{\mu}{2}(u - [r^k]_i)^2 \\ &\text{subject to } u \geq 0 \end{aligned}$$

Each of these has a closed form solution

$$\begin{aligned} [\tilde{u}^{k+1}]_i &= \frac{1}{2\mu} \left[- (1 + \mu(\beta - [r^k]_i)) \right. \\ &\quad \left. + \sqrt{(1 + \mu(\beta - [r^k]_i))^2 - 4\mu(\beta - y - \mu\beta[r^k]_i)} \right], \\ [u^{k+1}]_i &= \max([\tilde{u}^{k+1}]_i, 0), \end{aligned} \tag{4.23}$$

the unconstrained solution $[\tilde{u}^{k+1}]_i$ is found by finding the zeros of the derivative of the objective, which has a quadratic form. Note that the solution for $[\tilde{u}^{k+1}]_i$ is always real. This can be shown by minimizing the discriminant with respect to $[r^k]_i$, which results in a minimal value of $4\mu y \geq 0$ at $[r^k]_i = 1/\mu - \beta$.

4.4.4 The v Subproblem

Lastly, updating v follows suit with the previous sections:

$$\begin{aligned} v^{k+1} &= \arg \min_u L_A(\theta^{k+1}, u^{k+1}, v, \lambda^k, \gamma^k; \mu) \\ &= \arg \min_v \frac{1}{2} \|v - s^k\|_2^2 + \frac{1}{\mu} \|\tau \odot v\|_1, \end{aligned} \tag{4.24}$$

where we define $s^k = \theta^{k+1} - \gamma^k$. This minimization is also separable in the components of v and has a closed-form solution, the well-known soft-threshold shrinkage formula:

$$v^{k+1} = \text{soft}(s^k, \tau/\mu) = \text{sgn}(s^k) \max(|s^k| - \tau/\mu, 0), \tag{4.25}$$

with all operations considered componentwise.

4.4.5 The Lagrange Multiplier Update

The last step is to update the Lagrange multipliers (proportional to λ and γ in our notation). This is accomplished via

$$\begin{bmatrix} \lambda^{k+1} \\ \gamma^{k+1} \end{bmatrix} = \begin{bmatrix} \lambda^k \\ \gamma^k \end{bmatrix} - \left(G\theta^{k+1} - \begin{bmatrix} u^{k+1} \\ v^{k+1} \end{bmatrix} \right), \tag{4.26}$$

which can be thought of as an appropriately scaled gradient *ascent* step (as we are *maximizing* L_A with respect to the dual variables).

4.4.6 Convergence of the AL Method

In theory, as long as μ is sufficiently large, this approach is guaranteed to converge to the value of θ which optimizes (4.12) [127]. However, in practice if μ is very large, then convergence can be very slow. This means that the objective function changes very little between successive iterations, making it difficult to determine whether the algorithm has converged. As we will see in the experimental results, the change in the objective function can quickly go below a threshold as small as 10^{-8} , long before the

objective function has reached its minimum value. In practice, these algorithms are typically tuned to use the “best” μ which balances between being large enough to find the optimum of the original objective and being small enough to reach convergence quickly. This can be a difficult and laborious process, and these algorithms can be very sensitive to the choice of μ . Adaptive methods have been proposed that adjust μ throughout the course of the algorithm by balancing the size of two residual terms [128]. However, in our experience these methods resulted in μ values that were still very large, causing slow convergence.

4.4.7 Sparse Poisson Intensity Reconstruction Algorithm (SPIRAL)

A good alternative to AL methods is the Sparse Poisson Intensity Reconstruction Algorithm (SPIRAL) [33]. First, let

$$g(\theta) := -\log p(y|A\theta).$$

At iteration k , we compute a second-order Taylor-series approximation of g at θ^k and approximate the Hessian with a scaled identity matrix: $\nabla^2 g(\theta^k) \approx \alpha_k I$. This yields

$$\tilde{g}(\theta) := g(\theta^k) + \nabla g(\theta^k)^\top (\theta - \theta^k) + \frac{\alpha_k}{2} \|\theta - \theta^k\|_2^2.$$

Now instead of directly minimizing

$$\underset{\theta}{\text{minimize}} g(\theta) + \tau \|\theta\|_1 \quad \text{subject to } A\theta \succeq 0$$

(which is difficult) we can set

$$\begin{aligned} \theta^{k+1} &= \underset{\theta}{\arg \min} \quad \tilde{g}(\theta) + \tau \|\theta\|_1 \quad \text{subject to } A\theta \succeq 0 \\ &= \underset{\theta}{\arg \min} \quad \frac{1}{2} \|\theta - s^k\|_2^2 + \tau \|\theta\|_1 \quad \text{subject to } A\theta \succeq 0 \end{aligned}$$

where $s^k := \theta^k - \frac{1}{\alpha_k} \nabla g(\theta^k)$. This last is a much easier denoising problem. Without the constraints, we could solve this with soft-thresholding. With the constraints, solving this subproblem is more challenging.

First we transform the original nonsmooth objective into a differentiable one by setting $\theta = u - v$ with $u, v \succeq 0$:

$$\underset{u,v}{\text{minimize}} \frac{1}{2} \|u - v - s^k\|_2^2 + \tau \mathbf{1}^\top (u + v) \text{ subject to } u \succeq 0, v \succeq 0, A(u - v) \succeq 0.$$

Next we consider a Lagrangian dual formulation which eliminates the linear constraints and replaces them with simple bound constraints:

$$\underset{\lambda,\gamma}{\text{minimize}} \frac{1}{2} \|s^k + \gamma + A^\top \lambda\|_2^2 - \|s^k\|_2^2 \text{ subject to } \lambda \succeq 0, -\tau \mathbf{1} \preceq \gamma \preceq \tau \mathbf{1}.$$

This optimization can be solved via *alternating minimization*:

$$\begin{aligned} \gamma^j &= \text{mid} \left\{ -\frac{\tau}{\alpha_k} \mathbf{1}, -s^k - A^\top \lambda^{j-1}, \frac{\tau}{\alpha_k} \mathbf{1} \right\} \\ \lambda^j &= [-A(s^k + \gamma^j)]_+ \end{aligned}$$

and then setting

$$\theta^{k+1} = s^k + \gamma^* + A^\top \lambda^*.$$

One particularly nice property of this approach is that we guarantee primal feasibility regardless of which iteration we stop with. That is,

$$A\theta^{k+1} = As^k + A\gamma^j + \lambda^j = [A(s^k + \gamma^j)]_+ \succeq 0.$$

4.5 Algorithmic Comparison

We tested the above algorithm on the toy example displayed in Figure 4.4.7. The test image x^* was composed to a tumor image added to a muscle image. We considered mean intensity levels of $T/n = 1000, 100$, and 10 . The result of our method for these intensity levels is displayed in Figure 4.4.7. By explicitly considering the Poisson

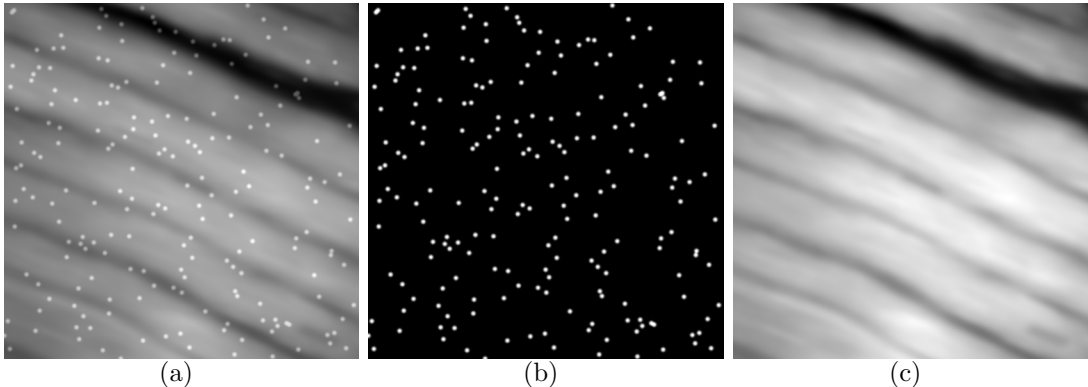


FIGURE 4.5: Intensity used in experiments. (a) True intensity. (b) True tumor image. (c) True muscle image.

likelihood in our formulation, we make it possible to collect microendoscopic data much more rapidly and still remain robust to noise.

Convergence plots are displayed in Figure 4.4.7. At all intensity levels, the SPIRAL method gives the lowest objective function value without the need for tuning or selecting the variable μ . As noted above, the AL method can be quite sensitive to μ . While the theory suggests that as long as μ is sufficiently large AL methods will converge, we see in practice that for large μ standard convergence criteria are met long before the AL method approaches the optimum. These challenges are obviated with the SPIRAL approach. For the remainder of our experimental comparison, we will only be using the SPIRAL algorithm in order to perform the reconstructions.

4.6 Simulations

4.6.1 *Simulation Setup*

In our simulations, we consider two basic tissue components: nuclei and muscle fibers. In pathology, these nuclei may correspond to healthy normal tissue, or possibly a malignant tumor. Our goal is to separate out these nucleus locations for further processing (e.g., determination of their size and density can be diagnostically relevant). In addition, we consider a component that corresponds to a background of

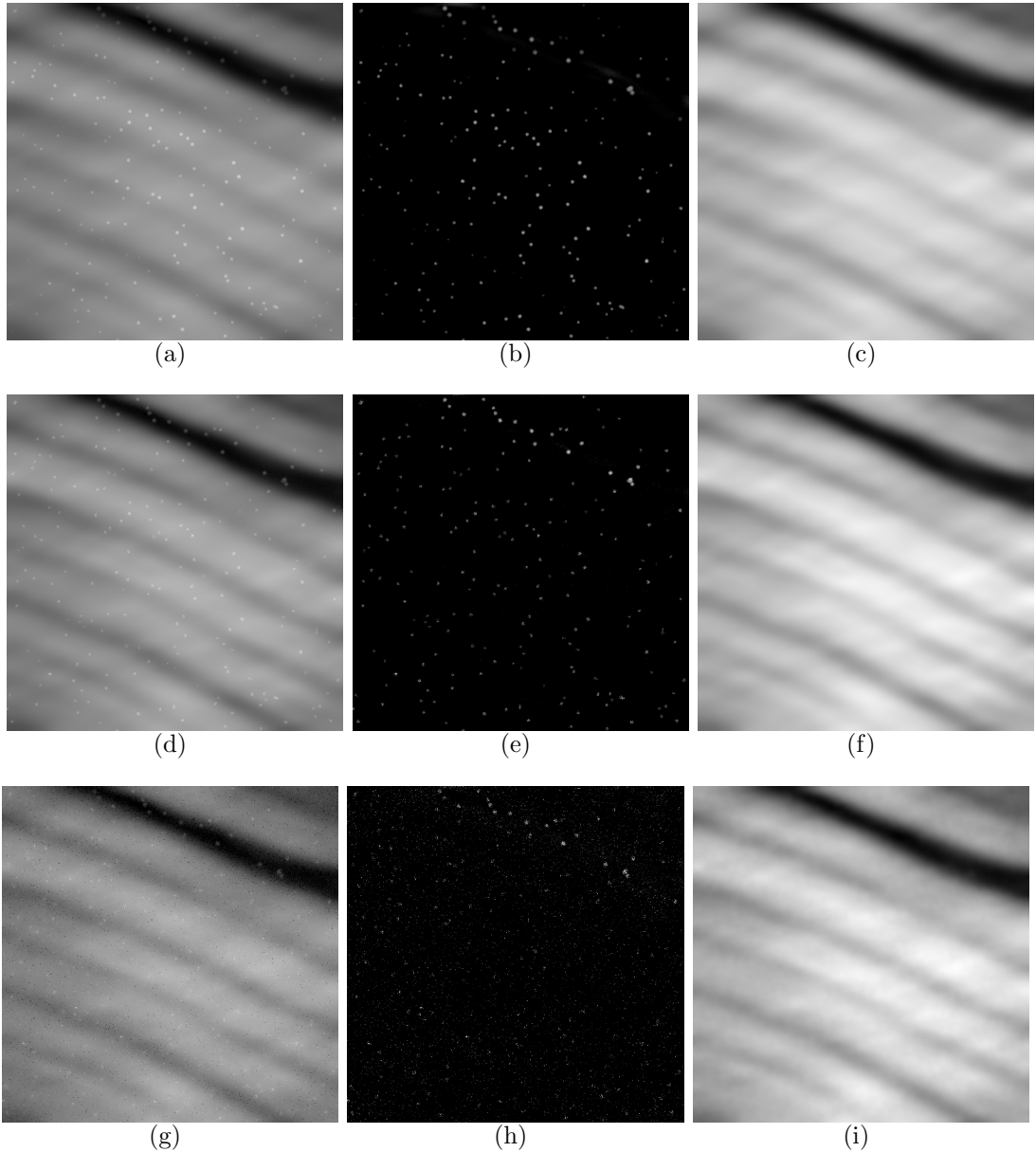


FIGURE 4.6: Decomposition results. (a) Estimated intensity for $T = 1000$. (b) Estimated tumors for $T = 1000$. (c) Estimated muscle for $T = 1000$. (d) Estimated intensity for $T = 100$. (e) Estimated tumors for $T = 100$. (f) Estimated muscle for $T = 100$. (g) Estimated intensity for $T = 10$. (h) Estimated tumors for $T = 10$. (i) Estimated muscle for $T = 10$.

non-binding contrast agent we refer to as *haze* due to visual artifacts it causes in the images.

The simulated nuclei image is generated by passing some randomly located bright

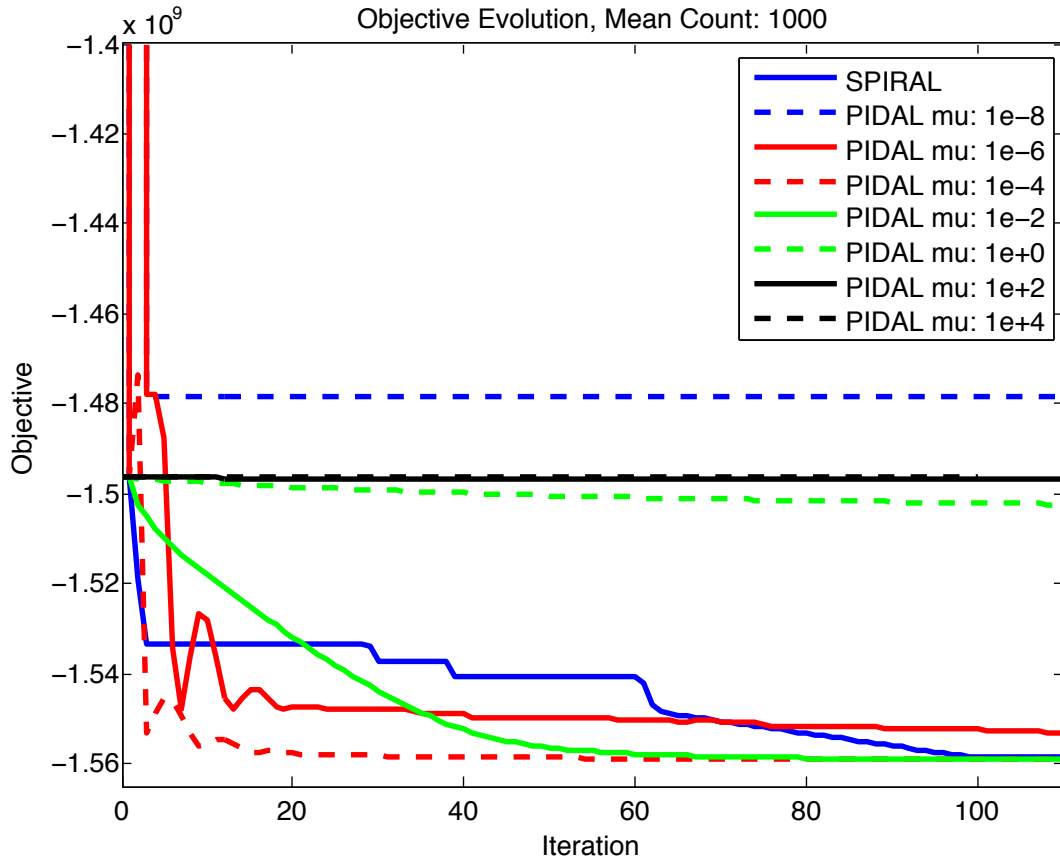


FIGURE 4.7: For $T/n = 1000$. Objective function decay as a function of iteration number for SPIRAL and an augmented Lagrangian method for various values of μ . Note that at all intensity levels, the augmented Lagrangian methods are very sensitive to the choice of μ , while the SPIRAL method gives the lowest objective function value without the need for selecting μ . (a) $T/n = 1000$. (b) $T/n = 100$. (c) $T/n = 10$.

dots through a round low-pass Gaussian filter. The muscle component is taken from a real muscle tissue image followed by minor processing in order to eliminate unwanted vessel and fiber components while preserving natural muscle texture. As the haze refers to the general blurred background in the observations, we use low-pass filtered Gaussian noise to simulate this component. The generated components are shown in Fig. 4.3 (a)–(c).

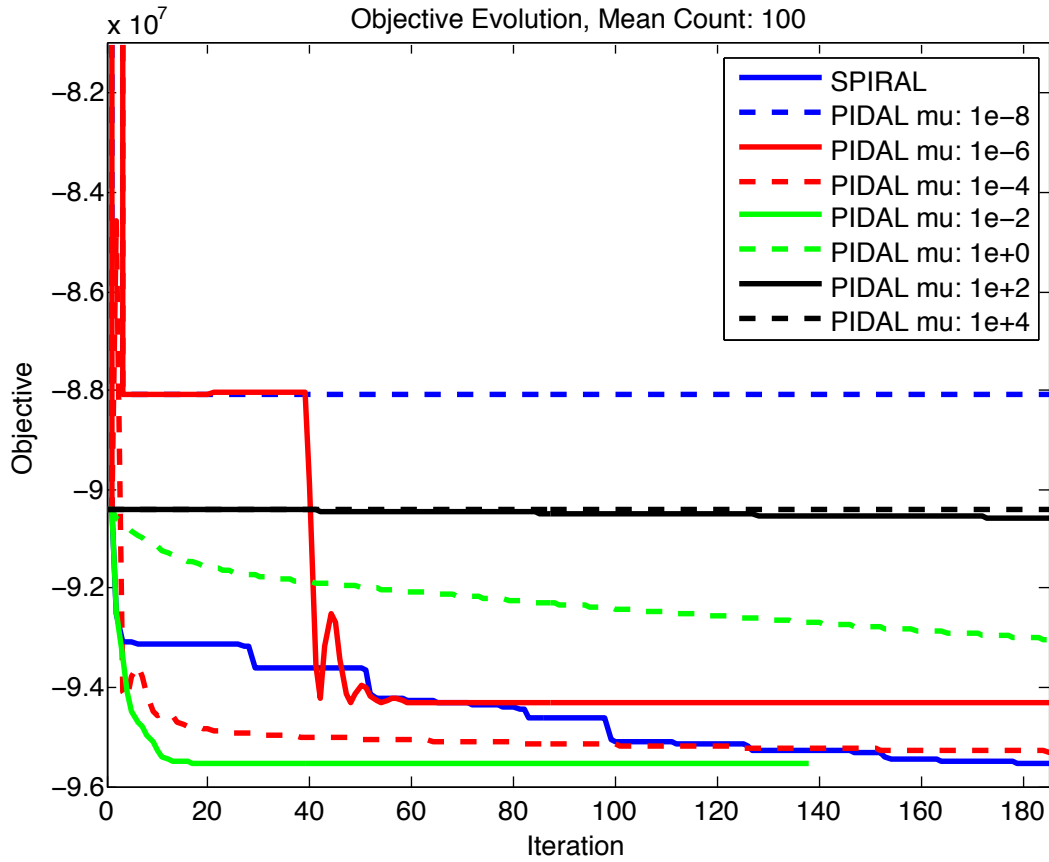


FIGURE 4.8: For $T/n = 100$. Objective function decay as a function of iteration number for SPIRAL and an augmented Lagrangian method for various values of μ . Note that at all intensity levels, the augmented Lagrangian methods are very sensitive to the choice of μ , while the SPIRAL method gives the lowest objective function value without the need for selecting μ . (a) $T/n = 1000$. (b) $T/n = 100$. (c) $T/n = 10$.

The fact that different components have different spectral densities (brightness) gives us the chance to achieve better performance via adding additional spectral bands. We consider three different sets of spectra in our simulations, and are shown in Fig. 4.4 (a)–(c). Fig. 4.4 (d) shows the coherence $\mu(A)$ of sensing matrix A versus the number of spectral bands, where we defined coherence in (4.7). Generally, the more spectral bands we have, the lower the coherence level. As addressed in Sec. 4.3,

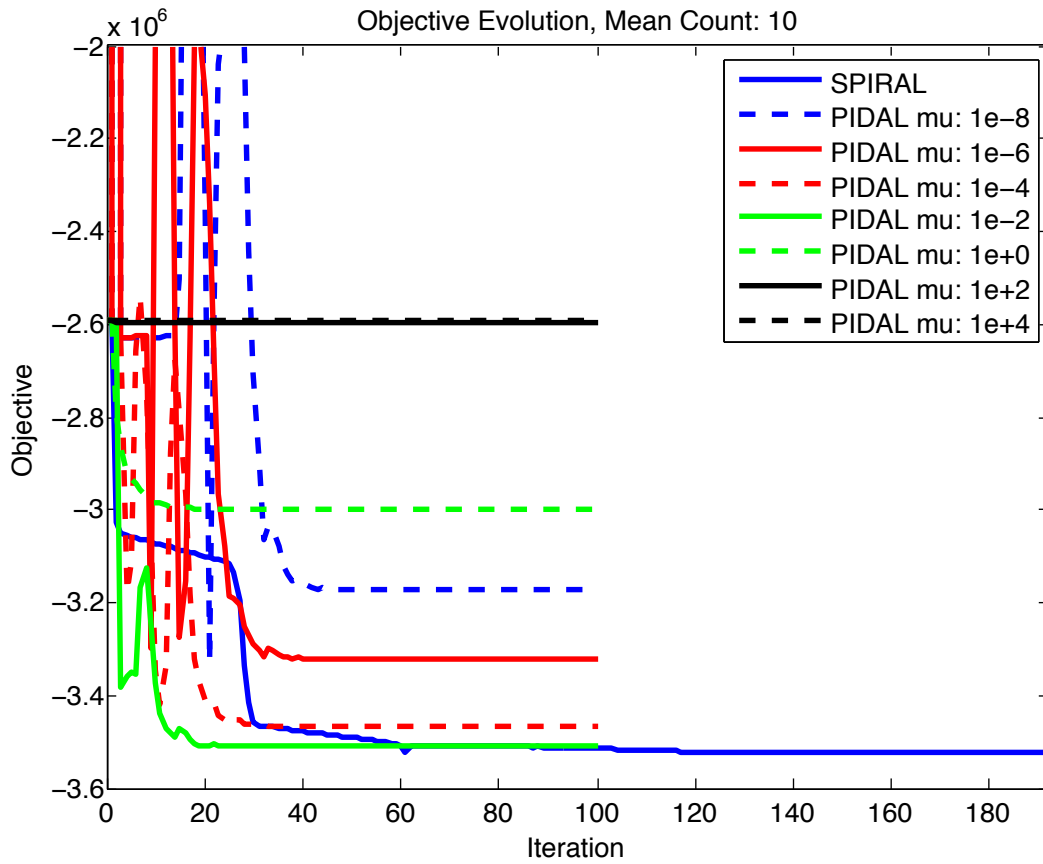


FIGURE 4.9: For $T/n = 10$. Objective function decay as a function of iteration number for SPIRAL and an augmented Lagrangian method for various values of μ . Note that at all intensity levels, the augmented Lagrangian methods are very sensitive to the choice of μ , while the SPIRAL method gives the lowest objective function value without the need for selecting μ . (a) $T/n = 1000$. (b) $T/n = 100$. (c) $T/n = 10$.

lower coherence benefits reconstruction performance.

We constrain the total observation time to be constant. That is, the total number of photons in all observations is the same regardless of the number of spectral channels M . Typical observations are shown in Fig. 4.10.

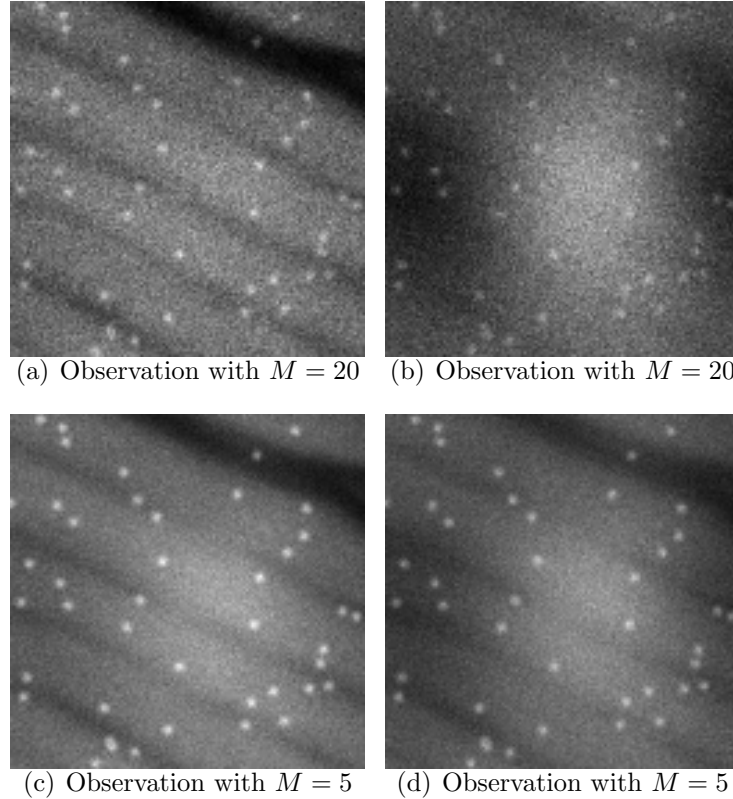


FIGURE 4.10: Typical observations with $T/n = 1000$ using the Case 3 spectra where (a) and (b) are generated using $M = 20$; (c) and (d) are generated using $M = 5$. Bigger M enjoys less coherence but suffers from more noise.

4.6.2 Simulation Result

We show example reconstructions for two different intensity levels ($T/n = 1000$ and $T/n = 100$) in Fig. 4.11. These show the visual degradation in performance that occurs when the coherence increases. Reconstructions from more observations (lower coherence) show better performance with more accuracy in the muscle component and better shape and brightness in the nuclei component. In Table 4.1 shows reconstruction errors with corresponding coherence values for the resulting spectral mixing matrices (A). We use the RMSE expressed as a percentage to evaluate the accuracy of the reconstructions:

$$\text{RMSE (\%)} = 100 \cdot \|\hat{x} - x\|_2 / \|x\|_2 \quad (4.27)$$

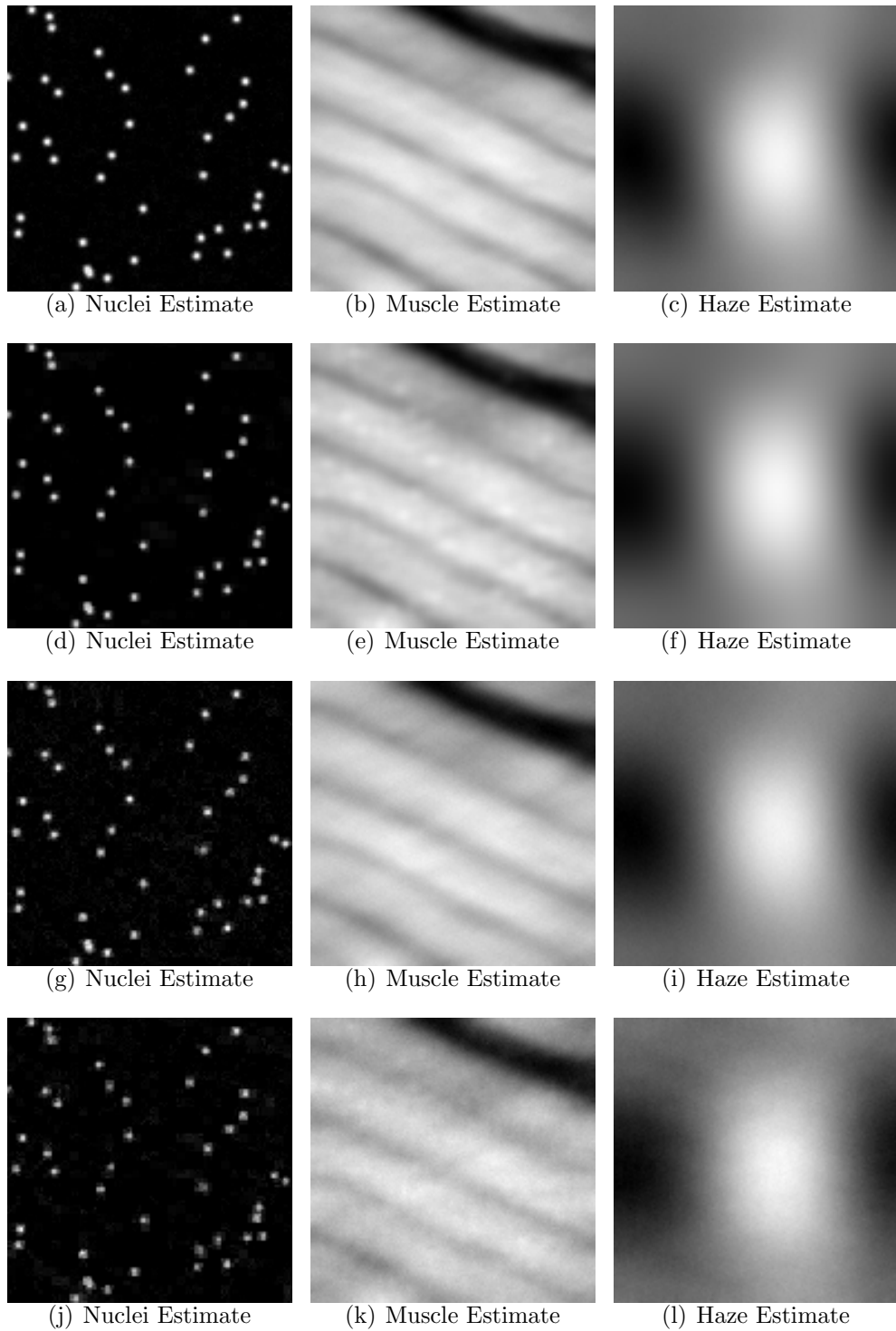


FIGURE 4.11: Reconstructions with $T/n = 1000$ where (a)–(c) have low coherence (spectra Case 3 with 20 spectral bands), (d)–(f) have high coherence (spectra Case 3 with 5 spectral bands) Reconstructions with $T/n = 100$ where (g)–(i) have low coherence (spectra Case 3 with 20 spectral bands), (j)–(l) have high coherence (spectra Case 3 with 5 spectral bands)

Table 4.1: MSE and coherence results for the experiments. Bold entries highlight settings with similar performance metrics predicted by our theory based on the spectral signatures and the number of spectral bands.

			Case 1	Case 2	Case 3
$M = 5$	$\mu(A)$	0.5435	0.6621	0.9709	
RMSE (%)	$T/n = 1000$	2.4260	2.5785	5.2896	
	$T/n = 100$	5.9388	6.3726	8.2410	
$M = 12$	$\mu(A)$	0.5077	0.5426	0.6108	
RMSE (%)	$T/n = 1000$	2.3925	2.3615	2.5438	
	$T/n = 100$	5.8921	5.9692	6.2952	
$M = 20$	$\mu(A)$	0.5028	0.5249	0.5407	
RMSE (%)	$T/n = 1000$	2.3448	2.3466	2.3307	
	$T/n = 100$	5.8037	5.7696	5.9125	

As expected from the theory, with lower coherence (μ) smaller RMSE can be achieved for sufficiently small M . We can also see from the bold entries in this table that the coherence is an excellent predictor for the relative RMSE values.

4.7 Experiments on Real Data

In this section we compare the result of sparse component analysis for analyzing real data from a mouse sarcoma model. The imaging device is a fluorescence microendoscope device that has previously been described in detail in [120] was used to collect images of acriflavine stained tissues. The system contained a 455 nm light emitting diode (Luxeon V Star, LXHL-LR5C), excitation filter (Semrock, FF01?452/45?25) dichroic mirror (Chroma 485 DCLP), emission filter (Semrock, FF01?550/88?25), CCD camera (Point Grey Research, GRAS-14S5), and coherent fiber bundle (Sumitomo, IGN-08/30). The fiber bundle was composed of 30,000 fibers giving a circular field of view of approximately 750 μm in diameter. The resolution of the system was 4.4 μm . Images were produced by placing the fiber bundle in contact with the acriflavine stained tissue surface. Acriflavine (0.01% w/v, Sigma-Aldrich) dissolved in

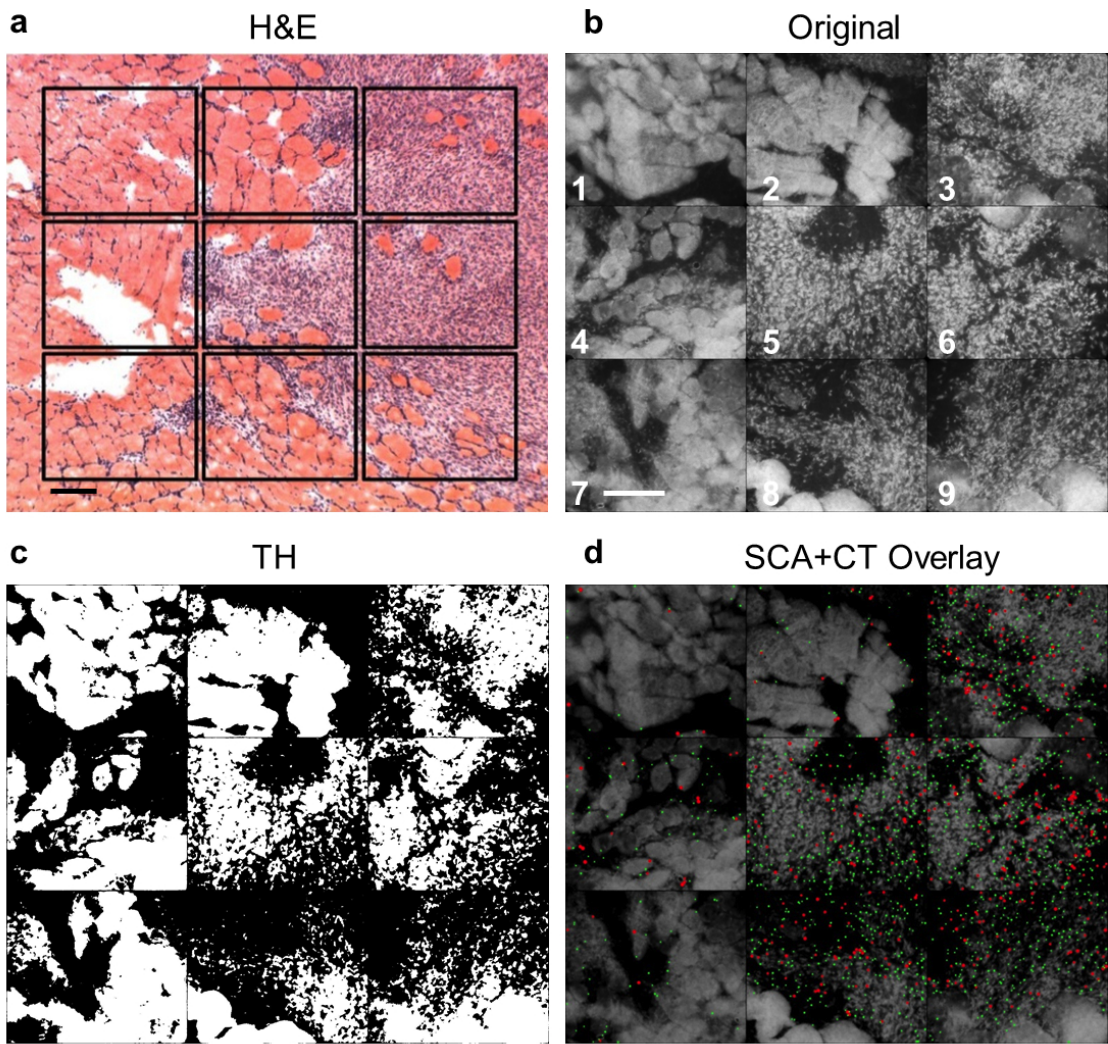


FIGURE 4.12: Optimal methodology for computing nuclear size and density in a panel of tissue section images. The specific locations where fluorescence microendoscopy (FM) images (Original, (b)) were collected are indicated by squares in the H&E section (H&E, (a)). Nuclei were isolated and quantified by using thresholding (TH) and sparse component analysis followed by the circle transform (SCA+CT), which is illustrated in (c) and (d) respectively. For SCA+CT, nuclei are overlaid onto the original image. Nuclei that are greater than $8 \mu\text{m}$ in diameter are false colored red, while those that are equal to or less than $8 \mu\text{m}$ are false colored green. Scale bar 200 μm .

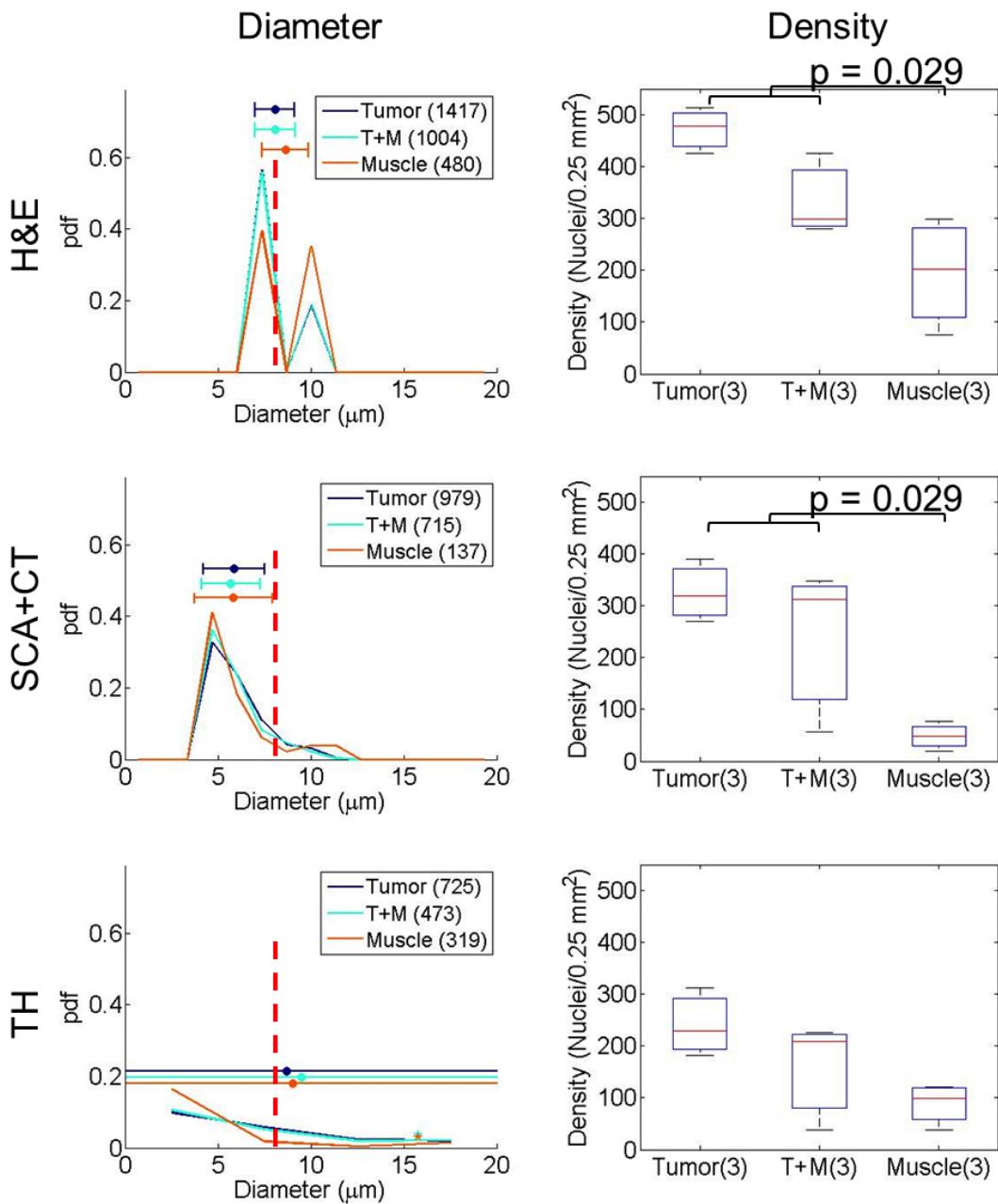


FIGURE 4.13: The nuclear size and density were calculated using both SCA+CT (row 2) and TH (row 3) for a cohort of 8 tumor, 6 T+M, and 13 muscle images. For diameter, the parenthetical values indicate the number of nuclei whose diameter was quantified. For density, the parenthetical values indicate the number of images in which the density was calculated. The dotted red line corresponds to an 8 μm diameter. Significant differences are seen between positive images (tumor and T+M) and negative images (muscle) images for nuclear density as determined by SCA+CT ($p = 0.0028$).

phosphate buffered saline (PBS) was topically applied to all specimens immediately prior to imaging.

The images collected from this device are high signal-to-noise ratio in that the effects of Poisson noise no longer dominate. However, similar computational techniques for sparse component analysis (SCA) can be used to analyze this data [36]. After SCA was applied to isolate nuclei, the nuclear size and density were quantified by computing the circle transform [129] on the nuclei image to detect approximately circular objects (i.e., nuclei). This methodology (referred to as SCA+CT) was compared to traditional binary intensity thresholding (TH) approach in which an image was thresholded to detect pixels containing nuclei, and each set of connected nuclei pixels was declared to correspond to a single nucleus. For all images captured with the fluorescence microendoscope, a thresholding level at 50% of the maximum was optimal because it enabled nuclei throughout the images to be isolated. These two different quantitative strategies were compared to examine their effectiveness in isolating nuclei in a heterogeneous tissue background.

Willcoxon rank sums (non-parameteric, two-tailed, $\alpha = 0.95$) were used in determining whether quantitative image parameters (e.g., nuclear size and density) were significantly different between positive (tumor, and tumor+muscle) and negative (muscle) tissue types for the bulk tissue image set and between LR+ and LR-(local recurrence positive and negative, respectively) margins for the *in vivo* image set. A significance level of $p < 0.05$ was considered to reject the null hypothesis for all analyses.

4.7.1 Comparison of Nuclear Size and Density Quantified using SCA+CT and TH to Histology

Images captured from frozen tissue sections mounted on glass slides were used to facilitate direct comparison of the SCA+CT and TH outputs to hematoxylin and eosin

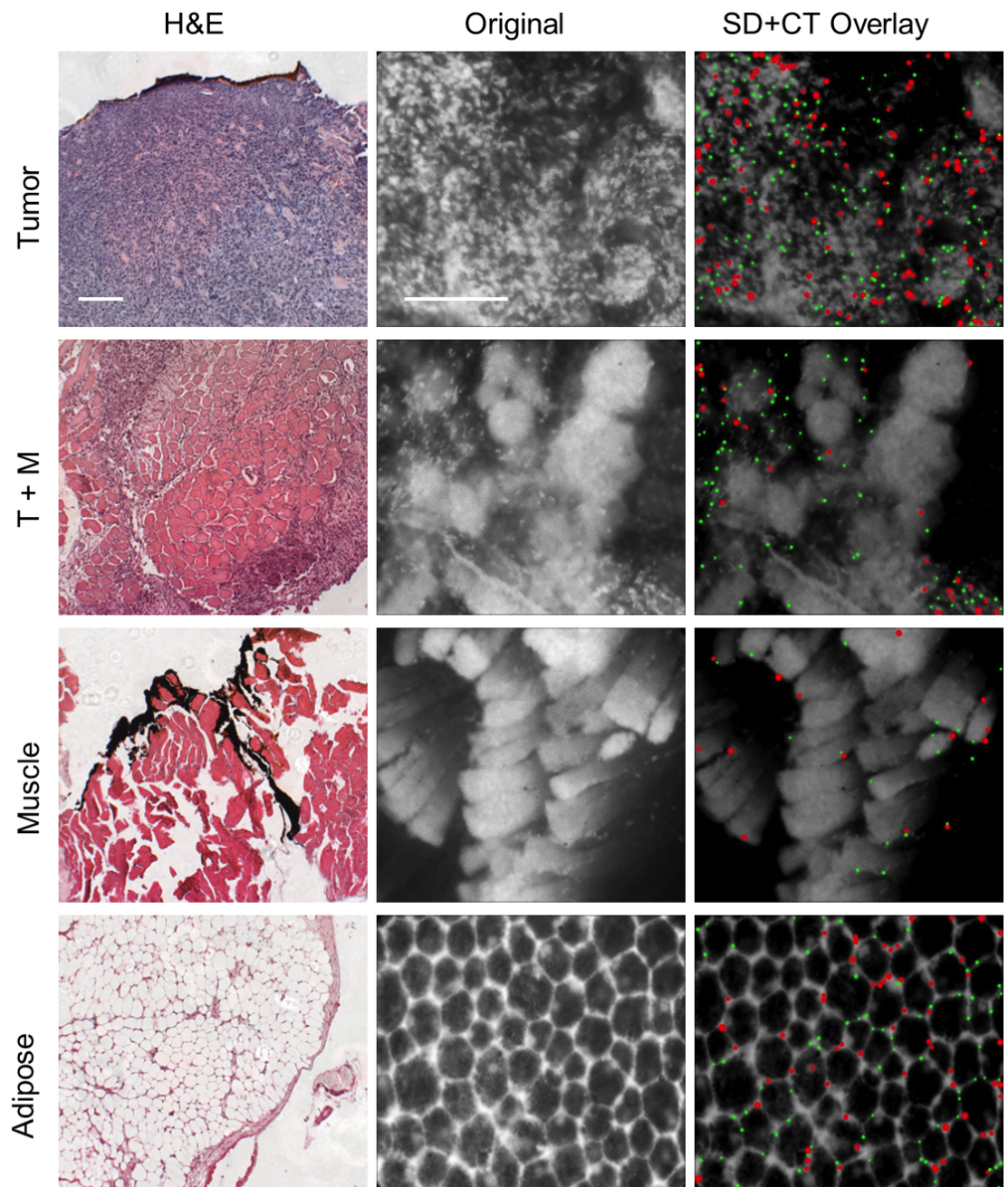


FIGURE 4.14: Comparison between ex vivo tissue types. Representative H&E images of tumor, tumor + muscle (T+M), muscle, and adipose tissue and their corresponding fluorescence microendoscopy (FM) image (Original) are shown (a)-(d) respectively. Nuclei were isolated and quantified by using thresholding (TH) and sparse component analysis followed by the circle transform (SCA+CT), which is illustrated in columns 3. For SCA+CT, nuclei are overlaid onto the original image. Nuclei that are greater than $8 \mu\text{m}$ in diameter are false colored red, while those that are equal to or less than $8 \mu\text{m}$ are false colored green. Scale bar 200 μm .

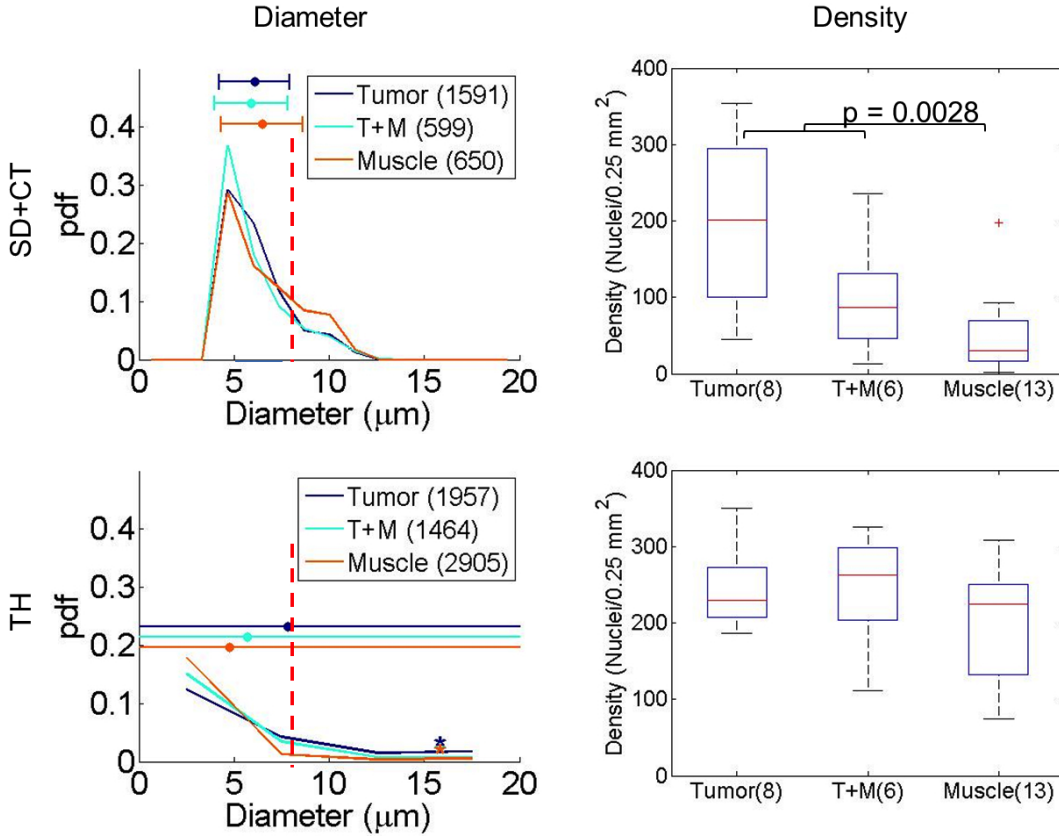


FIGURE 4.15: The nuclear size and density were calculated using both SCA+CT (row 1) and TH (row 2) for a cohort of 8 tumor, 6 T+M, and 13 muscle images. For diameter, the parenthetical values indicate the number of nuclei whose diameter was quantified. For density, the parenthetical values indicate the number of images in which the density was calculated. The dotted red line corresponds to an 8 μm diameter. Significant differences are seen between positive images (tumor and T+M) and negative images (muscle) images for nuclear density as determined by SCA+CT ($p=0.0028$).

(H&E) stained micrographs. Fig. 4.12 contains a panel of representative fluorescence microendoscopy (FM) images and the corresponding H&E en face section micrograph (Fig. 4.12(a)). The specific locations where FM images were collected are indicated by squares in the H&E section. The tissue types in the H&E section correspond well with the tissue types observed in the FM images. Nuclei in the panel of images were isolated with TH (Fig. 4.12(c)) and SCA+CT (Fig. 4.12(d)) as described previously. While TH incorrectly isolates very large sections of muscle tissue, SCA+CT

correctly isolates nuclei that more closely correspond to the size and density of nuclei observed in the H&E micrograph – which is considered the gold standard. The SCA+CT panel (Fig. 4.12(d)) is shown as an overlay in which nuclei isolated through SCA+CT are overlaid onto the original image. Nuclei that are greater than $8 \mu\text{m}$ in diameter are false colored red, while those that are equal to or less than $8 \mu\text{m}$ are false colored green. This two-color scheme is used throughout the remainder of the manuscript to highlight the bimodal distribution observed in Fig. 4.13. Next, the nuclear size and density for images in the panel that contained mostly tumor tissue (3, 6, 9), mostly muscle tissue (1, 4, 7), and a mixture of tumor+muscle tissue (2, 5, 8) were quantified using TH and SCA+CT and compared to the nuclear size and density in the corresponding region from the H&E micrograph (Fig. 4.12). As seen, SCA+CT most closely reflects the range and distribution of nuclear sizes observed in H&E stained section. Furthermore, SCA+CT preserves the differences in density between positive (tumor and tumor+muscle) and negative (muscle) images that are observed in H&E section ($p < 0.05$). No significant differences are seen in nuclear density when using TH.

4.7.2 Comparison of Nuclear Size and Density in Positive and Negative Excised Tumor Margins

SCA+CT was applied to ex vivo FM images from the margins of freshly excised tumors, and representative images are shown in Fig. 4.14. The first row of Fig. 4.14 contains an H&E micrograph of tumor and the corresponding FM image (Original).

The nuclei from these images were isolated using TH and SCA+CT, which can be seen in the third column. The SCA+CT processed tumor image shows a dense, disorganized collection of nuclei, which is characteristic of malignant tissue. Rows two through four of Fig. 4.14 contains images of tumor+muscle, muscle, and adipose respectively. SCA+CT processed tumor+muscle image contains a slightly less

LR+ Path+

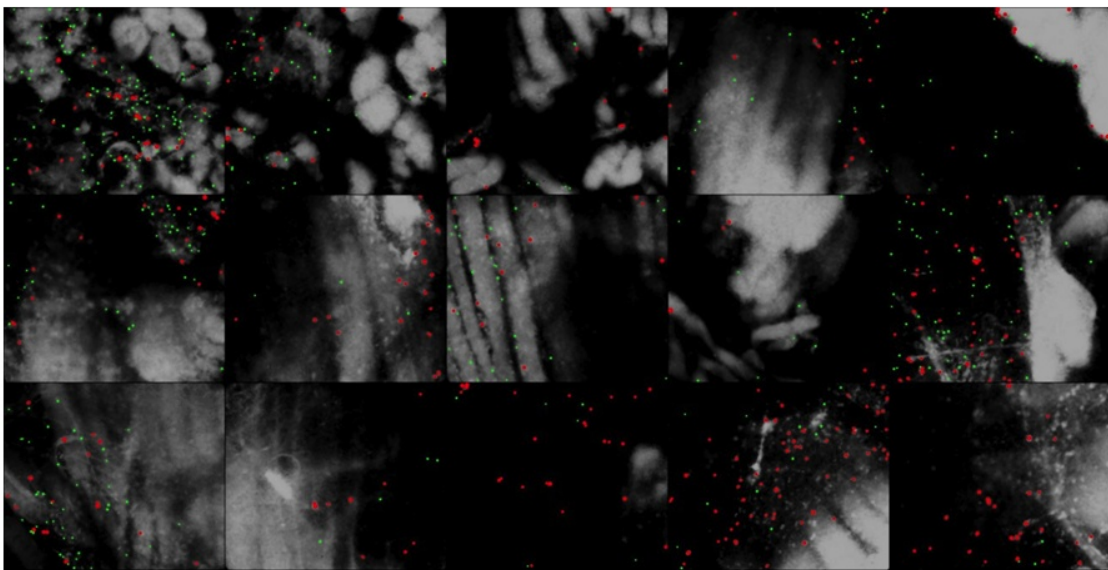


FIGURE 4.16: Fluorescence microendoscopy (FM) image panels of a local recurrence positive (LR+) pathology positive (Path+) *in vivo* tumor margin. Nuclei that are greater than $8 \mu\text{m}$ in diameter are false colored red, while those that are equal to or less than $8 \mu\text{m}$ are false colored green. Scale bar $200 \mu\text{m}$.

dense collection of nuclei than is seen in the tumor images, which is characteristic of residual tumor, while the SCA+CT processed muscle image contains few nuclei, as is characteristic of muscle or fibrous tissue. The adipose image processed with SCA+CT contains evenly spaced nuclei, as is expected with adipose tissue in which nuclei are pushed to the periphery of the adipocytes. Probability density functions and boxplots of the differences observed in nuclear size and density respectively were calculated using both SCA+CT (Fig. 4.15, top row) and TH (Fig. 4.14, bottom row) for a cohort of 8 tumor, 6 tumor+muscle, and 13 muscle images. The range and distribution of sizes observed in SCA+CT again are very similar to the range and distribution observed in the H&E panel in Fig. 4.13. Significant differences are seen between positive images (tumor and tumor+muscle) and negative images (muscle) images for nuclear density as determined by SCA+CT ($p = 0.005$). No significant differences are detected using TH.

LR+ Path-

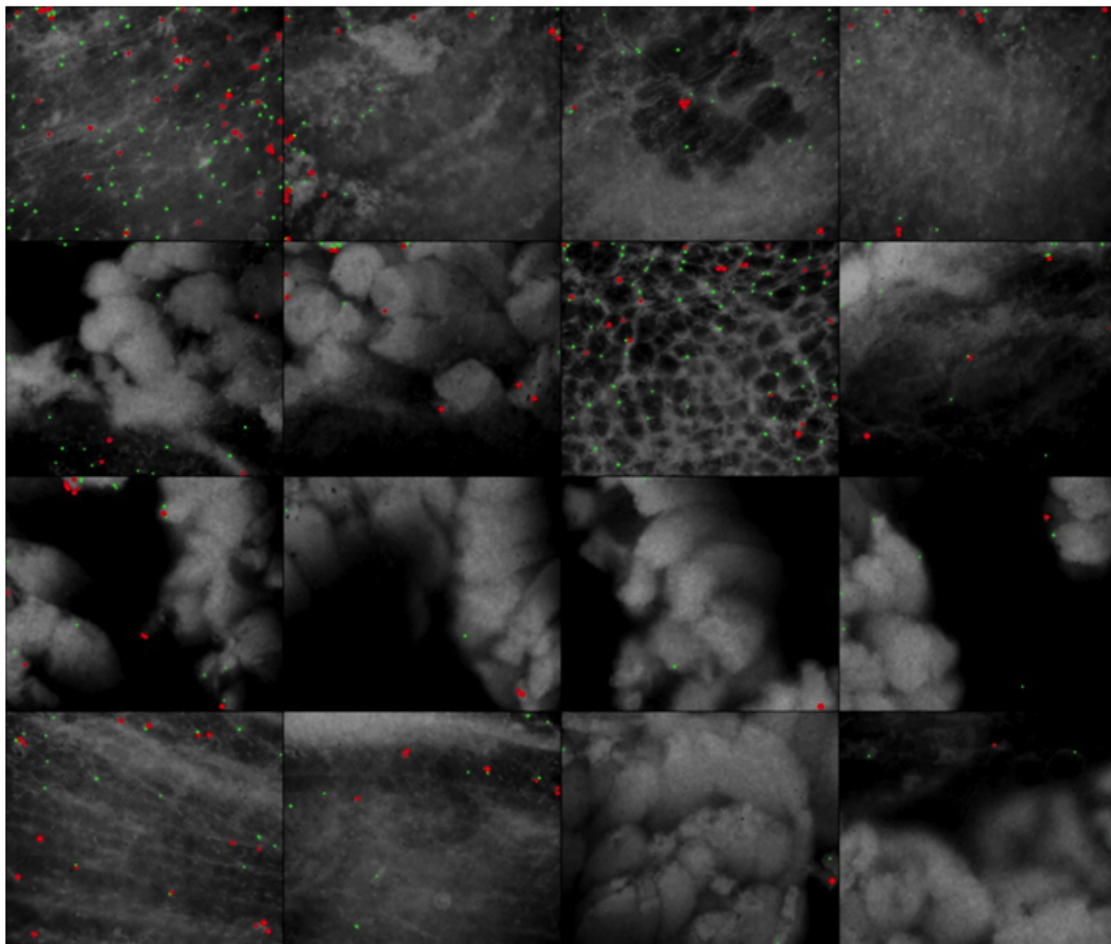


FIGURE 4.17: Fluorescence microendoscopy (FM) image panels of a local recurrence positive (LR+) pathology negative (Path-) *in vivo* tumor margin. Nuclei that are greater than $8 \mu\text{m}$ in diameter are false colored red, while those that are equal to or less than $8 \mu\text{m}$ are false colored green. Scale bar $200 \mu\text{m}$.

4.7.3 Quantification of Nuclear Size and Density from Images of the Resected Tumor Cavity

Panels of *in vivo* FM images captured from pathologically confirmed positive and negative tumor margins were analyzed with TH and SCA+CT (Figs. 4.16–4.18). In this case, two independent endpoints were measured. First, a pathological diagnosis of the excised margin was obtained, which yielded the clinical endpoint of patho-

LR- Path-

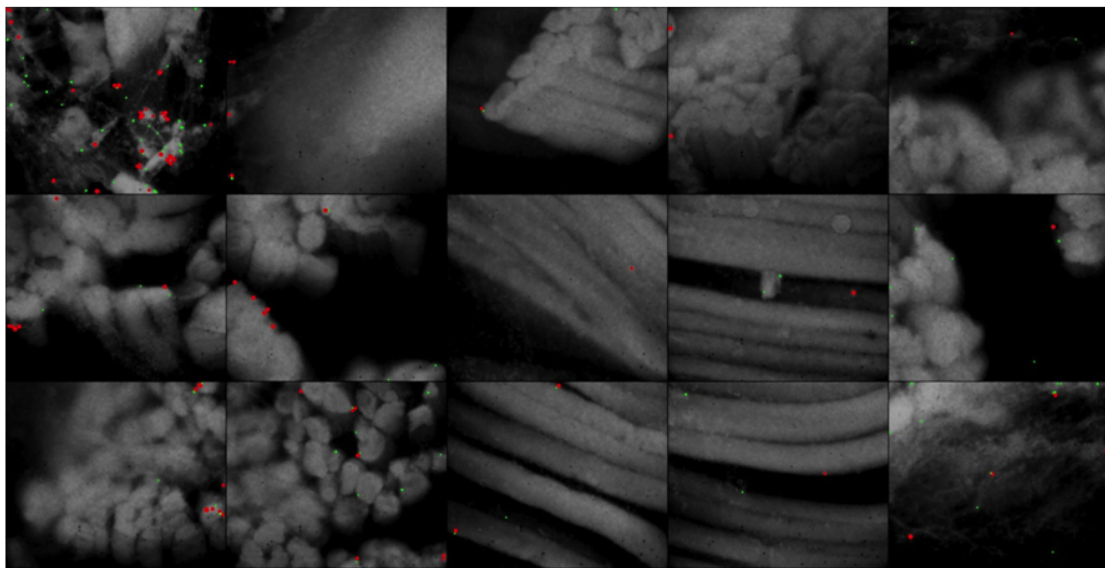


FIGURE 4.18: Fluorescence microendoscopy (FM) image panels of a local recurrence negative (LR-) pathology negative (Path-) *in vivo* tumor margin. Nuclei that are greater than $8 \mu\text{m}$ in diameter are false colored red, while those that are equal to or less than $8 \mu\text{m}$ are false colored green. Scale bar $200 \mu\text{m}$.

logically positive (Path+) and negative (Path-) margins. Additionally, mice were monitored for local recurrence at the excision site for 120 days to distinguish between mice that recurred locally (LR+) and mice that did not recur locally (LR-). FM image panels of a LR+/Path+, LR+/Path-, and LR-/Path- were captured *in vivo* by translating the probe over the resection cavity. SCA+CT is able to isolate nuclei from each panel, regardless of the presence of background, and shows distinct differences between LR+ and LR- margins for nuclear density (Fig. 4.19, $p = 0.0002$). No significant differences are observed using TH. When only examining the density (determined by SCA+CT) of the smaller green nuclei, more significant differences are seen between LR+ and LR- margins ($p = 0.0001$); conversely, when only examining the density of the larger red nuclei, less significant differences are seen ($p = 0.0064$). This suggests that using a combination of size and density information may lead to higher contrast between LR+ and LR- margins. It is noteworthy

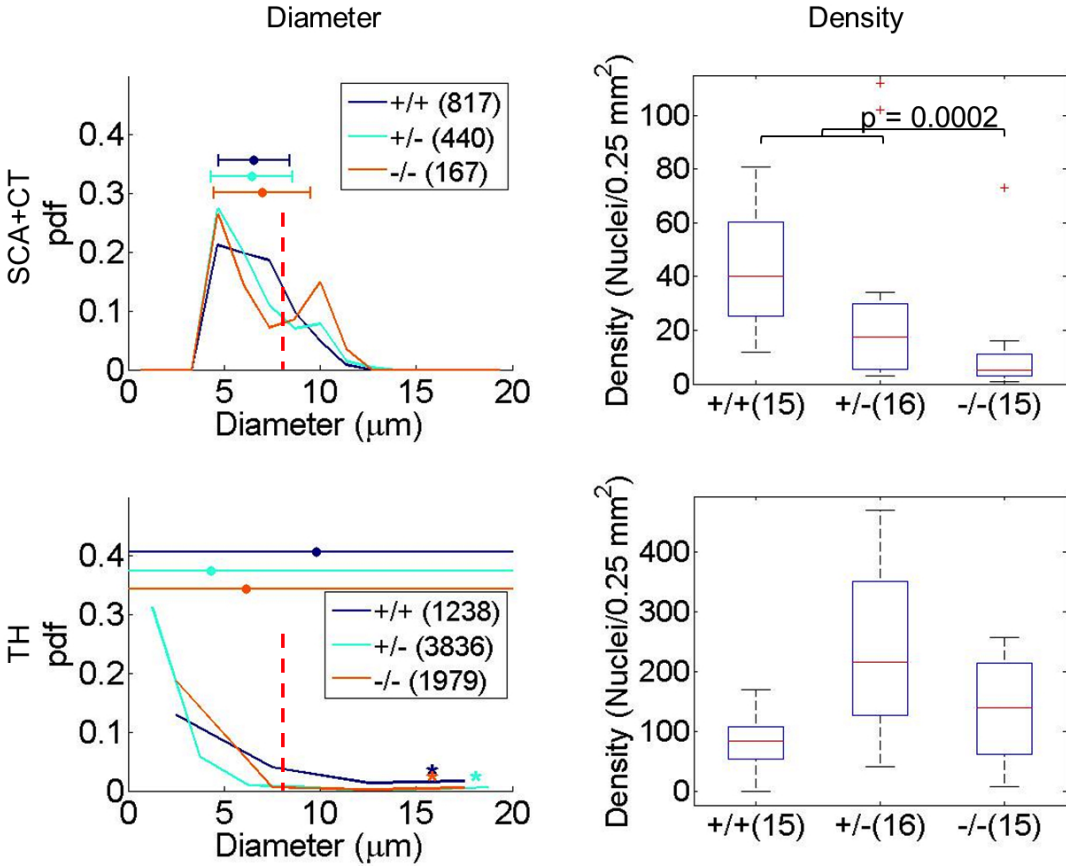


FIGURE 4.19: The nuclear size and density present in the three margins (Figs. 4.16–4.18) were calculated using both SCA+CT (top row) and TH (bottom row). For diameter, the parenthetical values indicate the number of nuclei whose diameter was quantified. For density, the parenthetical values indicate the number of images in which the density was calculated. The dotted red line corresponds to an 8 μm diameter. Significant differences are seen between the two LR+ positive margins and the LR- negative margin for nuclear density as determined by SCA+CT ($p = 0.0002$).

that the LR+/Path- margin has densities that are on par with the LR+/Path+ margin and significantly higher than the LR-/Path- margin even though the originally resected margin was found to be negative based on pathological evaluation. This underscores the importance of a strategy such as that described here which provides an opportunity to examine the resected cavity directly, which cannot be achieved by conventional pathology. This is of significance given that lack of residual cells on the excised margin may not always imply disease free margins in the tumor bed.

4.7.4 Discussion of Results on Real Data

In summary, fluorescence imaging of tissue micro-anatomy combined with a specialized algorithm for delineation and quantification of nuclear features is a means for rapid, non-destructive and automated detection of microscopic residual disease in surgical tumor margins. This strategy has the potential to be extended to other tumors and organ sites with significant and non-uniform background heterogeneity and can seamlessly translated to the in vivo setting obviating the need for a labor intensive and subjective process to determine the presence of residual disease in tumor margins.

4.8 Conclusions

Choosing the ideal number of spectral bands for tissue separation using multispectral observations introduces a myriad of tradeoffs among hardware costs, signal diversity, and photon noise. If M denotes the number of spectral bands observed, then the optimal value of M will depend on both the spectral profiles of the different tissue types which must be distinguished and the total amount of available light, which is proportional to the total data acquisition time. The nature of these tradeoffs can be explored using concepts developed within the compressed sensing literature, and can help optical engineers design cheap yet effective tools for the problem at hand. This chapter also demonstrates how the SPIRAL optimization method described in Chapter 3 can be more robust than popular augmented Lagrangian (AL) methods because there is no need to choose a good value of the AL parameter. We have also demonstrated how our methods can be used to isolate nuclei on real data and leads to the ability to detect disease in surgical margin assessment.

5

Multiphoton Fluorescence Microscopy Image Formation Using Exponentiated Total Variation

This chapter showcases SPIRAL as a method that can be used for reconstructing multiphoton fluorescence microscopy (MPM) data. We detail the application, a cross-validation procedure for automated parameter tuning, and show that a variation of SPIRAL which uses an exponential transform outperforms competing approaches on real-world datasets.

5.1 Introduction

Fluorescence microscopy is widely used to generate high-resolution images of living tissue and organisms in order to study cellular dynamics. Such systems typically produce high-contrast images of multiple fluorescent dyes against a black background, resulting in strong fluorophore visibility and specificity. Confocal microscopy is a popular form of fluorescence microscopy, but suffers from a trade-off between very low photon counts and detections of fluorescent events far outside the focal plane [130]. Multi-photon laser scanning microscopy (MPLSM), in contrast, yields obser-

vations with significantly less out-of-focus contamination by triggering fluorescent events using tightly focused, high peak power, low mean power, and fast (e.g. femtosecond) pulses from multiple lasers [131, 132, 133]. Consider a two-photon excitation, where the a single wavelength of the laser, usually 700–1000 nm, is insufficient to excite a fluorophore with an excitation peak in the 400–500 nm range to trigger a fluorescence event. However, an event can be triggered if two photons are absorbed instead, an event that occurs only if the photon density is high enough, such as at the focal point of the pulsed laser. Since the excitation is spatially isolated, the need for rejecting out-of-plane light allows us to eliminate a light-limiting confocal pinhole. Furthermore, even though the individual pulses have high peak energy, the low average power of the laser makes the technology safe for several *in vivo* imaging applications.

Multi-photon imaging uses laser raster scanning to assemble an image. The technique is based on the non-linear interactions between light and excitable molecules [134]. At very high photon densities, two or more photons may be simultaneously absorbed by a fluorescent molecule causing it to fluoresce, provided the sum of the individual photon energies is equivalent to the energy required for a single photon to induce fluorescence. In the case of two-photon imaging, the excitation wavelength is set to about twice that of the absorption peak of the fluorophore being observed. Normally, this wavelength would not produce any appreciable excitation. However, if a high-power, ultra-short pulse laser is used, it is possible to achieve instantaneous photon densities that are sufficient to give rise to a significant yield of two-photon events in the focal volume of an objective lens, while maintaining a mean power level that will not damage the specimen. In this manner, fluorophore excitation is confined to the focal volume because the photon density is insufficient to generate appreciable multi-photon events outside of this region. Optical sectioning is achieved because there is no appreciable fluorophore excitation above or below the focal vol-

ume (i.e. the plane of focus) thereby elegantly avoiding the problem of out-of-focus interference. An additional advantage of multiphoton imaging for in vivo studies is that photo-toxic effects are minimized because fluorophore excitation is confined to the plane of the optical section being observed [134, 135].

This chapter describes novel reconstruction strategies for extracting all the data possible from the weak fluorescence signals that are typically obtained when observing living specimens in a laser-scanning microscope using nonlinear optical techniques such as multi-photon (MP) imaging [134, 136]. The central problem is that fluorescence signals have poor signal-to-noise ratios (SNR) because of statistical fluctuations in photon flux. SNR can be increased by the use of higher laser powers and/or more efficient photodetectors. However, fluorescence saturation due to ground state depletion imposes an absolute upper limit to the level of laser excitation that can be profitably used. Also, as current photodetectors in laser-scanning microscopy have quantum efficiencies of around 40%, there is not much scope for dramatic improvements in photodetector design. SNR can also be increased by long scan times, but this (a) is time-consuming in large-scale experiments, (b) results in series motion artifacts and loss in temporal resolution, and (c) introduces photo-toxic effects when imaging living specimens.

5.1.1 *Data Acquisition Modes*

The emitted light from a MPLSM system can be acquired in a number of ways. In the integrated intensity mode, light entering a photomultiplier tube is transformed into a voltage that is then quantized by an ADC into a discrete measurement. Our system is capable of 16 bit resolution. In contrast, photon-counting mode counts the discrete number of photon counts at our detector, and the data collected is then an integer corresponding to the number of photons counted at each spatial location. This later mode more consistently preserves the Poisson statistics that underlie the relationship

to the photon intensity and our observed data. While a thorough statistical characterization of the integrated intensity mode may be possible, the photon-counting mode offers increased reliability for subsequent quantitative analysis.

5.2 Problem Formulation

We formulate the data analysis as an estimation problem. Let $f \in \mathbf{R}_+^n$ denote the multidimensional photon density function represented as a vector. That is, f_i is the intensity at the i th spatial location. The data analysis objective is to accurately estimate f from a collection of nonnegative photon counts $y \in \mathbf{Z}_+^n$. The challenge is that there may be very few (or even no) photons detected at each location i , leading to a very difficult and ill-posed problem. As in Chapter 3, we model this process with a inhomogeneous Poisson process,

$$y \sim \text{Poisson}(f).$$

If we normalize f by dividing by the total photon flux, $I_f := \sum_{i=1}^n f_i$, then the result characterizes the *spatial distribution* of fluorophores in the specimen. In practice, I_f is determined by both the fluorescence of the specimen (which in turn is determined by the total amount of fluorescent dye or endogenous fluorophores in the sample) and the *stare time*, or amount of time the MPLSM spends collecting photons at each spatial location.

Under the Poisson model, given a candidate photon density estimate f , we can compute the negative log likelihood of y given this estimate as

$$-\log p(y | f) = \sum_{i=1}^n f_i - y_i \log(f_i) + C,$$

where C is a constant independent of f .

In general, we wish to estimate f as accurately as possible while simultaneously limiting the I_f . While a higher intensity generally makes the estimation problem

easier (in terms of achieving lower errors), there are many practical reasons for limiting the intensity. First, long stare times are impractical for large-scale screening applications and or living specimens which are moving. If a long stare time is used for moving objects, substantial motion blur will corrupt the observations. Second, the amount of fluorescent protein used must be limited in many applications to avoid photo-toxic effects.

This paper shows that standard processing methods for MPLSM data are highly inaccurate for small photon flux, and in this regime sophisticated photon density estimation methods can produce far more accurate estimates.

5.3 Prior Work

Classical intensity estimation approaches based on fixed binning/aggregation (i.e., histograms) or smoothing strategies (Gaussian filtering) tackle the problem of low photon counts by averaging data in a non-adaptive manner, which may lead to excessive smoothing and loss of resolution. This is demonstrated in the experimental results below. To address these challenges, previous work considered adaptive gridding and total variation regularized estimators, which we review in this section. As we demonstrated in our experiments, however, the proposed formulation outperforms this prior work in terms of reducing visual artifacts while preserving true biological structures.

5.3.1 *Adaptive Gridding*

Earlier approaches to the intensity estimation problem underlying multiphoton microscopy include data-adaptive binning and smoothing strategies based on a novel multiresolution analysis (MRA) framework for density estimation. The proposed MRA-based approach is based on a maximum likelihood (ML) density estimation procedure, coupled with a data-adaptive partition of the spatial domain. The prin-

inciple of ML is arguably the most natural criterion to employ in intensity estimation, since by definition it seeks to identify the intensity function that is most likely to have generated the data y . In other words, the ML criterion can be interpreted as determining an optimal generative (probabilistic) model for the data. Informally speaking, ML estimation can be viewed as an optimal form of *denoising* to improve the signal-to-noise ratio. The data-adaptive partitioning is nonparametric, meaning that it makes essentially no a priori assumptions (i.e., does not assume a pre-defined underlying parametric model) about the biological structure under study.

The partitioning process is performed by considering a large collection of possible partitions, Recursive Dyadic Partitions (RDPs), and selecting the partition that is determined to best fit to the data and the biological structure, based on the ML criterion. The RDPs are defined by the set of all possible subimages whose sidelengths are equal to a dyadic (power of 2) integer number of image pixels. These subimages are formed by recursively splitting the image into quarters again and again, and they effectively define a collection of “multiscale-pixels” at varying spatial resolutions. Each RDP corresponds to a particular “pixelization” of the image domain, with pixel sizes varying across the image as shown in Fig. 5.1. To avoid confusion, we will call these multiscale pixels the “bins” of the partition. Any RDP can be represented with a binary tree, which describes the recursive partitioning process that generated the bins. Note that by repeating the recursive partitioning to completion produces bins that are equivalent to the original set of high-resolution pixels.

Let P denote a specific RDP. The ML density estimate, constrained to P , is determined by ML estimates (MLEs) of the photon density for each bin. This results in a density estimate denoted by $\hat{f}^{y,P}$, where the superscripts y and P denote the dependence on the data y and the partition P . The spatial aggregation resulting from the restriction to the partition P can make $\hat{f}^{y,P}$ quite stable and robust. However,

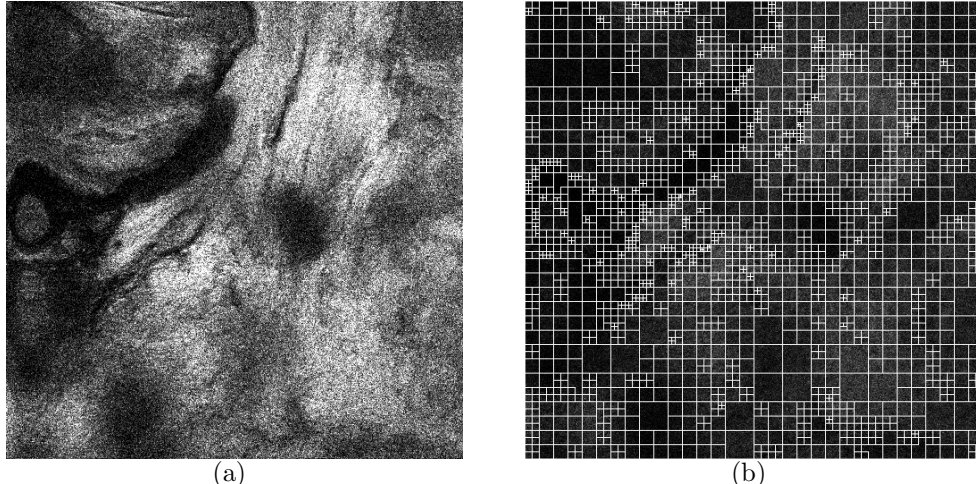


FIGURE 5.1: Adaptive gridding example. (a) Original data. (b) Corresponding recursive dyadic partition.

a poor choice of P may result in an undesirable loss in spatial resolution. This is an instance of the classic bias-variance tradeoff in statistics. An adaptive choice of the partition P can mitigate this tradeoff by selecting a partition that is optimally matched to the structural characteristics of the data.

The photon density can be modeled as a constant or smoothly varying function on each bin (e.g., a linear or polynomial fit). The ML photon density estimation process constrained to a given P is relatively straightforward. If a constant model is employed for each bin, then the ML density estimate is simply proportional to the ratio of the total number of photons detected in that bin to the bin area/volume. If spatially varying models are employed, then fast and robust numerical methods exist for ML estimation [97, 137].

The most crucial aspect of this method is the partition selection step. This is accomplished by optimizing a combination of the ML fit value and a measure of the complexity of the partition, over the choice of partition. Because each photon detection is statistically independent when conditioned on $\hat{f}^{y,P}$, the ML value is

simply the product of $\hat{f}_i^{y,P}$ density levels for each detection i , $i = 1, \dots, n$. Maximizing the likelihood over all possible partitions equates to minimizing the negative log-likelihood. Denoting by $-\log p(y | \hat{f}^{y,P})$ the negative log-likelihood value for the density estimate based on partition P , we select the optimal partition and thus optimal estimator according to the following minimization:

$$\begin{aligned}\hat{P} &= \arg \min_P -\log p(y | \hat{f}^{y,P}) + \tau \text{pen}(P) \\ \hat{f}^{\text{AG}} &= \hat{f}^{y,\hat{P}},\end{aligned}$$

where $\text{pen}(P)$ is a complexity regularization function and $\tau > 0$ is a regularization parameter. The purpose of the regularization function is to optimally balance the bias-variance tradeoff by weighting complicated partitions with many bins more heavily than simple partitions with fewer bins. Generally speaking, the regularization makes our estimator favor simpler partitions with more robustness to noise over more complicated partitions that may have slightly larger ML values but inherently lower SNR. Choice of the regularization function is a delicate matter, and in our previous work we have used mathematical error analysis techniques to design optimal regularization methods [137, 97]. For example, in the case of photon density estimation, we have proved that by taking $\text{pen}(P)$ to be proportional to the number of bins in P and by setting τ proportional to $\log N$, where $N = \sum_{i=1}^n y_i$ is the total number of photon counts, the resulting partition \hat{P} and corresponding estimate \hat{f}^{AG} estimate satisfy the following estimation error bound:

$$\mathbf{E} \left\| \frac{\hat{f}^{\text{AG}}}{I_{\hat{f}^{\text{AG}}}} - \frac{f}{I_f} \right\|_1 < K \left(\frac{N}{\log N} \right)^{-1/3}, \quad (5.1)$$

where \mathbf{E} denotes the expectation over random realizations of photon counts distributed according to the true density function f , $\|\hat{f}^{\text{AG}}/I_{\hat{f}^{\text{AG}}} - f/I_f\|_1$ denotes the

sum of pixels errors (in absolute value) between the intensity-normalized f and \hat{f}^{AG} , N is the total photon count, and $K > 0$ is a constant independent of N .

This shows that the reconstruction tends to the photon density f as the number of photon detections increases; that is \hat{f}^{AG} is asymptotically consistent. In fact, the error decays to zero at a rate of $N^{-1/3}$ (ignoring the constant and logarithmic factors which are negligible when the total number of photons is large). We have shown that it is mathematically impossible to improve on this rate [97], which shows that no other method can significantly outperform our approach. Remarkably, the entire reconstruction process can be computed in approximately linear-time (i.e., the number of arithmetic operations is proportional to the number of pixels in the original data acquisition).

5.3.2 Total Variation Regularized Poisson Denoising

Regularization based on a (TV) seminorm has also garnered significant recent attention [100, 101]. This seminorm is described in detail below; in general, it measures how much an image varies across pixels by analyzing the image gradient magnitude, so that a highly textured or noisy image will have a large TV seminorm, while a smooth or piecewise constant image would have a relatively small TV seminorm. This is often a useful alternative to wavelet-based regularizers, which are also designed to be small for piecewise smooth images but can result in spurious large, isolated wavelet coefficients and related image artifacts.

We define the anisotropic TV seminorm as

$$\|f\|_{\text{TV}} := \sum_{i=1}^{n_1-1} \sum_{j=1}^{n_2-1} |f_{i+1,j} - f_{i,j}| + |f_{i,j+1} - f_{i,j}|,$$

this is a slight abuse of notation as here we are using two-dimensional pixel coordinates $f_{i,j}$ with $i = 1, \dots, n_1$, $j = 1, \dots, n_2$, and hence $n = n_1 n_2$. The TV seminorm

is simply a measure of the magnitude of all vertical and horizontal first-order differences. Said differently, one can think of an image with a small TV seminorm as one that is sparse with respect to an overcomplete representation of these first-order differences (neglecting the mean of f), meaning the image has few abrupt changes in pixel intensity yet many regions of homogeneous signal level. This property makes TV especially well suited for image denoising. In particular, our previous work [33] detailed in Chapter 3, considered estimating f using

$$\hat{f}^{\text{TV}} = \arg \min_f -\log p(y | f) + \tau \|f\|_{\text{TV}}.$$

5.4 SPIRAL-TVX Reconstruction for Poisson Data

As shown in the below experimental results, both the adaptive gridding and total variation methods described in Section 5.3 are subject to significant spurious artifacts, especially in conjunction with the cross-validation procedure developed in Sec 5.5 below. To reduce these artifacts without compromising the final image quality, we consider total variation regularization on the *log-intensity*, defined as

$$\theta := \log f,$$

where the logarithm is considered componentwise.

Specifically, we compute an estimate (denoted \hat{f}) of the observed photon intensity (denoted f), by solving the optimization problem

$$\hat{\theta} = \arg \min_{\theta} -\log p(y | \theta) + \tau \|\theta\|_{\text{TV}} \quad (5.2)$$

$$\hat{f} = \exp \theta, \quad (5.3)$$

where the exponentiation is computed pixel-wise. In this expression,

$$-\log p(y | \theta) = \sum_{i=1}^n \exp(\theta_i) - y_i \theta_i \quad (5.4)$$

is the log likelihood of the observed data if it is generated by intensity $f = \exp \theta$; it measures the goodness-of-fit of any candidate intensity estimate.

To this is added a TV regularization term, which was detailed in Section 5.3.2. The parameter $\tau > 0$ is a regularization parameter which controls the amount of smoothing performed by the regularization. In many settings it is chosen by hand to produce visually appealing images, but we propose a robust cross-validation procedure in Section 5.5 which allows this parameter to be set automatically based upon the data.

5.4.1 Optimization algorithm

In previous work, we developed the Sparse Poisson Intensity Reconstruction Algorithm (SPIRAL) [33]. This framework can be extended to handle the proposed estimator 5.3. First, let

$$\phi(\theta) := -\log p(y | \theta).$$

At iteration k , we compute a second-order Taylor-series approximation of ϕ at θ^k and approximate the Hessian with a scaled identity matrix: $\nabla^2 \phi(\theta^k) \approx \alpha_k I$. This yields

$$\tilde{\phi}(\theta) := \phi(\theta^k) + \nabla \phi(\theta^k)^T (\theta - \theta^k) + \frac{\alpha_k}{2} \|\theta - \theta^k\|_2^2.$$

Now instead of directly minimizing $\phi(\theta) + \tau \|\theta\|_{\text{TV}}$ (which is difficult) we can set

$$\begin{aligned} \theta^{k+1} &= \arg \min_{\theta} \tilde{\phi}(\theta) + \tau \|\theta\|_{\text{TV}} \\ &= \arg \min_{\theta} \frac{1}{2} \|\theta - s^k\|_2^2 + \frac{\tau}{\alpha_k} \|\theta\|_{\text{TV}} \end{aligned}$$

where

$$s^k := \theta^k - \frac{1}{\alpha_k} \nabla \phi(\theta^k).$$

This last minimization can be thought of as a simpler, and computationally easier denoising problem which we solve using the FISTA algorithm [101].

5.5 Cross-Validation Method for Choosing τ

In all of the above methods, careful selection of the regularization parameter is crucial to achieve good performance. In this section, we detail a cross-validation procedure that can be used in such a scenario, and can be applied to all the methods considered thus far.

Here we assume that we have access to two independent realizations from the same underlying intensity f , one we will use for training which we denote as y^T , and the other for validation, which we denote as y^V . We assume that

$$\begin{aligned} y^T &\sim \text{Poisson}(pf) \\ y^V &\sim \text{Poisson}((1-p)f), \end{aligned} \tag{5.5}$$

where $p \in (0, 1)$ controls the proportion of intensity allocated for the training data. We allow this generalization as it may be beneficial to aggregate more photons for the training data (say 90%) and a few photons for the validation data (the remaining 10%).

If such data is not available, it may be artificially created by Poisson thinning - essentially for each photon we flip a biased coin to determine if it belongs in the training set or validation set. This Poisson thinning is equivalent to the following procedure, starting with a single image of photon counts $y \sim \text{Poisson}(f)$, we let

$$\begin{aligned} y^T &\sim B(y, p), \\ y^V &= y - y^T, \end{aligned} \tag{5.6}$$

where $B(y, p)$ is the binomial distribution with parameters y and p , where p represents the probability of heads of the biased coin ($p = 0.9$ in the above example). It is straightforward to show that model (5.6) is actually equivalent to model (5.5) when the binomial draws are independent.

With our data in hand, we are able to detail the cross-validation procedure. Consider a general penalized maximum likelihood problem applied to the training data, where we explicitly consider the dependence on τ , the regularization parameter:

$$\hat{f}_\tau = \arg \min_f -\log p(y^T | pf) + \tau \text{pen}(pf).$$

For many settings of the regularization parameter τ , say for $\tau \in T = \{\tau_1, \dots, \tau_K\}$, we generate a sequence of estimates $\{\hat{f}_\tau\}_{\tau \in T}$. We then select the regularization setting that achieves the maximal likelihood on the validation set, and use that setting in our final estimator:

$$\begin{aligned}\hat{\tau} &= \arg \min_{\tau \in T} -\log p(y^V | (1-p)\hat{f}_\tau) \\ \hat{f} &= \hat{f}_{\hat{\tau}}\end{aligned}$$

For certain estimation strategies, it can be shown that this cross-validation procedure preserves the error decay rates, such as those presented in (5.1), and is hence also near-optimal. The proof of this claim follows through a straightforward application of the results in [138].

5.6 Experimental Results on Multiphoton Microscopy Data

In this section, we show the effectiveness of the described reconstruction algorithms in conjunction with the cross-validation procedure. Here we compare a total of five different approaches for reconstructing Poisson data:

- Fixed Gridding: Here we *uniformly* aggregate the data into bins of size $d \times d$ pixels, as if we acquired lower-resolution data with higher SNR per pixel.
- Gaussian Smoothing: We low-pass filter the image using a Gaussian PSF, the amount of smoothing is dictated by the PSF width σ .
- Adaptive Gridding: The RDP-based estimation strategy detailed in Sec. 5.3.1.

- SPIRAL-TV: The SPIRAL algorithm (Chapter 3, summarized in Sec. 5.3.2) using the total variation penalty.
- SPIRAL-TVX: The SPIRAL algorithm using the exponentiated transformation, described in Sec. 5.4.

The first two approaches represent simple estimators that practitioners commonly employ to decrease the Poisson noise in the data, the remainder are more sophisticated approaches that use advanced tools from signal processing. All parameters were automatically selected via a cross-validation procedure. For the fixed gridding and Gaussian smoothing methods, we use cross-validation to select the bin size and blur PSF width. For visualization, images were scaled to increase contrast.

We examine the results of our algorithm on three datasets:

Stationary Specimens Images collected for 0.1, 0.5, 1, 5, 10, 30, 60, and 120 seconds at a constant power and gain setting. The power and gain settings needed to be constant for photon counting mode, collection time modulates the number of photons collected. These results are shown in Fig. 5.2, and a closer examination to an interesting ROI for a subset of the scan times is shown in Fig. 5.3.

Dynamic Specimens Dataset of MDA breast cancer cell line imaged live for NADH autofluorescence. Note that these are *live cells* that move and deform between acquisitions, and hence there is not an exact correspondence between acquisitions. Images are collected for 0.1, 1, 5, 10, 30, 60, and 120 seconds at a constant power and gain setting. The power and gain settings needed to be constant for photon counting mode, collection time modulates the number of photons collected. This dataset is under higher magnification than the Stationary Specimens dataset so it contains more interesting features like cellular

protrusions. These results are shown in Fig. 5.4, and a closer examination to an interesting ROI for a subset of the scan times is shown in Fig. 5.5.

Mouse Embryonic Stem Cells These cells are imaged using NADH autofluorescence - an endogenous contrast agent. Again note that these live cells move and deform between acquisitions. Images collected for 0.1, 1, 5, 10, 30, 60, and 120 seconds at a constant power and gain setting. The power and gain settings needed to be constant for photon counting mode, collection time modulates the number of photons collected. These results are shown in Fig. 5.6, and a closer examination to an interesting ROI for a subset of the scan times is shown in Fig. 5.7.

From these set of results, we see that the SPIRAL-TVX algorithm combined with the cross-validation procedure is able to reconstruct the photon-limited data with the highest fidelity.

5.7 Conclusions

In this chapter we have shown that SPIRAL-TV, and an extension, SPIRAL-TVX produce state-of-the-art results on data acquired from a multiphoton fluorescence microscope. Coupled with a cross-validation method, the resulting procedure can automatically apply an appropriate amount of smoothing to the data, which yields accurate estimation of images, without the need for lengthy scan times.

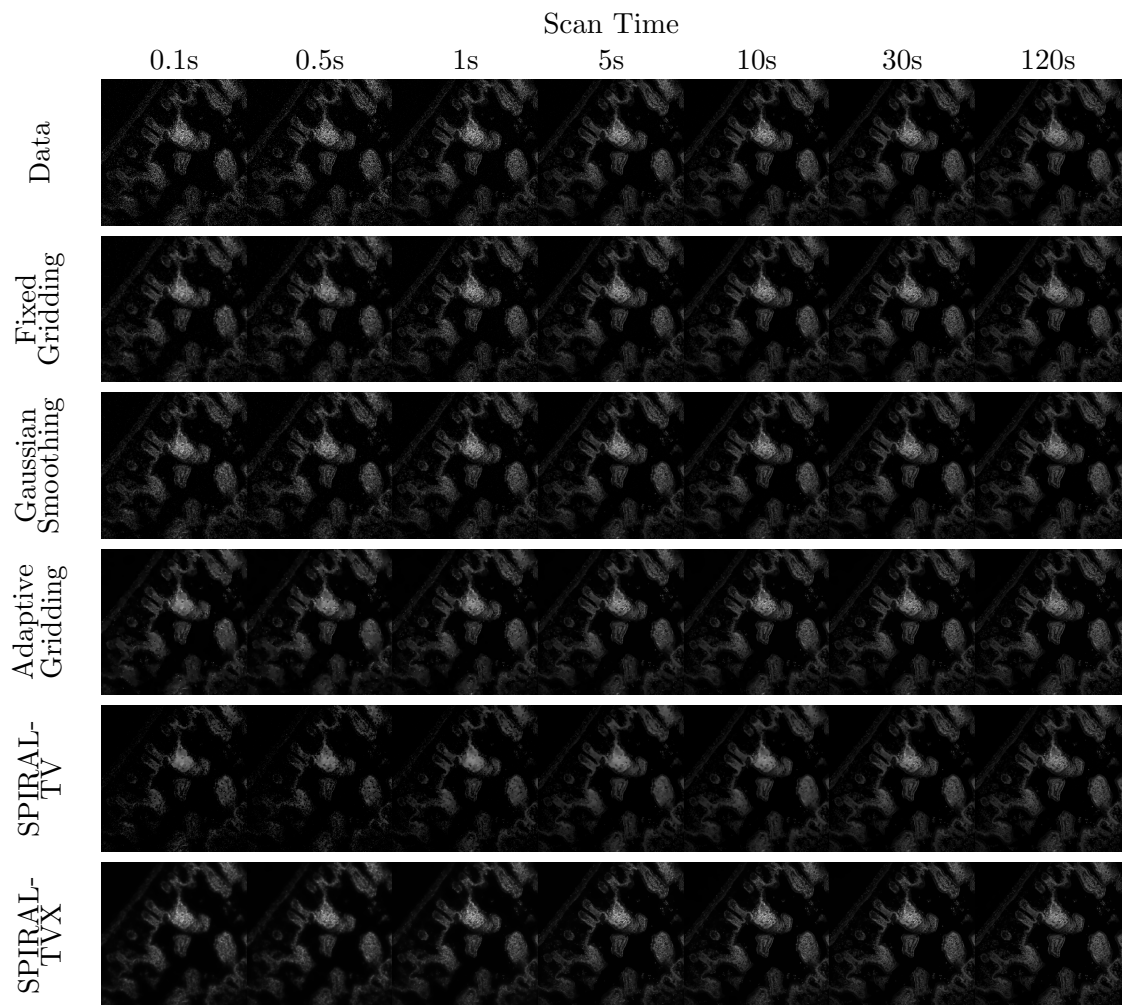


FIGURE 5.2: Results on the Stationary Specimens dataset, showing all methods and scan times

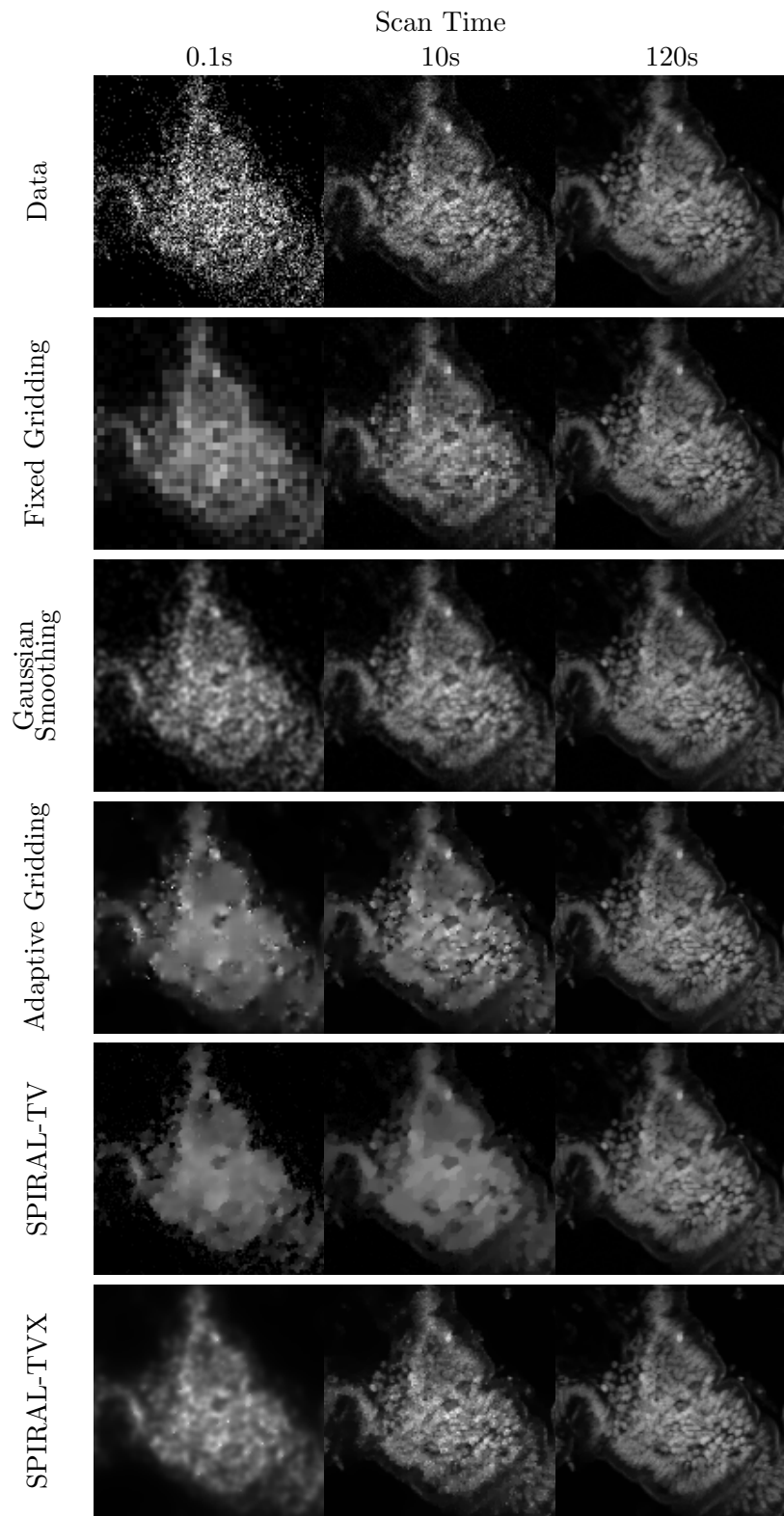


FIGURE 5.3: An interesting ROI on the Stationary Specimens dataset, showing all methods for a subset of scan times

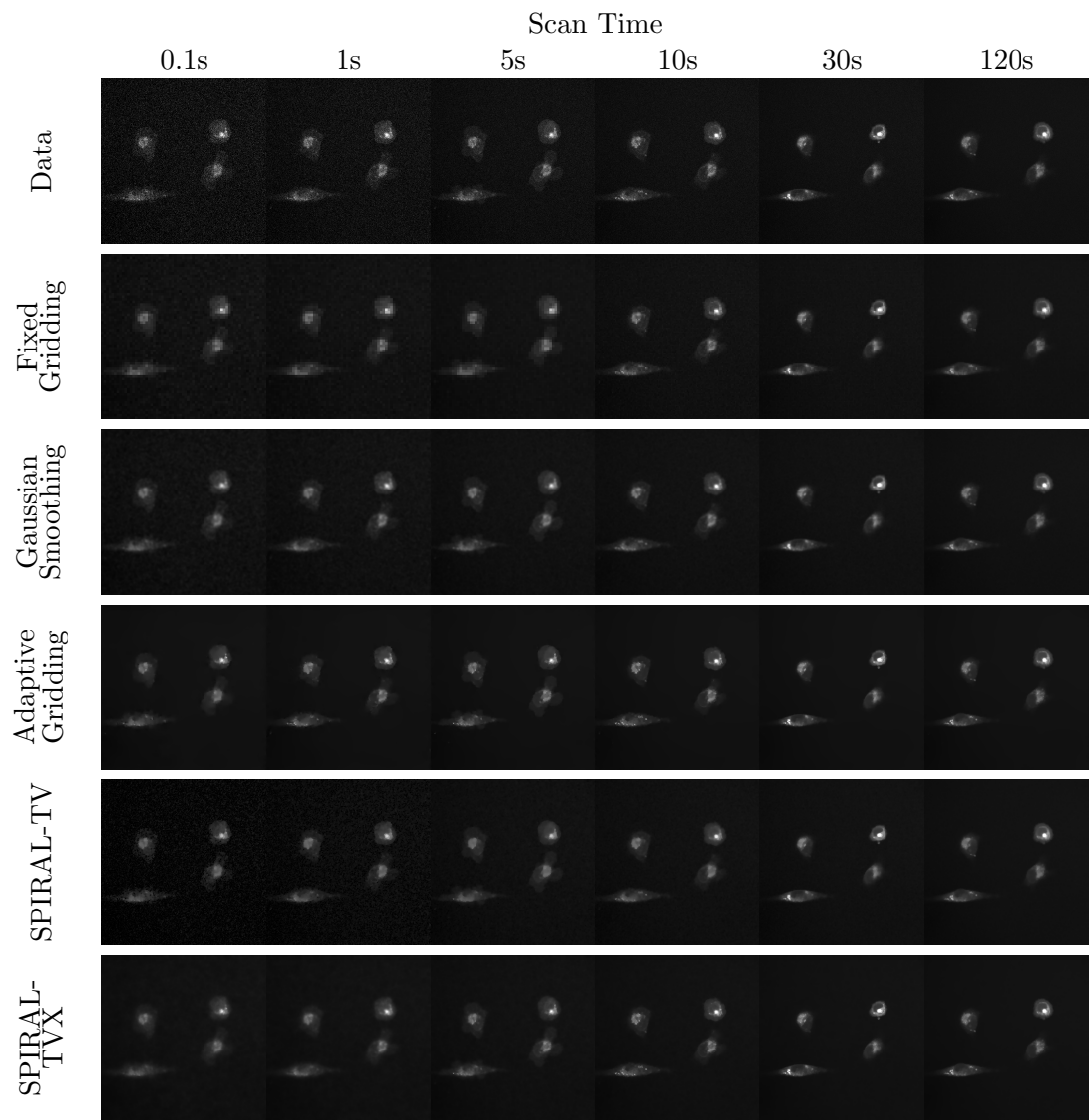


FIGURE 5.4: Results on the Dynamic Specimens dataset, showing all methods and scan times

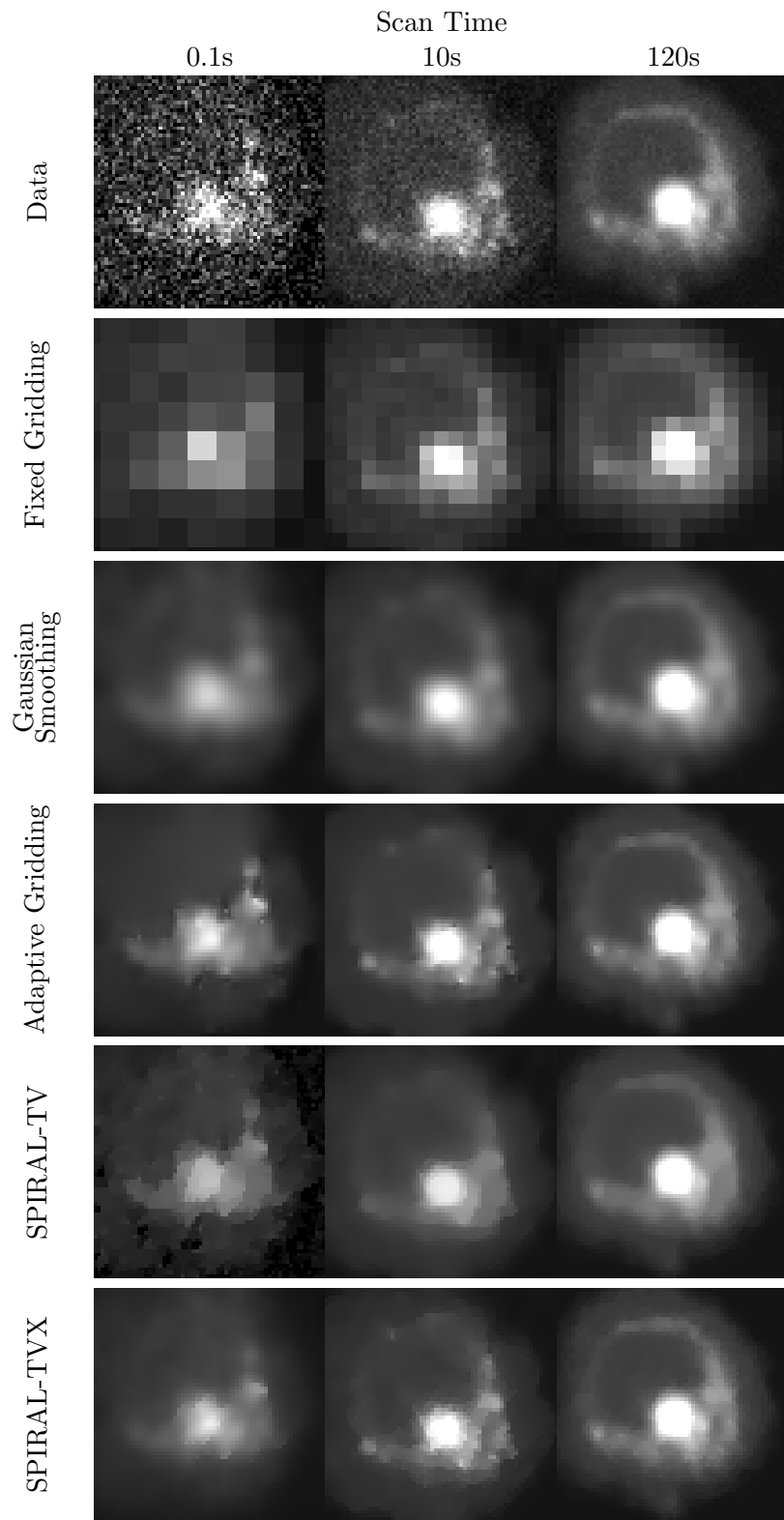


FIGURE 5.5: An interesting ROI on the Dynamic Specimens dataset, showing all methods for a subset of scan times

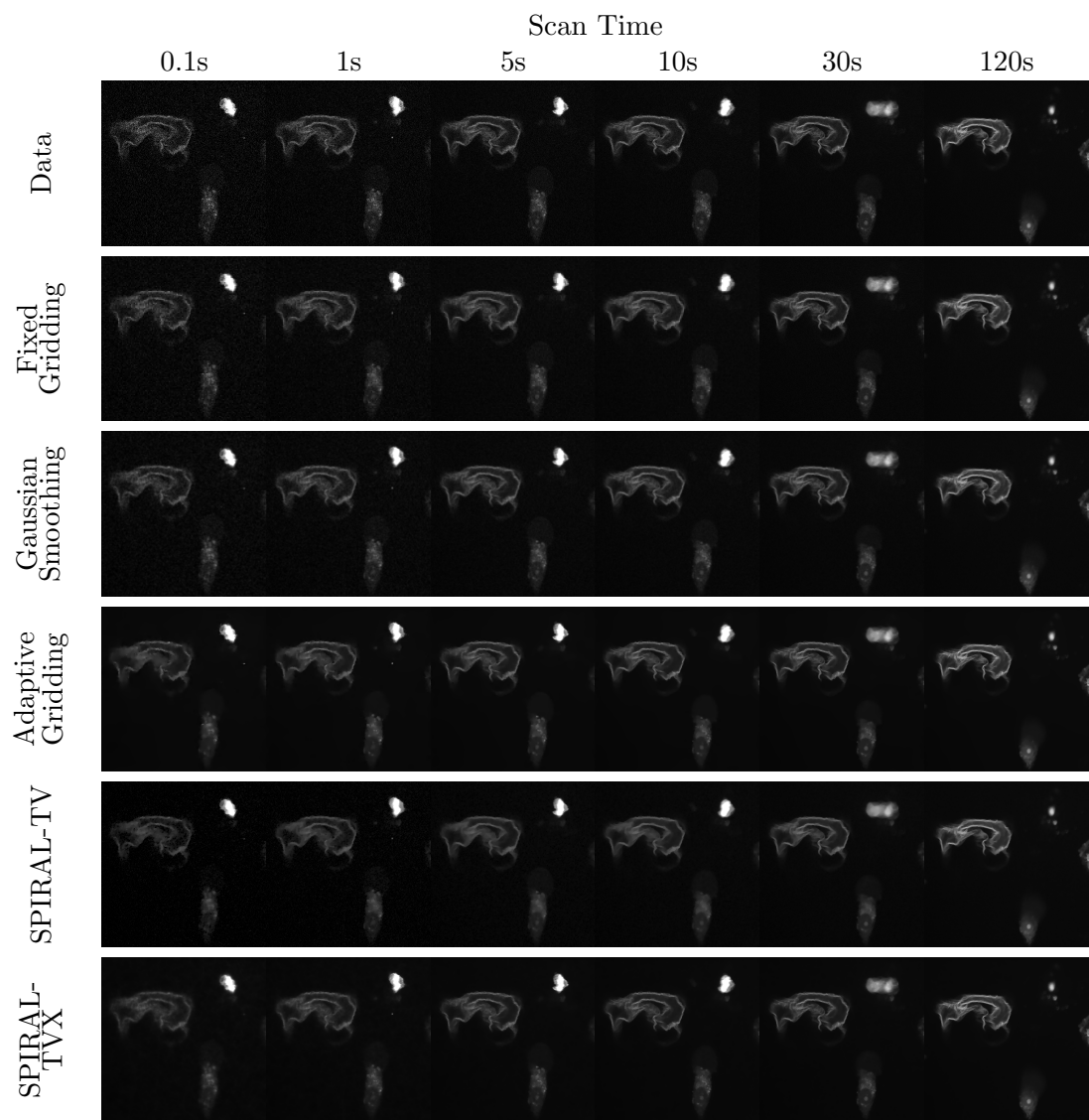


FIGURE 5.6: Results on the Mouse Embryonic Stem Cells dataset, showing all methods and scan times

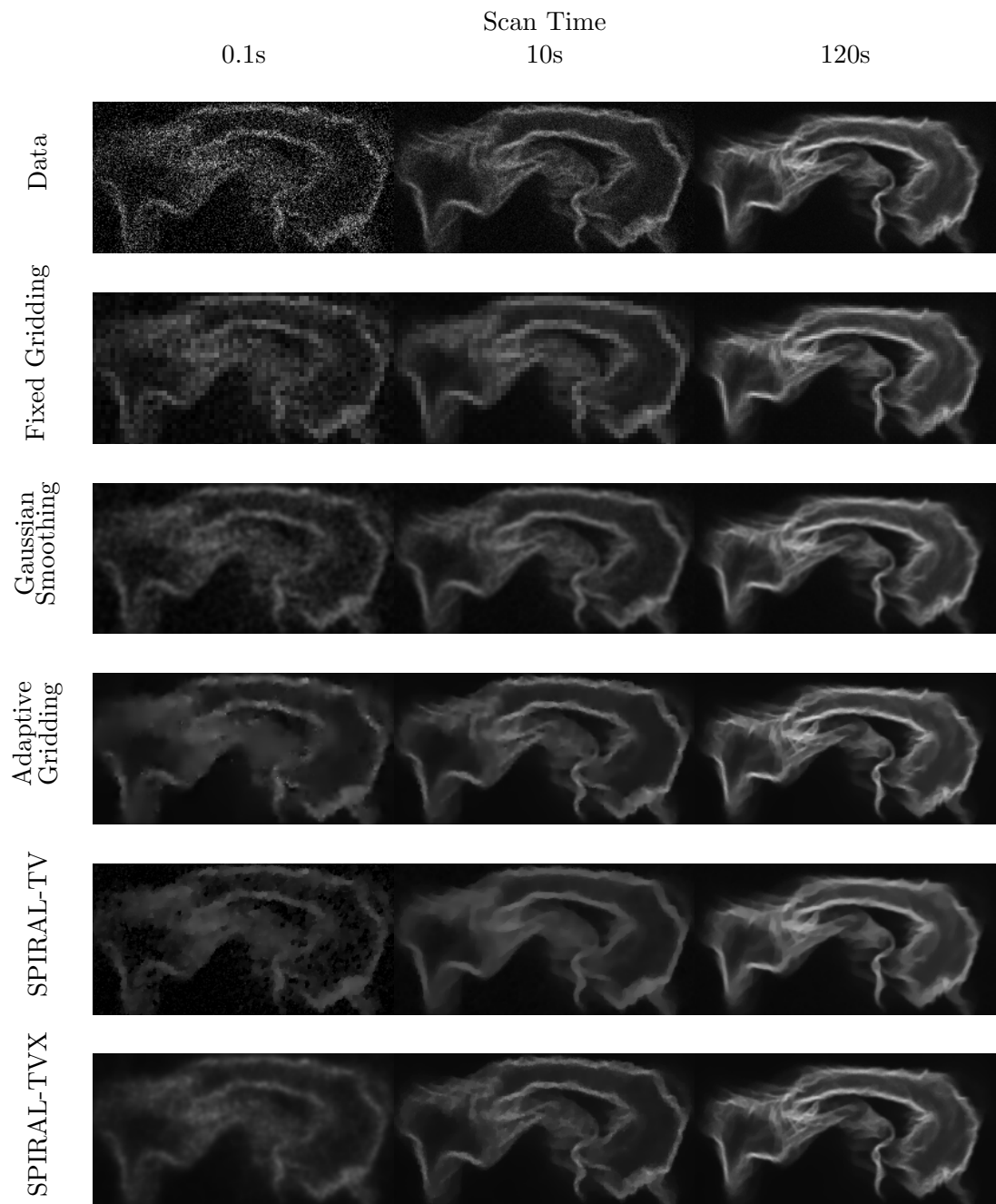


FIGURE 5.7: An interesting ROI on the Mouse Embryonic Stem Cells dataset, showing all methods for a subset of scan times

6

Conclusion

This thesis has addressed significant gaps in the current state of computational imaging by providing advances in three key areas that together form the computational imaging framework: image models, imaging hardware, and reconstruction algorithms. An itemized list of contributions, with citations to resulting publications, is provided in the next section. While this work offers solutions to many outstanding problems, it simultaneously reveals several avenues for future work. I close this chapter with directions for further exploration.

6.1 Summary of Contributions

The following summarizes my key contributions and directions for future work.

- I introduced a novel, straightforward to implement, joint spatio-temporal compressive imaging system based on compressive coded apertures. This solution is able to capture the type of incoherent measurements required in compressed sensing. I have proven bounds on the performance of this system, and showed it to be effective in a set of numerical experiments. [27].

- I extended our compressive coded aperture to adaptive video reconstruction using an optical flow formulation. This approach allows our imaging system to be adaptive to scene content and offers enhanced reconstruction accuracy by using a more complex model of scene motion [31].
- I proposed a novel reconstruction algorithm for Poisson noise which arises in photon-limited imaging. I demonstrated global convergence of the algorithm, and showed favorable reconstruction results in a limited-angle tomography numerical simulation [33]. Additionally, I showed that this approach is relatively robust to selection of tuning parameters within the method, which is in contrast to the popular alternating direction method of multipliers (ADMM) method which necessitate good selection of an augmented Lagrangian parameter [37].
- I used our SPIRAL algorithm as a method for analyzing photon-limited imaging data for quantitative tissue analysis [37, 38]. In collaboration with Prof. Nimmi Ramanujam’s research group, I have demonstrated that our algorithms can be used for the robust identification of tumor nuclei, and hence act as a method for intraoperative margin assessment.
- I also used SPIRAL was also used for understanding fundamental performance limits of compressed sensing in Poisson noise [73, 139]. I demonstrated via numerical experiments that there exists a fundamental tradeoff in the number of measurements (measurement diversity) versus the SNR per measurement (measurement quality) that arises due to photon flux preservation constraints in the realistic modeling of compressive imaging systems at low light levels.
- I developed a novel reparameterization of the SPIRAL reconstruction algorithm, and used a cross-validation framework to achieve state-of-the-art results on multiphoton fluorescence microscopy data, see Chapter 5. Not only does this

demonstrate the wide applicability of the SPIRAL approach, but also shows that as a practical consequence, great reduction in scan times are possible by using our algorithms over competing approaches often used in the microscopy community.

- By formulating sparse dictionary learning as a penalized maximum likelihood reconstruction, I was able to leverage our SPIRAL technique to solve an important subproblem when estimating the sparse coefficients [118].
- I developed a suite of reconstruction algorithms that take advantage of known bounds on the signal intensity in order to improve performance in imaging and video applications [25, 28, 29, 30]. When such side information is known, I showed that incorporating these constraints improves performance with negligible change in the computational cost of the methods.

6.2 Future Work

Although this thesis proposes solutions to many important problems in signal processing, it necessarily opens the door for further exploration. Here I discuss several avenues of interest, organized according to the three key areas identified in Sec. 1.13.

Image and scene models Many of the scene models adopted in this thesis allow for a careful theoretical analysis of performance. However, in many real-world applications, more complex models usually yields empirical gains in reconstruction accuracy. From a theoretical perspective, these gains are difficult to analyze and hence poorly understood. For example, the optical flow-based reconstruction techniques used in [31] resulted in improved performance, yet do not come equipped with traditional compressed-sensing performance guarantees.

Additionally, other low-dimensional structures can be used to our advantage. One such example are subspace models or union-of-subspace models that have been shown to be useful for recovering missing data [140, 141]. We outline a particular example of how subspace tracking methods can be used for background estimation in photon limited video in Sec. 6.3 below.

Imaging hardware We have demonstrated that by designing novel camera systems, we may reduce the number of measurements required to reconstruct salient details in dynamic scenes. We have shown this via numerical experiments, and also by theoretical analysis using the tools from compressed sensing. However, this opens the door to exploring new ways of designing coded aperture mask patterns. We have extended our designs to focus sensing power on regions of the scene that contain motion [31], however it is unclear if these techniques are optimal. This question is especially interesting when reconstruction is not our primary goal. It may be desirable to design mask patterns with other tasks in mind, such as target identification or scene classification.

One exciting avenue in coded aperture design is designing the masks in such a way as to obtain a coarse low-resolution estimate very quickly (often by performing a convolution), which can be used as an excellent initialization for an iterative algorithm, or can be used to estimate the salient motion in the scene to aid in the reconstruction. Such ideas are based on the use of a low resolution Hadamard code in [142], however their architecture relies on sequential measurements using the Rice single-pixel camera, rather than the snapshot acquisition capable using our compressive coded apertures.

Reconstruction algorithms As we design imaging systems that collect large datasets, such as videos, it becomes computationally intractable to process the data using traditional batch algorithms. Furthermore, batch algorithms are unable

to produce estimates on-the-fly, which precludes their use in delay sensitive applications, such as video surveillance. Hence there is a clear need for designing effective online reconstruction techniques. We show how the techniques described in this thesis can be used to form the basis of novel online methods for background estimation in photon limited video in Sec. 6.3 below.

However, a solid theoretical understanding of the performance of many online algorithms is lacking, as well as automated methods for selecting many parameters of the method which will be needed for a successful application of the methodology. All of these areas are fertile grounds to be explored.

Additionally, many of the extensions of SPIRAL have used an exponential transformation (such as SPIRAL-TVX described in Sec. 5.4). It is unclear how this may impact some of the theoretical guarantees associated with the algorithm. Furthermore, generalizations of such a transformation can be considered that may have other desirable properties, such as having objective functions with bounded curvature, and hence are Lipschitz continuously differentiable over the entire feasible domain. Using such transformations in conjunction with robust penalization strategies (such as total variation) modify the effect of these regularization schemes, and further study is needed to understand their properties.

6.3 Online Subspace Tracking from Streaming Poisson Data

In many applications, the dimensionality of the ambient space of the data often belies the true complexity of the signals of interest we wish to elicit. That is, the pertinent information contained in a dataset has much fewer degrees of freedom than the ambient dimension would imply. Such is the case in a low-dimensional linear or subspace model. This model assumes that the data, which live in an n -

dimensional Euclidean space, predominantly lie within the span of a set of $d \ll n$ vectors. Notationally, we say that the data vector $f \in \mathbf{R}^n$ can be well approximated by a vector $v \in \mathbf{R}^n$ that lies in a d -dimensional subspace $\mathbf{S} \subset \mathbf{R}^n$, meaning that v can be written as $v = Ua$, where the span of the columns of the matrix $U \in \mathbf{R}^{n \times d}$ form the subspace \mathbf{S} , and $a \in \mathbf{R}^d$ are the subspace coefficients.

This model is often successfully employed when we have a set of T vectors $\{x_t\}_{t=1}^T$ that can be approximated by a set of vectors $\{v_t\}_{t=1}^T$ that share the same subspace representation, but may have different subspace coefficients $\{a_t\}_{t=1}^T$. Grouping the vectors into respective matrices $F \in \mathbf{R}^{n \times T}$, $V \in \mathbf{R}^{n \times T}$, and $A \in \mathbf{R}^{d \times T}$, we see that this model is equivalent to approximating the data with a matrix that has a rank- d matrix factorization, $F \approx V = UA$, the foundation of principal component analysis (PCA).

The principal interest of this work is the application of subspace models to the analysis of photon-limited video. The problem of subspace tracking has been examined before in the context of missing data in Gaussian noise [140], as well as a modification that uses an ℓ_1 -based objective to provide robustness to outliers [143]. Some of the work on foreground estimation can be thought of as an online extension of the work on robust PCA [144].

In this work we would adopt a Poisson observation model for the frames:

$$y_t \sim \text{Poisson}(f_t), \quad t = 1, \dots, T,$$

where the $f_t \in \mathbf{R}_+^n$ are the nonnegative intensities at the detector, and the $y_t \in \mathbf{Z}_+^n$ are our observation vectors of nonnegative integer photon counts. Using matrix representations of the observations and intensities, we could instead write $Y \sim \text{Poisson}(F)$.

In the batch case, we estimate our subspace by

$$\begin{aligned}\widehat{U} &= \arg \min_{U \in \mathbf{R}^{n \times d}} \Phi(U) \\ \text{subject to } U^\top U &= I_d,\end{aligned}$$

where our cost function is defined as

$$\begin{aligned}\Phi(U) &:= \min_{A \in \mathbf{R}^{d \times T}} \phi(UA) \\ \text{subject to } UA &\geq 0,\end{aligned}$$

where

$$\phi(F) := \sum_{t=1}^T \sum_{i=1}^n [F_{i,t} - Y_{i,t} \log(F_{i,t} + \beta)] \propto -\log p(Y | F).$$

In the definition of ϕ above, $\beta > 0$ is a small parameter that ensures that f is Lipschitz continuously differentiable (see [33, Lemma 1]).

We can modify the above batch algorithm to work online by using a stochastic gradient descent approach by splitting the objective across time:

$$\phi(F) = \sum_{t=1}^T \phi_t(f_t), \quad \phi_t(f) := \sum_{i=1}^n f_i - [y_t]_i \log(f_i + \beta).$$

A similar framework is adopted in [140] for tracking a subspace from observations with missing entries possibly corrupted by Gaussian noise.

The algorithm then proceeds as follows. Given a current subspace estimate \widehat{U}_t , we estimate the subspace coefficients a_t using the current observation y_t :

$$\begin{aligned}\widehat{a}_t &= \arg \min_{a \in \mathbf{R}^d} \phi_t(\widehat{U}_t a) \\ \text{subject to } \widehat{U}_t a &\geq 0.\end{aligned}\tag{6.1}$$

The SPIRAL algorithm described in Chapter 3 can be modified to solve the minimization in (6.1). Next we update our subspace by traveling along a geodesic of the

Grassmannian a distance controlled by a step size parameter η_t , accomplished via the update

$$\widehat{U}_{t+1} = \widehat{U}_t + \left\{ (\cos(\sigma\eta_t) - 1) \frac{\widehat{v}_t}{\|\widehat{v}_t\|_2} + (\sin(\sigma\eta_t)) \frac{\widetilde{r}_t}{\|\widetilde{r}_t\|_2} \right\} \frac{\widehat{a}_t^\top}{\|\widehat{a}_t\|_2},$$

where $\widehat{v}_t = \widehat{U}_t \widehat{a}_t$, $\widetilde{r}_t := (I - \widehat{U}_t \widehat{U}_t^\top) r_t$, with r_t being the residual vector

$$[r_t]_i = \frac{[y_t]_i}{e_i^\top \widehat{U}_t \widehat{a}_t + \beta} - 1,$$

and $\sigma = \|\widehat{v}_t\|_2 \|\widetilde{r}_t\|_2$. Notice that the update to the subspace is only a rank-1 matrix, making this update procedure computationally efficient.

6.3.1 Preliminary Experimental Results

Here we present promising initial experimental results. This experiment shows that the proposed method is able to successfully track the background of a video, even under changes in illumination conditions. This video is divided into three time epochs, one with the background lights on, an intermediate period with the lights off, then a third where the lights are turned back on. Additionally, there are a few people walking through the frames, in all three epochs of the video. In Fig. 6.1, we show three frames of the video sequence (frames 368, 1024, and 1400), which are each taken from one of these epochs. We compare against a simple averaging method to eliminate noise. Note that the data is extremely noisy we have an average photon count of 4 in each image for the duration of the video. Using the subspace tracking formulation, we can estimate the background by removing the people walking in the video. However, we can be very robust to changes in the illumination. Notice the ceiling lights - they accurately track the ground truth. However, a simple averaging approach yields a result that is a superposition between the two illumination conditions.

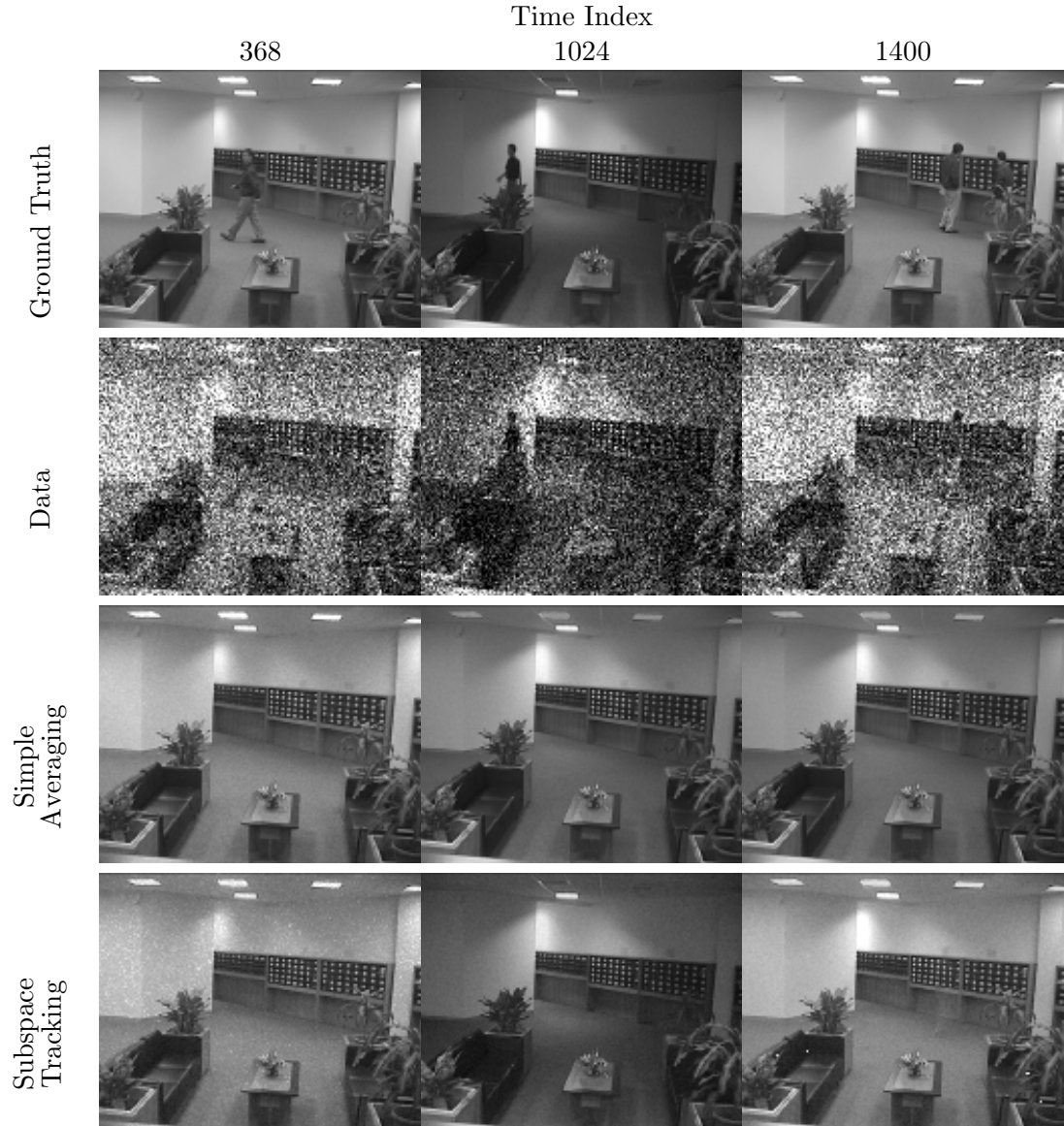


FIGURE 6.1: Preliminary results on the proposed subspace tracking method. Notice how the subspace tracking method is able to be more robust to illumination changes versus averaging, yet is able to remove the people in the foreground.

6.3.2 Future Work Conclusions

We have proposed a method for tracking time-evolving subspaces from Poisson data. Preliminary experiments suggest that this is an effective method for background estimation in video. Our future work includes more advanced modeling of the fore-

ground, and investigating alternative formulations and approaches to solve the resulting subproblems.

Bibliography

- [1] D. J. Brady, P. Potuluri, B. Guenther, E. Cull, Y. Qi, and K. Chapman, “Point of dispense drug verification using coded aperture Raman spectroscopy and image analysis,” in *Applied Industrial Optics: Spectroscopy, Imaging and Metrology*. Optical Society of America, 2010.
- [2] M. Brogi, I. A. G. Snellen, R. J. d. Kok, S. Albrecht, J. Birkby, and E. J. W. de Mooij, “The signature of orbital motion from the dayside of the planet τ Boötis b,” *Nature*, vol. 486, no. 7404, pp. 502–504, Jun. 2012.
- [3] K. Krishnamurthy, “Spectral image processing theory and methods: Reconstruction, target detection, and fundamental performance bounds,” Ph.D., Duke University, 2011.
- [4] H. H. Barrett and K. J. Myers, *Foundations of Image Science*. Wiley-Interscience, 2004.
- [5] Y. Chi, L. L. Scharf, A. Pezeshki, and R. Calderbank, “Sensitivity to basis mismatch in compressed sensing,” *IEEE Transactions on Signal Processing*, vol. 59, no. 5, pp. 2182–2195, May 2011.
- [6] E. J. Candès, J. Romberg, and T. Tao, “Robust uncertainty principles: Exact signal reconstruction from highly incomplete frequency information,” *IEEE Transactions on Information Theory*, vol. 52, no. 2, pp. 489–509, 2006.
- [7] E. J. Candès and T. Tao, “Near-optimal signal recovery from random projections: Universal encoding strategies?” *IEEE Transactions on Information Theory*, vol. 52, no. 12, pp. 5406–5425, December 2006.
- [8] D. L. Donoho, “Compressed sensing,” *IEEE Transactions on Information Theory*, vol. 52, no. 4, pp. 1289–1306, 2006.
- [9] J. A. Tropp, “Just relax: Convex programming methods for identifying sparse signals in noise,” *IEEE Transactions on Information Theory*, vol. 52, no. 3, pp. 1030–1051, Mar. 2006.

- [10] J. Romberg, “Compressive sensing by random convolution,” *SIAM Journal on Imaging Sciences*, vol. 2, no. 4, p. 1098, 2009.
- [11] E. J. Candès, “Modern statistical estimation via oracle inequalities,” *Acta Numerica*, vol. 15, pp. 257–325, 2006.
- [12] D. L. Donoho and I. M. Johnstone, “Asymptotic minimaxity of wavelet estimators with sampled data,” *Statistica Sinica*, vol. 9, no. 1, pp. 1–32, January 1999.
- [13] S. J. Wright, R. D. Nowak, and M. A. T. Figueiredo, “Sparse reconstruction by separable approximation,” *IEEE Transactions on Signal Processing*, vol. 57, no. 7, pp. 2479–2493, 2009.
- [14] E. J. Candès and T. Tao, “Decoding by linear programming,” *IEEE Transactions on Information Theory*, vol. 51, no. 12, pp. 4203–4215, 2005.
- [15] M. B. Wakin, J. N. Laska, M. F. Duarte, D. Baron, S. Sarvotham, K. F. Kelly, and R. G. Baraniuk, “An architecture for compressive imaging,” in *2006 IEEE International Conference on Image Processing*. IEEE, Oct. 2006, pp. 1273–1276.
- [16] W. U. Bajwa, J. D. Haupt, G. M. Raz, S. J. Wright, and R. D. Nowak, “Toeplitz-structured compressed sensing matrices,” in *IEEE/SP 14th Workshop on Statistical Signal Processing, 2007. SSP ’07*, Madison, WI, USA, 2007, pp. 294–298.
- [17] E. J. Candès and T. Tao, “The Dantzig selector: Statistical estimation when p is much larger than n ,” *The Annals of Statistics*, vol. 35, no. 6, pp. 2313–2351, Dec. 2007.
- [18] J. D. Haupt and R. D. Nowak, “Signal reconstruction from noisy random projections,” *IEEE Transactions on Information Theory*, vol. 52, no. 9, pp. 4036–4048, Sep. 2006.
- [19] Z. T. Harmany, R. F. Marcia, and R. M. Willett, “Sparse Poisson intensity reconstruction algorithms,” in *2009 IEEE/SP 15th Workshop on Statistical Signal Processing, SSP ’09*, Cardiff, United Kingdom, 2009, pp. 634–637.
- [20] R. M. Willett and R. D. Nowak, “Multiscale Poisson intensity and density estimation,” *IEEE Transactions on Information Theory*, vol. 53, no. 9, pp. 3171–3187, 2007.

- [21] M. S. Crouse, R. D. Nowak, and R. G. Baraniuk, “Wavelet-based statistical signal processing using hidden Markov models,” *IEEE Transactions on Signal Processing*, vol. 46, no. 4, pp. 886–902, Apr. 1998.
- [22] R. G. Baraniuk, V. Cevher, M. F. Duarte, and C. Hegde, “Model-based compressive sensing,” *IEEE Transactions on Information Theory*, vol. 56, no. 4, pp. 1982–2001, 2010.
- [23] S. Ji, Y. Xue, and L. Carin, “Bayesian compressive sensing,” *IEEE Transactions on Signal Processing*, vol. 56, no. 6, pp. 2346–2356, Jun. 2008.
- [24] R. F. Marcia, Z. T. Harmany, and R. M. Willett, “Compressive coded aperture imaging,” in *Proceedings of SPIE Computational Imaging VII*, San Jose, CA, USA, 2009, pp. 72460G–72460G–13.
- [25] ——, “Compressive coded apertures for high-resolution imaging,” *Proceedings of SPIE*, vol. 7723, no. 1, pp. 772304–772304–11, Apr. 2010.
- [26] R. F. Marcia, R. M. Willett, and Z. T. Harmany, “Compressive optical imaging: Architectures and algorithms, compressive optical imaging: Architectures and algorithms,” in *Optical and Digital Image Processing: Fundamentals and Applications, Optical and Digital Image Processing*, G. Cristobal, P. Schelkens, and H. Thienpont, Eds. Wiley-VCH Verlag GmbH & Co, Apr. 2011, pp. 485–505.
- [27] Z. T. Harmany, R. F. Marcia, and R. M. Willett, “Spatio-temporal compressed sensing with coded apertures and keyed exposures,” *ArXiv e-prints*, Nov. 2011.
- [28] Z. T. Harmany, D. O. Thompson, R. M. Willett, and R. F. Marcia, “Gradient projection for linearly constrained convex optimization in sparse signal recovery,” in *2010 17th IEEE International Conference on Image Processing (ICIP)*. IEEE, Sep. 2010, pp. 3361–3364.
- [29] D. O. Thompson, Z. T. Harmany, and R. F. Marcia, “Sparse video recovery using linearly constrained gradient projection,” in *2011 IEEE International Conference on Acoustics, Speech and Signal Processing (ICASSP)*. IEEE, May 2011, pp. 1329–1332.
- [30] J. Hernandez, Z. T. Harmany, D. O. Thompson, and R. F. Marcia, “Bounded gradient projection methods for sparse signal recovery,” in *2011 IEEE International Conference on Acoustics, Speech and Signal Processing (ICASSP)*. IEEE, May 2011, pp. 949–952.

- [31] Z. T. Harmany, A. Oh, R. F. Marcia, and R. M. Willett, “Motion-adaptive compressive coded apertures,” *Proceedings of SPIE*, vol. 8165, no. 1, pp. 81 651C–81 651C–5, Sep. 2011.
- [32] Z. T. Harmany, R. F. Marcia, and R. M. Willett, “Sparsity-regularized photon-limited imaging,” in *2010 IEEE International Symposium on Biomedical Imaging: From Nano to Macro*. IEEE, Apr. 2010, pp. 772–775.
- [33] ——, “This is SPIRAL-TAP: Sparse Poisson Intensity Reconstruction ALgorithms—Theory and Practice,” *IEEE Transactions on Image Processing*, vol. 21, no. 3, pp. 1084–1096, Mar. 2012.
- [34] ——, “SPIRAL out of convexity: Sparsity-regularized algorithms for photon-limited imaging,” *Proceedings of SPIE*, vol. 7533, no. 1, pp. 75 330R–75 330R–12, Feb. 2010.
- [35] R. M. Willett, Z. T. Harmany, and R. F. Marcia, “Poisson image reconstruction with total variation regularization,” in *2010 17th IEEE International Conference on Image Processing (ICIP)*. IEEE, Sep. 2010, pp. 4177–4180.
- [36] J.-L. Starck, M. Elad, and D. L. Donoho, “Image decomposition via the combination of sparse representations and a variational approach,” *IEEE Transactions on Image Processing*, vol. 14, no. 10, pp. 1570–1582, 2005.
- [37] Z. T. Harmany, J. Mueller, J. Q. Brown, N. Ramanujam, and R. M. Willett, “Tissue quantification in photon-limited microendoscopy,” *Proceedings of SPIE*, vol. 8138, no. 1, pp. 81 380F–81 380F–6, Sep. 2011.
- [38] Z. T. Harmany, X. Jiang, and R. M. Willett, “The value of multispectral observations in photon-limited quantitative tissue analysis,” in *2012 IEEE Statistical Signal Processing Workshop (SSP)*, 2012.
- [39] M. Shankar, R. Willett, N. Pitsianis, T. Schulz, R. Gibbons, R. T. Kolste, J. Carriere, C. Chen, D. Prather, and D. Brady, “Thin infrared imaging systems through multichannel sampling,” *Applied Optics*, vol. 47, no. 10, pp. B1–B10, 2008.
- [40] A. F. Coskun, I. Sencan, T.-W. Su, and A. Ozcan, “Lensless wide-field fluorescent imaging on a chip using compressive decoding of sparse objects,” *Optics Express*, vol. 18, no. 10, pp. 10 510–10 523, 2010.
- [41] L. C. Potter, E. Ertin, J. T. Parker, and M. Cetin, “Sparsity and compressed sensing in radar imaging,” *Proceedings of the IEEE*, vol. 98, no. 6, pp. 1006–1020, 2010.

- [42] J. Gu, S. K. Nayar, E. Grinspun, P. N. Belhumeur, and R. Ramamoorthi, “Compressive structured light for recovering inhomogeneous participating media,” in *Proceedings of the European Conference on Computer Vision*, 2008.
- [43] M. Mohtashemi, H. Smith, D. Walburger, F. Sutton, and J. Diggans, “Sparse sensing dna microarray-based biosensor: Is it feasible?” in *2010 IEEE Sensors Applications Symposium*, Feb 2010, pp. 127 –130.
- [44] M. Sheikh, O. Milenkovic, and R. Baraniuk, “Designing compressive sensing dna microarrays,” in *2nd IEEE International Workshop on Computational Advances in Multi-Sensor Adaptive Processing, 2007*, December 2007, pp. 141 –144.
- [45] M. Lustig, D. Donoho, and J. M. Pauly, “Sparse MRI: The application of compressed sensing for rapid MR imaging,” *Magnetic Resonance in Medicine*, vol. 58, no. 6, pp. 1182–1195, December 2007.
- [46] A. Gurbuz, J. McClellan, and W. Scott, “A compressive sensing data acquisition and imaging method for stepped frequency GPRs,” *IEEE Transactions on Signal Processing*, vol. 57, no. 7, pp. 2640 –2650, July 2009.
- [47] P. Ye, J. Paredes, G. Arce, Y. Wu, C. Chen, and D. Prather, “Compressive confocal microscopy,” in *IEEE International Conference on Acoustics, Speech and Signal Processing, 2009*, April 2009, pp. 429 –432.
- [48] J. Bobin, J.-L. Starck, and R. Ottensamer, “Compressed sensing in astronomy,” *Selected Topics in Signal Processing, IEEE Journal of*, vol. 2, no. 5, pp. 718 –726, October 2008.
- [49] M. F. Duarte, M. A. Davenport, D. Takhar, J. N. Laska, T. Sun, K. F. Kelly, and R. G. Baraniuk, “Single pixel imaging via compressive sampling,” *IEEE Signal Processing Magazine*, vol. 25, no. 2, pp. 83–91, 2008.
- [50] J. G. Ables, “Fourier transform photography: a new method for X-ray astronomy,” *Proceedings of the Astronomical Society of Australia*, vol. 1, p. 172, 1968.
- [51] R. H. Dicke, “Scatter-hole cameras for X-rays and gamma-rays,” *Astrophysical Journal*, vol. 153, pp. L101–L106, 1968.
- [52] E. Caroli, J. B. Stephen, G. D. Cocco, L. Natalucci, and A. Spizzichino, “Coded aperture imaging in X- and gamma-ray astronomy,” *Space Science Reviews*, vol. 45, pp. 349–403, 1987.

- [53] G. Skinner, “Imaging with coded-aperture masks,” *Nucl. Instrum. Methods Phys. Res.*, vol. 221, pp. 33–40, Mar. 1984.
- [54] R. Accorsi, F. Gasparini, and R. C. Lanza, “A coded aperture for high-resolution nuclear medicine planarimaging with a conventional anger camera: experimental results,” *IEEE Trans. Nucl. Sci.*, vol. 28, pp. 2411–2417, 2001.
- [55] G. R. Gindi, J. Arendt, H. H. Barrett, M. Y. Chiu, A. Ervin, C. L. Giles, M. A. Kuojoory, E. L. Miller, and R. G. Simpson, “Imaging with rotating slit apertures and rotating collimators,” *Medical Physics*, vol. 9, pp. 324–339, 1982.
- [56] S. R. Meikle, R. R. Fulton, S. Eberl, M. Bahlbom, K. Wong, and M. J. Fulham, “An investigation of coded aperture imaging for small animal SPECT,” *IEEE Trans. Nucl. Sci.*, vol. 28, pp. 816–821, 2001.
- [57] A. Levin, R. Fergus, F. Durand, and W. T. Freeman, “Image and depth from a conventional camera with a coded aperture,” in *Proc. of Intl. Conf. Comp. Graphics. and Inter. Tech.*, 2007.
- [58] A. Agrawal and Y. Xu, “Coded exposure deblurring: Optimized codes for psf estimation and invertibility,” in *IEEE Computer Vision and Pattern Recognition*, 2009.
- [59] R. Raskar, A. Agrawal, and J. Tumblin, “Coded exposure photography: Motion deblurring using fluttered shutter,” in *ACM Transactions on Graphics (TOG)*, ser. SIGGRAPH ’06. New York, NY, USA: ACM, 2006, pp. 795—804.
- [60] A. Veeraraghavan, D. Reddy, and R. Raskar, “Coded strobing photography: Compressive sensing of high speed periodic videos,” *IEEE Transactions on Pattern Analysis and Machine Intelligence*, vol. 33, no. 4, pp. 671–686, 2011.
- [61] R. F. Marcia and R. M. Willett, “Compressive coded aperture superresolution image reconstruction,” in *Proc. IEEE Int. Conf. Acoust., Speech, Signal Processing (ICASSP)*, 2008.
- [62] ——, “Compressive coded aperture video reconstruction,” in *Proceedings of the 16th European Signal Processing Conference, EUSIPCO 2008*, Lausanne, Switzerland, August 2008.
- [63] N. J. A. Sloane and M. Harwit, “Masks for Hadamard transform optics, and weighing designs,” *Appl. Opt.*, vol. 15, no. 1, p. 107, 1976.

- [64] A. Ashok and M. A. Neifeld, “Pseudorandom phase masks for superresolution imaging from subpixel shifting,” *Appl. Opt.*, vol. 46, no. 12, pp. 2256–2268, 2007.
- [65] S. R. Gottesman and E. E. Fenimore, “New family of binary arrays for coded aperture imaging,” *Appl. Opt.*, vol. 28, 1989.
- [66] E. Candès, “Compressive sampling,” in *Int. Congress of Mathematics*, vol. 3, 2006, pp. 1433–1452.
- [67] E. J. Candès, J. K. Romberg, and T. Tao, “Stable signal recovery from incomplete and inaccurate measurements,” *Communications on Pure and Applied Mathematics*, vol. 59, no. 8, pp. 1207–1223, 2006.
- [68] J. D. Haupt, W. U. Bajwa, G. M. Raz, and R. D. Nowak, “Toeplitz compressed sensing matrices with applications to sparse channel estimation,” *IEEE Transactions on Information Theory*, vol. 56, no. 11, pp. 5862–5875, 2010.
- [69] R. Robucci, J. D. Gray, L. K. Chiu, J. Romberg, and P. Hasler, “Compressive sensing on a CMOS separable-transform image sensor,” *Proceedings of the IEEE*, vol. 98, no. 6, pp. 1089–1101, 2010.
- [70] V. Majidzadeh, L. Jacques, A. Schmid, P. Vandergheynst, and Y. Leblebici, “A (256*256) pixel 76.7mW CMOS imager/compressor based on real-time in-pixel compressive sensing,” in *IEEE International Symposium on Circuits and Systems*, 2010, pp. 2956–2959.
- [71] W. Chi and N. George, “Phase-coded aperture for optical imaging,” *Optics Communications*, vol. 282, pp. 2110–2117, 2009.
- [72] J. Haupt and R. Nowak, “Compressive sampling vs. conventional imaging,” in *Proc. IEEE Intl. Conf. on Imaging Processing*, 2006, pp. 1269–1272.
- [73] M. Raginsky, R. M. Willett, Z. T. Harmany, and R. F. Marcia, “Compressed sensing performance bounds under Poisson noise,” *IEEE Transactions on Signal Processing*, vol. 58, no. 8, pp. 3990–4002, August 2010.
- [74] M. A. T. Figueiredo, R. D. Nowak, and S. J. Wright, “Gradient projection for sparse reconstruction: Application to compressed sensing and other inverse problems,” *IEEE Journal of Selected Topics in Signal Processing*, vol. 1, no. 4, pp. 586–597, Dec. 2007.

- [75] R. G. Baraniuk, M. A. Davenport, R. A. DeVore, and M. B. Wakin, “A simple proof of the restricted isometry property for random matrices,” *Constructive Approximation*, vol. 28, no. 3, pp. 253–263, 2008.
- [76] L. Rudin, S. Osher, and E. Fatemi, “Nonlinear total variation based noise removal algorithms,” *Physica D: Nonlinear Phenomena*, vol. 60, no. 1-4, pp. 259 – 268, 1992.
- [77] E. J. Candès and D. L. Donoho, “New tight frames of curvelets and optimal representations of objects with piecewise C^2 singularities,” *Communications on Pure and Applied Mathematics*, vol. 57, no. 2, pp. 219–266, 2004.
- [78] NASA JPL Space Science Institute. (2008) Pia10497: Saturn in recline. <Http://photojournal.jpl.nasa.gov/catalog/PIA10497>.
- [79] L. Applebaum, W. U. Bajwa, M. F. Duarte, and R. Calderbank, “Asynchronous code-division random access using convex optimization,” *Physical Communication*, vol. 5, no. 2, pp. 129–147, Jun. 2012.
- [80] J. W. Stayman, N. Subotic, and W. Buller, “An analysis of coded aperture acquisition and reconstruction using multi-frame code sequences for relaxed optical design constraints,” in *Proceedings SPIE 7468*, 2009.
- [81] R. S. Varga, *Geršgorin and His Circles*. Berlin, Germany: Springer-Verlag, 2004.
- [82] D. L. Snyder and M. I. Miller, *Random Point Processes in Time and Space*, 2nd ed. Springer, 1991.
- [83] R. M. Willett and M. Raginsky, “Performance bounds on compressed sensing with Poisson noise,” in *IEEE International Symposium on Information Theory, 2009. ISIT 2009.*, Seoul, South Korea, 2009, pp. 174–178.
- [84] D. J. Lingenfelter, J. A. Fessler, and Z. He, “Sparsity regularization for image reconstruction with Poisson data,” in *Proceedings of SPIE Computational Imaging VII*, San Jose, CA, USA, 2009, pp. 72460F–72460F–10.
- [85] J. A. Fessler and H. Erdoğan, “A paraboloidal surrogates algorithm for convergent penalized-likelihood emission image reconstruction,” in *1998. Conference Record. 1998 IEEE Nuclear Science Symposium*, vol. 2, Toronto, Ontario, Canada, 1998, pp. 1132–1135.

- [86] F. J. Anscombe, “The transformation of Poisson, binomial and negative-binomial data,” *Biometrika*, vol. 35, no. 3/4, pp. 246–254, Dec. 1948.
- [87] P. Fryzlewicz, “Data-driven wavelet-Fisz methodology for nonparametric function estimation,” *Electronic Journal of Statistics*, vol. 2, pp. 863–896, 2008.
- [88] P. Fryzlewicz and G. P. Nason, “A Haar-Fisz algorithm for Poisson intensity estimation,” *Journal of Computational and Graphical Statistics*, vol. 13, no. 3, pp. 621–638, 2004.
- [89] D. Donoho, “Nonlinear wavelet methods for recovery of signals, densities, and spectra from indirect and noisy data,” in *Proceedings of Symposia in Applied Mathematics*, American Mathematical Society, 1993, pp. 173–205.
- [90] C. Kervrann and A. Trubuil, “An adaptive window approach for Poisson noise reduction and structure preserving in confocal microscopy,” in *IEEE International Symposium on Biomedical Imaging: Nano to Macro, 2004.*, vol. 1, 2004, pp. 788–791.
- [91] M. Jansen, “Multiscale Poisson data smoothing,” *Journal of the Royal Statistical Society, series B: Statistical methodology*, vol. 68, no. 1, p. 27, 2006.
- [92] E. Kolaczyk, “Wavelet shrinkage estimation of certain poisson intensity signals using corrected thresholds,” *Statistica Sinica*, vol. 9, pp. 119–135, 1999.
- [93] R. Willett, “Multiscale-analysis of photon-limited astronomical images,” in *Statistical Challenges in Modern Astronomy IV*, ser. Astronomical Society of the Pacific Conference Series, vol. 371, 2007.
- [94] B. Zhang, J. M. Fadili, and J.-L. Starck, “Wavelets, ridgelets, and curvelets for Poisson noise removal,” *IEEE Transactions on Image Processing*, vol. 17, no. 7, pp. 1093–1108, 2008.
- [95] R. D. Nowak and E. D. Kolaczyk, “A statistical multiscale framework for Poisson inverse problems,” *IEEE Transactions on Information Theory*, vol. 46, no. 5, pp. 1811–1825, 2000.
- [96] R. Nowak and E. Kolaczyk, “A multiscale map estimation method for Poisson inverse problems,” in *32nd Asilomar Conf. Signals, Systems, and Comp.*, vol. 2, 1998, pp. 1682–1686.
- [97] E. Kolaczyk and R. Nowak, “Multiscale likelihood analysis and complexity penalized estimation,” *Ann. Statist.*, vol. 32, pp. 500–527, 2004.

- [98] E. Kolaczyk and R. Nowak, “Multiscale generalised linear models for nonparametric function estimation,” *Biometrika*, vol. 92, no. 1, pp. 119–133, 2005.
- [99] R. M. Willett and R. D. Nowak, “Platelets: A multiscale approach for recovering edges and surfaces in photon-limited medical imaging,” *IEEE Transactions on Medical Imaging*, vol. 22, no. 3, pp. 332–350, 2003.
- [100] T. Chan and J. Shen, *Image Processing And Analysis: Variational, PDE, Wavelet, And Stochastic Methods*. Society for Industrial and Applied Mathematics, 2005.
- [101] A. Beck and M. Teboulle, “Fast gradient-based algorithms for constrained total variation image denoising and deblurring problems,” *IEEE Transactions on Image Processing*, vol. 18, no. 11, pp. 2419–2434, 2009.
- [102] S. Ahn and J. A. Fessler, “Globally convergent image reconstruction for emission tomography using relaxed ordered subsets algorithms,” *IEEE Transactions on Medical Imaging*, vol. 22, no. 5, pp. 613–626, 2003.
- [103] F.-X. Dupé, J. M. Fadili, and J.-L. Starck, “A proximal iteration for deconvolving Poisson noisy images using sparse representations,” *IEEE Transactions on Image Processing*, vol. 18, no. 2, pp. 310–321, 2009.
- [104] M. A. T. Figueiredo and J. M. Bioucas-Dias, “Deconvolution of Poissonian images using variable splitting and augmented Lagrangian optimization,” in *2009 IEEE/SP 15th Workshop on Statistical Signal Processing, SSP ’09*, Cardiff, United Kingdom, 2009, pp. 733–736.
- [105] S. Setzer, G. Steidl, and T. Teuber, “Deblurring Poissonian images by split Bregman techniques,” *J. Visual Commun. Image Represent.*, 2009, in Press.
- [106] T. Goldstein and S. Osher, “The split Bregman method for L_1 -regularized problems,” *SIAM J. Imaging Sci.*, vol. 2, no. 2, pp. 323–343, 2009.
- [107] N. Dey, L. BlancFeraud, C. Zimmer, P. Roux, Z. Kam, J. Olivo-Marin, and J. Zerubia, “Richardson-Lucy algorithm with total variation regularization for 3D confocal microscope deconvolution,” *Microscopy Research and Technique*, vol. 69, no. 4, pp. 260–266, Apr. 2006.
- [108] P. L. Combettes and V. R. Wajs, “Signal recovery by proximal forward-backward splitting,” *Multiscale Modeling & Simulation*, vol. 4, no. 4, p. 1168, 2005.

- [109] C. Chaux, J.-C. Pesquet, and N. Pustelnik, “Nested iterative algorithms for convex constrained image recovery problems,” *SIAM J. Imag. Sci.*, vol. 2, no. 2, pp. 730–762, 2009.
- [110] J. Barzilai and J. M. Borwein, “Two-point step size gradient methods,” *IMA Journal of Numerical Analysis*, vol. 8, no. 1, pp. 141–148, January 1988.
- [111] S. P. Boyd and L. Vandenberghe, *Convex Optimization*. New York: Cambridge University Press, 2004.
- [112] R. T. Rockafellar and R. J.-B. Wets, *Variational Analysis*. Springer, 2009.
- [113] W. W. Hager, D. T. Phan, and H. Zhang, “Gradient-based methods for sparse recovery,” *SIAM Journal on Imaging Sciences*, vol. 4, no. 1, p. 146, 2011.
- [114] R. T. Rockafellar, *Convex Analysis*. Princeton Univ Press, 1997.
- [115] J. Fessler, “Image reconstruction toolbox,” <http://www.eecs.umich.edu/~fessler/code>.
- [116] M. Raginsky, S. Jafarpour, R. Willett, and R. Calderbank, “Fishing in Poisson streams: focusing on the whales, ignoring the minnows,” in *Proceedings of the Forty-Fourth Conference on Information Sciences and Systems*, 2010, arXiv:1003.2836.
- [117] J. Salmon, C.-A. Deledalle, R. M. Willett, and Z. T. Harmany, “Poisson noise reduction with non-local PCA,” in *2012 IEEE International Conference on Acoustics, Speech and Signal Processing (ICASSP)*, Mar. 2012, pp. 1109–1112.
- [118] J. Salmon, Z. T. Harmany, C.-A. Deledalle, and R. M. Willett, “Poisson noise reduction with non-local PCA,” *ArXiv e-prints*, Jun. 2012.
- [119] M. Mäkitalo and A. Foi, “Optimal inversion of the Anscombe transformation in low-count Poisson image denoising,” *IEEE Transactions on Image Processing*, vol. 20, no. 1, pp. 99 –109, Jan. 2011.
- [120] T. J. Muldoon, M. C. Pierce, D. L. Nida, M. D. Williams, A. Gillenwater, and R. Richards-Kortum, “Subcellular-resolution molecular imaging within living tissue by fiber microendoscopy,” *Optics Express*, vol. 15, no. 25, pp. 16 413–16 423, Dec. 2007.

- [121] T. J. Muldoon, S. Anandasabapathy, D. Maru, and R. Richards-Kortum, “High-resolution imaging in Barrett’s esophagus: A novel, low-cost endoscopic microscope,” *Gastrointestinal Endoscopy*, vol. 68, no. 4, pp. 737–744, 2008.
- [122] N. Chenouard, I. Bloch, and J.-C. Olivo-Marin, “Particle tracking in fluorescent microscopy images improved by morphological source separation,” in *Proc. ICIP*, 2009.
- [123] J. A. Tropp, “Greed is good: Algorithmic results for sparse approximation,” *IEEE Transactions Information Theory*, vol. 50, no. 10, pp. 2231–2242, 2004.
- [124] D. L. Donoho and M. Elad, “Optimally sparse representation in general (nonorthogonal) dictionaries via ℓ_1 minimization,” *Proceedings of the National Academy of Sciences*, vol. 100, no. 5, pp. 2191–2202, 2003.
- [125] H. V. Henderson and S. R. Searle, “On deriving the inverse of a sum of matrices,” *SIAM Review*, vol. 23, no. 1, p. 53, 1981.
- [126] D. J. Tylavsky and G. R. Sohie, “Generalization of the matrix inversion lemma,” *Proceedings of the IEEE*, vol. 74, no. 7, pp. 1050– 1052, Jul. 1986.
- [127] J. Nocedal and S. J. Wright, *Numerical Optimization*, 2nd ed., ser. Springer series in operations research. Springer, 1999.
- [128] S. P. Boyd, N. Parikh, E. Chu, B. Peleato, and J. Eckstein, “Distributed optimization and statistical learning via the alternating direction method of multipliers,” *Foundations and Trends in Machine Learning*, vol. 3, pp. 1–122, 2010.
- [129] D. H. Ballard, “Generalizing the Hough transform to detect arbitrary shapes,” *Pattern Recognition*, vol. 13, no. 2, pp. 111–122, 1981.
- [130] J. B. Pawley, Ed., *Handbook of Biological Confocal Microscopy*. New York: Plenum Press, 1995.
- [131] W. Denk, J. Strickler, and W. Webb, “Two-photon laser scanning fluorescence microscopy,” *Science*, vol. 248, no. 4951, pp. 73–76, 1990.
- [132] University of Wisconsin Laboratory for Optical and Computational Instrumentation, “Multiple-photon excitation fluorescence microscopy,” <http://www.loci.wisc.edu/multiphoton/mp.html> on Nov. 28, 2006.

- [133] W. Denk and K. Svoboda, “Photon upmanship: Why multiphoton imaging is more than a gimmick,” *Neuron*, vol. 18, no. 3, pp. 351–357, 1997.
- [134] W. Denk, J. H. Strickler, and W. W. Webb, “Two-photon laser scanning fluorescence microscopy,” *Science*, vol. 248, no. 4951, pp. 73–76, 1990.
- [135] J. M. Squirrell, D. L. Wokosin, J. G. White, and B. D. Bavister, “Long-term two-photon fluorescence imaging of mammalian embryos without compromising viability,” *Nature Biotechnology*, vol. 17, no. 8, pp. 763–7, 1999.
- [136] J. White and J. M. S. K. W. Eliceri, “Applying multiphoton imaging to the study of membrane dynamics in living cells,” *Traffic*, vol. 2, no. 11, pp. 775–80, 2001.
- [137] R. Willett and R. Nowak, “Multiscale Poisson intensity and density estimation,” *IEEE Trans. Inform. Theory*, vol. 53, no. 9, pp. 3171–3187, September 2007.
- [138] P. L. Bartlett, S. Boucheron, and G. Lugosi, “Model selection and error estimation,” *Machine Learning*, vol. 48, no. 1, pp. 85–113, 2002.
- [139] M. Raginsky, S. Jafarpour, Z. T. Harmany, R. F. Marcia, R. M. Willett, and R. Calderbank, “Performance bounds for expander-based compressed sensing in Poisson noise,” *IEEE Transactions on Signal Processing*, vol. 59, no. 9, pp. 4139–4153, Sep. 2011.
- [140] L. Balzano, R. D. Nowak, and B. Recht, “Online identification and tracking of subspaces from highly incomplete information,” *ArXiv e-prints*, Jun. 2010.
- [141] B. Eriksson, L. Balzano, and R. D. Nowak, “High-rank matrix completion and subspace clustering with missing data,” *ArXiv e-prints*, Dec. 2011.
- [142] A. C. Sankaranarayanan, C. Studer, and R. G. Baraniuk, “CS-MUVI: video compressive sensing for spatial-multiplexing cameras,” in *2012 IEEE International Conference on Computational Photography (ICCP)*, Apr. 2012, pp. 1–10.
- [143] J. He, L. Balzano, and J. C. Lui, “Online robust subspace tracking from partial information,” *ArXiv e-prints*, Sep. 2011.
- [144] E. J. Candès, X. Li, Y. Ma, and J. Wright, “Robust principal component analysis?” *Journal of the ACM*, vol. 58, no. 3, pp. 11:1–11:37, Jun. 2011.

Biography

Zachary Taylor Harmany was born in Allentown, PA, USA, on June 23, 1983, to Charles C. and Pearl R. Harmany. He was also raised in Allentown, PA, living in the city until the age of seven, when his family moved to the quieter suburb of South Whitehall. He graduated from Parkland High School in 2001.

He began his undergraduate education in the fall of 2001 as a physics major at The Pennsylvania State University at University Park, PA. Ultimately he decided to also major in electrical engineering. His undergraduate advisor was the late Prof. Nirmal K. Bose, to whom he owes cultivating an appreciation for detail in work and precision of thought. He received the B.S. degree (*magna cum laude*) with honors in electrical engineering and the B.S. degree (*cum laude*) in physics from Penn State in 2006.

In the fall of 2006, he began his graduate study towards a doctoral degree in electrical and computer engineering at Duke University, under the tutelage of Prof. Rebecca Willett. His focus is in signal processing, a unique discipline that fuses physics, statistics, and mathematics. He was a Medical Imaging Training Grant fellow, which offered a unique opportunity to study the medical imaging field as an exciting application area for signal processing techniques. He graduated from Duke University in the Fall of 2012. His research interests now include machine learning, compressed sensing, nonlinear optimization, functional neuroimaging, and signal and image processing with applications in medical imaging, astronomy, and night vision. His hobbies include weightlifting, repairing espresso machines, and playing guitar.